

XXXIV INTERNATIONAL SCIENTIFIC CONFERENCE

ON TRANSPORT, ROAD-BUILDING, AGRICULTURAL, HOISTING & HAULING AND MILITARY TECHNICS AND TECHNOLOGIES

trans & MOTAUTO - 2026 -

22-25.06.2026, VARNA, BULGARIA

PROCEEDINGS

ISSN 1313-5031 (Print)
ISSN 2535-0307 (Online)

SCIENTIFIC-TECHNICAL UNION OF MECHANICAL ENGINEERING - INDUSTRY 4.0
BULGARIA

XXXIV INTERNATIONAL SCIENTIFIC CONFERENCE

trans & MOTAUTO '26

PROCEEDINGS

ISSN 1313-5031 (Print), **ISSN** 2535-0307(Online)
YEAR IX, USSUE 1 (13), SOFIA, BULGARIA 2026

22-25.06.2026
VARNA, BULGARIA

Publisher: Scientific-technical union of mechanical engineering „Industry-4.0"

INERNATIONAL EDITORIAL BOARD

CHAIRMAN: Dr.h.c. Prof. DSc PETAR KOLEV, BULGARIA

Assoc. Prof. Aleksandar Kostikj	NM	Prof. Miho Mihov	BG
Assoc. Prof. Andrey Ferenets	RU	Prof. Murat Dogruel	TR
Assoc. Prof. Beti Angelevska	NM	Assoc. Prof. Naser Lajqi	KO
Prof. Dainis Berjoza	LV	Assoc. Prof. Natalia Sidenko	LV
Prof. Daniela Todorova	BG	Prof. Natasa Tomic-Petrovic	RS
Prof. Emilia Andreeva-Moschen	AT	Prof. Nikolay Georgiev	BG
Assoc. Prof. Igor Penkov	EE	Prof. Nikolay Ovchenkov	RU
Prof. Igor Smirnov	UA	Prof. Oleg Sharkov	RU
Prof. Igor Taratorkin	RU	Acad. Polatbeg Zhunisbekov	KZ
Colonel Prof. Iliyan Lilov	BG	Assoc. Prof. Rinat Kurmaev	RU
Prof. Jozef Majerčák	SK	Prof. Sanjin Troha	HR
Prof. Lech Sitnik	PL	Prof. Teymuraz Kochadze	GE
Prof. Ljudmila Boyko	UA	Prof. Vadim Zhmud	RU
Prof. Madaminjon Aripdzanov	UZ	Prof. Wolfgang Fengler	DE
Assoc. Prof. Martin Kendra	SK	Assoc. Prof. Zoran Jovanovic	RS
Prof. Massimo Borghi	IT	Assoc. Prof. Ahmet H. Ertas	TR

C O N T E N T S

TRANSPORT TECHNICS. INVESTIGATION OF ELEMENTS. RELIABILITY

Dynamic analysis of hoist elevator for the case of load lifting
Ilir Doçi, Drita Abazi 5

Using laser surface microtexturing to improve tribological properties of surfaces
Jakub Brezina, Štefan Novotný, Janette Brezinová, Péter Pinke 10

Operation guidelines for proper arrangement of pumps in the marine steam propulsion system
Mrzljak Vedran, Prpić-Oršić Jasna, Jelić Maro, Baressi Šegota Sandi 15

Application possibilities of ultrasonic testing for quality control of resistance spot welds in the automotive industry
Ján Viňáš, Marie Kolaříková, Ladislav Kolařík 19

Implementation of Composite Materials into the Design of an Experimental Vehicle for the Shell Eco-Marathon Competition
Štefan Kender, Štefan Novotný 24

Application of SPC statistical process control method and measurement analysis of welded steel components in the motorcycle industry
Vid Božič 28

Evaluation of Adhesively Bonded Joints for Repair of Exterior Automotive Plastic Parts
Štefan Novotný, Jakub Brezina, Janette Brezinová 34

Comparative thermo-mechanical severity assessment of automotive brake discs under repeated braking cycles
Halil Demolli, Gezim Preniqi, Shkelzen Shabani 41

Using AI agents to create work instructions for NDT and VT product inspection in heavy industry.
Marek Grega, Janette Brezinová 45

Mesh-Converged Modal Profile Assessment of Functionally Graded Spur Gears
Shkelzen Shabani, Halil Demolli 50

TRANSPORT. SAFETY AND ECOLOGY. LOGISTICS AND MANAGEMENT

A new paradigm for analyzing the work of transport operators based on sEMG and MyoMotion studies
Iwona Grabarek, Sylwia Bęczkowska, Katarzyna Grzybowska, Zuzanna Zysk 53

Traffic safety in Serbia and automotive industry today
Nataša Tomić-Petrović 57

Technical validity of motorcycles and mopeds as a factor of road safety in the Republic of Croatia
Luka Zovak, Goran Košir, Goran Zovak, Marija Ferko 59

Methodological foundations for the organization of local transport systems in georgia
Izolda Dangadze, Teimuraz Kochadze, Gvantsa Ardjevanidze, Jumber Chogovadze, Romanoz Topuria 64

Analysis of the Effectiveness of Remediation of Identified Hazardous Locations in the Republic of Croatia
Ţeljko Šarić, Ivana Vuk, Tomislav Kučinić, Andrej Kunštek 67

Determining the use indicators of the wagon vehicle and improving the efficiency of the transportation process
Israil Shukur Oglu Elyazov, Etibar Bakhtiyar Oglu Guliyev 71

Simulation Modeling of Vehicle Passage Over a Road Irregularity for Forensic Accident Reconstruction
Svilen Stefanov, Tihomir Yotkov, Yoana Kotseva 77

ENGINES. EFFICIENCY

Development of a methodology for improving the performance of diesel engines using the acoustic emission method
Viktor Prokopenko, Maris Hauka, Juris Gutans, Guntis Strautmanis, Leonid Vinogradov 81

Impact of Ammonia Fuel on Waste Heat Availability in Marine Engines
Ozren Bukovac, Zvonimir Klasan 84

Experimental Analysis of Diesel Engine Performance Using the Intelligent Common Rail CR/EDC15 Injection System
Naser Lajqi, Shpetim Lajqi, Ilir Doçi, Kushtrim Lajqi 87

Prospects for the use of liquefied gas in marine diesel engines
Romanoz Topuria, Teimuraz Kochadze, Mikheil Lejava, Zaza Shubladze, Malxaz Tavdgiridze 94

Piston secondary dynamics and their effect on blow-by, friction and power loss.
Erjon Selmani, Shpresa Caslli, Fadil Likaj 98

Dynamic analysis of hoist elevator for the case of load lifting

Ilir Doçi, Drita Abazi
University of Prishtina, Faculty of Mechanical Engineering, Prishtina, Kosovo
E-mail: ilir.doci@uni-pr.edu

Abstract**:** *The paper examines a specific type of industrial elevator known as the hoist elevator that is used for lifting and lowering various materials. These elevators are used in various construction yards and usually are mounted close to the building being constructed. The elevator consists of many mechanical and electrical parts, and besides lifting and lowering the loads and the cage, it needs to stop at a certain height to unload. The vertical motion process is controlled by the operator on the ground. The work operation analyzed in this paper is load lifting from the ground up to a certain height. During this process, the elevator is heavily loaded, and oscillations will appear due to the lifting process. The type of analysis is dynamic analysis, and the methodology consists of 3D modeling of the elevator and carrying simulations with SimWise 4D software. This enables analysis of the lifting dynamics and identification of the nature and extent of forces, torques, and stresses on the elevator parts and the form and intensity of the oscillations. Results will be presented in graphical form and discussed. Conclusions from this study will be useful for motion dynamics, strength of elevator parts, and safety at work. The Hoist elevator is modeled based on the technical data from the manufacturer.*
Keywords*: HOIST ELEVATOR, INDUSTRIAL ELEVATORS, RACK AND PINION, LOAD LIFTING, OSCILLATIONS, MODELING, SIMULATIONS*

1. Introduction

The type of the Hoist elevator taken for the study is shown in Fig.1. The example is from a local construction yard in Prishtina City. It is a type of industrial elevators, also known as Self-climbing elevators. It is mounted on the ground close to the building being constructed and is connected with rods to the building floors. Main operations of the elevator are lifting and lowering of the load, which is placed in the cabin, and lifted together with the cabin to certain height. The lifting height is 25 m. The time of holding the lifted cabin in certain height depends on the time of cargo unloading. These motion processes creates a lot of stress, strain and forces in the parts and mechanisms of the elevator.

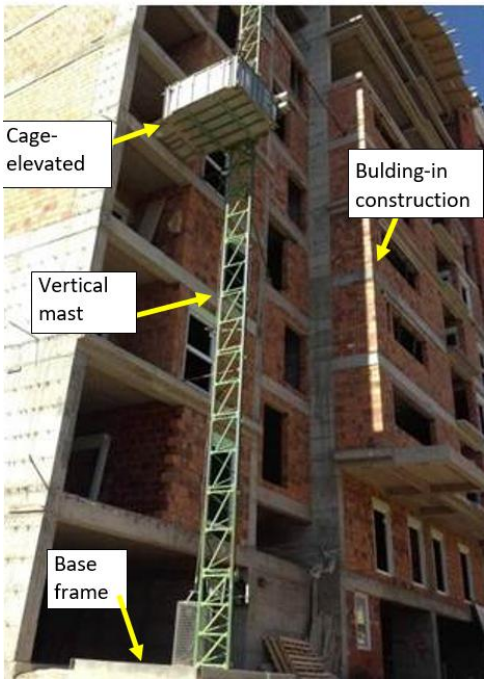


Fig.1. *Hoist Elevator in the Construction Yard*

The type of Hoist Elevator is Starlift ZL 1200M. It's main technical features are shown in Table 1 [1].

Main parts of the Hoist elevator, shown in Fig.1 and Fig.2, are Vertical mast, cage (cabin), bottom frame, rack and pinion drive mechanism, two electromotors and electrical controls which are usually manual.

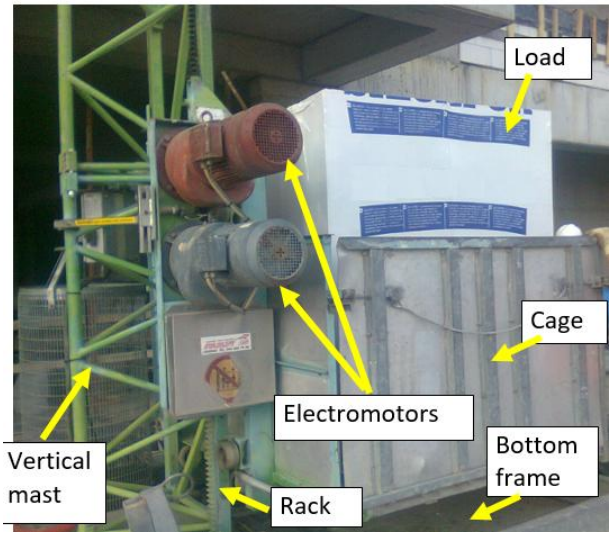


Fig.2. *Cabin and the drive mechanism of the Hoist Elevator*

Table.1. Technical features of Hoist elevator [1]

Elevator Features	Value
Model	Starlift ZL 1200
Capacity	1200 kg
Lifting height	25 m
Length of Mast	30 m
Tare weight	560 kg
Dimensions of cage	1.2 x 1.8 m x 1.5 m
Electromotor Power	2 x 4.4 kW
Rack Length	25 m
Pinion/ Gear Diameter	

The drive systems consist of two electro motors that are connected with two pinions, as a part of rack and pinion gearing systems to lift and lower the cage (Fig.2, Fig.3) [2]. Rack is a long bar with teeth attached to it. It connected through beams with other two vertical bars of the vertical mast, which is a truss system with three main vertical bars and sections of connected beams (Fig.1).

Results of the research will be focused for key parts of the elevator. Forces, force moments and stress during lifting with full loading are considered main influential parameters for measuring strength and strain in the elevator parts [4], [5], [6].

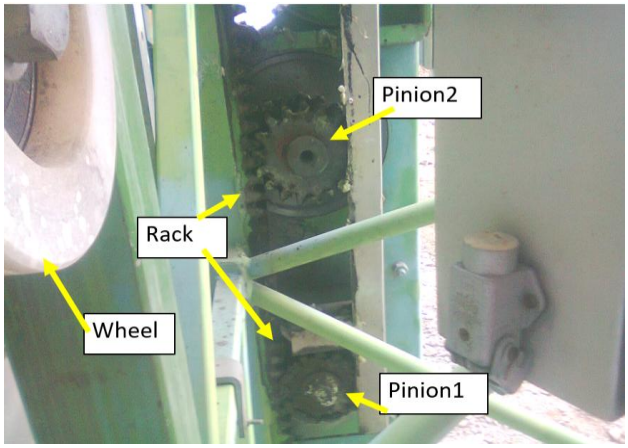


Fig.3. *Rack and pinion gear system in the vertical mast [1]*

Methodology of analysis is 3D model design with software and carrying simulations [5], [8]. Through simulations, which run in time, results will be acquired and presented in graphical form and then discussed. Analysis will be carried for the maximal lifting capacity Q = 1200 kg, Lifting velocity will be v_{lift} = *0.2 m/s*. These are a type of dynamic analysis.

About the Literature review, there are few papers that have studied Hoist elevators, shown in the References, with studies about dynamic analysis [4], [8], [11], drive systems [6], [9], professional investigation [7], design [10], elevator safety [12], [13], [14], motion control and regulation [15], [16].

2. Modeling of the Hoist elevator and carrying simulations

Prior to the simulations and analysis, the 3D model of the Hoist elevator is created with software SimWise 4D (Fig.4) [3]. The model has 195 parts and 488 constraints, and t hen interconnected. Majority of parts are teeth of the rack and pinions. After the 3D model design, simulations are carried out for certain amount of time to get the results. Analysis will be implemented using two numerical Methods that are integral part of the software: Finite Elements Method (FEM) and Numerical Kutta-Merson Method.

Load Q lifted has a form of box with dimensions: *Length =1.2 m, Width= 1.2 m, Height = 1 m.* In the model of the elevator, initial position is when the cage is in the starting lowest positions, close to the base frame, loaded and ready to be lifted (Fig.4)

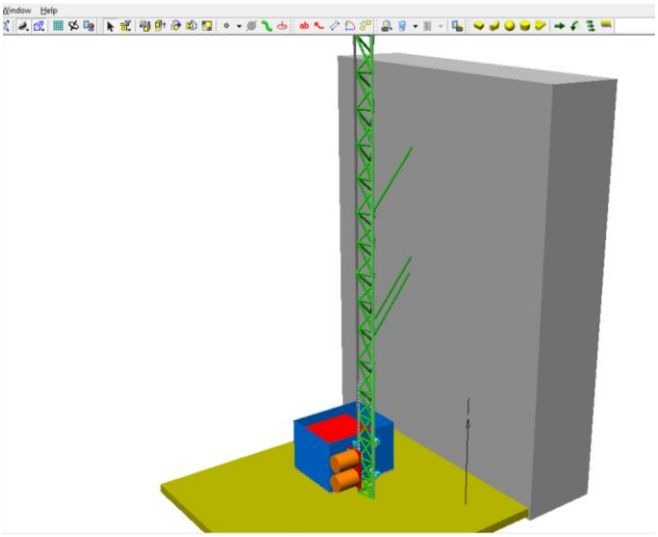


Fig. 4. *3D Model in the software design canvas of the Hoist elevator attached to the building [3]*

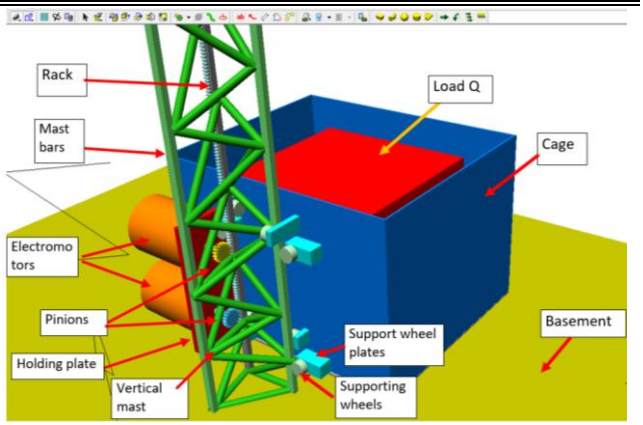


Fig. 5. *3D Model of the Hoist elevator with main parts [3]*

For adequate analysis of the elevator lifting motion, simulations will be organized as close as to the real lifting process [5], [8]. The cage will be lifted until the simulation time 8 s.

3. Results of elevator lifting

Results of the analysis will be presented for main dynamic parameters for some main parts of the elevator and will include important dynamic parameters: Forces and torque in the pinion, Forces in the pinion teeth, Forces in the Support wheels, stress in the Cage, stress in the Vertical bar of the Mast.

3.1. Force and Torque on the pinion

Pinions are gears, and one of the main parts of the drive system (Fig3. & Fig.6). They are connected in one side with shaft, and through the holding plate with the electromotor. On other side they are geared with their teeth to the teeth of the rack, and with their rotation lift up the cage. There are two pinions. Each pinion has diameter D_p = 125 mm, and has 18 teeth (Fig.6).

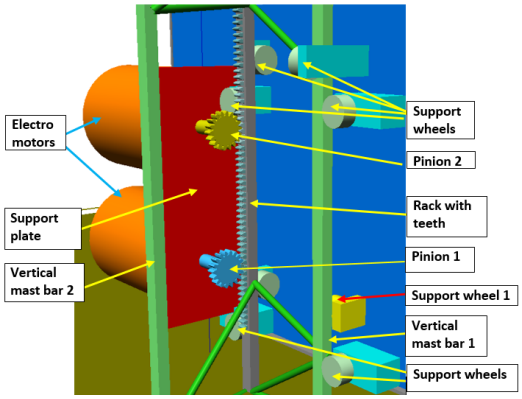


Fig.6. *Close view of the drive system (some beams of Vertical mast are hidden for better view)*

In Fig.7 is the graph of Total Force in *Pinion 1* (Fig.6), which appears from the gearing with the Rack as it rotates. This is the resultant force acting on gears. The length of simulation is 8.3 s.

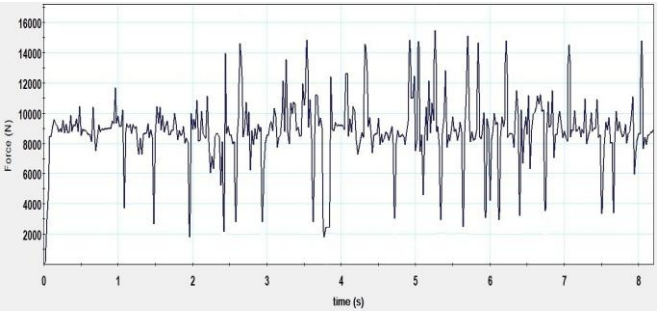


Fig. 7. *Resultant Force on the Pinion 1*

When the pinion starts to rotate and lift the cage, the curvature of the total force starts with the intensity around $F_{pav} \approx 9500\ N$ (Fig.7). Based on the fluctuations of the Force curvature, this can be approximated as a middle or average value of the force in entire lifting process, close to the static value. After the time $t = 1\ s$ the intensity does not change significantly, but the nature of the curvature shows increased oscillations. In some periods of the process, there are transient, short-term peaks of force values because of intense oscillations. These are particularly present in the period between $t = 2.3\ s$ and $t = 7\ s$.

During the entire process, the pinion is heavily loaded with dynamic forces with high oscillations that result in intense amplitudes. Maximum value of the force is $F_{pmax} \approx 15500\ N$, at the time $t \approx 5.3\ s$, appearing shortly, like a pulse. The maximal value of force is for about 63% higher than its average value $F_{pav} \approx 9500\ N$ which is a matter of concern.

Important parameter for the analysis is *Peak-to-peak amplitude* λ [5], [11]. It is the difference between the minimal and maximal values of force in a short period and represents maximal intensity of oscillations. In the time interval $5.7\ s < t < 5.8\ s$ the peak-to-peak amplitude is $\lambda_{tp} = 15000 - 2500 = 12500\ N$. The frequency of the oscillations during the lifting is around $v \approx 15\ Hz$ [5], [8], [11].

In the Fig.8 is the graph of the Torque (Force Moment) on the *Pinion 1* as it rotates and lifts. Average value of the torque is $M_{av} \approx 550\ Nm$. The form of torque curvature shows heavy oscillations in entire lifting process, similar to the graph of total force (Fig.7). In some periods of the lifting, there are short-term peaks of torque values because of intense oscillations. These are notably present after time $t = 1\ s$. Maximum value of the Torque is $M_{pmax} \approx 900\ N$, at the time $t \approx 4.3\ s$. This is also for about 63% higher than its average value, similar with the result of the total force.

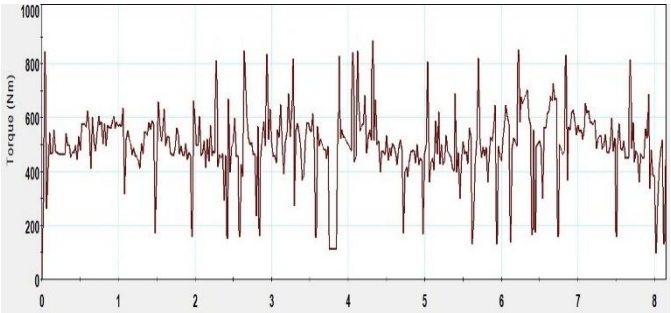


Fig. 8. *Torque (Force Moment) in the Pinion 1 (Nm)*

Conclusion is that pinions are heavy loaded parts that undergo forces and torque with high oscillations and amplitudes, and this can have negative effect in the durability and strength of the pinions.

3.2. Force on the teeth of the Pinion

It is important to find how the teeth of the pinion, as a key part of drive system, are loaded and strained. In the Fig.9 is the figure of two teeth of the Pinion 1, taken for analysis, named as *Tooth 1* and *Tooth 2*, shown with different colors. We will find the total force that acts on them. These two teeth are the first to be geared with the teeth of the Rack at the start of lifting, through the rotation of the Pinion 1.

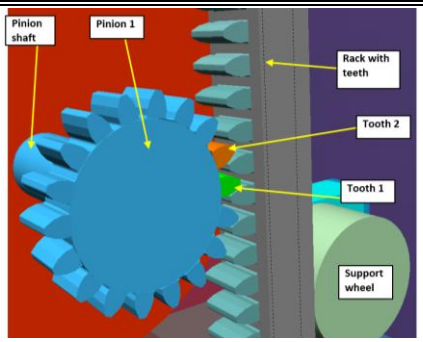


Fig.9. *View of Pinion 1 teeth's: Tooth 1 and Tooth 2*

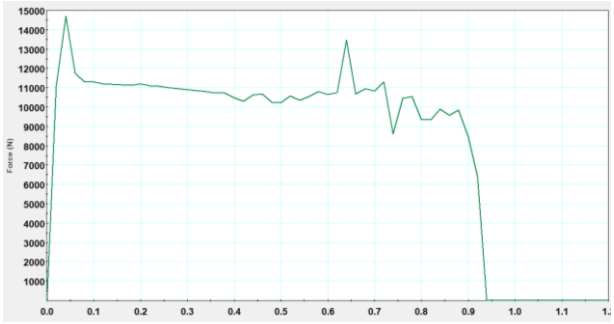


Fig. 10. *Total Force on the Tooth 1*

In Fig.10 is the graph of Total Force on the *Tooth 1* (shown in green in Fig.9). This is the first tooth at the start of the simulation that contacts another tooth of the Rack and starts rotating and lifting. The value of Force increases up to $F_{t1max} \approx 14800\ N$ at the start of the contact and lifting, which is the maximal value. After that, the curve of Force decreases to the value around $F_{t1a} \approx 10000\ N$, with oscillations. This value can be approximated as an average value of the Total Force. Then, the curve drops to zero at the time $t \approx 0.95\ s$, which means the *Tooth 1* has lost the contact with the Rack during rotation, and next teeth in the row has started to make the contact. During this short time of contact, we can notice that *Tooth 1* is heavily strained, with oscillating force acting on it. The maximal value of Force is for about 40% higher than its average value, which is a matter of concern.

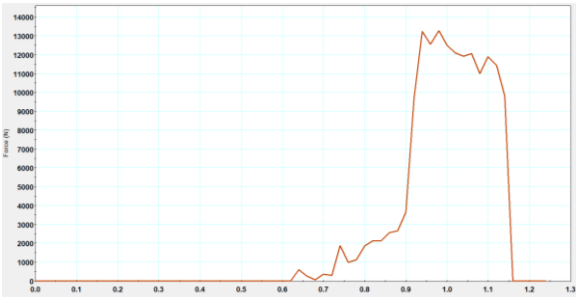


Fig. 11. *Force on the Tooth 2*

In Fig.11 is the graph of Total Force on the *Tooth 2* (shown in brown in Fig.9). This is the second tooth in the row that contacts another tooth of the Rack and continues rotating and lifting. The curve of Force starts to increase with oscillations at the time $t = 0.63\ s$, and reaches maximal value $F_{t2max} \approx 13200\ N$ at the time $t = 0.98\ s$. After that the curve of Force continues to appear shortly with oscillations, and drops to zero at the time $t = 1.16\ s$. At this time it loses the contact with the Rack during rotation. Even though the contact time is short, the force is dynamic, leading to the conclusion that the *Tooth 2* is also heavily strained part.

3.3. Force on the support Wheels

There are eight support wheels on the Drive system, some mounted parallel with Cage wall and some perpendicular to it, to enforce the stability of the lifting (Fig.5 & Fig.12). Diameter of each wheel is 100 mm. Four of them roll on the Rack, other four on the Vertical Mast Bar 1. In the Fig.12 is the close view of one support wheel taken for analysis, named as *Support Wheel 1*. It is attached perpendicularly to the Cage wall and rolls on the Vertical Mast Bar 1 (Fig.12).

In the Fig.13 is the graph of the Total Force. Based on the graph of Force in Fig.13 we can conclude that the support wheel is also heavily strained part. During the entire process, the wheel is heavily loaded with dynamic force that shows high oscillations and intense amplitudes. Based on the fluctuations of the force curve, the value $F_{wav} \approx 9000\ N$ can be approximated as an average value in entire lifting process, close to the static value. Maximum value of the force is $F_{pmax} \approx 14200\ N$, at the time $t \approx 5.3\ s$, appearing in short-term peak.

Based on this result, the maximal value of Force is for about 57% higher than its average value, which is also a matter of concern.

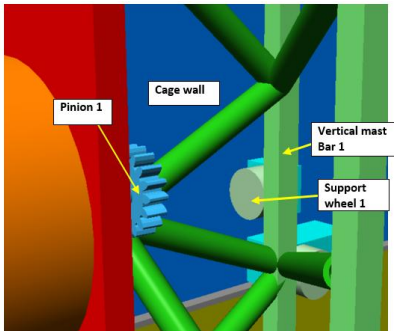


Fig.12. *View of the Support wheel 1*

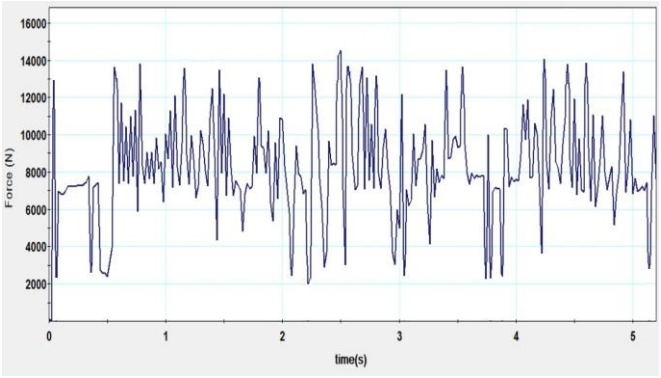


Fig. 13*. Force on the Support wheel 1*

3.4. Stresses on the Cage

In this part, we will present the stress (Von Misses) on one wall of the cage, which is connected with the drive system (Fig.14), and is considered heavily strained part of the cage. To calculate the stress the wall is meshed and calculated using Finite Elements Method (FEM). In the Fig.14 is shown visually the meshed wall in one moment in time and surface stress on the wall shown in different color. In the Bottom Left is the Legend of stress values.

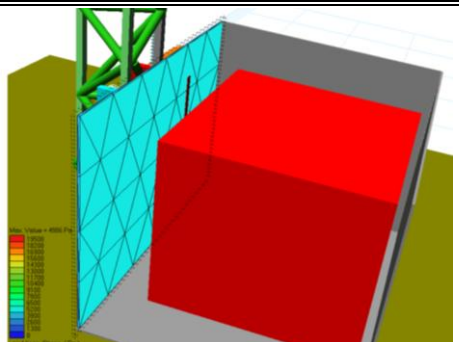


Fig. 14. *Surface Stress on the Cage wall, which is connected with the drive system*

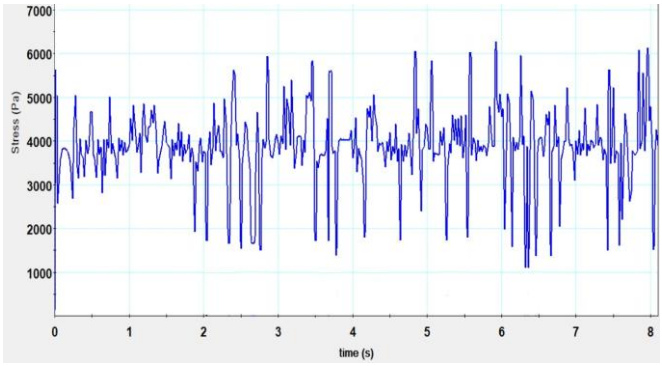


Fig.15. *Graph of the stress on the Cage wall*

In Fig.15 is the graph of stress in the Cage Wall. The form of the curvature of the stress is similar with the one on *Pinion 1* and *Support wheel*. There are heavy oscillations and high amplitudes. Average value of stress is $\sigma_{avg} \approx 4000\ Pa$. Maximum value of stress can reach $\sigma_{max} \approx 6200\ Pa$, but in the form of transient, short-term peaks of stress values as a result of intense oscillations. This value does not exceed the material durability of the cage which is $\sigma_{mat} = 2{,}69 \cdot 10^8\ Pa$, so the wall will handle the loading dynamics during the lifting process.

3.5. Stresses on the Vertical Mast Bar

Important for the research is analysis of the Vertical Mast used as a pivot and main support for lifting. We will present the stress (Von Misses) on one of the bars, in this case Vertical Mast Bar 1 (Fig.6). In the Fig.16 is a part of the model close to the Vertical bar 1. Here are shown the dispersion of stresses in one section of the Bar in one moment of time. Darker colors mean higher values of stress, presented in the Legend of values in the bottom left.

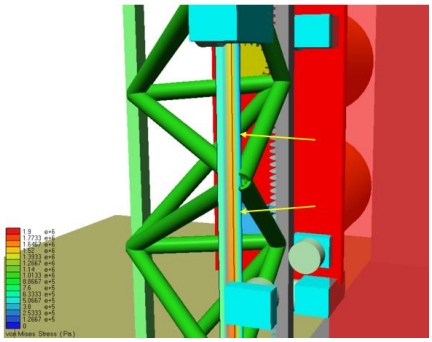


Fig. 16. *Surface Stress on the Vertical Mast Bar 1*

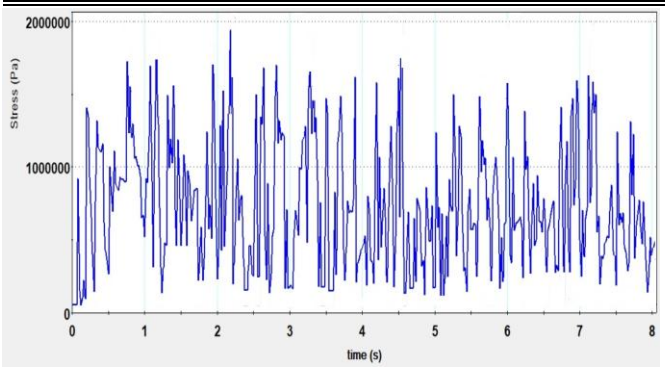


***Fig.17**. Graph of stress on the Vertical Mast Bar 1*

In Fig.17 is the graph of stress. The form of the curvature of stress shows heavy oscillations and high amplitudes, similar to previous graphs. Average value of stress is $\sigma_{avg} \approx 600000\ Pa$. Maximum value of stress can reach $\sigma_{max} = 1900000\ Pa = 1.9 \cdot 10^6\ Pa$ at time $t \approx 2.2\ s$, appearing in the form of transient, short-term peak. This value does not exceed the material durability of the Bar 1 that is $\sigma_{mat} = 3.31 \cdot 10^8\ Pa$, which means the Bar will handle the loading and stresses.

4. Conclusions

This study investigated the dynamic behavior of a construction hoist elevator during the lifting process under maximum loading conditions through 3D modeling and simulation methodology, using SimWise 4D software. Results of the analysis show dynamic and oscillatory forces, torques, and stresses that develop in the main structural parts and drive system of the Hoist Elevator.

Based on the results, the rack-and-pinion drive system, particularly the pinions and their teeth, is exposed to high dynamic loads with pronounced oscillations throughout the lifting process. Maximum force values on the pinion reached approximately 15.500 N, resulting in transient peak forces substantially exceeding average operating values that may negatively influence component durability and operational reliability.

Similar dynamic behavior was observed in the support wheels, which experienced substantial oscillatory forces, indicating that these components experience intensive loading conditions that may adversely affect long-term durability, wear resistance, and functionality.

Stress analysis of the Cage wall and Vertical mast bar showed oscillatory behavior with transient peaks; however, the calculated stresses remained significantly below the material strength limits, confirming the structural integrity under the analyzed conditions. Despite satisfying strength requirements, repeated dynamic loading and oscillations may contribute to long-term fatigue effects over prolonged service periods.

Overall, the study confirms that dynamic effects play a crucial role in the performance and safety of construction hoist elevators. Therefore, elevator design, maintenance, and safety evaluations should account not only for static loads but also for transient dynamic forces and oscillations. Consideration of these parameters can help to improve component durability, optimization of drive system performance, and enhancement of operational safety. Future studies may focus on vibration reduction methods, optimization of control systems, and fatigue-life assessment of heavily loaded components under repeated lifting cycles.

5. References

[1] Hoist elevator manual, Type Starlift ZL 1200M: http://www2.starlift.ch/wp-content/uploads/2016/05/1200.pdf

[2] Industrial Rack & pinion Elevator, https://2.imimg.com/data2/BB/HQ/MY-2743536/rack-7-pinion-elevator.pdf.

[3] *SimWise 4D*, Design Simulation, Technologies, https://www.design-simulation.com/SimWise4D/.

[4] Drita Abazi, *Shqyrtimi dinamik i skipit të ndërtimit me peshëngritje prej 1.2 ton gjatë ngritjes dhe lëshimit të ngarkesës*, Master Diploma Work, University of Prishtina, Faculty of Mechanical Engineering, Prishtina, 2015.

[5] Ilir Doci, Naser Lajqi, Afrim Sallahu, *Dynamic analysis of vehicles hydraulic lift for the case of load handling*, International Journal MTM (Machines Technologies Materials), Issue 9/2024.

[6] A. Verl, *Adaptive preloading for rack-and-pinion drive systems*, CIRP Annals, Publisher: Elsevier BV, 2018.

[7] ITEK- Technical-Technological Institute, *Professional analysis of construction hoist elevator Q=1000-1200 kg*, Prishtina, 2013.

[8] Ilir Doçi, *Influentia of the stoppage - braking system of elevator in the elevator's studs (rails) for the case of failure,* TMT 2006.

[9] B. Huang, L. Kang, B. Tan, J. Wang, Y. Zhang, *NVH Analysis and Optimization of Construction Hoist Drive System*, Issue 17/16, Energies, 2023.

[10] M. Čuchor, L. Kučera, M. Lukáč, *Design of Vehicle Lifting Equipment Using Progressive Methods*, LOGI – Scientific Journal on Transport and Logistics, Vol. 12 No. 1 2021. DOI: 10.2478/logi-2021-0022.

[11] S. Graham Kelly**,** *Mechanical Vibrations, Theory and applications*, Cengage Learning, 2012.

[12] *EN Standards of elevators with platform:* prEN 16719 ; EN 280:2013 (WI=00098021); EN 280:2013/prA1

[13] Steve Gonzalez, *Enhancing construction efficiency and safety with self climbing elevators*, Ctbuhr Research paper, 2015.

[14] Ilir Doçi, *Siguria e Mjeteve Transportuese I* (Safety of transportation Devices I), Book Chapter IX, Faculty of Mechanical Engineering, Prishtina, 2012.

[15] Sathy Rajendran and Brian Clarke, *Construction Hoists, Understanding Exposures & Controls*, Professional safety, www. Asee.org , July 2011.

[16] Yan Chen and Dr. Weidong Zhu, *Dynamics and Control of Elevator Systems*, Dynamic Systems and Vibrations Laboratory, University of Maryland Baltimore, 2007.

Using laser surface microtexturing to improve tribological properties of surfaces

Jakub Brezina[1], Štefan Novotný[1], Janette Brezinová[1], Péter Pinke[2]
Technical University of Košice, Faculty of Mechanical Engineering, Slovakia[1]
Óbudai Egyetem Bánki Donát, Faculty of Mechanical and Safety Engineering, Budapest, Hungary[2]
correspondence: jakub.brezina@tuke.sk

Abstract: *Tribological properties of functional surfaces are a key factor influencing the durability, reliability and efficiency of mechanical systems. One of the progressive approaches to surface modification is laser surface microtexturing, which allows for the precise creation of controlled microstructures capable of modifying contact conditions and lubricant retention at tribological interfaces. This article focuses on the application of laser-induced surface microtexturing to improve the tribological performance of hard nanocomposite coatings nACRo³ and nACRo⁴ . The experimental part of the research is dedicated to the preparation of microtextures on the substrate surface using a pulsed laser system, followed by the deposition of nanocomposite coatings nACRo³ and nACRo⁴ . The created microstructures are characterized in terms of their geometry, distribution and influence on the contact properties of the coated surfaces. The wettability of the microtextured surfaces was evaluated based on the measurement of the contact angle. Optimizing surface microtexture is an effective way to increase wettability and potentially improve lubrication conditions during technological processes of forming or tribological loading of materials.*
Keywords*: laser surface texturing, tribology, nanocomposite coating, wettability, contact angle, PVD coating, tool steel, die casting*

1. Introduction

The tribological properties of functional surfaces represent a key factor influencing the service life, reliability and operational efficiency of mechanical systems. Currently, growing demands to reduce energy losses, minimise wear and extend the service life of components are driving intensive research into new surface modification methods. The condition of the surface layer and the nature of the contact interface play a decisive role in load transfer, friction generation and the initiation of degradation processes during operation. For this reason, considerable attention is devoted to progressive surface engineering technologies that enable targeted modification of the topography and functional properties of surfaces according to the required operating conditions [1–3].

One of the promising methods for improving tribological properties is laser surface microtexturing [4,5,8]. This technology enables the precise and reproducible creation of microstructures with a defined geometric shape, dimensions and distribution on the material surface.

Laser surface microtexturing is a modern surface engineering technology based on the localised action of highly concentrated laser energy on the material surface [5,9]. Using precisely controlled pulsed laser systems, microstructures of various geometric shapes can be created, such as dimples, grooves, channels or regular grid-like structures, with dimensions ranging from a few micrometres to tens of micrometres. A significant advantage of this technology is the high precision of the process, the possibility of non-contact surface modification and the ability to be applied to materials with high hardness or to surfaces coated with protective coatings. Microtexture parameters, such as depth, diameter, density and the mutual arrangement of the microstructures, have a fundamental influence on the resulting tribological properties of the surface. A properly designed microtexture can reduce the real contact area between tribological pairs, promote the hydrodynamic effect of lubrication and stabilise the lubricating film during operation. In addition to tribological applications, laser microtexturing is also used to improve coating adhesion, increase corrosion resistance, control surface wettability and for the treatment of biologically active implants. Thanks to its flexibility and possibility of precise process control, laser microtexturing ranks among the promising technologies employed in the development of intelligent and highly functional surfaces for modern technical applications.

The advantages of laser microtexturing include high process flexibility, non-contact machining and the possibility of application to a wide range of engineering materials. The created microtextures can significantly influence contact conditions at the tribological interface, improve lubricant retention, promote the formation of a stable lubricating film and simultaneously reduce adhesive and abrasive wear mechanisms. In addition, the microstructures can act as lubricant reservoirs or trap wear particles, thereby contributing to the stabilisation of the tribological process [6,7,8].

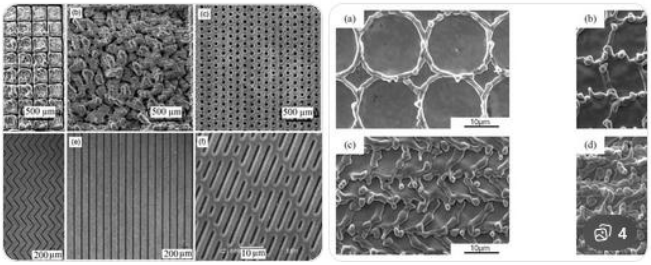


Fig. 1 *Microtextured surface produced by a pulsed laser system with regularly arranged microstructures designed to improve the tribological properties of the surface*

In the design of microtexture geometry, research in recent years has frequently drawn inspiration from natural surfaces that have been evolutionarily optimised to minimise friction, reduce adhesion or enable efficient liquid transport [13,14]. This approach, referred to as biomimetics or bionic surface design, is based on the study of structures found, for example, on shark skin, butterfly wings, lotus leaves or the surface of desert beetles. The surfaces of these organisms feature naturally formed micro- and nanostructures that provide specific functional properties, such as a self-cleaning effect, reduced flow resistance or increased wear resistance. Laser microtexturing therefore frequently employs textures in the form of regular dimples, grooves or hierarchical structures that mimic natural patterns. Biomimetic microtextures can significantly improve lubricant retention, stabilise the lubricating film and reduce contact stresses at the tribological interface. The results of several studies confirm that properly designed biomimetic structures can effectively reduce the coefficient of friction and wear rate compared to conventional smooth surfaces.

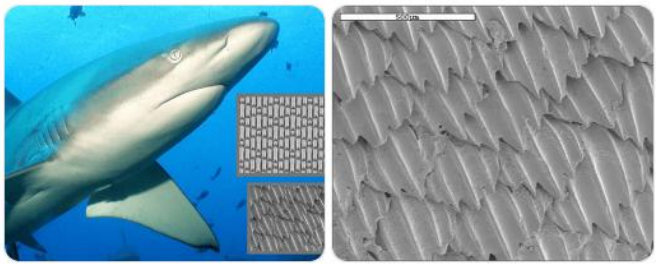


Fig. 2 *Biomimetic microtexture inspired by shark skin structure, used to reduce friction and optimise flow in tribological contact*

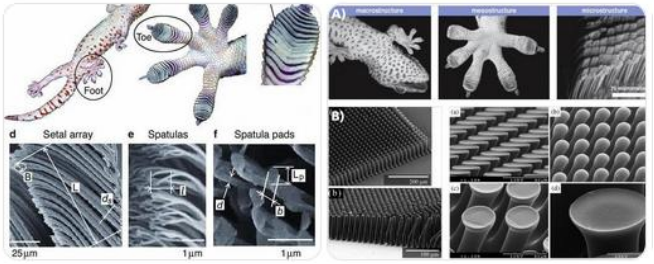


Fig. 3 *Biomimetic microstructure inspired by the surface of gecko foot pads, used to optimise the adhesive and frictional properties of functional surfaces.*

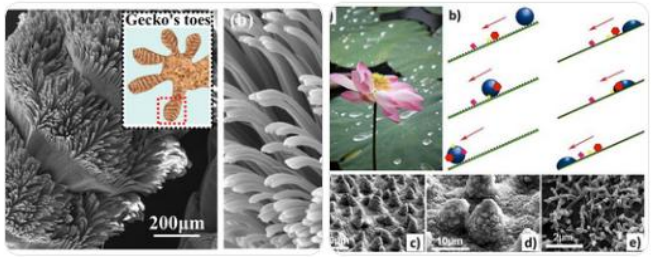


Fig. 4 *Surface structure inspired by snake skin, characterised by directionally oriented microgrooves that ensure friction reduction.*

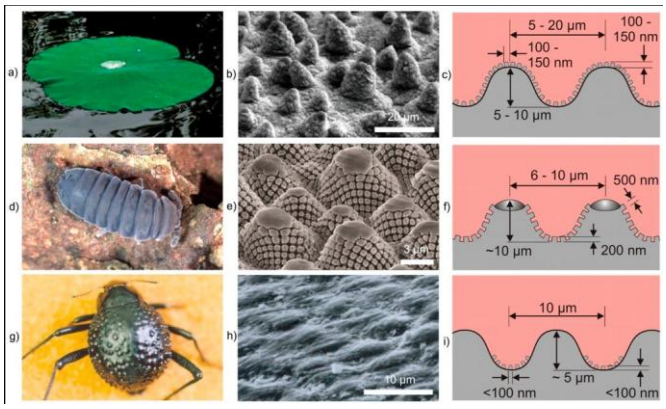


Fig. 5 *Biomimetic texture inspired by the surface of the desert beetle, used to control wettability and liquid retention on functional surfaces.*

In combination with modern hard coatings, laser microtexturing represents a promising approach to the development of highly functional surfaces intended for demanding operating conditions [10–12]. Of particular importance in this area are nanocomposite coatings, which are characterised by high hardness, good thermal stability and enhanced wear resistance. Among the progressive types of such coatings are the nanocomposite coatings nACRo³ and nACRo⁴ , which find application primarily in the field of cutting tools, engineering components and highly loaded functional surfaces. Their tribological behaviour, however, can be significantly affected by the nature of the substrate surface and its microgeometry [24-28].

This paper deals with the application of laser surface microtexturing to improve the tribological properties of nanocomposite coatings nACRo³ and nACRo⁴ . The experimental part of the study focuses on the preparation of microtextures using a pulsed laser system and the subsequent deposition of the aforementioned coatings on the modified substrate surface. Attention is paid to the characterisation of the created microstructures in terms of their geometry, distribution and influence on the contact characteristics of the surface. The tribological properties of the prepared surfaces are then analysed through friction and wear tests conducted under defined operating conditions. The work also includes a morphological analysis of the worn surfaces, which enables identification of the dominant wear mechanisms and evaluation of the effectiveness of the applied surface treatment.

2. Materials and Methods

Samples made from a material used in the manufacture of dies for high-pressure die casting of Al alloys were used for the experimental part. Specifically, this is the tool steel Uddeholm Dievar, alloyed with chromium, molybdenum and vanadium, and also containing further elements that improve its mechanical and thermal properties. This material is designed for operation at elevated temperatures and is characterised by high resistance to thermal fatigue and wear, which is typical of dies used in high-pressure aluminium die casting. In practice, it is used primarily for the manufacture of dies for aluminium alloys and their shaped and functional components. Products made from this steel are manufactured using powder metallurgy technology, which ensures a homogeneous microstructure and favourable in-service properties. The chemical composition of Uddeholm Dievar — a high-strength die steel — is given in Table 1, and the mechanical properties in Table 2.

Table 1: Chemical composition of Uddeholm Dievar substrate

Chemical element	C	Si	Mn	V	Mo	Cr
Weight [%]	0.38	0.2	0.5	0.6	2.3	5

Table 2: Mechanical properties of Uddeholm Dievar substrate

Tensile strength Rm [MPa]	Hardness [HRC]	Proof strength $Rp_{0.2}$ [MPa]	Elongation A [%]	Reduction of area [%]
1480	44	1210	13	55

Substrate Surface Texturing

The Piranha Multi FL205 laser system (ACSYS Lasertechnik), equipped with a ytterbium (Yb) fibre laser with a nominal power of 20 W, was used for substrate surface texturing. Two distinct morphological types of dimple textures were produced during experimental preparation: stochastically generated and regularly arranged. Regular textures were created in the form of grid structures with defined periodicities of 50 × 50 µm, 100 × 100 µm and 50 × 100 µm (Fig. 6). The primary objective of the surface treatment was to experimentally verify the hypothesis that dimple textures act as reservoirs for the release agent during the high-pressure die casting of aluminium alloys, thereby potentially influencing the tribological and adhesive conditions at the die-melt interface.

Application of nACRo3 and nACRo4 Coatings

Two types of physical vapour deposition (PVD) coatings — specifically nACRo3 and nACRo4 — were applied to both the textured and non-textured substrate surfaces, while a third group of samples remained uncoated. Deposition was carried out by means of advanced PVD technologies — cathodic arc evaporation and magnetron sputtering. Key process parameters, such as the supply of reactive gases (primarily nitrogen) and alloying elements (e.g. silicon), were controlled to ensure the required microstructure, high coating density and optimum adhesion to the substrate, which was supported by the use of appropriate interlayers (e.g. CrN or AlCrN).

The nACRo3 and nACRo4 coatings belong to the group of advanced nanocomposite protective layers based on the Al-Cr-N system and its modified variants. Their microstructure is derived from the concept of nc-(Al,Cr)N/a-Si_3 N_4 nanocomposites, in which nanocrystalline grains of the (Al,Cr)N phase with a typical size of approximately 5–10 nm are embedded in an amorphous or quasi-amorphous matrix. This characteristic architecture leads to a synergistic combination of high hardness, thermal stability and resistance to oxidative and tribological wear. The nanocomposite effect, based primarily on the restriction of dislocation movement (Hall–Petch mechanism) and the presence of an amorphous phase acting as a barrier to crack propagation, leads to increased hardness (approximately 30–40 GPa), toughness and resistance to delamination.

From the perspective of chemical composition and microstructural optimisation, the nACRo3 and nACRo4 coatings represent evolutionary modifications of classical AlCrN systems. The nACRo3 coating can be characterised as an older generation with a relatively higher chromium content and a lower proportion of amorphous phase. It is characterised by a fine-grained structure and a balanced ratio of hardness, adhesion and toughness. The presence of chromium promotes the formation of a stable passivation layer of $Cr_2 O_3$ at elevated temperatures, which increases the oxidation resistance of the coating. Typical hardness values range from 30 to 35 GPa, and the coating exhibits good resistance to abrasive wear and a favourable coefficient of friction. These properties predestine it primarily for applications with moderate thermal and mechanical loading, such as conventional metal cutting. The nACRo4 coating represents a newer generation with an optimised chemical composition, characterised by a higher aluminium content and often also a more pronounced proportion of amorphous phase (e.g. $Si_3 N_4$ -based). This modification leads to an even finer nanostructure and a more homogeneous phase distribution, manifested as an increase in hardness to approximately 35–40 GPa and improved resistance to plastic deformation. The higher aluminium content promotes the formation of a protective $Al_2 O_3$ layer, which ensures high oxidation stability even at temperatures exceeding 1000 °C and increases resistance to degradation processes, including recrystallisation under long-term thermal loading. From a tribological point of view, both coatings are characterised by a low coefficient of friction (approximately 0.4–0.6 depending on operating conditions) and high wear resistance even at high contact pressures. From an application standpoint, the nACRo3 and nACRo4 coatings are intended primarily for tooling applications, especially in the machining of difficult-to-cut materials such as high-temperature alloys, stainless steels and titanium alloys. Their high thermal stability enables effective use under dry machining or minimum quantity lubrication (MQL) conditions. While the nACRo3 coating offers a balanced compromise between mechanical and tribological properties under moderate loading, the nACRo4 coating is optimised for extreme conditions, such as high-speed machining where high temperatures and intense wear dominate. The differences between these coatings thus stem primarily from their chemical composition and nanostructural arrangement, which determine their resulting mechanical, thermal and tribological characteristics.

Evaluation of Surface Wettability of Samples

Within the experimental evaluation, the effect of surface texturing on surface wetting was analysed, with the contact angle as the primary monitored quantity. This parameter represents the fundamental quantitative indicator of wettability and enables evaluation of the interaction between the material surface and the liquid, which is closely linked to the surface energy and topography.

Measurements were performed on surfaces with both stochastic and regular textures, with the regular texture represented by grids with dimensions of 50 × 50 µm and 100 × 50 µm. The investigated surfaces were also coated with nACRo3 and nACRo4 PVD coatings, which can significantly influence not only the mechanical and tribological properties, but also the wetting behaviour of the surface through changes in its chemical composition and energy state. Wettability determination was carried out in accordance with the requirements of standard ISO 19403-2:2017 using the Advex Instruments measurement system. The contact angle was determined by the optical method as the angle between the tangent to the droplet and the sample surface at the three-phase boundary.

Three liquids with different physicochemical properties were selected as test media: distilled water as a reference solution and two technologically used release agents, Safety Lube 61014B and Safety Lube 68502. Each liquid was applied to the sample surface using a laboratory micropipette in the form of droplets with a defined volume. The contact angle between the sample surface and the liquid was then evaluated. To increase the reliability of the results, the measurements were performed repeatedly and subsequently subjected to statistical analysis.

3. Results

Surface Texturing

This subsection presents the results of substrate surface texturing. The created dimple structures with stochastic and regular arrangement are presented. The individual texture types are shown in Fig. 6.

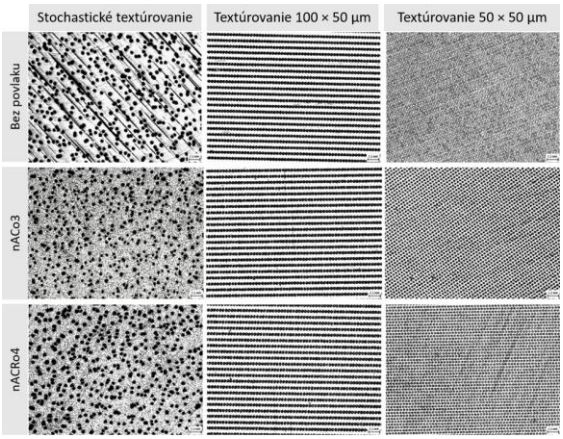


Fig. 6 Surface structuring of samples

Evaluation of Surface Wettability of Samples

The wettability of sample surfaces was evaluated by measuring contact angles. These measurements were carried out using two types of release agents, specifically Safety Lube 61014 and Safety Lube 68502. The obtained data were evaluated and mutually compared.



Fig. 6 Illustration of contact angle measurement at the droplet/substrate interface with Safety Lube 61014 B on uncoated samples

The results presented in Fig. 7 and 8 show that the release agent Safety Lube 61014B in combination with an uncoated sample exhibits the best wetting properties with the regular 100 × 50 µm texture. Conversely, for samples with nACRo3 and nACRo4 PVD coatings, the regular 50 × 50 µm texture appears most suitable in terms of wettability. This difference can be attributed to the combined effect of texture geometry and the modified surface properties of the coatings, which influence liquid spreading on the surface and droplet stability.

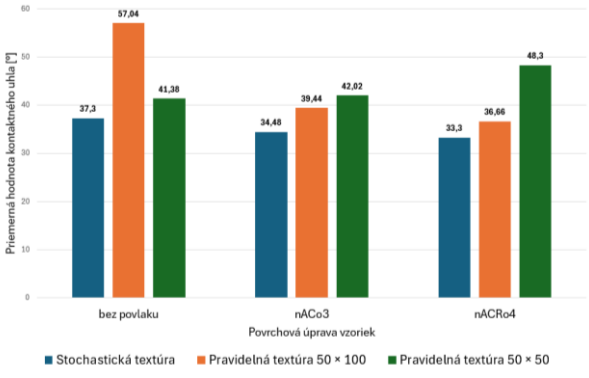


Fig. 7 Graphical representation of sample surface wettability with Safety Lube 61014 B

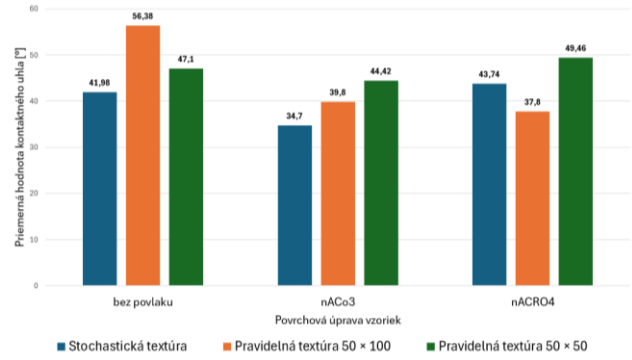


Fig. 8 Graphical representation of sample surface wettability with Safety Lube 68502

A lower surface contact angle is conditioned not only by the texture itself, but also by the type of applied coating. The results clearly show that the texture has a considerable influence on the contact angle value, and that the application of a PVD coating leads to its visible reduction. This finding has a significant impact on practical use in the technological processes of aluminium die casting, where the control of wettability is a key factor.

4. Conclusion

Based on the evaluation of contact angles, it can be stated that surface wettability was significantly influenced by both the type of surface treatment and the Safety Lube lubricant used. For both investigated lubricants, it was generally found that a lower contact angle indicates better surface wettability; the best results were achieved by samples with a regular 50 × 50 µm texture (for coated samples) or a regular 100 × 50 µm texture (for uncoated samples), or alternatively a stochastic texture depending on the coating type; surfaces without texture (“untextured”) exhibited higher contact angle values in most cases, indicating poorer wettability.

With Safety Lube 61014 B, a more pronounced effect of surface texturing was observed. The regular 50 × 50 µm texture achieved the lowest contact angle values, particularly on the nACRo3 surface, indicating improved spreading of the lubricant on the surface. Conversely, some coating-texture combinations led to an increase in contact angle, pointing to a different interaction between the lubricant and the surface microgeometry. The combination of a suitable texture and surface treatment can significantly improve the tribological properties of the surface; regular microtexture promotes more uniform lubricant spreading, although the effect of the texture also depends on the chemical character of the coating and the lubricant used.

Optimisation of surface microtexture represents an effective means of increasing wettability and potentially improving lubrication conditions in technological processes of forming or tribological loading of materials.

Acknowledgments: This research is the result of a project supported by project Visegrad Fund fellowship No. 62610056 - Scientific Cooperation in Advanced Surface Engineering: Joint Research on PTA and Laser Cladding for Die-Casting Mold Renovation. The Slovak Research and Development Agency, the VEGA Scientific Grant Agency "Possibilities of applying laser additive technologies in the restoration of functional surfaces" (1/0597/23), the Cultural and Educational Grant Agency KEGA "Hybrid education of students for the current needs of the automotive industry" (024TUKE-4/2025) and “Increasing the competences of graduates in the automotive production study program using virtual reality tools" (042TUKE-4/2026), "Innovative approaches to the restoration of functional surfaces by laser surface treatment" (APVV-20-0303) and "Integrity of protective multilayers under high-temperature exposure conditions" (APVV-24-0381).

5. References

1. ETSION, Izhak. Improving tribological performance of mechanical components by laser surface texturing. Tribology Letters. 2004, 17(4).
2. SCHILLE, J., SCHNEIDER, L., MAUERSBERGER, S. et al. High-rate laser surface texturing for advanced tribological functionality. Lubricants. 2020, 8(3).
3. MENEZES, P. L., KISHORE and KAILAS, S. V. Influence of surface texture on coefficient of friction and transfer layer formation during sliding. Wear. 2006, 261.
4. ARSLAN, A., MASJUKI, H. H., KALAM, M. A. et al. Effects of texture diameter and depth on the tribological performance of DLC coating under lubricated sliding condition. Applied Surface Science. 2015, 356.
5. SUGIHARA, T. and ENOMOTO, T. Improving anti-adhesion in aluminum alloy cutting by micro stripe texture. Precision Engineering. 2012, 36(2).
6. STRATAKIS, E., BONSE, J., HEITZ, J. et al. Laser engineering of biomimetic surfaces. Nature Reviews Physics. 2020, 2.
7. SKOULAS, E., MANOUSAKI, A., FOTAKIS, C. and STRATAKIS, E. Biomimetic surface structuring using cylindrical vector femtosecond laser beams. Scientific Reports. 2017, 7.
8. CAI, Y. et al. Enhancement of tribological performance with laser surface texturing: A review. Proceedings of the Institution of Mechanical Engineers, Part J: Journal of Engineering Tribology. 2025.
9. SHENG, Z. et al. Tribological effects of surface biomimetic micro-nano textures on metal cutting tools: A review. Biomimetics. 2025, 10(5).
10. LIN, N. et al. Surface texture-based surface treatments on Ti6Al4V alloys. Materials. 2018, 11.
11. MORABČÍKOVÁ, J. et al. Influence of laser texturing and coating on the tribological properties of tool steels. Machines. 2024, 12(5).
12. SONG, X. et al. Biomimetic lubricant-grafted surfaces on laser-textured coatings. Friction. 2024, 12(12).
13. BHUSHAN, Bharat. Introduction to Tribology. Hoboken: Wiley, 2013.
14. BHUSHAN, Bharat. Biomimetics: Bioinspired Hierarchical-Structured Surfaces for Green Science and Technology. Berlin: Springer, 2012.
15. PUOZA, J. C. et al. Research progress of surface texturing and thermal diffusion technologies in tribology. Surface Engineering and Applied Electrochemistry. 2025.
16. ROSENKRANZ, A., GRÜTZMACHER, S., GACHOT, C. and MÜCKLICH, F. Fundamentals of laser surface texturing for tribological applications. Lubricants. 2020, 8(10).
17. XING, Y., DENG, J., WU, G. and LI, S. Effect of laser surface texturing on tribological performance under starved lubrication conditions. Tribology International. 2021, 156.
18. ZHAO, H., WANG, X., LIU, Y. et al. Recent advances in biomimetic surface texturing for tribological applications. Coatings. 2021, 11(6).
19. ZHAO, L., WANG, Q., ZHANG, J. et al. Influence of laser micro-textures on wettability and tribological behavior of coated surfaces. Surface and Coatings Technology. 2021, 426.
20. VAZIRISERESHK, M. R., MARTINI, A., STRUBBE, D. and BAYLES, J. Solid lubricant performance with surface texturing under lubricated sliding conditions. Lubricants. 2021, 9(2).
21. LU, X., ZHOU, H., CHEN, Y. et al. Biomimetic micro/nanostructured surfaces fabricated by laser processing for multifunctional applications. Micromachines. 2022, 13(4).
22. BONSE, J., HÖHM, S., KIRNER, S. V., ROSENFELD, A. and KRÜGER, J. Laser-induced periodic surface structures — A scientific evergreen. IEEE Journal of Selected Topics in Quantum Electronics. 2022, 23(3).
23. PAIVA, J. M., FOX-RABINOVICH, G., LOCKS JUNIOR, E. et al. Tribological and wear performance of nanocomposite PVD hard coatings deposited on aluminum die casting tool. Materials. 2018, 11(3), 358. DOI: 10.3390/ma11030358.

24. LILLE, H., RYABCHIKOV, A., PEETSALU, P. et al. Residual stresses on various PVD hard coatings on tube and plate substrates. Coatings. 2020, 10(11), 1054. DOI: 10.3390/coatings10111054.
25. SERGEJEV, F., SURZENKOV, A., SAARNA, M. et al. Wear of different PVD coatings at industrial fine-blanking field tests. Materials Science (Medžiagotyra). 2015, 21(3), pp. 343–348. DOI: 10.5755/j01.ms.21.3.7249.
26. MORAČÍKOVÁ, J., MORAČÍK, R., KUSÝ, M. et al. Influence of laser surface texturing on tribological performance of tool steels. Journal of Materials Engineering and Performance. 2018, 27, pp. 5417–5426. DOI: 10.1007/s11665-018-3607-0.
27. PANJAN, M. et al. Surface topography of PVD hard coatings. Coatings. 2021, 11(11), 1387. DOI: 10.3390/coatings11111387.
28. DRNOVŠEK, A. et al. Surface roughness and its effect on adhesion and tribological performance of magnetron sputtered nitride coatings. Coatings. 2024, 14(8), 1010. DOI: 10.3390/coatings14081010.

Operation guidelines for proper arrangement of pumps in the marine steam propulsion system

Mrzljak Vedran[1], Prpić-Oršić Jasna[1], Jelić Maro[2], Baressi Šegota Sandi[3]
[1]Faculty of Engineering, University of Rijeka, Vukovarska 58, 51000 Rijeka, Croatia
[2]Maritime Department, University of Dubrovnik, Ćira Carića 4, 20000 Dubrovnik, Croatia
[3]Faculty of Informatics, Juraj Dobrila University of Pula, 52100 Pula, Croatia
E-mail: vedran.mrzljak@riteh.uniri.hr, jasna.prpic.orsic@riteh.uniri.hr, maro.jelic@unidu.hr, sandi.baressi.segota@unipu.hr

Abstract: *In this paper are investigated and presented the most influential operating parameters and the guidelines for proper arrangement of pumps in the condensing/feedwater heating system. The observed system operates in marine steam propulsion power plant. In the analyzed system operates three pumps: Condensate Pump (CP), Auxiliary Pump (AP) and FeedWater Pump (FWP). Considering all observed pumps, FWP is the dominant mechanical power consumer because it operates with the highest pressure difference and with the highest fluid mass flow rate. Used mechanical power and losses (energy and exergy) of all observed pumps are directly proportional to fluid mass flow rate through the pump - higher fluid mass flow rate through the pump will result with higher mechanical power used by pump and with higher losses (both energy and exergy) and vice versa. Energy and exergy efficiencies of the observed pumps have reverse proportional trends. The most influencing factor related to the pump efficiency (both energy and exergy) is the pump inlet pressure. Pump inlet pressure is directly proportional to the pump exergy efficiency, but simultaneously pump inlet pressure is reverse proportional to pump energy efficiency.*
KEYWORDS: PUMP ANALYSIS, PUMP ARRANGEMENT, OPERATION DYNAMICS, DEPENDENT VARIABLES, MARINE STEAM PROPULSION SYSTEM

1. Introduction

Pumps are inevitable components of any steam power plant or system [1]. At least two pumps (condensate pump and feedwater pump) must operate in the condensing/feedwater heating system of any steam power plant [2, 3]. Along with two mentioned ones, recent condensing/feedwater heating systems are complex ones and they usually have one or more additional auxiliary pump [4, 5].

Any condensing/feedwater heating system has a main goal to increase water temperature (as well as pressure) before it enters steam generator [6]. In such way can be obtained notable savings in a consumption of fuel used in steam generator [7]. Therefore, without pumps, such systems cannot be operable.

In the literature can be found analyses related to the entire condensing/feedwater heating system and guidelines for its proper operation [8, 9]. However, operation guidelines for proper arrangement of the pumps in that system are still missing.

In this paper are presented operation guidelines and the most influencing operating parameters which should be considered for proper pump arrangement in the condensing/feedwater heating system. The observed system and three pumps which operate in it are placed in marine steam propulsion power plant. The analysis will show relations between used mechanical power, efficiencies and losses (both energy and exergy) of all pumps and the operating parameters which have the dominant impact on them.

2. Pumps position in marine condensing/feedwater heating system and principle of their operation

Pumps observed in this paper are Condensate Pump (CP), Auxiliary Pump (AP) and FeedWater Pump (FWP) which operates in condensing/feedwater heating system of marine steam propulsion power plant, Fig. 1.

Along with the observed pumps, condensing/feedwater heating system is composed of two High Pressure Feedwater Heaters (HPFH1 and HPFH2) and with two Low Pressure Condensate Heaters (LPCH1 and LPCH2). Both High Pressure Feedwater Heaters get a steam for heating purposes from the High Pressure Cylinder (HPC) of the main turbine, while both Low Pressure Condensate Heaters get a steam for heating purposes from the Low Pressure Cylinder (LPC) of the main turbine. Between High Pressure Feedwater Heaters and Low Pressure Condensate Heaters is mounted Deaerator which get steam for heating and deaerating purposes from Intermediate Pressure Cylinder (IPC) of the main turbine. In addition, observed condensing/feedwater heating system has one additional auxiliary heater which collects all steam leakages from the entire plant and uses it for increasing water temperature before LPCH1.

CP collects condensate obtained in the main steam condenser and delivers it to the Deaerator, Fig. 1. AP is used for returning condensate obtained from heating steam to the main water line (all other heating steam condensate returns were performed by reducing condensate pressure using pressure reducing valves [10]). Finally, FWP takes water from the Deaerator, increase its pressure and delivers it through High Pressure Feedwater Heaters to the steam generator.

In Fig. 1 are also presented operating points on each pump inlet and outlet relevant for the analysis (for the CP relevant operating points are A and B, for AP relevant operating points are C and D, and for FWP relevant operating points are E and F).

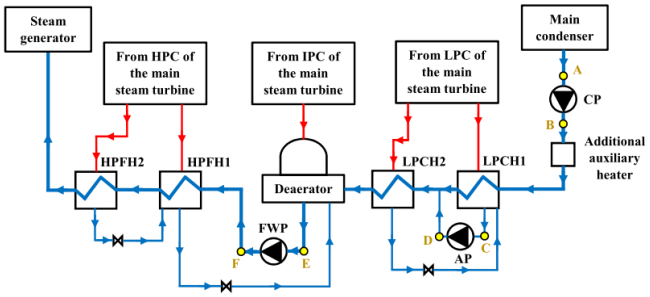


Fig. 1. *Pumps arrangement in the condensing/feedwater heating system of marine steam propulsion plant along with operating points required for the analysis*

For each of the observed pumps, in this paper is performed an energy analysis. Energy analysis of any pump is based on the comparison of ideal (isentropic) and real (polytropic) water pressure increase process. For the CP, both real and ideal pressure increase processes are presented in Fig. 2 (specific enthalpy-specific entropy diagram). For any other pump, the ideal and real pressure increase processes look the same like these in Fig. 2 (the only change occur in water operating parameters).

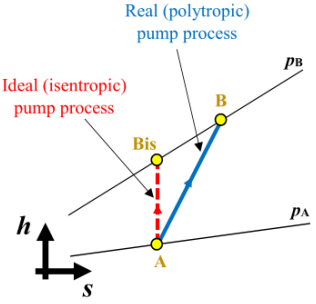


Fig. 2. *Ideal (isentropic) and real (polytropic) pressure increase process of condensate pump (CP) in h-s diagram*

Ideal (isentropic) pressure increase process neglects all the losses and water specific entropy remains always the same. Real (polytropic) pressure increase process considers the losses and water specific entropy increases, as presented in Fig. 2 [11].

Any pump consumes mechanical power for the pressure increase process. Due to neglecting all the losses which occur in the pressure increase process, in ideal process the same pump will consume the lowest possible mechanical power. In real exploitation, it is impossible to obtain an ideal process on any pump, but ideal process can and should be a guideline for losses reducing.

3. Equations for the energy analysis of pumps

Energy analysis of any system or component is based on the first law of thermodynamics [12, 13]. In an energy analysis exists some general equations and balances which should always be satisfied – they will be presented first, after which will be presented equations for the energy analysis of the specific pump.

3.1. General energy equations

The main energy balance equation valid for any system or component is [14]:

$$\dot{Q}_{\text{in}} + P_{\text{in}} + \sum \dot{E}n_{\text{in}} - \dot{Q}_{\text{out}} - P_{\text{out}} - \sum \dot{E}n_{\text{out}} - \dot{E}n_{\text{L}} = 0, \quad (1)$$

where $\dot{Q}$ is heat energy transfer, P is mechanical power, index in is related to the inlet (input), index out is related to outlet (output) and index L is related to loss. $\dot{E}n$ is a total energy flow of any fluid stream which is defined by an equation [15]:

$$\dot{E}n = \dot{m} \cdot h, \quad (2)$$

where $\dot{m}$ is mass flow rate and h is fluid specific enthalpy. If in the component or system did not occur fluid leakages, valid mass flow rate balance is [16]:

$$\sum \dot{m}_{\text{in}} = \sum \dot{m}_{\text{out}}. \quad (3)$$

General energy efficiency equation, valid for any system or component is [17]:

$$\eta_{\text{en}} = \frac{\text{CUMULATIVE ENERGY OUTPUT}}{\text{CUMULATIVE ENERGY INPUT}}. \quad (4)$$

3.2. Equations for the energy analysis of observed pumps

All equations for the energy analysis of the observed pumps are developed according to guidelines and recommendations from the literature [18-20]. The energy analysis equations will be presented for the Condensate Pump (CP) only, for other pumps the equations are the same (pressure increase processes are defined according to Fig. 2), but the operating points, presented in Fig. 1, for each pump differs. Different operating points for each pump denotes different pressures, temperatures and mass flow rates for each pump. Markings in the CP energy analysis equations are related to operating points from Fig. 1 and Fig. 2.

CP mass flow rate balance is:

$$\dot{m}_{\text{A}} = \dot{m}_{\text{B}} = \dot{m}_{\text{Bis}}. \quad (5)$$

Ideal (isentropic) mechanical power of CP which will be theoretically consumed is:

$$P_{\text{ID,CP}} = \dot{m}_{\text{A}} \cdot (h_{\text{Bis}} - h_{\text{A}}). \quad (6)$$

Real (polytropic) mechanical power consumed by CP is:

$$P_{\text{RE,CP}} = \dot{m}_{\text{A}} \cdot (h_{\text{B}} - h_{\text{A}}). \quad (7)$$

CP energy loss is:

$$\dot{E}n_{\text{L,CP}} = P_{\text{RE,CP}} - P_{\text{ID,CP}}. \quad (8)$$

Energy efficiency of CP is:

$$\eta_{\text{en,CP}} = \frac{P_{\text{ID,CP}}}{P_{\text{RE,CP}}}. \quad (9)$$

4. Fluid (water) operating parameters required for the analysis of all observed pumps

In each operating point for all observed pumps from Fig. 1, water operating parameters are found in [21] and presented in Table 1. It should be highlighted that in [21] were found water pressure, temperature and mass flow rate in each operating point of all observed pumps, other operating parameters are calculated by NIST-Refprop 9.0 software [22]. In Table 1 are presented operating parameters of the real (polytropic) pressure increase process in each pump.

As described before, ideal (isentropic) pressure increase process of each pump is the process between the same pressures, with the same fluid mass flow rates, but in such process is assumed that fluid specific entropy remains constant from the pump inlet until the pump outlet. For each observed pump, water operating parameters in ideal (isentropic) pressure increase process are presented in Table 2.

Table 1. *Water operating parameters at each pump inlet and outlet – real (polytropic) pressure increase process*

Pump	O.P.*	Temperature (K)	Pressure (kPa)	Mass flow rate (kg/s)	Specific enthalpy (kJ/kg)	Specific entropy (kJ/kg·K)
CP	**A**	305.88	5	10.947	137.15	0.47423
	B	305.92	520	10.947	137.78	0.47460
AP	**C**	358.93	60	1.491	359.29	1.14370
	D	358.98	520	1.491	359.86	1.14400
FWP	**E**	426.32	520	15.593	645.87	1.87390
	F	428.03	10300	15.593	659.20	1.88010

* O.P. = Operating point (refers to Fig. 1 and Fig. 2)

Table 2. *Water operating parameters at each pump inlet and outlet – ideal (isentropic) pressure increase process*

Pump	O.P.*	Pressure (kPa)	Mass flow rate (kg/s)	Specific enthalpy (kJ/kg)	Specific entropy (kJ/kg·K)
CP	**A**	5	10.947	137.15	0.47423
	Bis	520	10.947	137.66	0.47423
AP	**C**	60	1.491	359.29	1.14370
	Dis	520	1.491	359.75	1.14370
FWP	**E**	520	15.593	645.87	1.87390
	Fis	10300	15.593	656.53	1.87390

* O.P. = Operating point (refers to Fig. 1 and Fig. 2)

5. Results and obtained operation guidelines related to the arrangement of observed pumps

In Fig. 3 is presented mechanical power (both ideal and real) used by each observed pump in the marine condensing/feedwater heating system. As ideal (isentropic) pressure increase process of each pump neglects all the losses which occur during such process (neglects increase in water specific entropy), for each pump is obtained that mechanical power used in the ideal pressure increase process is lower in comparison to real pressure increase process.

From Fig. 3 can be derived several important conclusions. When comparing all observed pumps, FWP is the dominant mechanical power consumer because it operates with the highest pressure difference and with the highest fluid mass flow rate (the same conclusion is also valid for any other steam power plant [23, 24]). CP uses much lower mechanical power in comparison to FWP, while mechanical power used by AP can almost be neglected in comparison to other observed pumps. For AP this is an expected phenomenon because AP is the auxiliary pump which operates with the lowest pressure difference and the lowest fluid mass flow rate (in comparison to other observed pumps).

More important conclusion clearly seen in Fig. 3 is that mechanical power used by each of the observed pumps is directly proportional to fluid mass flow rate through the pump – higher fluid mass flow rate will require higher mechanical power for the pump

drive and vice versa. This conclusion is not valid for the observed pumps which operate in a marine steam propulsion system only – the same conclusion can be derived from various other steam power plants and systems [25, 26].

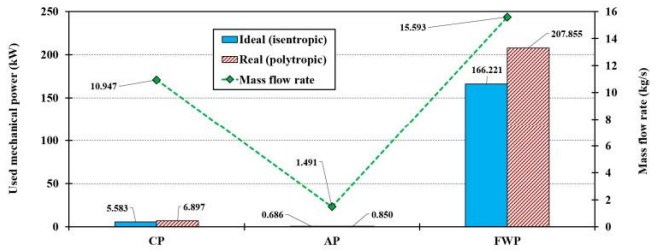


Fig. 3. *Ideal (isentropic) and real (polytropic) mechanical power used by pump in relation to fluid mass flow rate through the pump*

In Fig. 4 is presented energy and exergy losses of each observed pump in relation to fluid mass flow rate throughout the pump. It should be noted that in this paper is performed energy analysis (and consequentially is obtained energy loss of each pump), while the exergy analysis (and consequentially exergy loss of each pump) is performed in [21] from which the results are adopted. It is interesting to present both energy and exergy losses for all observed pumps in the same place, Fig. 4, because it can be clearly seen that regardless of the used analysis (energy or exergy) both losses will follow the same trend. The highest losses (both energy and exergy) are obtained for the FWP, followed by CP, while the lowest losses (again both energy and exergy) are obtained for the AP.

However, the more important conclusion from Fig. 4 is that pump losses (both energy and exergy) and fluid mass flow rate through the pump are directly proportional – higher fluid mass flow rate will result with higher losses and vice versa. The same conclusion is not valid for the observed pumps only, this conclusion can also be derived if other condensing/feedwater heating systems from various other steam power plants are observed [4, 5].

From Fig. 3 and Fig. 4 can be derived unique conclusion related to the observed pumps used mechanical power and losses – both used mechanical power and losses (energy and exergy) of the observed pumps are directly proportional to fluid mass flow rate through the pump. Higher fluid mass flow rate through the pump will result with higher mechanical power used by pump and with higher losses (both energy and exergy) and vice versa. Therefore, the fluid mass flow rate is the dominant parameter on which depends the amount of power used by the pump and pump losses.

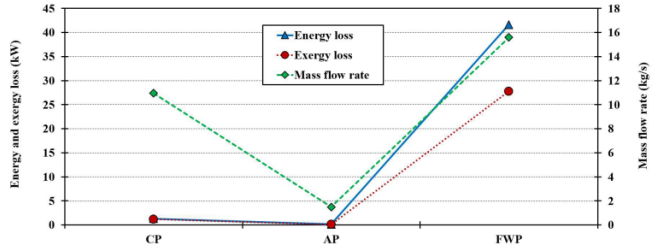


Fig. 4. *Pump energy and exergy loss in relation to fluid mass flow rate through the pump*

This analysis also considers which operation parameter is dominantly related to the efficiencies of the observed pumps (both energy and exergy efficiencies). Unlike fluid mass flow rate which is proportional to pump used mechanical power and losses, efficiencies (both energy and exergy) are proportional to the pump inlet pressure, Fig. 5. Again, exergy efficiency of each observed pump is taken from [21] where the exergy analysis is performed, while in this research is obtained energy efficiency of each pump.

From Fig. 5 can clearly be seen that energy and exergy efficiencies of the observed pumps have reverse proportional trends. In energy analysis is obtained that the highest energy efficiency (equal to 80.95%) has CP, followed by AP (80.70%) and the lowest energy efficiency has FWP (equal to 79.97%). In exergy analysis, CP has the lowest efficiency (equal to 82.86%), followed by AP (86.62%) while the highest exergy efficiency has FWP (equal to 86.63%).

Pump inlet pressure is directly proportional to the pump exergy efficiency (higher pump inlet pressure results with higher pump exergy efficiency and vice versa), but simultaneously pump inlet pressure is reverse proportional to pump energy efficiency (higher pump inlet pressure results with lower pump energy efficiency and vice versa). Such trends of both energy and exergy efficiency in relation to pump inlet pressure are characteristic of the observed pumps from marine condensing/feedwater heating system, such trends cannot be confirmed in other steam power plants.

Finally, this analysis confirms that the most influencing factor related to the pump efficiency is the pump inlet pressure, the trends between efficiencies of the pumps and pump inlet pressure require further research with an aim to obtain relations valid in general.

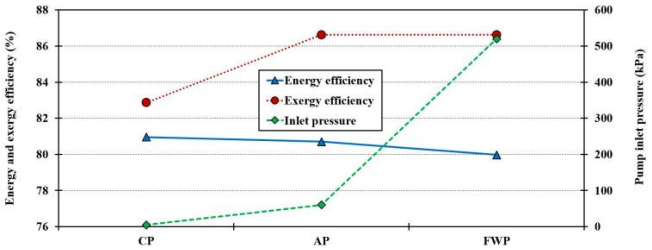


Fig. 5. *Pump energy and exergy efficiency in relation to the pump inlet pressure*

After finding the most influential operating parameters which has the dominant impact on the operation and arrangement of the pumps, it should be highlighted that a recent Artificial Intelligence (AI) methods allow optimization of operation (not only for the pumps but also for the entire condensing/feedwater heating system) [27-30].

6. Conclusions

In this paper are investigated and presented the most influential operating parameters and the guidelines for proper arrangement of pumps in the condensing/feedwater heating system. The observed system operates in marine steam propulsion power plant. In the analyzed system operates three pumps: Condensate Pump (CP), Auxiliary Pump (AP) and FeedWater Pump (FWP). The most important conclusions derived from this analysis are:

- As ideal (isentropic) pressure increase process of each pump neglects all the losses which occur during such process (neglects increase in water specific entropy), for any observed pump used mechanical power will be lower in ideal (isentropic) than in real (polytropic) pressure increase process.
- FWP is the dominant mechanical power consumer because it operates with the highest pressure difference and with the highest fluid mass flow rate. CP uses much lower mechanical power in comparison to FWP, while mechanical power used by AP can almost be neglected in comparison to other observed pumps.
- Used mechanical power and losses (energy and exergy) of the observed pumps are directly proportional to fluid mass flow rate through the pump. Higher fluid mass flow rate through the pump will result with higher mechanical power used by pump and with higher losses (both energy and exergy) and vice versa.
- Energy and exergy efficiencies of the observed pumps have reverse proportional trends. In energy analysis is obtained that the highest energy efficiency (equal to 80.95%) has CP, followed by AP (80.70%) and the lowest energy efficiency has FWP (equal to 79.97%). In exergy analysis, CP has the lowest efficiency (equal to 82.86%), followed by AP (86.62%) while the highest exergy efficiency has FWP (equal to 86.63%).
- The most influencing factor related to the pump efficiency (both energy and exergy) is the pump inlet pressure. Pump inlet pressure is directly proportional to the pump exergy efficiency (higher pump inlet pressure results with higher pump exergy efficiency and vice versa), but simultaneously pump inlet pressure is reverse proportional to pump energy efficiency (higher pump inlet pressure results with lower pump energy efficiency and vice versa).

- Some of the obtained relations and conclusions in this research have general validity, but the exact connection and trends between pump inlet pressure and pump efficiencies (both energy and exergy) requires further research.

7. Acknowledgment

This work was supported by the Croatian Science Foundation under the project number HRZZ-IP-2022-10-2821; University of Rijeka scientific grants: Funded by the European Union – NextGenerationEU – ENERGOPT - uniri-iz-25-6; GENE-CLASS - uniri-iz-25-220 and VEDRO - uniri-iz-25-10; SPIN projects IP.1.1.03.0120, IP.1.1.03.0028 and IP.1.1.03.0039; University North project UNIN-TEH-25-1-8; the EU NextGeneration under the Juraj Dobrila University of Pula institutional research project number IIP_010144 and IIP_010136; and the EC Digital Europe Programme EDIH Adria 101083838.

8. References

[1] Sutton, I. (2017). Plant design and operations. Gulf Professional Publishing

[2] Elhelw, M., Al Dahma, K. S., & el Hamid Attia, A. (2019). Utilizing exergy analysis in studying the performance of steam power plant at two different operation mode. Applied Thermal Engineering, 150, 285-293. (doi:10.1016/j.applthermaleng.2019.01.003)

[3] Kopac, M., & Hilalci, A. (2007). Effect of ambient temperature on the efficiency of the regenerative and reheat Çatalağzı power plant in Turkey. Applied Thermal Engineering, 27(8-9), 1377-1385. (doi:10.1016/j.applthermaleng.2006.10.029)

[4] Adibhatla, S., & Kaushik, S. C. (2014). Energy and exergy analysis of a super critical thermal power plant at various load conditions under constant and pure sliding pressure operation. Applied thermal engineering, 73(1), 51-65. (doi:10.1016/j.applthermaleng.2014.07.030)

[5] Ahmadi, G. R., & Toghraie, D. (2016). Energy and exergy analysis of Montazeri steam power plant in Iran. Renewable and Sustainable Energy Reviews, 56, 454-463. (doi:10.1016/j.rser.2015.11.074)

[6] Noroozian, A., Mohammadi, A., Bidi, M., & Ahmadi, M. H. (2017). Energy, exergy and economic analyses of a novel system to recover waste heat and water in steam power plants. Energy conversion and management, 144, 351-360. (doi:10.1016/j.enconman.2017.04.067)

[7] Mitrović, D., Zivkovic, D., & Laković, M. S. (2010). Energy and exergy analysis of a 348.5 MW steam power plant. Energy Sources, Part A: Recovery, Utilization, and Environmental Effects, 32(11), 1016-1027. (doi:10.1080/15567030903097012)

[8] Mrzljak, V., Lorencin, I., Anđelić, N., & Car, Z. (2021). Thermodynamic Analysis of a Condensate Heating System from a Marine Steam Propulsion Plant with Steam Reheating. Journal of Marine Science and Application, 20(1), 117-127. (doi:10.1007/s11804-021-00191-5)

[9] Naserabad, S. N., Mehrpanahi, A., & Ahmadi, G. (2019). Multi-objective optimization of feed-water heater arrangement options in a steam power plant repowering. Journal of Cleaner Production, 220, 253-270. (doi:10.1016/j.jclepro.2019.02.125)

[10] Mrzljak, V., Poljak, I., & Žarković, B. (2018). Exergy analysis of steam pressure reduction valve in marine propulsion plant on conventional LNG carrier. NAŠE MORE: znanstveni časopis za more i pomorstvo, 65(1), 24-31. (doi:10.17818/NM/2018/1.4)

[11] Mrzljak, V., Žarković, B., & Poljak, I. (2017). Energy and exergy analysis of sea water pump for the main condenser cooling in the LNG carrier steam propulsion system. Mathematical Modeling, 1(3), 144-147.

[12] Kanoğlu, M., Çengel, Y. A., & Dinçer, İ. (2012). Efficiency evaluation of energy systems. Springer Science & Business Media.

[13] Dincer, I., & Rosen, M. A. (2012). Exergy: energy, environment and sustainable development. Newnes.

[14] Poljak, I., Orović, J., Mrzljak, V., & Bernečić, D. (2020). Energy and exergy evaluation of a two-stage axial vapour compressor on the LNG carrier. Entropy, 22(1), 115. (doi:10.3390/e22010115)

[15] Mrzljak, V., Prpić-Oršić, J., & Poljak, I. (2018). Energy power losses and efficiency of low power steam turbine for the main feed water pump drive in the marine steam propulsion system. Pomorski zbornik, 54(1), 37-51. (doi:10.18048/2018.54.03)

[16] Aljundi, I. H. (2009). Energy and exergy analysis of a steam power plant in Jordan. Applied thermal engineering, 29(2-3), 324-328. (doi:10.1016/j.applthermaleng.2008.02.029)

[17] Mrzljak, V., Poljak, I., & Mrakovčić, T. (2017). Energy and exergy analysis of the turbo-generators and steam turbine for the main feed water pump drive on LNG carrier. Energy conversion and management, 140, 307-323. (doi:10.1016/j.enconman.2017.03.007)

[18] Erdem, H. H., Akkaya, A. V., Cetin, B., Dagdas, A., Sevilgen, S. H., Sahin, B., ... & Atas, S. (2009). Comparative energetic and exergetic performance analyses for coal-fired thermal power plants in Turkey. International Journal of Thermal Sciences, 48(11), 2179-2186. (doi:10.1016/j.ijthermalsci.2009.03.007)

[19] Mrzljak, V., Poljak, I., & Medica-Viola, V. (2017). Dual fuel consumption and efficiency of marine steam generators for the propulsion of LNG carrier. Applied Thermal Engineering, 119, 331-346. (doi:10.1016/j.applthermaleng.2017.03.078)

[20] Jahangiri, A., & Ameri, M. (2020). Interaction effects of natural draft dry cooling tower (NDDCT) performance and 4E (energy, exergy, economic and environmental) analysis of steam power plant under different climatic conditions. Sustainable Energy Technologies and Assessments, 37, 100599. (doi:10.1016/j.seta.2019.100599)

[21] Koroglu, T., & Sogut, O. S. (2018). Conventional and advanced exergy analyses of a marine steam power plant. Energy, 163, 392-403. (doi:10.1016/j.energy.2018.08.119)

[22] Lemmon, E. W., Huber, M. L., & McLinden, M. O. (2010). NIST Standard Reference Database 23, Reference Fluid Thermodynamic and Transport Properties (REFPROP), version 9.0, National Institute of Standards and Technology. R1234yf. fld file dated December, 22, 2010.

[23] Khanmohammadi, S., Azimian, A. R., & Khanmohammadi, S. (2013). Exergy and exergo–economic evaluation of Isfahan steam power plant. International Journal of Exergy, 12(2), 249-272. (doi:10.1504/IJEX.2013.053386)

[24] Ameri, M., Ahmadi, P., & Hamidi, A. (2009). Energy, exergy and exergoeconomic analysis of a steam power plant: A case study. International Journal of energy research, 33(5), 499-512. (doi:10.1002/er.1495)

[25] Poljak, I., Orović, J., & Mrzljak, V. (2018). Energy and exergy analysis of the condensate pump during internal leakage from the marine steam propulsion system. Pomorstvo, 32(2), 268-280. (doi:10.31217/p.31.2.12)

[26] Ameri, M., Mokhtari, H., & Bahrami, M. (2016). Energy, exergy, exergoeconomic and environmental (4E) optimization of a large steam power plant: a case study. Iranian Journal of Science and Technology, Transactions of Mechanical Engineering, 40(1), 11-20. (doi:10.1007/s40997-016-0002-z)

[27] Baressi Šegota, S., Lorencin, I., Anđelić, N., Mrzljak, V., & Car, Z. (2020). Improvement of marine steam turbine conventional exergy analysis by neural network application. Journal of Marine Science and Engineering, 8(11), 884. (doi:10.3390/jmse8110884)

[28] Lorencin, I., Anđelić, N., Mrzljak, V., & Car, Z. (2019). Genetic algorithm approach to design of multi-layer perceptron for combined cycle power plant electrical power output estimation. Energies, 12(22), 4352. (doi:10.3390/en12224352)

[29] Ebrahimgol, H., Aghaie, M., Zolfaghari, A., & Naserbegi, A. (2020). A novel approach in exergy optimization of a WWER1000 nuclear power plant using whale optimization algorithm. Annals of Nuclear Energy, 145, 107540. (doi:10.1016/j.anucene.2020.107540)

[30] Anđelić, N., Baressi Šegota, S., Lorencin, I., Poljak, I., Mrzljak, V., & Car, Z. (2021). Use of Genetic Programming for the Estimation of CODLAG Propulsion System Parameters. Journal of Marine Science and Engineering, 9(6), 612. (doi:10.3390/jmse9060612)

Application possibilities of ultrasonic testing for quality control of resistance spot welds in the automotive industry

Ján Viňáš[1,*], Marie Kolaříková[2], Ladislav Kolařík[2]
Technical University of Košice, Faculty of Mechanical Engineering, Košice, Slovakia[1]
Czech Technical University in Prague, Faculty of Mechanical Engineering, Prague, Czech Republic[2]
jan.vinas@tuke.sk

Abstract: *This study investigates the application possibilities of ultrasonic testing for quality control of resistance spot welds used in the automotive industry. Experimental resistance spot welds were produced on galvanized DP600 and H420LAD steel sheets using different welding current values. The weld quality was evaluated by metallographic analysis, EDX surface analysis and several ultrasonic testing approaches, including automatic C-scan evaluation and manual A-scan interpretation. The obtained ultrasonic results were correlated with metallographic observations and macrostructural characteristics of welded joints to assess the sensitivity of ultrasonic methods for detecting weld imperfections and evaluating weld nugget formation. The results confirmed that welding current significantly influences weld geometry, weld nugget formation and the occurrence of internal defects. Among the samples investigated, the most acceptable weld quality was achieved at a welding current of 7.6 kA for both investigated steel grades. The study also demonstrated the potential of advanced ultrasonic testing methods for rapid and reliable non-destructive inspection of resistance spot welds in automotive manufacturing.*
Keywords*: RESISTANCE SPOT WELDING; ULTRASONIC TESTING; C-SCAN; DP600 STEEL; H420LAD STEEL; NON-DESTRUCTIVE TESTING*

1. Introduction

Resistance spot welding (RSW) is one of the most widely used joining technologies in modern manufacturing industries. Its importance is particularly evident in the automotive sector, where thousands of spot welds are used to join sheet metal components during the production of vehicle body structures. These welds represent key structural joints that directly influence the stiffness, strength and crashworthiness of the vehicle body [1-2]. A typical automotive body structure contains several thousand resistance spot welds connecting sheet metal components (Fig. 1). Because a single vehicle may contain several thousand welds, maintaining consistent weld quality is essential for ensuring the reliability and safety of the final product. In industrial practice, the quality of resistance spot welds is usually evaluated through parameters such as weld nugget diameter, mechanical strength and the occurrence of internal defects. Traditionally, destructive testing methods, including peel tests, tensile tests or chisel tests, have been used to verify the integrity of welded joints. Although these techniques provide reliable information about joint strength, their application in mass production is limited because the tested components must be destroyed. For this reason, significant attention has been devoted to the development and implementation of non-destructive testing (NDT) techniques capable of evaluating weld quality without damaging the inspected structure [3-4].

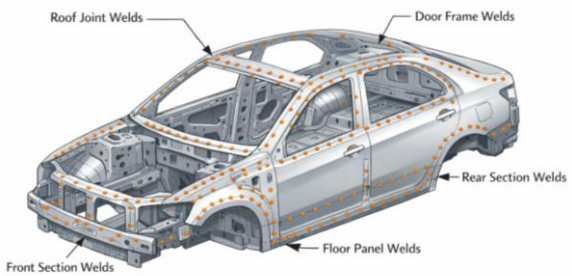


Fig. 1. *Distribution of resistance spot welds in a typical automotive body structure.*

Among the available NDT techniques, ultrasonic testing (UT) has become one of the most commonly used methods for the inspection of resistance spot welds. The method utilizes high-frequency acoustic waves that propagate through the welded joint and reflect from material interfaces or internal discontinuities. By analysing these reflected signals, it is possible to detect defects such as cracks, porosity, lack of fusion or insufficient weld nugget formation [5-6]. Compared with other inspection techniques, including radiographic testing, eddy current inspection or infrared thermography, ultrasonic testing offers a favourable balance between detection capability, penetration depth and practical applicability in industrial environments. Previous studies indicate that ultrasonic testing, together with radiography and infrared thermography, belongs among the few NDT methods capable of detecting the majority of typical resistance spot welding defects [7-8]. Despite its advantages, the ultrasonic inspection of spot welds is not without difficulties. The weld region is relatively small and consists of multiple overlapping layers of sheet material with a welded nugget formed between them. Such geometry can complicate the propagation of ultrasonic waves and make signal interpretation more demanding. As a result, the reliability of the inspection may depend on several factors, including probe positioning, coupling conditions, signal attenuation or the experience of the operator performing the measurement [9-10]. To overcome these limitations, recent research has focused on improving both the hardware and the data processing methods used in ultrasonic inspection systems. Advanced techniques such as C-scan imaging or phased-array ultrasonic testing allow a more detailed visualization of weld geometry and internal structures. These methods provide improved capability for evaluating weld nugget dimensions and identifying internal defects that may not be easily detectable using conventional ultrasonic inspection approaches [11-12]. Another significant research direction is the application of artificial intelligence and machine learning algorithms for the analysis of ultrasonic inspection data. These approaches enable automated interpretation of complex ultrasonic signals and support real-time monitoring of weld quality directly during the welding process. By analysing large datasets of measured signals, AI-based systems can recognize patterns related to specific types of weld defects, filter measurement noise and improve the accuracy of defect identification. As a consequence, the influence of operator subjectivity can be reduced and the reliability of automated inspection systems can be significantly improved [13-14]. Considering the growing demand for reliable quality assurance in high-volume industrial production, ultrasonic testing continues to represent an important tool for the non-destructive evaluation of resistance spot welds [15]. The aim of this study is to investigate the application possibilities of ultrasonic testing for the quality control of resistance spot welds and to evaluate the sensitivity of ultrasonic methods in detecting internal weld defects and determining the detectability limits of imperfections depending on their size and type.

2. Materials and experimental methods

Within the experimental work, the quality of weld joints produced by resistance spot welding was analyzed on various grades of double-sided galvanized steel sheets used in automotive body production. The evaluated weld joints were made on sheets of high-strength dual-phase steel DP600 with a nominal thickness of

0.9 mm, supplied in accordance with the requirements of EN 10338. The material was protected by an electrolytically deposited zinc coating (EG) with a coating weight of approximately 50 $g \cdot m^{-2}$, corresponding to a thickness of approximately 5 µm per side (designation ZE50/50). As a second base material, H420LAD steel, in accordance with EN 10268, was used. The material had a nominal thickness of 0.9 mm and was coated with an electrolytically deposited zinc layer (EG) with a thickness of approximately 7 µm per side (≈ ZE70/70).

Table 1. *Chemical composition of dual-phase steel DP600 (% Wt.) (Fe bal.)*

C	Si	Mn	P	S	Al	Nb	Cr	Ti	Mo
0,11	0,26	1,68	0,014	0,01	0,015	0,09	0,2	0,15	0,11

Table 2. *Mechanical properties of steel DP600*

Tensile strength [MPa]	Yield strength [MPa]	Elongation A80 [%]
600	330	20

Table 3. *Chemical composition of steel H420LAD (% Wt.). (Fe bal.)*

C	Si	Mn	P	S	Al	Nb	V	Ti
0,1	0,03	1,5	0,025	0,01	0,015	0,09	0,2	0,15

Table 4. *Mechanical properties of steel H420 LAD*

Tensile strength [MPa]	Yield strength [MPa]	Elongation A80 [%]
590	480	18

The resistance spot welding process was performed using a programmable pneumatic resistance spot welding machine VTS BP 20. Welding electrodes with CuCr electrode caps were used during the experiments. CuCr welding electrode caps with a tip diameter of 6 mm were used for all welding experiments. The electrode geometry and welding conditions were selected according to common industrial practice for welding galvanized automotive steel sheets.

For the DP600 steel sheets, the welding current varied in the range from 6.0 kA to 8.0 kA (samples A-E), while for the H420LAD steel sheets the welding current ranged from 6.6 kA to 8.0 kA (samples F-I). In all experiments, a constant welding time of 14 periods and a constant electrode force of 2.6 kN were maintained. The investigated welds included both acceptable weld joints and welds containing intentionally generated imperfections such as insufficient fusion, excessive electrode indentation, localized porosity and unstable weld nugget formation. Different welding current levels were selected in order to simulate various welding conditions occurring in automotive manufacturing practice.

Table. 5: *Parameters of resistance spot welding*

Samples	**Welding Current (kA)**	**Welding Time (periods)**	**Electrode Force (kN)**
A	6,0	14	2,6
B	6,6	14	2,6
C	7,0	14	2,6
D	7,6	14	2,6
E	8,0	14	2,6
F	6,6	14	2,6
G	7,0	14	2,6
H	7,6	14	2,6
I	8,0	14	2,6

As part of the metallographic analysis, the surface of the contact areas on the sheet surfaces was also examined using light microscopy performed on a Tesla BS 301 electron microscope, while the chemical EDX analysis was carried out by point analysis using a Jeol 10000 chemical analyzer.

An ultrasonic inspection system Matrixeye VI with automatic C-scan evaluation, manufactured by Toshiba, was used for the experimental measurements. Imagel R03-GEL1 was applied as the coupling medium between the ultrasonic probe and the tested samples. The software automatically evaluates the weld quality as either OK (acceptable) or NOK (unacceptable) according to predefined evaluation criteria.

In addition to the Matrixeye VI system, ultrasonic measurements were also compared with the Tessonics RSWA F2 ultrasonic system operating with automatic evaluation based on an inscribed circle method. The system utilized a 15 MHz ultrasonic probe and automatically evaluated weld quality according to the measured weld nugget diameter and indentation depth.

Manual ultrasonic evaluation was additionally performed using an Olympus EPOCH 650 device equipped with a straight-beam ultrasonic probe. In this case, A-scan signals were manually interpreted by an experienced operator in order to evaluate weld integrity and detect the presence of internal imperfections. Unlike automatic C-scan systems, the A-scan method strongly depended on operator experience and signal interpretation.

The obtained ultrasonic results were subsequently compared with metallographic analyses and destructive evaluation methods in order to verify the sensitivity and reliability of the applied ultrasonic testing approaches.

Examples of the applied ultrasonic evaluation methods are shown in Fig. 2. The approaches investigated included automatic C-scan evaluation using diagonal measurement, automatic weld evaluation based on the inscribed circle method and manual interpretation of A-scan signals.

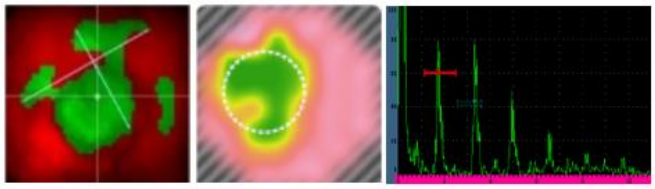


Fig. 2. *Examples of ultrasonic evaluation methods used for resistance spot weld inspection: automatic C-scan evaluation using diagonals (left), inscribed circle evaluation (center), and manual A-scan interpretation (right) [16].*

3. Results and discussion

3.1 Metallographic evaluation of welds

The macrostructures of the investigated resistance spot welds produced on DP600 steel sheets are shown in Figs. 3–5. The welds were produced using different welding current values to evaluate the influence of welding parameters on weld formation and weld quality.

Weld A produced at a welding current of 6 kA is shown in Fig. 3. The weld exhibits insufficient weld nugget formation and the presence of visible internal discontinuities, indicating inadequate heat input during the welding process. Such weld morphology may negatively influence the mechanical properties and load-bearing capacity of the joint.

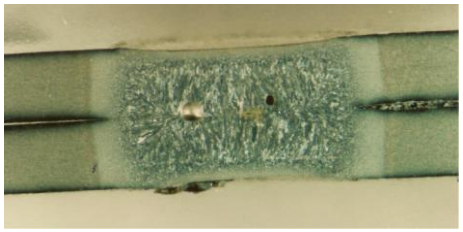


Fig. 3. *Macrostructure of Weld A produced at a welding current of 6 kA.*

Weld D, shown in Fig. 4, demonstrated the most acceptable weld morphology among the samples investigated. The weld nugget exhibited relatively uniform geometry and a stable fusion zone without pronounced macroscopic defects. The weld area appeared continuous and symmetrical, indicating suitable welding conditions for the investigated DP600 steel sheets.



Fig. 4. *Macrostructure of Weld D produced at a welding current of 7.6 kA.*

The macrostructure of Weld E produced at the highest welding current of 8 kA is shown in Fig. 5. Excessive heat input caused visible degradation of the weld region and irregularities near the electrode indentation. The results indicate that increasing the welding current does not necessarily lead to improved weld quality. On the contrary, excessive current may contribute to weld metal expulsion, surface degradation and the formation of internal defects.

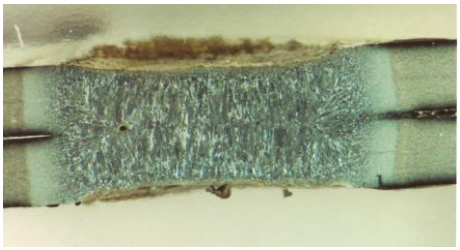


Fig. 5. *Macrostructure of Weld E produced at a welding current of 8.0 kA.*

Overall, the experimental results confirmed that the welding current significantly influences weld nugget formation, weld geometry and the occurrence of welding imperfections in DP600 steel sheets. An optimal range of welding parameters is therefore essential for achieving stable weld quality and reliable mechanical performance of resistance spot welded joints.

The macrostructures of the investigated resistance spot welds produced on H420LAD steel sheets are shown in Figs. 6–8. The welds were produced using different welding current values to evaluate the influence of welding current on weld nugget formation and overall weld quality.

The macrostructure of Weld F produced at a welding current of 6.6 kA is shown in Fig. 6. The weld exhibited insufficient fusion between the joined sheets and visible imperfections in the central part of the weld nugget. Small cavities and localized discontinuities were observed in the weld region, indicating inadequate heat input during the welding process. The observed imperfections were probably associated with the presence of Zn coating residues and unstable melting conditions in the contact region between the galvanized sheets and the welding electrodes. The weld nugget exhibited limited dimensions and non-uniform morphology, which may negatively affect the mechanical properties of the welded joint.

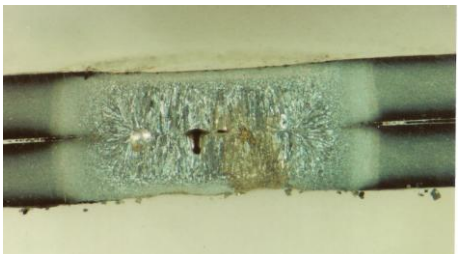


Fig. 6. *Macrostructure of Weld F produced at a welding current of 6.6 kA.*

The macrostructure of Weld H produced at a welding current of 7.6 kA is shown in Fig. 7. This weld exhibited the most acceptable weld morphology among the samples investigated. The weld nugget was continuous and symmetrical without significant macroscopic defects. Only minor local imperfections were observed in the transition regions between the weld nugget and the heat-affected zone. The results indicate that the selected welding current provided suitable thermal conditions for stable weld formation in H420LAD steel sheets.

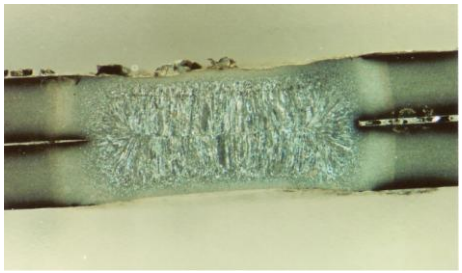


Fig. 7. *Macrostructure of Weld H produced at a welding current of 7.6 kA.*

The macrostructure of Weld I produced at the highest welding current of 8.0 kA is documented in Fig. 8. Increasing the welding current resulted in excessive heat input, leading to significant weld nugget growth and visible surface deformation in the region beneath the electrode indentation. The weld nugget exhibited the largest width and height among all investigated samples. Local surface irregularities and indications of weld metal expulsion were observed near the weld region. These features indicate overheating of the weld area and excessive melting of material under the electrodes.

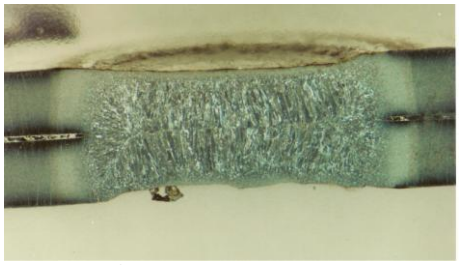


Fig. 8. *Macrostructure of Weld I produced at a welding current of 8.0 kA.*

Based on the performed metallographic analysis, it can be concluded that the welding current significantly affected weld nugget formation, weld geometry and the occurrence of welding imperfections. Under the applied welding conditions, including a welding time of 14 periods and electrode force of 2.6 kN, the most suitable weld quality was achieved at a welding current of 7.6 kA.

3.2 Surface and EDX analysis

Figure 9 shows the surface of sample C in the center of the electrode indentation. Numerous chemical analyses were performed on the surfaces of the samples tested in order to determine the precise chemical compositions, as documented in Fig. 9 for the presented sample C.

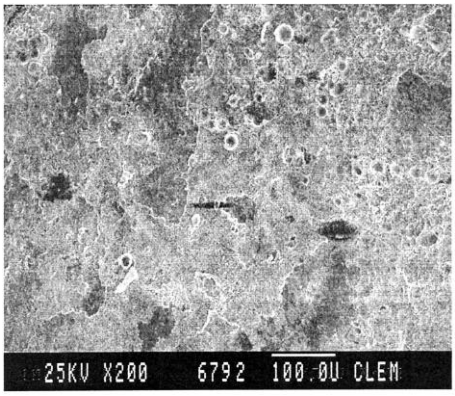


Fig. 9. *Surface of sample C in the center of the welding electrode indentation.*

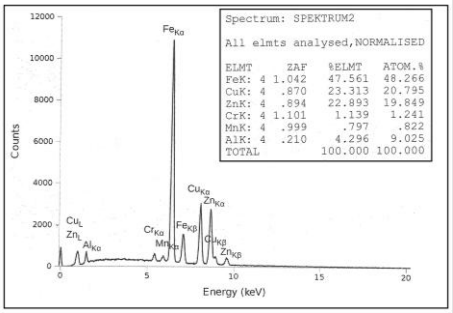


Fig. 10. *Result of EDX analysis on the surface of welded sample C.*

A point chemical analysis was performed on the surface of the welded joint. The presence of Fe and brass, i.e., a CuZn alloy, was identified on the sample surface. The presence of brass on the surface of the electrode indentation had already been observed during the visual inspection, while the EDX analysis only confirmed its occurrence.

The brass layer was formed as a result of Zn diffusion from the sheet coating into the contact surface of the welding electrode tip made of CuCr alloy. During resistance spot welding, the temperature in the weld area exceEDX 1300 °C. In the welding process, melting of the Zn coating first occurs at the contact interface between the electrode tip and the galvanized sheet at approximately 420 °C. The molten Zn adheres to the welding electrode tip, resulting in the formation of a thin brass layer on the contact surface of the electrode tip. At temperatures above 907 °C, Zn evaporation from the weld region occurs. However, due to the applied electrode force during the welding process, the evaporation of Zn from the weld area is partially suppressed. Part of the Zn adheres to the electrode tip, while another part penetrates into the base material. A significant portion of Zn is expelled from the weld area due to the dynamic effect of Zn vapors. EDX surface analyses also confirmed the presence of Cr, Mn, and Al. Chromium was present both as a strengthening alloying element in the Cu alloy of the electrode tips and as part of the chemical composition of the base material. Manganese originated from the base material composition. Aluminum was identified both as an alloying element used during the coating process of automotive steel sheets and as an alloying element in the base material, where it contributes to the stabilization of the investigated steel grade.

3.3 Ultrasonic testing evaluation of welds

Ultrasonic testing results confirmed a strong correlation between weld quality and the ultrasonic response obtained from the investigated welded joints. The automatic C-scan systems enabled rapid visualization of weld nugget geometry and identification of regions with unstable fusion or internal discontinuities.

Representative examples comparing ultrasonic C-scan evaluation, computed tomography and metallographic analysis are shown in Fig. 11. The comparison confirmed good correlation between ultrasonic signal response and the real weld nugget geometry observed by destructive and tomographic methods.

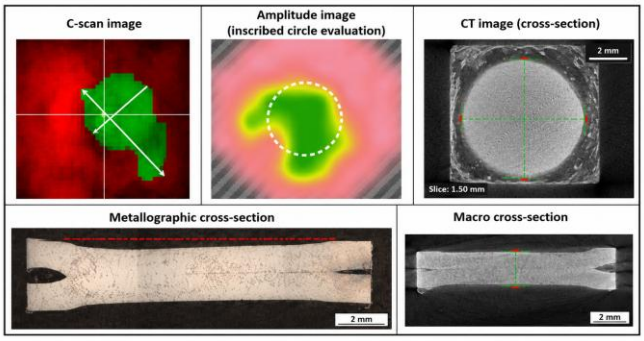


Fig. 11. *Comparison of ultrasonic C-scan evaluation (left), inscribed circle evaluation (center), CT image (top right), metallographic section (bottom left) and macro cross-section (bottom right) for a selected resistance spot weld [16].*

Welds produced using lower welding current values exhibited irregular ultrasonic indications and reduced weld nugget dimensions. In several cases, the ultrasonic systems classified these welds as NOK due to insufficient weld nugget formation and unstable signal response. These observations were consistent with the metallographic analyses, where incomplete fusion and localized imperfections were observed.

The most stable ultrasonic response was obtained for welds produced at a welding current of 7.6 kA. The corresponding C-scan images exhibited continuous and symmetrical weld nugget areas with uniform signal distribution. These results correlated well with the metallographic observations, where the welds demonstrated acceptable weld morphology and stable fusion zones.

Welds produced using excessive welding current values showed irregular ultrasonic signal behavior caused by weld metal expulsion and excessive electrode indentation. In these cases, the automatic evaluation algorithms occasionally overestimated the weld nugget dimensions due to irregular signal reflections from the deformed weld region.

Comparison of the investigated ultrasonic evaluation approaches showed that automatic C-scan methods provide rapid weld quality assessment suitable for industrial in-line inspection. However, manual A-scan interpretation enabled more detailed identification of local imperfections and signal irregularities. The results indicate that combining automatic ultrasonic evaluation with operator-based signal interpretation may improve the reliability of resistance spot weld quality control.

The comparison of ultrasonic images with CT and metallographic observations confirmed that ultrasonic evaluation methods can identify changes in weld nugget geometry and internal weld discontinuities. Nevertheless, significant differences were observed between individual evaluation algorithms when determining the weld nugget diameter.

Figure 12 summarizes the weld nugget diameters determined using different ultrasonic testing evaluation approaches for selected weld imperfections.

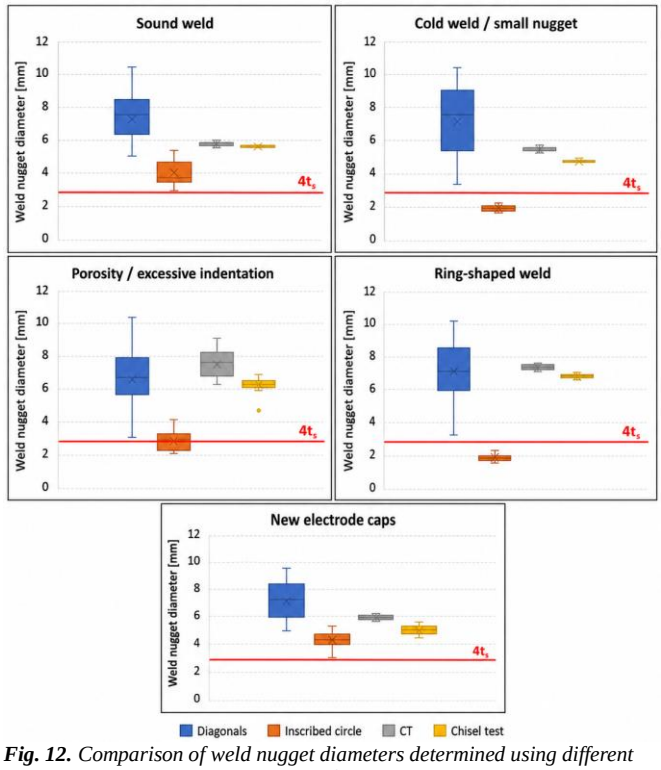


Fig. 12. *Comparison of weld nugget diameters determined using different ultrasonic testing evaluation methods for selected resistance spot weld imperfections [16].*

The red line shown in Fig. 12 represents the minimum acceptable weld nugget diameter according to the $4\sqrt{t}$ criterion commonly used for resistance spot weld evaluation. The results indicate noticeable differences between automatic C-scan evaluation methods and

destructive verification methods. The diagonal-based evaluation method tended to overestimate weld nugget dimensions, while the inscribed circle method provided more conservative results. The comparison also confirmed that manual evaluation and CT measurements provide more reliable information about internal weld quality and the presence of welding imperfections.

4. Conclusion

The presented study investigated the application possibilities of ultrasonic testing for the quality control of resistance spot welds produced on DP600 and H420LAD steel sheets commonly used in automotive body structures. The experimental results confirmed that welding current significantly affects weld nugget formation, weld geometry and the occurrence of welding imperfections. Metallographic analyses showed that insufficient welding current resulted in unstable weld formation and local discontinuities, while excessive welding current caused weld metal expulsion and surface degradation. For both investigated steel grades, the most suitable weld morphology was achieved at a welding current of 7.6 kA under the applied welding conditions. The performed ultrasonic inspections demonstrated that ultrasonic testing represents an effective non-destructive method for evaluating resistance spot weld quality. Automatic C-scan evaluation methods enabled rapid weld assessment, while manual A-scan interpretation provided more detailed information about internal imperfections and signal behavior. The comparison of ultrasonic results with metallographic observations confirmed the capability of ultrasonic methods to detect variations in weld quality and internal defects. The obtained results indicate that advanced ultrasonic testing systems have significant potential for implementation in automotive production as reliable tools for rapid in-line quality control of resistance spot welds. The results obtained also demonstrated that ultrasonic testing can significantly reduce the need for destructive testing methods in high-volume automotive production. Future research will focus on the implementation of advanced automated ultrasonic evaluation systems for real-time industrial weld quality monitoring.

Acknowledgements

This research was supported by the Visegrad Fellowship Program No. 62610048 and No. 2610076, for which the authors express their gratitude. The authors also acknowledge the support of the Slovak Research and Development Agency (APVV) through the projects “Innovative Approaches to the Restoration of Functional Surfaces by Laser Surface Treatment” (APVV-20-0303) and “Integrity of Protective Multilayers under High-Temperature Exposure Conditions” (APVV-24-0381), the VEGA Scientific Grant Agency through the project “Possibilities of Applying Laser Additive Technologies in the Restoration of Functional Surfaces” (1/0597/23), and the KEGA Cultural and Educational Grant Agency through the project “Hybrid Education of Students for the Current NeEDX of the Automotive Industry” (024TUKE-4/2025).

5. References

1. D. Ulbrich, J. Moravec, M. Smrž, Ultrasonic inspection of resistance spot welds in automotive structures, **Materials 16**, 7029 (2023)
2. Y. Zhou, *Resistance Spot Welding of Steel Sheets*, Woodhead Publishing, Cambridge (2015)
3. A.F. Andreoli, A.P. Tschiptschin, S.D. Brandi, Correlation between peel test and real-time ultrasonic monitoring of spot weld quality, **Soldagem Inspec. 21**, 326–335 (2016)
4. W. Dai, Y. Huang, J. Liu, Online quality inspection of resistance spot welding using process signals, **J. Manuf. Syst. 63**, 226–236 (2022)
5. Z. Chen, J. Zhang, Y. Zhou, Ultrasonic nondestructive evaluation of resistance spot welds for zinc-coated steel sheets, **Ultrasonics 49**, 298–304 (2009)
6. P. Liu, Y. Zhang, X. Li, On-line measurement of nugget diameter in resistance spot welding using ultrasonic signals, **Measurement 223**, 113764 (2024)
7. L. Yang, H. Wang, Q. Li, Ultrasonic nondestructive testing of spot welds in automotive structures, **Sensors 24**, 4771 (2024)
8. Ó. Martín, A. Sánchez, J.M. Prado, Advances in quality control of resistance spot welding processes, **Metals 12**, 1810 (2022)
9. J. Buckley, Improvements in ultrasonic inspection of resistance spot welds, **NDT.net 13** (2008)
10. K. Nomura, T. Shibata, H. Sato, Non-contact ultrasonic measurement of weld nugget diameter in resistance spot welding, **Ultrasonics 130**, 106875 (2023)
11. J. Liu, H. Fujii, K. Nakata, Ultrasonic C-scan detection for stainless steel spot welds, **ISIJ Int. 54**, 1876–1883 (2014)
12. D. Ulbrich, M. Smrž, J. Moravec, Correlation between ultrasonic signals and mechanical properties of spot welds, **Materials 15**, 1704 (2022)
13. Y. Li, H. Zhang, Deep learning for ultrasonic defect detection in weld inspection, **NDT E Int. 118**, 102372 (2021)
14. S. Mohanty, A.K. Mishra, Machine learning applications in ultrasonic non-destructive evaluation, **Measurement 187**, 110315 (2022)
15. R. Blitz, G. Simpson, *Ultrasonic Methods of Non-Destructive Testing*, Springer, London (2016)
16. M. Kolaříková, J. Viňáš, L. Kolařík, M. Petřík, D. Stárek, Verification of sensitivity of different ultrasonic testing methods for resistance spot welds, Proc. **PROMATTEN** 2025, Prague (2025)

Implementation of Composite Materials into the Design of an Experimental Vehicle for the Shell Eco-Marathon Competition

Štefan Kender*, Štefan Novotný

1 Technical University of Košice, Faculty of Mechanical Engineering, Department of Automotive Production, Mäsiarska 74, 040 01 Košice, Slovakia

* Correspondence: stefan.kender@tuke.sk

Abstract:. *The current optimization of materials in the automotive industry is primarily driven by the objective of progressively reducing vehicle curb weight, which serves as a critical instrument for lowering greenhouse gas emissions and enhancing energy efficiency. Empirical data demonstrate a direct correlation between weight reduction and fuel consumption: a 10% decrease in vehicle mass generates an approximate 7% reduction in fuel consumption. Composite materials, defined as heterogeneous systems consisting of at least two components—a continuous matrix (binder) and a discontinuous reinforcement (fibers, particles, or layers)—enable a synergistic effect of mechanical properties that are unattainable with monolithic metallic materials. In structural applications, polymer matrices (including both thermosets and thermoplastics) predominate in combination with high-strength carbon, aramid, or glass fiber reinforcements. These material systems exhibit extreme specific strength, a high modulus of elasticity, fatigue resistance, and anisotropic properties that allow for the directional optimization of stiffness. For components requiring maximum dimensional stability and self-supporting (monocoque) capabilities, sandwich configurations are utilized, typically integrating an aramid honeycomb core between high-performance composite face sheets. The qualitative parameters of the resulting components are directly dependent on the chosen manufacturing technology and the fiber-to-resin ratio. The Vacuum Infusion (VI) method represents a highly efficient process in which a vacuum-sealed mold ensures the uniform saturation of dry reinforcement with liquid resin. This procedure minimizes porosity, achieves a high fiber volume fraction—reaching up to 70% in advanced systems—and guarantees high production reproducibility and surface quality without the need for secondary machining. Despite their technical superiority, the primary limiting factors for widespread implementation remain the high economic cost of raw materials and the complexity of manufacturing cycles. Prospective development is focused on streamlining processes for mass production, implementing sustainable bio-fibers as reinforcing components, and addressing the challenges of recyclability and component replacement at the end of the life cycle. Advanced composite structures thus form the essential material foundation for the next generation of ultra-lightweight and safe transport vehicles.*

KEYWORDS: *COMPOSITE MATERIALS, MATRICES, FILLER, SANDWICH COMPOSITE, ARAMID HONEYCOMB, CARBON FIBERS.*

1. Introduction

Weight reduction and improvement of aerodynamic properties are among the key objectives of modern automotive engineering. Carbon fibre reinforced polymer matrix composites (CFRP) enable the design of lightweight yet stiff structural components that cannot be achieved using conventional metallic materials at the same mass [1]. These materials are characterised by exceptional specific stiffness and strength, excellent corrosion resistance and favourable fatigue properties [2, 8].

The Shell Eco-Marathon (SEM) is an international competition for vehicles with extremely low fuel consumption. In its current organised form it has been held since 1985, encompassing the Prototype and UrbanConcept categories on three continents [6]. The Faculty of Mechanical Engineering at TUKE has actively participated in SEM since 1994. Previous models were built from steel tubular frames with plastic body panels (total mass 45–55 kg). The new Prototype 2025 replaced the frame with a self-supporting sandwich composite monocoque body with the aim of significantly reducing mass and aerodynamic drag.

.2. Aerodynamic design and cfd analysis

2.1 Body Shape Optimisation

The body design was carried out in the CATIA V5/R16 CAD environment. The primary requirement was minimum aerodynamic drag while complying with the SEM competition regulations [6] and driver dimensional requirements. Through iterative optimisation of seven shape variants, the final form was selected – a streamlined body with an elliptical cross-section and an elongated rear section inspired by a teardrop aerodynamic profile.

2.2 CFD Flow Simulation

Aerodynamic evaluation of the shape variants was carried out by numerical CFD (Computational Fluid Dynamics) flow simulation. The steady-state simulation was solved by the finite volume method in the CATIA V5/R16 flow module with a computational domain of 2.5×10^{6} cells. Parameters: air ($\rho = 1.225$ kg/m³, $\mu = 1.789 \times 10^{-5}$ Pa·s), $v_\infty = 11$ m/s, Aref = 0.142 m². The velocity distribution around the body is shown in Fig. 1 – significant acceleration occurs over the upper surface, and a low-pressure wake forms behind the body.

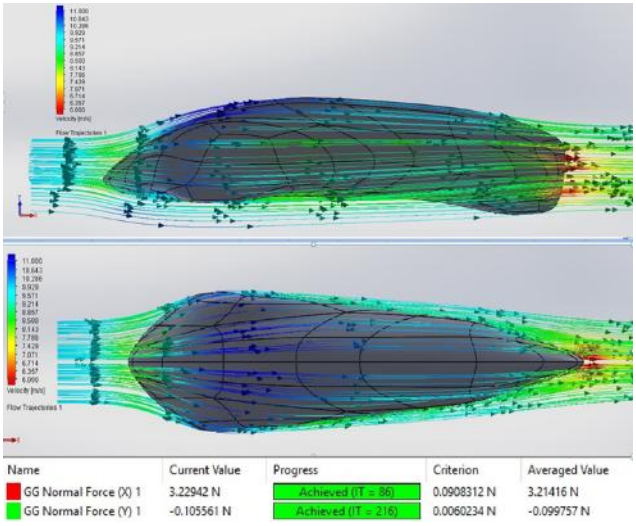


Fig. 1 Velocity streamlines around the Prototype 2025 body – CFD simulation ($v_\infty = 11$ m/s)

The CFD simulation results are summarised in Tab. 1. The drag force was determined from $FD = \frac{1}{2} \cdot \rho \cdot v^2 \cdot Cd \cdot Aref$. For Prototype 2025 at v = 30 km/h: $FD = 0.5 \times 1.225 \times 8.33^2 \times 0.092 \times$

0.142 = 0.56 N, corresponding to only 25.2 % of the drag force of the previous model (FD,old = 2.22 N).

Tab. 1 Comparison of aerodynamic characteristics

Parameter	Prev. model	Prototype 2025
Drag coeff. Cd [–]	0,26	0,20
Frontal area Aref [m²]	0,142	0,142
Drag force v=30 km/h [N]	2,22	0,56
Inlet velocity v∞ [m/s]	11,0	11,0

3. Composite sandwich structure

3.1 Material Components

The Prototype 2025 body is a sandwich composite structure. The outer and inner CFRP skins consist of a carbon twill 2/2 woven fabric (200 g/m², biaxial orientation [0°/90°]) with a vacuum infusion epoxy matrix [1]. A hybrid interlayer of woven CF/aramid fabric (sandwich mid-plane) increases toughness and impact energy absorption [4]. The core is an aramid Nomex® honeycomb (cell size 9.5 mm, ρc = 48 kg/m³), providing high bending stiffness at minimum mass [3, 11].

Tab. 2 Mechanical properties of sandwich material components

Material	E [GPa]	σ_u [MPa]	ρ [kg/m³]	thk./ply [mm]
CFRP fabric twill 2/2, 200 g/m²	62	560	1 520	0,28
Hybrid CF/aramid, 240 g/m²	45	420	1 380	0,30
Aramid Nomex® honeycomb, 48 kg/m³	–	3,2*	48	6,00
Epoxy matrix (VI system)	3,5	85	1 200	–

3.2 Sandwich Lay-up and Fibre Volume Fraction

The sandwich laminate is designed symmetrically about the core, thereby preventing deformations caused by the coupling effect [1, 2]. Detailed ply sequence, thicknesses and fibre volume fraction Vf are given in Tab. 3. The average Vf = 52.6 % achieved by the VI process significantly exceeds hand lay-up (Vf ≈ 30–40 %) and directly correlates with improved specific mechanical properties [9].

Tab. 3 Lay-up of the Prototype 2025 body sandwich structure

Layer	Material	thk. [mm]	N vrs.	Vf [%]
Outer skin (top)	CFRP fabric	0,84	3	55,1
Hybrid interlayer	CF/aramid fabric	0,60	2	48,6
Sandwich core	Aramid Nomex® honeycomb	6,00	–	–
Inner skin (bottom)	CFRP fabric	0,84	3	54,2
Total thickness	–	8,28	–	52,6 (Ø)

4. Manufacturing – vacuum infusion (vi)

Vacuum Infusion technology was used to manufacture both body components (chassis section and top cover). The dry reinforcement was placed in a rigid polyester mould, the mould was sealed with an airtight film, and liquid epoxy resin was drawn through a distribution network into the reinforcement under vacuum ($p \leq -0.95$ bar) [9]. Infusion rate ≈ 0.8 m²/h at p = −0.93 bar. Cure: 24 h at 23 °C, post-cure 4 h at 60 °C.

The VI process provided: Vf > 50 %, porosity < 1 %, repeatable quality and a closed manufacturing process with no VOC emissions. Body mass: mcar = 7.8 kg.



Fig. 2 Mould preparation and placement of CFRP reinforcement fabrics prior to infusion



Fig. 3 Manufacturing of the chassis section by Vacuum Infusion

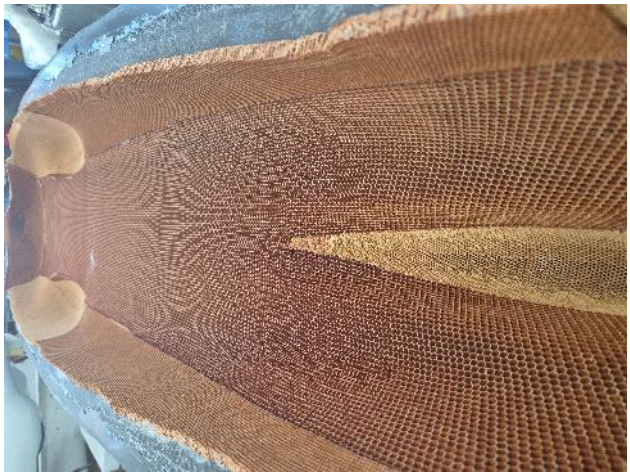


Fig. 4 Bonding of aramid honeycomb into the sandwich structure

5. Numerical structural analysis (ansys)

5.1 Finite Element Model

The structural integrity of the chassis section was verified by FEA in ANSYS Mechanical 2024 R1. The geometry (STEP from CATIA V5) was modelled using 3D shell elements SHELL281 (8-node, quadratic) with orthotropic material lay-up definitions according to Tab. 2 and 3 [12]. Mesh: global element size 4 mm, refined to 2 mm at axle attachments. Total elements: 186 452, nodes: 312 668.

5.2 Boundary Conditions and Loading

Constraint points: four axle attachments + two engine mounts (all translational DOFs fixed, rotations free). Loading: self-weight (g = 9.81 m/s²), driver load mdriver = 65 kg → F = 637 N applied as pressure on the seat surface, dynamic factor fd = 2.5 (road unevenness). Total design load: Fdesign = 1 600 N.

5.3 Numerical Analysis Results

FEA results are given in Tab. 4. The maximum von Mises equivalent stress σmax = 52.8 MPa occurs in the CFRP skin at the front axle attachment. Safety factor SF = σ_u□/σmax = 650/52.8 = 12.3 – a significant structural margin. Core safety factor SF = τ_u/τmax = 1.72/0.38 = 4.5. Maximum deflection δmax = 2.1 mm over the chassis length of 1 460 mm corresponds to a relative deflection of L/δ ≈ 695.

Tab. 4 FEA results for the chassis section (ANSYS Mechanical 2024 R1)

Result quantity	Value	Unit
Max. von Mises stress σmax	52,8	MPa
Allowable stress CFRP σ_u□	650	MPa
SF – skin (σ_u□/σmax)	12,3	–
Max. core shear τmax	0,38	MPa
Honeycomb shear strength τ_u	1,72	MPa
SF – core (τ_u/τmax)	4,5	–
Max. deflection δmax	2,1	mm
Design load	1 600	N
Element count (SHELL281)	186 452	–
Node count	312 668	–



Fig. 5 Chassis section of the Prototype 2025 body after demoulding

6. Results and discussion

6.1 Overall Vehicle Parameters

The total vehicle mass including the powertrain (35 cm³, 1 kW), steering, wheels with ceramic bearings and safety components reached mtotal = 35 kg. Body mass decreased from 14.6 kg to 7.8 kg (−46.6 %) as a direct result of the transition to the sandwich composite monocoque.

6.2 Shell Eco-Marathon Europe 2025 Competition Results

The Prototype 2025 vehicle competed in the Prototype ICE – Gasoline category. The TUKE team achieved a best result of 825 km/l – a team historical record and an improvement of 25.4 % over the previous best result of 658 km/l. A summary comparison of parameters is given in Tab. 5.

Tab. 5 Parameter comparison of the previous model and Prototype 2025

Parameter	Prev. model	Prot. 2025
Total mass [kg]	40	35
Body mass [kg]	14,6	7,8
Drag coeff. Cd [–]	0,26	0,20
Drag force v=30 km/h [N]	2,22	0,56



Fig. 6 Prototype 2025 vehicle at Shell Eco-Marathon Europe 2025

The achieved result confirms that the combination of aerodynamic optimisation (CFD), low mass of the sandwich composite body (VI technology) and minimisation of rolling resistance (ceramic bearings) represents an effective approach to significantly improving the fuel efficiency of prototype vehicles [7, 10].

7. Conclusion

Based on the results achieved, the following conclusions can be drawn:

1. CFD body optimisation (CATIA V5) reduced Cd from 0.26 to 0.20
2. The sandwich body (CFRP / hybrid CF+aramid / aramid honeycomb, VI technology) achieved a mass of 7.8 kg – a reduction of 46.6 % while retaining full monocoque function.
3. Vacuum Infusion ensured Vf = 52.6 % (vs. ≈ 35 % for hand lay-up), achieving an optimum specific mechanical property ratio.

4. FEA in ANSYS (SHELL281) confirmed structural integrity: σmax = 52.8 MPa → SF = 12.3; δmax = 2.1 mm at a design load of 1 600 N.
5. Total vehicle mass: 35 kg (−32.7 % compared to the previous model)
6. The competition result of 825 km/l is the TUKE team historical record (an improvement of 25.4 % over the previous record of 658 km/l).

Future research will focus on shortening the VI production cycle, automating the infusion process and the use of bio-fibres and recyclable thermoplastic matrices in line with sustainability principles.

Acknowledgement

This paper was produced within the grant project KEGA 024TUKE-4/2025 – Hybrid Education of Students for the Current Needs of the Automotive Industry and project IVG-25-02 – Development and Manufacturing of an Experimental Composite Vehicle for Shell Eco-Marathon 2025.

References

[1] DANIEL, I.M., ISHAI, O.: Engineering Mechanics of Composite Materials. 2nd ed. Oxford University Press, New York, 2006. ISBN 978-0-19-515097-1.

[2] BARBERO, E.J.: Introduction to Composite Materials Design. 3rd ed. CRC Press, Boca Raton, 2018. ISBN 978-1-138-19680-9.

[3] VINSON, J.R.: The Behavior of Sandwich Structures of Isotropic and Composite Materials. Technomic Publishing, Lancaster, 1999. ISBN 978-1-56676-699-3.

[4] PARK, S.J.: Carbon Fibers. 2nd ed. Springer, Dordrecht, 2018. ISBN 978-981-13-0538-2. https://doi.org/10.1007/978-981-13-0538-2

[5] FONG, A. et al.: A review on the hybrid polymer composites comprising natural fibre and nanomaterial reinforcement. Journal of Composite Materials, 2025, vol. 59, no. 22, pp. 2615–2646. https://doi.org/10.1177/00219983251334861

[6] SHELL INTERNATIONAL LIMITED: Shell Eco-Marathon Official Rules 2025 – Chapter I. London, 2024. [Online]. [cited 15.03.2025]. Available at: https://www.shell.com/make-the-future/shell-ecomarathon/rules.html

[7] BUDINSKI, K.G., BUDINSKI, M.K.: Engineering Materials: Properties and Selection. 9th ed. Pearson Education, Upper Saddle River, 2010. ISBN 978-0-13-712842-6.

[8] VASILIEV, V.V., MOROZOV, E.V.: Advanced Mechanics of Composite Materials and Structural Elements. 3rd ed. Elsevier, Amsterdam, 2013. ISBN 978-0-08-098231-1.

[9] LOOS, A.C., SPRINGER, G.S.: Curing of Epoxy Matrix Composites. Journal of Composite Materials, 1983, vol. 17, no. 2, pp. 135–169. https://doi.org/10.1177/002199838301700205

[10] WIEDEMANN, J.: Leichtbau: Elemente und Konstruktion. 3rd ed. Springer, Berlin, 2007. ISBN 978-3-540-33656-5.

[11] HEXCEL CORPORATION: HexWeb® Aramid Fibre Honeycomb – Product Data Sheet. Stamford, 2023. [Online]. [cited 10.02.2025]. Available at: https://www.hexcel.com/user_upload/assets/datasheets/Honeycomb/7740.pdf

[12] ANSYS INC.: ANSYS Mechanical User's Guide, Release 2024 R1. Canonsburg, PA: ANSYS Inc., 2024.

Application of SPC statistical process control method and measurement analysis of welded steel components in the motorcycle industry

Vid Božič
Prade, street VII/4., 6000 Koper, Slovenia
Vid.bozic1@gmail.com

Abstract: *Variability is a fact of industrial production. Every process produces products that are not exactly the same. For successful quality control and management, several different methods of preventive quality assurance have been developed in the early stages of the product development process. The SPC method is used in conditions from the initial process batches and in the stages of serial production. The SPC statistical process control method is indispensable for a modern, future-oriented manufacturing company. In this paper, I would like to present the SPC statistical method on a practical example from the motorcycle industry, with measurement results under the conditions of the first pre-series of a complex welded steel component.*
Keywords*: STATISTICAL PROCESS CONTROL, PROCESS CAPABILITY, BMW STEEL FRAME*

1. Introduction

Measurements in Mechanical Engineering is one of the subjects of my first year of study at the Faculty of Mechanical Engineering. Measurement uncertainty, measurement techniques in production, quality methods were presented well and interestingly. At home, we have had a dusty steel component of a BMW motorcycle - the rear frame - for almost 20 years. It is a project of my father, which he was carrying out at the Tomos factory at that time. I was interested in how the measurements were carried out, with which method they proved the stability of the process. And that is how this paper on the SPC method was created, which I would like to present at the conference.

The contribution is, on the one hand, the result of a study of SPC, as one of the most commonly used statistical methods of quality assurance, and on the other hand, an insight into measurements and ever-current analyses of an otherwise outdated steel frame.

Understanding of Quality

As a rule, the quality of an organization's final product is the joint result of the work of employees, teams and departments, and everyone is responsible for it, at least for that part of the process in which they are involved. Every organization should take into account three key principles: achieving the greatest possible satisfaction of its customers, continuously improving its processes and achieving the best possible cooperation of employees in the realization of the quality goals it has set.

It is impossible to sell products of very poor quality, even at a low price, because no one will want them. It is also impossible to sell products of superior quality that exceed a certain threshold price that customers are still willing to pay. Target or project quality is the quality that is created in the development of a product. Comparative quality or manufacturing quality is obtained by comparing the real product and the requirements that were set in the development [1].

The new approach to quality processes, which is based on the prevention of inadequate quality, is professionally more demanding than just quality control and is associated with a new organizational principle that states that each department, function or employees in the organization bear their share of responsibility for the quality of the product.

Quality assurance means preparing people to do better the useful things they should do anyway. The concept of “zero defects” is synonymous with “doing it right the first time”. It is intended not only for production workers but for all employees [2]. Preventing poor quality is establishing and integrating a quality system into the company and not just solving individual problems on a daily basis. We must ensure that we recognize and anticipate quality problems early enough through systematic work, methods and systems, and then manage the entire process in such a way that these problems do not occur at all.

Successful companies put quality in the leading position, while many unsuccessful companies only take into account their own requirements, forgetting about the requirements of customers and ensuring the quality of their products and services.

Quality assurance method SPC

Statistical tools help to understand and control process variability. Statistical process control tools help to understand the capability of a machine or process and to control the course of the process. The primary purpose of statistical process control is to prevent the production of a substandard product.

There are many methods for quality assurance, and they can be roughly divided into three groups: statistical methods, methods for preventive quality assurance, and methods for solving problems in a group.

With the help of statistical methods, we can collect and organize a lot of data to show the real situation. Statistical methods are based on probability and are helpful in ensuring quality in all business functions of the company. They do not eliminate errors, but only serve to detect and identify problems more quickly and objectively, but it makes no sense to introduce them into practice if there is no system for solving problems behind them. Namely, the methods must be subordinated to the goal of improvement.

To determine quality, to more easily detect the causes of errors, to analyze causes and consequences, six basic statistical methods have been established in the world, and one of them is the SPC method - statistical process control. The SPC method, precisely because of its usefulness, can also be considered a method for preventive quality assurance, as shown in Fig. 1.

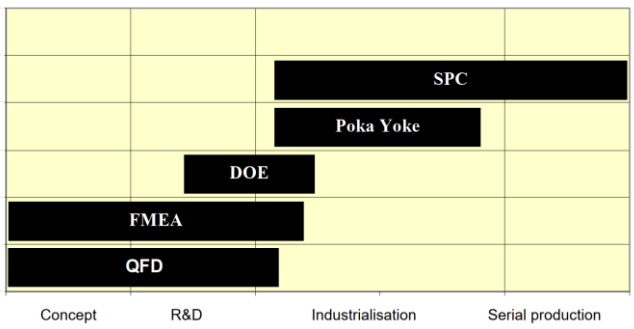


Fig. 1: *Quality assurance methods in the product life cycle [3].*

Using statistical methods, we can determine additional properties of our measurement from a set of product measurements. The most important statistical parameters for a set of measurements are the arithmetic mean (also called the average

value) and the standard deviation, also called the standard deviation.

In general, more measurements mean that their average would be closer to the true value of the measurement. However, it is important to be aware that a larger number of measurements is also more time-consuming and is not always worth it. 20 measurements give us a better result than ten measurements. The average of 50 measurements is only slightly closer to the true value. Usually, in practice, we perform 4 to 15 measurements. If the measurement result is unstable, it is interesting to know how widely the measured values are scattered around the average value. The dispersion of the measurements gives us information about the uncertainty of our process.

When we have a large number of measured values, the standard deviation is a common way to quantitatively assess the dispersion of the measurements. The standard deviation of a set of measurements tells us how far the average of the differences between individual measured values is from the average value of the entire set.

In the simplest case, about two thirds of the measured values will fall in the interval between the average value minus the standard deviation and the average value plus the standard deviation. Approximately 95 % of all measurements will be in the interval of two standard deviations from the average value.

The standard deviation is therefore a value that is obtained only from a sufficiently large number of measurements. In practice, we can calculate an approximation of the standard deviation, which we denote by σ. In practice, we no longer calculate the standard deviation manually, but use mathematical and statistical software. In addition to using computers, we can calculate an approximation of the standard deviation using a conventional statistical pocket calculator, into which we enter the measured values, using the function key σ. Mathematically, the expression for the approximation of the standard deviation can be written as:

$$S = \sqrt{\frac{\sum_{i=1}^{n}(x_i - \bar{x})^2}{n-1}}$$

$$\sigma = \sqrt{\frac{\sum_{i=1}^{N}(x_i - \mu)^2}{N}}$$

where:
σ = standard deviation for the population S = standard deviation for the sample x_i = value of an individual measured unit μ = arithmetic mean of the population N = number of units in the population n = number of units in the sample.

The standard deviation is a numerical value that shows the tendency of data variability. The larger the value of the standard deviation, the greater the differences between the data, which means the greater the variability of the process from which the data is taken.

Process Capability Cp and Cpk

The basis of statistical control is random control, in which the properties obtained from a sample are transferred to the whole. Measurement values in the field of industry most often have a normal distribution, also called a Gaussian or bell curve. This also applies to random control if there are no systematic influences. Capability is calculated for machines and processes, and in this case we determine capacity and capability.

To determine the process capability as the long-term behavior of a process with random fluctuations in the mean value, we capture the mean values of a large number of individual random checks and display them as a normal distribution. If there are systemic influences on the process behavior, we must investigate them by investigating the process flow in order to then obtain the starting points for optimizing the process. To evaluate the process, we need several mean values from individual random checks of the range n > 3 (usually n = 5).

Process/machine capability analysis is an analysis of the dispersion of the process/machine and whether it is within the upper and lower tolerance limits.

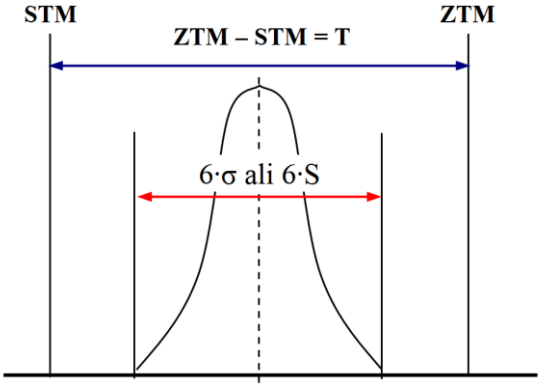


Fig. 2 *Presentation of machine capability cm (6·S) and process capability Cp (6·σ)*

The process is analyzed within ± 3·σ of the process mean, which is where 99.73 % of the population is. The potential capability Cp is defined by the ratio between the width of the tolerance field (ZTM – STM) and 6·σ of the process. This is the potential and theoretical capability of the process when the process mean lies exactly between ZTM and STM, which is almost impossible in practice [3].

A stable process can be represented by a measure of its variability, which is six times the standard deviation (6·σ). Comparing six times the standard deviation of the process (6·σ) with the difference between the tolerance limits is the measure of process capability Cp according to the formula:

$$c_p = \frac{ZTM - STM}{6 \cdot \sigma}$$

where:
- ZTM upper tolerance limit,
- STM lower tolerance limit,
- σ standard deviation of the process.

Unfortunately, Cp does not show how well the mean tendency of the process matches the required nominal process measure, so we use the one-sided process variability Cps, Cpz, Cpk.

Cps and Cpz: one-sided process variability – they measure not only the actual process variability relative to the allowed, but also the location of the central tendency of the process.

The critical or actual process capability Cpk is defined by the ratio of the distance of the process mean value from the nearest tolerance limit (ZTM or STM) and 3·σ of the process. Cpk is considered a measure of process capability and is always the smaller of Cps and Cpz. Cps and Cpz are calculated using the following formulas:

$$c_{ps} = \frac{\bar{x} - STM}{3 \cdot \sigma}$$

$$c_{pz} = \frac{ZTM - \bar{x}}{3 \cdot \sigma}$$

$$c_{pk} = \min(c_{ps};\ c_{pz})$$

In summary: Capacity (machine capacity Cm and process capacity Cp) compares the spread of measurements with the width of the

tolerance field on the drawing. Capability (machine capacity Cmk and process capacity Cpk) expresses the difference between the standard deviation of the average measurement and the nearest tolerance limit.

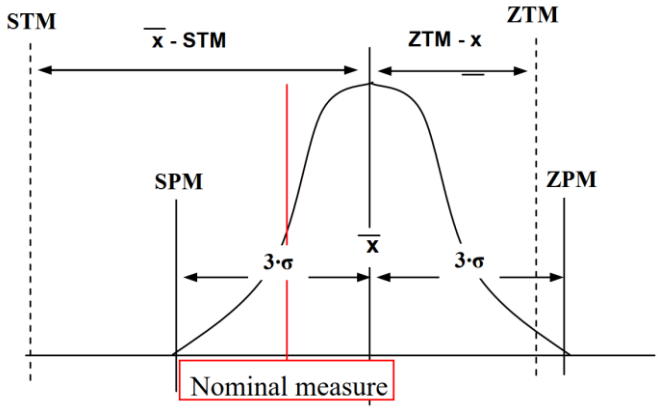


Fig. 3 *Presentation of Cps and Cpz parameters [4].*

The data for capability depends on the width of the tolerance field on the drawing. If we have products with different tolerances, we must determine the capability of processes and machines for each tolerance range.

Table 1: *Correlation between Cpk and PPM.*

Cpk	PPM
1,00	2.700
1,10	967
1,20	318
1,30	96
1,40	26
1,50	6,8
1,60	1,6
1,70	0,34
1,80	0,06
2,00	0,0018

The relationship between Cpk and PPM, the expected number of defective products per million produced, is shown in the table above. In the motorcycle, automotive and other industries, companies want to achieve a Cpk process capability of at least 1.00 (2700 defective products per million produced). This means a 99.73 % production success rate.

Implementation of SPC method

When the SPC method was introduced in car production in the late 1980s, vehicle manufacturers soon began to demand that their suppliers immediately implement this method. In such cases, the usual path of new organization or investment with careful planning, information and decision-making procedures was not possible, since the future of the company often depended on a large customer, who did not allow for a choice. In cases where there is no compulsion to implement the SPC method, it is advisable to carry out the aforementioned procedure, i.e. in the sense of project management rules.

The constantly increasing demands for reducing costs and increasing quality are also the driving force in the development of process-driven production, which covers the entire process chain from planning work and resources through purchasing, control to organizing the SPC method in production. A very widespread program for performing SPC analysis is Gauss SPC.

Control Charts and SPC method

SPC is a method for quality management, and a control chart is a tool (graphic tool) that performs this control. Control charts and the statistical process control (SPC) method are closely related, as control charts are the most commonly used tool within the SPC method.

SPC is a broader methodology that uses statistical techniques to monitor, control and improve processes, and control charts are a graphical representation that makes this possible. The charts contain control limits (upper ULC and lower ULC), which are statistically calculated. When a point on the chart crosses these limits, the SPC method signals that the process has gone out of control and that action is needed. Control charts therefore provide immediate, real-time information about the operation of the process. It is a kind of preventive action - instead of looking for defects in the finished products, SPC with control charts allows us to prevent the production of non-conforming products by observing trends.

The image in Fig 4 shows a presentation of the results of the SPC analysis of one quality characteristic: with control charts in the central part, below are the measurement results in a table (20 columns - samples mean different times of products taken from production - one sample includes five products. In total, 100 measured products). On the right side above are the results of key statistics, and on the right below is a graphic display.

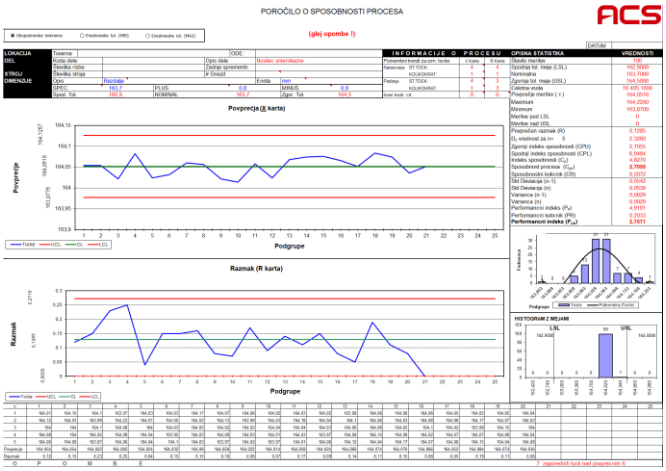
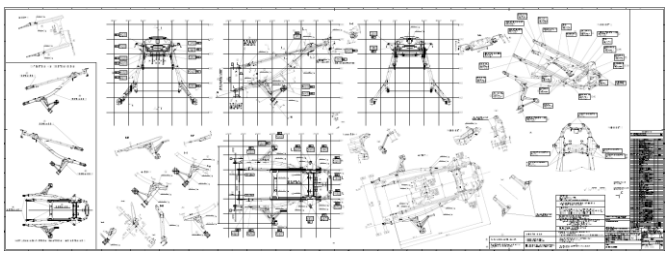


Fig. 4 *SPC analysis [5].*

2. Case study of SPC statistical process control

We have been storing a steel rear frame of a BMW motorcycle in our garage for many years. I was curious about how Tomos actually became nominated by a German company for such a demanding welded product and how the measurements were taken. Question gave rise to a short chronological story, which I will briefly present in the rest of the article.

The value of the successful supplier increased when BMW entrusted Tomos factory the task to enter the competition with other companies in the segment of complex welded components. My father joined the company in 2003 and shortly after his arrival he was entrusted with the management of the project named BMW K71 with a large format drawing containing dimensional and technological requirements. The product is the rear frame of the motorcycle BMW F 800 S/ST made from steel structure, as indicated in the fig. 5.



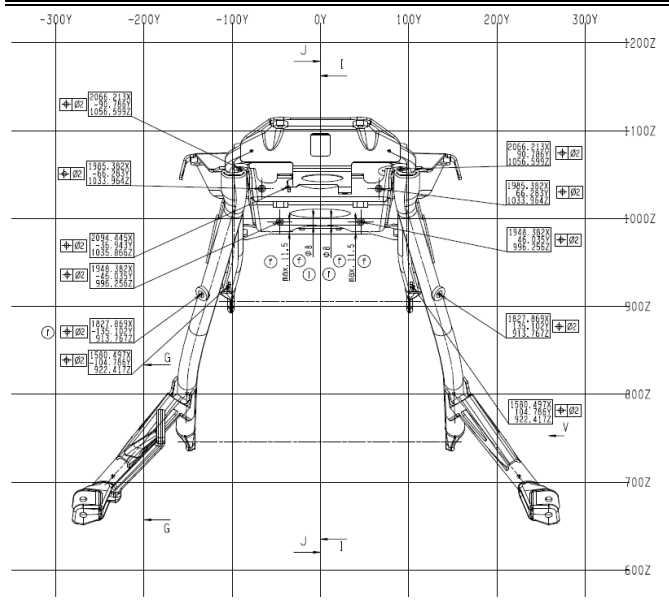


Fig. 5 *Drawing of rear frame BMW F 800 S/ST. Above: assembly drawing. Below: detail view [5].*

They received a 3D model from BMW's development department in Munich and began building the first prototype. The first prototype was made using various rapid prototyping techniques, from DMLS - direct metal laser sintering technic, to waterjet technology and the skilled hands of a master named Alfio in the prototype workshop, who hammered and welded everything together in the right place according to the drawing. The images below show the first prototype (see left image of Fig. 6) and a detail of the complex 3D sheet metal.



Fig. 6 *First prototype, made by hand and rapid prototyping technics..*

BMW later assessed the company in several areas and decided to nominate the company to produce this product. Soon after, they received an order to produce three functional prototypes using materials and dimensional accuracy according to the drawing. The result of the functional prototype is shown in Fig. 7.



Fig. 7 *Functional prototype. Left: assembly and construction. Right: detail.*

The measurements were performed on a 3D measuring machine. The experience of the measurer and the measurement conditions were very important.



```
PART NAME : Okvir K71 vpen
REV NUMBER : 7 678 666
SER NUMBER : 292_640 nov
STATS COUNT : 1
Je vpenjalna priprava na istem mestu? : YES
------------------------------------------------------------------
Oznaka : Stev.1 - varjeno 10.02.2006
------------------------------------------------------------------
***** 1. Polozaj zgornjih vpenjalnih lukenj ************
DIM LOC26= LOCATION OF POINT PNT2 UNITS=MM
AX MEAS NOMINAL +TOL -TOL DEV OUTTOL
X 1471.000 1471.000 0.050 -0.050 0.000 0.000 #
Z 906.100 906.100 0.050 -0.050 0.000 0.000 #
***** 2. Polozaj spodnje vpenjalne luknje - L ************
DIM LOC1= TRUE POSITION OF CIRCLE CIR SP L UNITS=MM
AX MEAS NOMINAL +TOL -TOL BONUS DEV OUTTOL
X 1444.792 1444.600 0.192
Z 745.192 746.600 -1.408
TP MMC 3.000 0.000 2.842 0.000 #
***** 3. Polozaj spodnje vpenjalne luknje - D ************
DIM LOC2= TRUE POSITION OF CIRCLE CIR SP D UNITS=MM
AX MEAS NOMINAL +TOL -TOL BONUS DEV OUTTOL
X 1444.828 1444.600 0.228
Z 746.738 746.600 0.138
TP MMC 3.000 0.000 0.532 0.000 #
***** 4. Razdalja med spodnjima vpenjalnima luknjama ************
DIM DIST1= 2D DISTANCE FROM CIRCLE CIR SP D TO CIRCLE CIR SP L PAR
TO YAXIS, NO_RADIUS UNIT
S=MM
AX MEAS NOMINAL +TOL -TOL DEV OUTTOL
M 304.805 304.000 3.000 0.000 0.805 0.000 #
***** 5. Kot zgornjega nosilca ************
DIM ANGL1= 3D ANGLE (COMPLEMENT) FROM PLANE PLN NOS ZG TO ZAXIS
AX MEAS NOMINAL +TOL -TOL DEV OUTTOL
A 15.598 15.500 0.750 -0.750 0.098 0.000 #

CMM DEA Mistral st. 01555 : Instrument
3 micron + 4*10E-6*L : Uncertainty of measurement
```

Fig. 8 *Functional prototype measurement and detail of measuring results.*

After successfully building functional prototypes, the team arranged with BMW to visit Berlin, where their measurements and assembly of the motorcycles are taking place. Fig. 9 shows one of three functional motorcycles with a visible connection of the rear steel frame to the front frame, made of aluminum alloys.



Fig. 9 *Functional prototype in BMW Berlin..*

A little later, intensive work on the industrialization or serial production of a complex product using robotic welding took place in Koper. The team from the Varstroj Lendava and technologist Branko were key at that time to ensure that the line was set up in accordance with the time project and successfully tested in the first pre-series (see Fig 10 and Fig. 11).



Fig. 10 *Industrialization and robotic welding phase*



Fig. 11 *Technologist Branko Stanič did an exceptional job with the final welding settings.*

The measurements on the 3D machine had to be carried out in accordance with the agreement and protocol of the BMW company. Knowledge of the measurement systems, accuracy and also the uncertainty of the measurements was important. Tracking and timely control in the stages before series production proved to be successful and comparable to the measurement results in Germany.



Fig. 12 *The measurement expert, Samo Strle did an excellent job.*

All measurements that were carried out, from the initial series to the confirmation of series production by the customer BMW, were analyzed using the SPC method. Adjustments and corrections were made. On my father's server I found some SPC analyses of the first pre-series and measurements of key quality characteristics.

From the control charts, we would understand that the average of the mean values and the average of the ranges are just fine.

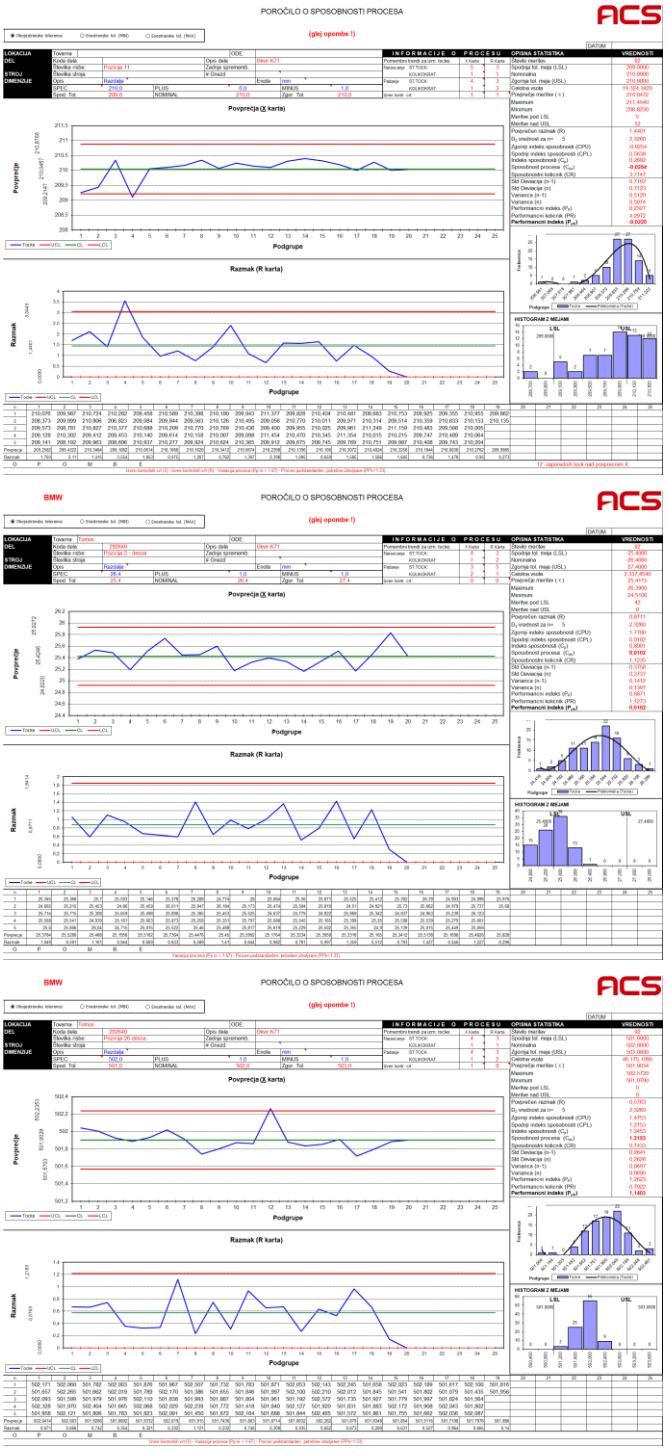


Fig. 13 *SPC analysis of three (3) mean quality characteristics [5].*

The critical process capability calculations in the upper right corner of all three measurements show a different picture. The best result was achieved in the last quality characteristic diagram and the dimension 502 mm ± 1mm, when the process capability was Cpk = 1.21.

Conclusions

Tools and techniques for ensuring production quality vary widely, from simple ones in the form of graphs and diagrams to complex statistical methods. The statistical approach to quality advocates the principle that no two products are exactly the same and that there is always some difference between them.

Statistical techniques and tools are used to study the differences or variations in product characteristics. As a rule, worn-out, poorly maintained machines, inexperienced and unskilled workers, inferior materials and inadequate environmental conditions will increase the range of normal variability and thus reduce the capability of the machine or process.

Calculation of statistics, mean and standard deviation, process stability Cpk seem simple, until we have to bring the process and the values of these statistics to the desired values required by the customer. That's when the real work begins, setting up machines and technological parameters, finding reasons why statistics "run away" outside the limits.

However, Tomos succeeded then, serial production successfully started welding the frame in 2006. And soon the next orders came to Koper: from BMW, Ducati, KTM and other big players in the motorcycle industry segment.

3. References

1. D. Kač, *Integrirano obvladovanje kakovosti* (Ljubljana, Obrtnik, 2004)
2. P. Crosby, *The eternally successful organisation* (New York, McGraw-Hill Book Company, 1988)
3. A. Šostar, *Management kakovosti* (Maribor, Fakulteta za strojništvo, 2000. ISBN 86–435– 0345–2)
4. J. Marolt, B. Gomišček, *Management kakovosti* (Kranj, Moderna organizacija, 2005. ISBN 961–232–174–4)
5. S. Božič, *Project documentation* (Koper, 2003 – 2026)

Evaluation of Adhesively Bonded Joints for Repair of Exterior Automotive Plastic Parts

Štefan Novotný 1*, Jakub Brezina 2, Janette Brezinová 1

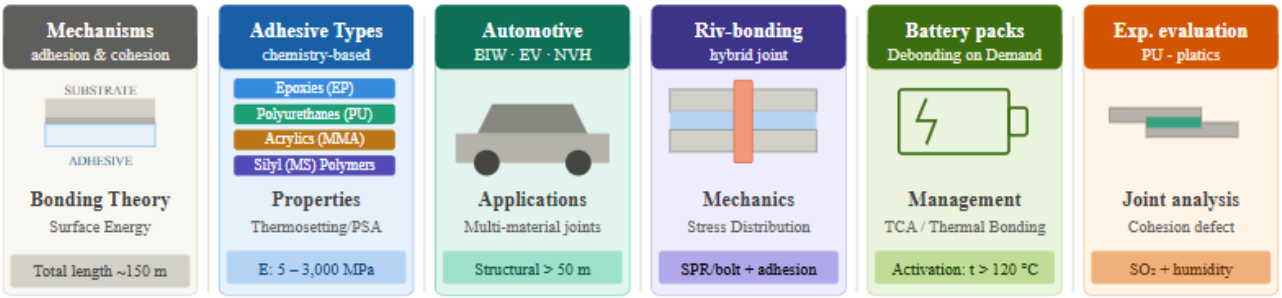
1 Technical University of Košice, Faculty of Mechanical Engineering, Department of Automotive Production, Mäsiarska 74, 040 01 Košice, Slovakia

2 Technical University of Košice, Faculty of Mechanical Engineering, Department of Technology, Materials and Computer Aided Manufacturing, Mäsiarska 74, 040 01 Košice, Slovakia

* Correspondence: stefan.novotny@tuke.sk

Abstract: This paper deals with the possibility of renovating exterior plastic automotive components using adhesive bonding technology. The research focuses on the evaluation of the shear strength of adhesive joints formed using adhesive systems commonly applied in automotive repair practice. The experimental investigation was carried out using selected adhesives, and the shear strength of the bonded joints was evaluated. To simulate real operating conditions of vehicles, accelerated laboratory tests were performed in which the bonded joints were exposed to various degradation environments. Subsequently, changes in the shear strength of the adhesive joints were evaluated after their exposure to these conditions. The study also examined the influence of road de-icing agents commonly used in winter road maintenance on the quality and integrity of the adhesive joints. Based on the analysis of fracture surfaces, the failure mechanisms of the joints were identified and classified as adhesive or cohesive failure. The obtained results provide a basis for assessing the applicability of adhesive bonding technology for the renovation of exterior plastic automotive components and contribute to the optimization of repair procedures used in automotive maintenance practice.

Graphical abstract:



Graphical abstract: Five key themes of the review and an experimental evaluation

Keywords: adhesive bonding; structural adhesives; body-in-white; riv-bonding; EV battery pack; debonding-on-demand; polyurethane adhesives; accelerated degradation

1. Introduction

Over the past two decades the automotive industry has faced pressure from multiple concurrent challenges. Increasingly stringent CO_2 emission targets (EU: 95 g/km in 2021, 0 g/km from 2035) force manufacturers to reduce vehicle mass and electrify drivetrains. At the same time, passive-safety requirements demand the use of ultra-high-strength steels (UHSS, DP, TRIP) and press-hardened steels (PHS) in crash-load paths. Aluminium alloys, carbon-fibre-reinforced polymers (CFRP), magnesium alloys, and hybrid materials are entering the body-in-white (BIW) as lightweight alternatives [1, 2]. When heterogeneous combinations of these materials are used in a single structure, classical resistance spot welding (RSW) encounters physical limits: differing melting points, formation of brittle intermetallic phases, and galvanic corrosion preclude direct welding of aluminium to high-strength steel. Adhesive bonding overcomes these constraints and simultaneously distributes stress uniformly across the bond area, thereby increasing structural stiffness and fatigue resistance of the body [1]. A consolidated example is the Lotus Elise and Evora sports car body, where the combination of structural adhesive bonding and self-piercing riveting (SPR) enabled a 40 % weight saving over a conventional steel welded structure while achieving superior torsional stiffness. Today, adhesive bonding is standard in the production of aluminium-intensive vehicles (Audi A8, Jaguar XJ) as well as in CFRP-intensive platforms (BMW i3, i8) [1, 10]. Electromobility is the dominant growth driver: battery-pack assembly alone requires structural, thermally conductive, and sealing adhesives, creating an entirely new application segment that did not exist a decade ago [2]

2. State of the Art

2.1 Adhesion Mechanisms and Theory of Adhesive Joints

The strength and durability of an adhesive joint result from a combination of physico-chemical mechanisms at the adhesive–substrate interface: (1) mechanical adhesion, interlocking of the cured adhesive in surface micro-roughness; (2) adsorption adhesion, van der Waals forces and hydrogen bonds at adequate wettability; (3) diffusion adhesion, inter-chain diffusion of polymer molecules (relevant for bonding compatible polymers); (4) chemical adhesion, covalent bonds (silane primers) resistant to hydrolysis. The key parameter is the substrate surface energy: metals are readily wetted, polyolefins require surface activation [1, 5]. Joint strength is characterized either by classical shear strength in MPa (ISO 4587) or by fracture-mechanics parameters (fracture energy G_c). The latter approach, employing cohesive zone models and DCB/ENF tests, yields more predictively robust results and is preferred in crash simulations [1]. Failure modes per ISO 10365:2022 are: adhesive failure (AF, failure at the interface), cohesive failure (CF, failure within the adhesive body, the desired outcome), and substrate failure (SF, joint strength exceeds material strength). A particular challenge is posed by so-called kissing bonds, areas of zero bond strength caused by silicone contamination, which are difficult to detect by standard UT methods [1].

2.2 Classification and Properties of Structural Adhesives

Structural adhesives in the automotive industry must satisfy a demanding combination of requirements: high static and dynamic strength, toughness in crash loading (impact peel resistance), temperature resistance from −40 °C to +180 °C, compatibility with the e-coat process (175–185 °C), and increasingly also reversibility (DoD). The four main chemical classes, as seen in Fig. 1 are: epoxy, polyurethane, acrylic (MMA), and MS polymer [1, 3]. Epoxy adhesives are the dominant class in BIW structural bonding. They are characterised by high elastic modulus (E > 1000 MPa), low creep, and temperature resistance up to 180 °C. One-component (1K) systems cure in the e-coat oven; two-component (2K) systems cure at room temperature.

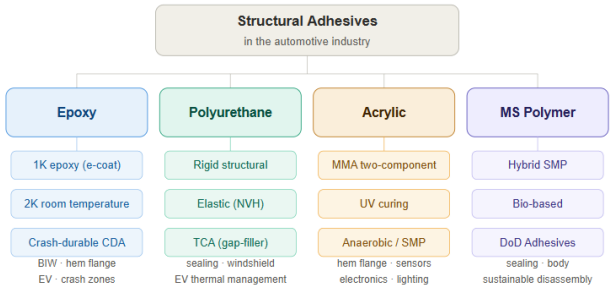


Fig. 1 Hierarchical classification of structural adhesives used in the automotive industry by chemical basis and typical applications

A key parameter for crash applications is CDA (crash-durable adhesive) resistance — a minimum of 20 N/mm in the impact peel test (ISO 11343). Modern CDA epoxies contain elastomeric core-shell rubber particles that increase fracture toughness without reducing the modulus [1, 11]. Polyurethane (PUR) adhesives have a lower modulus (E ~ 5–500 MPa) but higher elongation at break (> 100 %) and are preferred for hem flange bonding, windshield sealing, and NVH damping panels. Thermally conductive PUR gap-fillers (TCA, λ = 2–10 W/(m·K)) represent a key system for EV battery thermal management. Acrylic (MMA) adhesives cure rapidly at room temperature and bond well to oily surfaces. MS polymer adhesives combine the flexibility of silicone with the paintability of polyurethane — excellent for sealing and increasingly investigated for DoD applications [2, 4].

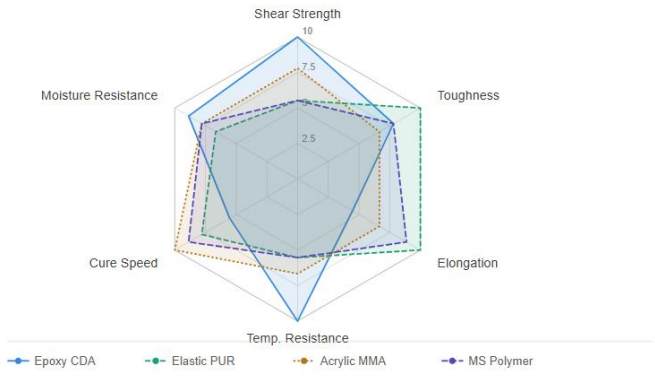


Fig. 2 Comparison of typical properties of the four classes of structural adhesives on six evaluation axes (relative rating 0–10)

2.3 Applications in Body-in-White (BIW)

The application of structural adhesives in BIW bodies takes several forms: fully bonded joints, hybrid combinations with SPR or spot welding, and hem flange bonding. A modern BIW typically contains 50–150 m of adhesive bond with a total adhesive mass of 5–15 kg [1]. Bonding fulfils three primary functions in the body: (1) structural — increases stiffness and fatigue resistance; (2) sealing — prevents corrosion and water ingress; (3) acoustic — reduces noise and vibration transmission (NVH) [1, 10]. In aluminium body construction, adhesive is applied to the entire bonding area of frame profiles before mechanical joining (SPR or clinching). This combination achieves higher stiffness than either process alone and simultaneously provides corrosion protection at the Al–Al or Al–steel interface. For primary crash load paths (longitudinal members, B-pillars, sills), exclusively CDA with proven impact peel resistance are used — at impact speeds of 2 m/s they deform plastically rather than fracturing in a brittle manner, contributing to controlled deformation of the crumple zone [11]. A trend is the reduction of cure temperature below 140 °C to save e-coat oven energy [10].

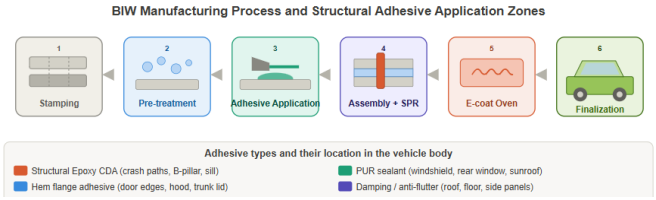


Fig. 3 BIW manufacturing process and structural adhesive types by location: CDA crash paths (orange), hem flange (blue), PUR sealant (green), damping/anti-flutter (purple)

2.4 Bonding of Dissimilar Materials

Dissimilar-material joining is one of the most important areas for adhesive bonding from a multi-material architecture perspective. The main challenges are: (1) galvanic corrosion between carbon fibres (CFRP, cathode) and aluminium (anode) — requires an electrically insulating adhesive layer of ≥ 0.3 mm; (2) large CTE mismatch — $\alpha_{CFRP} \approx 0–2 \cdot 10^{-6}\ K^{-1}$ vs. $\alpha_{Al} \approx 23 \cdot 10^{-6}\ K^{-1}$, generating differential thermal stress that must be absorbed by the elastic adhesive layer; (3) surface energy mismatch between polar and non-polar materials [1, 4]. Adhesive bonding circumvents these problems because it is carried out at room or mildly elevated temperature, does not induce metallurgical changes, and the elastic adhesive layer absorbs differential thermal expansion. For Al–CFRP joints, the established approach combines sulphuric acid anodising (SAA) of aluminium with a silane primer and a toughened epoxy adhesive; the alternative of sandblasting + atmospheric plasma is suited to series production owing to its speed and absence of liquid chemicals [4, 16]. For adhesive selection in multi-material applications, toughened epoxies with a shear modulus of 1–3 GPa and elongation at break > 5 % are preferred — a compromise between the stiffness required for structural load transfer and the ductility needed to accommodate thermal and mechanical deformation. Key commercial systems include Loctite EA 9321, 3M DP490, and Sika SikaPower-4720 [4]. The review by Karthikeyan and Naveen [16] shows that the greatest strength improvement in composite adhesive joints is achieved by combining plasma or laser surface treatment (improving wettability, removing peel-ply residues) with a stepped-lap geometry. Schanz et al. [15] showed that laser treatment that exposes carbon fibres can improve short-term adhesion but accelerates galvanic corrosion in salt spray testing — highlighting that surface pre-treatment must be evaluated holistically [15].

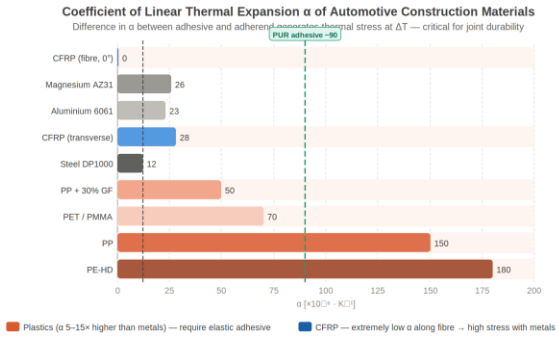


Fig. 4 Coefficients of linear thermal expansion α of selected materials. Large differences between CFRP (α ≈ 0–2·10⁻⁶ K⁻¹), metals (12–26·10⁻⁶ K⁻¹) and plastics (30–200·10⁻⁶ K⁻¹) generate thermal stresses absorbed by the adhesive layer

2.5 Hybrid Joints: Riv-Bonding

Self-piercing riveting (SPR) has established itself since the late 1990s as the dominant mechanical joining technology for aluminium-intensive vehicles. However, on its own, SPR provides a stress concentration at the rivet and limited fatigue performance. The combination of SPR with structural adhesive bonding — referred to in English-language literature as riv-bonding or bond-riveting — represents a synergistic hybrid: SPR ensures immediate handling strength and accurate part positioning during adhesive cure, while the cured adhesive distributes the shear load over the full bond area and prevents peel [13]. The mechanical properties of riv-bonded joints were systematically studied by Domitner et al. [13] for the Al 6061–CFRP combination. Static shear strength of the riv-bonded joint (4.6–5.0 kN) exceeded both standalone SPR (2.8–3.5 kN) and standalone bonding (4.2–4.5 kN). Fatigue performance was even more impressive: standalone SPR reached ≈ 80,000 cycles to failure, riv-bonding ≈ 390,000 cycles — an increase of nearly 5 times. Crack initiation in riv-bonding always starts near the rivet foot, not at the adhesive interface, confirming the integrity of the adhesive bond [13].

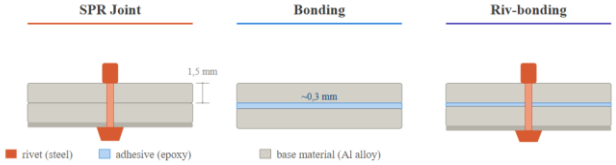


Fig. 5 Cross-section comparison of the three basic joint variants: self-piercing riveting (SPR), pure adhesive bonding, and hybrid riv-bonding

From a fatigue perspective, riv-bonded joints typically achieve twice the fatigue limit of equivalent SPR joints [17]. This is explained by the adhesive layer absorbing the micro-deformations around the rivet that would otherwise initiate fatigue cracks. The quality of the adhesive layer in the vicinity of the rivet (absence of voids, uniform thickness) is therefore critical for fatigue performance [13]. Practical deployment of riv-bonding is complicated by several technological aspects. When the rivet penetrates uncured adhesive, it causes localised displacement and air entrapment around the rivet foot. Sequential process (adhesive first, then SPR) must be carefully optimised with respect to adhesive open time, squeeze-out control, and robot path planning to avoid contamination of the tooling [13, 17]. Similar hybrid approaches are also being developed in combination with clinch-bonding and hole-hemming. The common principle in all variants is the combination of a mechanical element providing immediate strength and peel resistance with an adhesive layer for load distribution and fatigue performance [13, 18].

2.6 Adhesive Bonding in EV Battery Packs

Electric vehicle battery packs currently represent the fastest-growing application area for automotive adhesives. In the cell-to-module-to-pack (CTM) architecture, as seen in Fig. 6, adhesives are used at three levels: (1) bonding of cells to the cooling plate using a thermally conductive gap-filler (TCA, λ = 2–10 W/(m·K)); (2) structural bonding of modules to the pack frame using 2K epoxy (E > 1000 MPa); (3) housing sealing for IP67 water ingress resistance. Rodrigues et al. [2] emphasise that TCA selection is critical for maintaining the Li-ion cell temperature window (15–45 °C) and preventing thermal runaway [2]. The trend is towards cell-to-pack (CTP) and cell-to-chassis (CTC) architectures, where cells are directly integrated without a modular level. This places extreme demands on the structural adhesive: it must compensate for thermal expansion at ΔT = 60–80 K, resist chemical exposure (electrolyte, gases during thermal runaway), and allow disassembly for recycling via DoD [2]. Cell-to-cell bonding is adapted to the cell type: for cylindrical cells the gaps between cells are filled with TCA gap-filler ensuring both thermal contact and mechanical stability; for prismatic cells a flat bond of uniform thickness is preferred. The adhesive layer must withstand cyclic mechanical loading from cell swelling during charge/discharge (volumetric change up to 4 % per cycle) [2]. Structural bonding of battery housings is carried out with 2K epoxy systems with E > 1000 MPa and shear strength > 15 MPa. The sealing function (IP67 protection) is fulfilled by PUR or MS polymer sealants cured at room temperature, which simultaneously compensate for dimensional tolerances of the housing [2]. From a future-research perspective, Rodrigues et al. [2] identified as critical the need to develop reversible (debondable) adhesive systems for EV battery packs that would allow safe and non-destructive disassembly of cells at end of life, which is currently a major bottleneck for battery recycling.

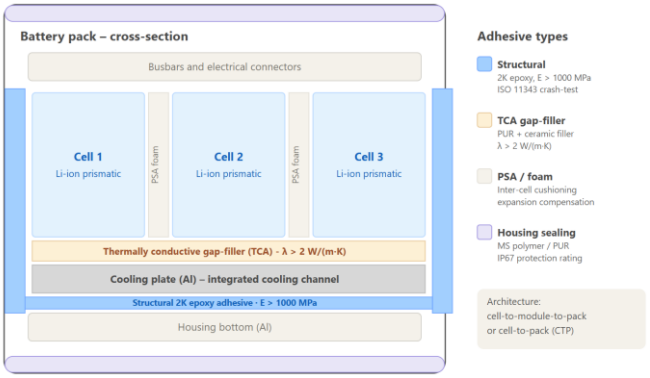


Fig. 6 Schematic cross-section of an EV battery pack showing the application points of four functional adhesive types: TCA gap-filler, structural epoxy, PUR sealant, PSA foam

2.7 Surface Preparation and Durability of Adhesive Joints

Surface preparation is the most critical single factor influencing joint durability [1]. For metal substrates (Al, steel), a combination of mechanical treatment (sandblasting, laser texturing), chemical activation (anodising, phosphating), and physical activation (plasma, flame) is used. For CFRP, laser treatment and atmospheric plasma are effective for removing peel-ply residues and increasing wettability [15, 16]. For plastic adherends, atmospheric plasma is the industrial standard — it increases the surface energy of polyolefins from ~30 mJ/m² to > 50 mJ/m² by generating polar groups (–OH, C═O). Results indicate that water absorption is the dominant degradation mechanism — after 1000 h at 50 °C, strength can decrease by 30–50 %. Automotive reference standards include

accelerated cyclic tests per VDA 233-152 and salt spray per DIN EN ISO 9227.

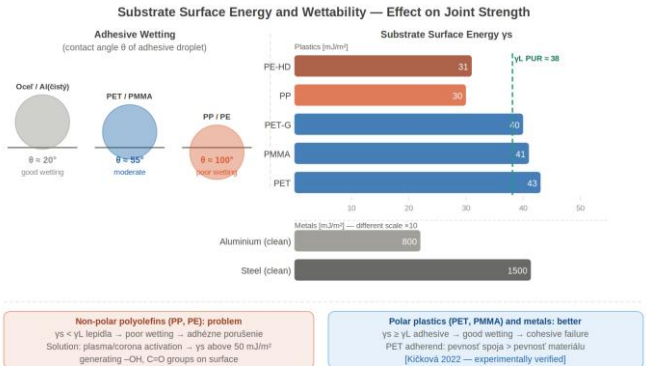


Fig. 7 Surface energy γs of plastic adherends and its effect on wettability by PUR adhesive (γL ≈ 38 mJ/m²). Non-polar polyolefins PP/PE-HD (γs < γL) exhibit poor wettability and require plasma activation

2.8 Sustainability and Debonding-on-Demand (DoD)

The conflict between the high durability of adhesive joints and the requirement for end-of-life recyclability of components has become one of the most intensively studied topics in adhesive research. The EU Battery Regulation (2023/1542) requires manufacturers to demonstrate that at least 70 % of battery active materials can be recovered — which is currently incompatible with permanently bonded cell-to-pack architectures [1, 7]. Current adhesive joints are designed as permanent by their nature. Disassembly in practice involves mechanical cutting, which damages substrates and prevents reuse of high-value components (CFRP panels, battery cells). Debonding-on-demand (DoD) adhesive systems offer an alternative: they can be deactivated by a controlled external stimulus as seen in figure 8 - heat, electric current, chemical trigger, and a mechanical trigger, without substrate damage [1, 7].

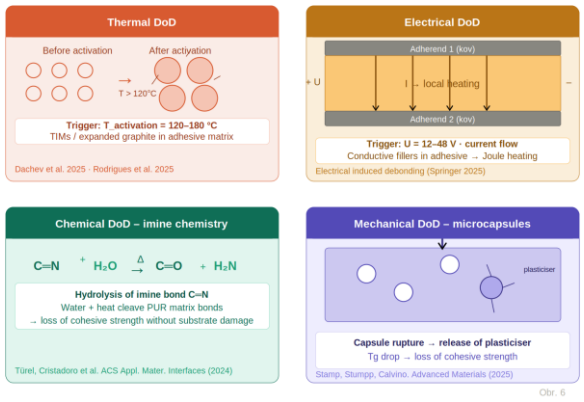


Fig. 8 Four fundamental debonding-on-demand mechanisms: thermal (TIMs/capsules), electrical (Joule heating), chemical (imine bond hydrolysis), and mechanical (microcapsule rupture, releasing plasticizer)

Türel et al. [7] published a study of DoD polyurethane adhesives based on imine chemistry (hydrolysis of C═N bonds in contact with water at T > 80 °C). Joints can be cleanly separated by immersion in hot water without organic solvents. Stamp et al. [20] developed a hybrid SMP (Shape Memory Polymer) system combining thermoplastic DoD behaviour with the typical mechanical properties of structural epoxies. For automotive applications, however, the main challenge remains satisfying contradictory requirements: the adhesive must resist temperatures of –40 to +180 °C, chemical exposure, and fatigue loading for 15+ years in service, while remaining reversible on demand in less than 60 seconds. Commercialisation of DoD technologies for series production remains the key challenge for the coming decade [1, 7, 8].

3. Materials and Methods

3.1 Adherends Used

To verify the knowledge discussed in the preceding sections, an experimental study was carried out evaluating the adhesive joints of three commercial two-component polyurethane adhesives (RIGID, FLEX, TPO; RETECH) on three types of plastic adherends representing different polymer groups: (1) polyethylene terephthalate (PET) — a polar semi-crystalline polyester; (2) polymethyl methacrylate (PMMA), a polar amorphous acrylic with high gloss; (3) polypropylene (PP), a non-polar semi-crystalline polyolefin. All three adhesives are black 2K adhesives in a 1: 1 mix ratio, curing at room temperature.



Fig. 9 Used polyurethane adhesives from RETECH – products RIGID, FLEX, TPO

3.2 Experimental Methodology

Bond areas were pre-treated by sanding (P 180 grit) perpendicular to the loading axis, degreased with RETECH degreaser, and activated with the manufacturer's universal activator. Surface roughness was evaluated with a Mitutoyo Surftest SJ-301 profilometer (ISO 21920-2:2021; Ra, Rz, Rt). Lap-shear specimens were each tested by EN 1465, as seen on Fig.10, on a TIRA test 2300 machine. Degradation environments: (1) SO_2 + humidity condensation chamber at 40 °C, 4 weeks by norm ISO 22479:2019; (2) Salt solution (20 % NaCl)

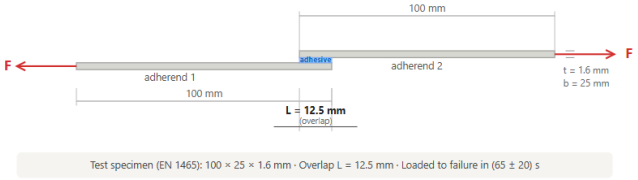


Fig. 10 Geometry of the lap shear joint per EN 1465

4. Results and Discussion

This chapter presents the results of the lap-shear test (EN 1465) for 3 adhesive and 3 adherend (9 in total) combinations under three experimental conditions: after curing (reference state), after exposure in the SO_2 + humidity condensation chamber, and after exposure in salt solution. Each combination was represented by n = 6 test specimens; results are evaluated by descriptive statistical parameters (mean $\bar{x}$, standard deviation SD, coefficient of variation CV) and the percentage strength change vs. the reference state. The coefficient of variation (CV) remained below 25 % for most combinations.

4.1 Strength After Curing — Reference State

After curing (reference state, no degradation), RIGID achieved the highest strength across all three adherends: PET 5.42 ± 0.21 MPa (CV = 3.9 %), PMMA 3.17 ± 0.36 MPa (CV = 11.4 %), and PP

0.77 ± 0.05 MPa (CV = 6.5 %). FLEX ranked second for PET (3.71 ± 0.24 MPa) and PP (0.97 ± 0.07 MPa), while for PMMA its strength (2.79 MPa) was almost equal to TPO (2.39 MPa). The adhesive ranking for polar adherends (PET, PMMA) is consistently RIGID > FLEX > TPO; for PP the ranking is FLEX > TPO > RIGID. The low absolute values for PP (0.77–0.97 MPa) vs. PET (2.63–5.42 MPa) directly correlate with the surface energy and confirm the need for surface activation prior to bonding polyolefins.

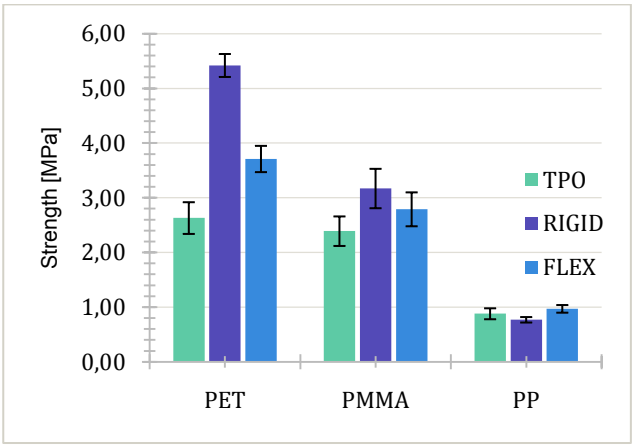


Fig. 11 Strength After Curing ($\bar{x} \pm 1$ SD, n = 6)

4.2 Effect of SO_2 + Humidity

Exposure in the condensation chamber (40 °C, SO_2 + humidity, 4 weeks) led to a consistent decrease in joint strength across all adhesive–adherend combinations. The acidic SO_2 atmosphere in combination with condensing humidity promotes hydrolytic degradation of urethane and ester bonds within the PUR network, resulting in reduced crosslink density and interfacial weakening. The most pronounced decreases were observed for FLEX adhesive on PP adherend (−24.7 %, from 0.97 MPa to 0.73 MPa) and for FLEX on PET (−14.8 %, from 3.71 MPa to 3.16 MPa), attributable to the higher network permeability and lower acid resistance of the flexible formulation. RIGID exhibited the best environmental resistance: decreases were limited to −8.1 % (PET: 4.98 MPa), −11.7 % (PMMA: 2.80 MPa), and −16.9 % (PP: 0.64 MPa), confirming the superior chemical resistance of its stiff epoxy-like network. TPO showed intermediate behaviour (−13.3 % to −21.6 % depending on adherend). The PMMA–TPO combination exhibits elevated scatter (CV = 54.3 %) — results included in the analysis, but conclusions must be interpreted with caution.

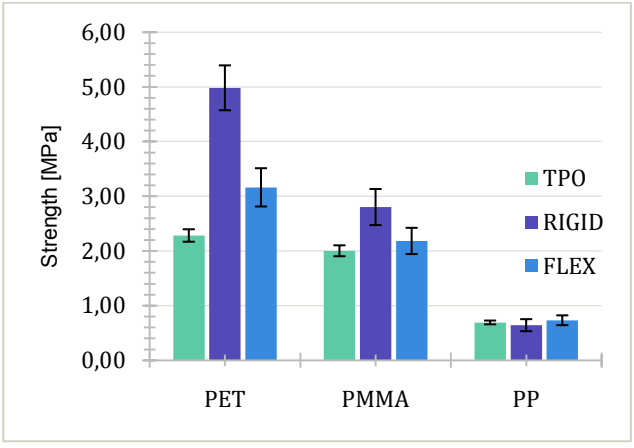


Fig. 12 Strength After SO_2 + Humidity Exposure ($\bar{x} \pm 1$ SD, n = 6)

4.3 Effect of Salt Solution

Salt solution (20 % NaCl, 2 weeks) produced a consistently degradational effect across all adhesive–adherend combinations, generally more severe than SO_2 + humidity exposure for the FLEX formulation and comparable for RIGID and TPO. For PP–FLEX, a strength decrease of −52.6 % was recorded (from 0.97 MPa to 0.46 MPa), representing the most pronounced negative effect in the entire dataset. Similarly, PET–FLEX decreased by −46.1 % (from 3.71 MPa to 2.00 MPa), indicating the particular sensitivity of the flexible PUR formulation to an ionic environment — probably due to higher network permeability and weaker ester-bond resistance to hydrolysis in the presence of chloride ions. RIGID showed the best resistance: PMMA–RIGID decreased by only −9.7 % (from 3.17 MPa to 2.87 MPa) and PET–RIGID by −11.3 % (from 5.42 MPa to 4.81 MPa); PP–RIGID decreased by −23.4 % (from 0.77 MPa to 0.59 MPa), confirming its superior environmental resistance relative to the other formulations. TPO showed moderate decreases (−14.1 % to −19.3 %) for all three adherends, indicating good to moderate stability in salt solution.

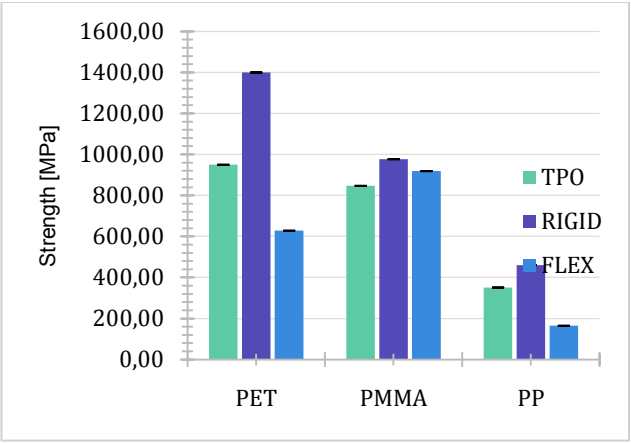


Fig. 13 Strength After Salt Solution Exposure ($\bar{x} \pm 1$ SD, n = 6)

4.4 Effect of Environment on Strength — Summary

The most stable system is RIGID–PET: strength remained above 4.80 MPa across all three environments (5.42 MPa reference; 4.98 MPa after SO_2 ; 4.81 MPa after salt). The most sensitive system is FLEX–PP: a drop from 0.97 MPa (reference) to 0.46 MPa (salt) represents a loss of −52.6 %. Both degradation environments consistently reduced joint strength across all 9 adhesive–adherend combinations: SO_2 + humidity caused moderate losses (−8.1 % to −24.7 %), while salt solution produced more severe degradation for FLEX adhesive (up to −52.6 %) and moderate losses for RIGID and TPO (−9.7 % to −23.4 %). Overall adhesive performance ranking (averaged across all adherends and environments): RIGID (2.89 MPa) > FLEX (1.98 MPa) > TPO (1.76 MPa).

4.5 Failure Mode Analysis

The failure character of adhesive joints was evaluated by visual classification per EN ISO 10365:2022 immediately after each test. Cohesive failure (CF) within the adhesive body was achieved for all combinations with PET and PMMA adherends, confirming adequate adhesion to these surfaces. For PP adherend, mixed (CF+AF) or adhesive failure (AF) was typical, correlating with the low substrate surface energy. After salt solution exposure, FLEX–PET and FLEX–PP combinations exhibited a transition from

cohesive to adhesive failure, related to degradation of the adhesive–adherend interface.

5. Conclusions

The experimental study evaluated the lap-shear strength (EN 1465) of three commercial 2K PUR adhesives (RIGID, FLEX, TPO) bonded to three automotive plastic substrates (PET, PMMA, PP) in reference conditions and after accelerated degradation in SO_2 + humidity and salt solution environments. The following conclusions can be drawn: (1) Polar PET adherend bonded with RIGID adhesive provides the highest and most stable lap-shear strength (4.81–5.42 MPa) across all tested environments, making it the most reliable system for exterior plastic repair applications. (2) Non-polar PP requires dedicated surface activation prior to bonding — without it, strengths are 60–85 % lower than for polar adherends (PET, PMMA). (3) SO_2 + humidity exposure (40 °C, 4 weeks, ISO 22479:2019) caused moderate strength reduction across all adhesive–adherend combinations (−8.1 % to −24.7 %), with the greatest sensitivity observed for FLEX adhesive on PP (−24.7 %) and PET (−14.8 %), attributable to the higher permeability of the flexible PUR network and its susceptibility to acid-accelerated hydrolysis of urethane bonds. (4) Salt solution (20 % NaCl, 2 weeks) is critically degrading for FLEX adhesive — PET–FLEX decreased by −46 % and PP–FLEX by −53 % — disqualifying this formulation for applications exposed to road de-icing agents; RIGID and TPO maintained moderate resistance (−9.7 % to −23.4 %). (5) RIGID adhesive exhibits the highest and most reliable strength combined with low scatter (CV 4–23 %) and is recommended for structural repair of exterior plastic body parts in environments with chemical exposure. (6) TPO adhesive represents a cost-effective compromise with moderate resistance to both degradation environments. Adhesive bonding has moved from a supplementary role to an indispensable competence in the automotive industry, joining dissimilar BIW materials, enabling hybrid riv-bonding joints with superior fatigue performance, and fulfilling structural, sealing, and thermally conductive functions in EV battery packs. The experimental results confirm that adhesive selection must account for substrate type, degradation environment, and required durability — a single PUR formulation is insufficient for the entire portfolio of automotive exterior plastics.

Acknowledgments: This research is the result of a project supported by project Visegrad Fund fellowship No. 62610056 - Scientific Cooperation in Advanced Surface Engineering: Joint Research on PTA and Laser Cladding for Die-Casting Mold Renovation, Slovak Research and Development Agency VEGA Scientific Grant Agency "Possibilities of applying laser additive technologies in the restoration of functional surfaces" (1/0597/23), Cultural and Educational Grant Agency KEGA "Hybrid education of students for the current needs of the automotive industry" (024TUKE-4/2025), "Innovative approaches to the restoration of functional surfaces by laser surface treatment" (APVV-20-0303) and "Integrity of protective multilayers under high-temperature exposure conditions" (APVV-24-0381).

REFERENCES

[1] DACHEV, D., KAZILAS, M., ALFANO, G., OMAIREY, S. Towards Reliable Adhesive Bonding: A Comprehensive Review of Mechanisms, Defects, and Design Considerations. Materials. 2025, vol. 18, no. 12, art. 2724. ISSN 1996-1944. DOI: 10.3390/ma18122724.

[2] RODRIGUES, V. C. M. B., KASAEI, M. M., MARQUES, E. A. S., CARBAS, R. J. C., DA SILVA, L. F. M. Adhesive bonding in automotive battery pack manufacturing and dismantling: a review. Discover Mechanical Engineering. 2025, vol. 4, no. 1, art. 25. ISSN 2731-6564. DOI: 10.1007/s44245-025-00107-5.

[3] AKHAVAN-SAFAR, A., MARQUES, E. A. S., CARBAS, R. J. C., DA SILVA, L. F. M. Structural Adhesive Bonding for Automotive Applications. 1st ed. Amsterdam: Elsevier, 2025. 384 p. ISBN 978-0-443-23912-0.

[4] PARK, S. K., SHIN, J. H., CHO, H. J. Dissimilar material bonding technology for lightweight future mobility: A review. International Journal of Adhesion and Adhesives. 2024, vol. 128, art. 103616. ISSN 0143-7496. DOI: 10.1016/j.ijadhadh.2023.103616.

[5] ZHANG, Y. S., LI, G. Y., SENKARA, J. Current Research and Challenges in Innovative Technology of Joining Dissimilar Materials for Electric Vehicles. In: Advanced High Strength Steel and Press Hardening: Proceedings of the 4th International Conference (ICHSU2018). Singapore: World Scientific, 2019, pp. 363–380. ISBN 978-981-3277-97-7.

[6] INTROSPECTIVE MARKET RESEARCH. Automotive Adhesives Market: Global Industry Analysis and Forecast 2025–2035. Report, 2025. Available online: https://introspectivemarketresearch.com/reports/automotive-adhesives-market/.

[7] TÜREL, T., CRISTADORO, A. M., LINNENBRINK, M., TOMOVIĆ, Ž. Harnessing Imine Chemistry for the Debonding-on-Demand of Polyurethane Adhesives. ACS Applied Materials & Interfaces. 2025, vol. 17, no. 1, pp. 1234–1245. ISSN 1944-8244. DOI: 10.1021/acsami.4c19435.

[8] HYDER, M. J., GODLEMAN, J., CHIPPINDALE, A. M. et al. Thermally and Base-Triggered "Debond-on-Demand" Chain-Extended Polyurethane Adhesives. Macromolecules. 2025, vol. 58, no. 1, pp. 234–247. ISSN 0024-9297. DOI: 10.1021/acs.macromol.4c02775.

[9] DEMIRAL, M. Strength in Adhesion: A Multi-Mechanics Review Covering Tensile, Shear, Fracture, Fatigue, Creep, and Impact Behavior of Polymer Bonding in Composites. Polymers. 2025, vol. 17, no. 19, art. 2600. ISSN 2073-4360. DOI: 10.3390/polym17192600.

[10] ASSEMBLY MAGAZINE. Structural Adhesives for Automotive Assembly. August 2025. Available online: https://www.assemblymag.com/articles/99405-structural-adhesives-for-automotive-assembly.

[11] BAEK, D., SIM, K.-B., KIM, H.-J. *Mechanical Characterization of Core-Shell Rubber/Epoxy Polymers for Automotive Structural Adhesives as a Function of Operating Temperature* — Polymers, 2021, vol. 13, no. 5, art. 734. DOI: 10.3390/polym13050734.

[12] DUPONT. Driving the future of EV battery assembly with adhesives. White paper, January 2025. Available online: https://chargedevs.com/whitepapers/driving-the-future-of-ev-battery-assembly-with-adhesives/.

[13] DOMITNER, J., SILVAYEH, Z., SOMMITSCH, C., GUBELJAK, N. Load-Bearing Capacities and Fracture Modes of Self-Piercing-Riveted, Adhesive-Bonded and Riv-Bonded Aluminum Joints at Quasi-Static and Cyclic Loadings. Journal of Materials Engineering and Performance. 2023, vol. 32, no.

4, pp. 1789–1801. ISSN 1059-9495. DOI: 10.1007/s11665-022-07677-5.

[14] ADARSH, S. J., NATARAJAN, A. Review on the advancements and relevance of emerging joining techniques for aluminium to polymers/carbon fibre-reinforced polymer lightweight hybrid structures. Proceedings of the Institution of Mechanical Engineers, Part L: Journal of Materials: Design and Applications. 2022, vol. 236, no. 7, pp. 1283–1310. ISSN 1464-4207. DOI: 10.1177/14644207221090331.

[15] SCHANZ, J. et al. Adhesively bonded CFRP/Al joints: Influence of the surface pretreatment on corrosion during salt spray test. Materials and Corrosion. 2022, vol. 73, no. 4, pp. 567–582. ISSN 0947-5117. DOI: 10.1002/maco.202112752.

[16] KARTHIKEYAN, N., NAVEEN, J. Progress in adhesive-bonded composite joints: A comprehensive review. Journal of Reinforced Plastics and Composites. 2025, vol. 44, no. 3-4, pp. 145–178. ISSN 0731-6844. DOI: 10.1177/07316844241248236.

[17] HAN, L., CHRYSANTHOU, A., O'SULLIVAN, J. M. Self-piercing riveting—a review. International Journal of Advanced Manufacturing Technology. 2017, vol. 92, no. 5–8, pp. 1777–1824. ISSN 0268-3768. DOI: 10.1007/s00170-017-0156-x.

[18] ANG, H. Q. An Overview of Self-piercing Riveting Process with Focus on Joint Failures, Corrosion Issues and Optimisation Techniques. Chinese Journal of Mechanical Engineering. 2021, vol. 34, art. 2. ISSN 1000-9345. DOI: 10.1186/s10033-020-00526-3.

[19] DOMITNER, J., SILVAYEH, Z., PREDAN, J. et al. Riv-Bonding of Aluminum Alloys with High-Strength Steels against the Favorable Joining Direction. Journal of Materials Engineering and Performance. 2022, vol. 31, no. 6, pp. 4567–4581. ISSN 1059-9495. DOI: 10.1007/s11665-022-06647-1.

[20] STAMP, C.-H., STUMPP, J., CALVINO, C. Adhesives with Debonding-On-Demand Capability: Leveraging Responsive Microcapsules for Mechanically-Induced Debonding. Advanced Materials. 2025, vol. 37, no. 12, art. 2414308. ISSN 0935-9648. DOI: 10.1002/adma.202414308.

[21] EVONIK INDUSTRIES. Evonik unveils innovative "Debonding on Demand" concept for more sustainable adhesives. Press release, April 2025. Available online: https://www.evonik.com/en/news/press-releases/2025/04/evonik-unveils-innovative--debonding-on-demand--concept-for-more.html.

Comparative thermo-mechanical severity assessment of automotive brake discs under repeated braking cycles

Halil Demolli, Gezim Preniqi, Shkelzen Shabani
University of Prishtina, Prishtina, Kosovo
E-mail: halil.demolli@uni-pr.edu, gezim.preniqi@student.uni-pr.edu, shkelzen.shabani@uni-pr.edu

Abstract: *This paper presents a comparative finite element assessment of the thermo-mechanical severity of automotive brake discs for Mercedes-Benz A180, E220 and E350 under intensive and repeated braking cycles. Transient thermal and structural simulations were evaluated for 27 cases covering high-speed, interurban and urban braking profiles. Gray cast iron EN-GJL-250/G3000 was used as the disc material, while heat flux, convection and radiation were considered as thermal boundary conditions. Maximum temperature, heat flux, total elastic deformation and von Mises stress were normalised and combined through several severity-index scenarios. The results show that the repeated 120-0-120-0 km/h braking cycle is the governing condition for all vehicles. A180 reached the highest raw temperature, stress and deformation, while the equal-weight severity indices confirmed the same critical braking profile within each vehicle group. All cases remained below the selected thermal and mechanical limits.*

Keywords: BRAKE DISC, FEA, THERMO-MECHANICAL ANALYSIS, SEVERITY INDEX, VON MISES STRESS

1. Introduction

The brake disc is one of the main safety-related components in a passenger vehicle. During braking, the kinetic energy of the vehicle is converted into heat at the pad-disc interface. This creates a coupled thermal and structural problem because the temperature field, thermal gradients, elastic deformation and equivalent stress evolve at the same time. If the generated heat is not dissipated efficiently, brake fade, surface distortion, local cracking or accelerated wear may occur [1, 2, 11].

For this reason, finite element analysis is useful for thermo-mechanical evaluation of brake discs under transient thermal and structural loading [2,3]. Repeated braking is particularly important because the second braking event may start before the disc returns to the initial thermal state, which can increase heat accumulation and thermo-mechanical severity [1,11]. The present paper condenses a larger numerical study of three vehicle classes and proposes a normalized severity assessment based on maximum temperature, heat flux, total elastic deformation and von Mises stress. Recent regulatory and scientific references on brake wear emissions are used only to frame the future extension of the model [5–10].

Thermo-mechanical brake analysis is more demanding than purely thermal calculation because temperature is not only an output. It also becomes a structural load through thermal expansion. Non-uniform heating creates local expansion differences, and if these are constrained by disc geometry, hub contact or support conditions, additional thermal stresses appear. For gray cast iron discs, this coupled response is decisive because the material is widely used for its thermal conductivity and damping capacity, but it remains sensitive to local tensile stress and thermal gradients [2,3,11].

The contribution of this paper is not a new material model or a validated failure criterion; rather, it is a compact severity-based interpretation of a larger set of numerical results. Instead of presenting many individual ANSYS images, the paper reduces the response to comparable indicators: maximum temperature, maximum heat flux, total elastic deformation and equivalent von Mises stress.

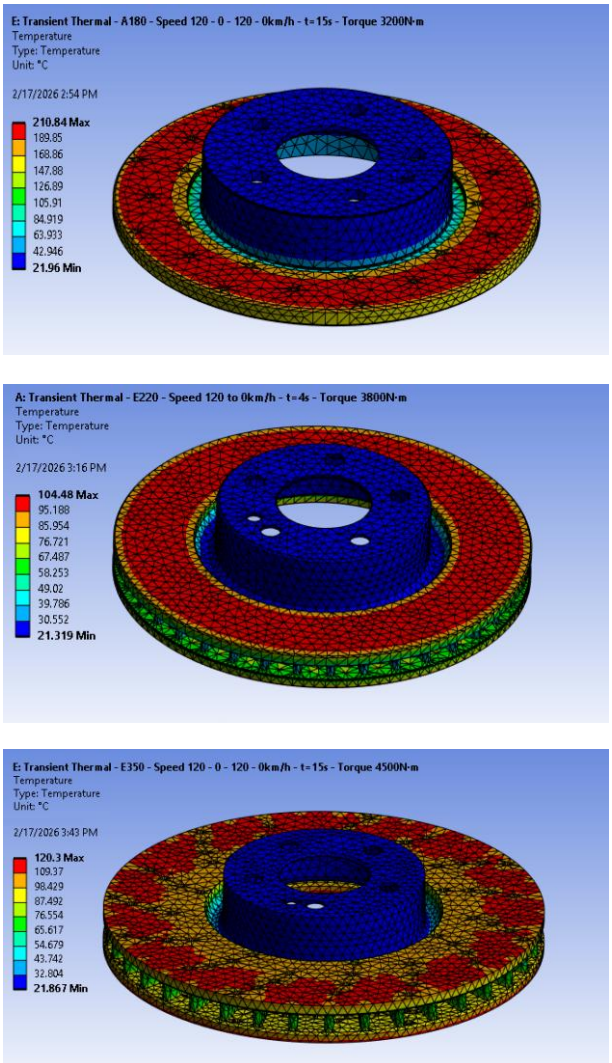


Fig. 1. Brake disc models for different vehicle types.

2. Material and methods

The cases examined are based on brake disc simulations for three models of Mercedes-Benz passenger vehicles: A180, E220 and E350. The numerical model considers 27 cases: nine braking scenarios for each vehicle. The scenarios include high-speed braking from 120 km/h, interurban braking from 80 km/h and urban repeated braking from 50 km/h. Each speed group contains emergency braking, progressive braking and repeated braking with a thermal recovery interval.

Table 1: *Condensed braking scenario matrix*

Group	Cases	Speed scenario	Time profile
High speed	1, 10, 19; 2, 11, 20 3, 12, 21	120 → 0; 120 → 0; 120→0→120→0	4 s; 12 s; 4+7+4 s
Interurban	4, 13, 22; 5, 14, 23 6, 15, 24	80 → 0; 80 → 0; 80 → 0 → 80 → 0	4 s; 12 s; 4+7+4 s
Urban	7, 16, 25 8, 17, 26 9, 18,27	50→0→50→0→50→0	5+10+5+10+5; 5+20+5+20+5; 5+30+5+30+5

The brake disc material is gray cast iron EN-GJL-250/G3000.

Table 2: *Main material data used in the FEM model*

Property	Value	Unit
Density	7200	kg/m^3
Young modulus	$1.1x10^5$	MPa
Poisson ratio	0.26	-
Thermal conductivity	52	$W/(m\cdot^0C)$
Specific heat	460	$J/(kg\cdot^0C)$
Adopted thermal reference temperature ~400 °C	~400	^0C

The use of one material model for the three vehicles allows a direct comparison of the influence of braking profile and disc configuration. The differences in the response can therefore be interpreted through the imposed thermal loading, heat dissipation capacity and structural stiffness rather than through changes in material constants.

The FEM workflow combines Transient Thermal and Static Structural analysis in ANSYS Workbench [3]. Heat flux is applied to the friction surface, while convection and radiation are used to represent heat dissipation from the disc surface. The obtained temperature field is then transferred to the structural model to evaluate total elastic deformation and equivalent von Mises stress.

The selected output quantities are engineering indicators. Maximum temperature identifies the risk of thermal overload and brake fade tendency. Heat flux represents the severity of the thermal input. Elastic deformation indicates the geometric response of the disc, while von Mises stress gives a compact measure of combined mechanical and thermal stress.

The braking process was treated as conversion of vehicle kinetic energy into heat at the pad-disc contact region. Equations (1)-(4) follow standard brake-energy balance, heat-partition and transient thermal FEM practice [1].

$$E_k = 0.5 \cdot m \cdot v_0^2 \quad (1)$$

where m is the vehicle mass and v_0 is the initial braking speed.

The heat absorbed by one disc was estimated through an energy-partition approach, in which the vehicle kinetic energy is distributed according to brake-force distribution, disc-side heat partition and contact-side distribution factors [1, 11, 12]:

$$Q_d = \lambda \cdot \alpha \cdot \beta \cdot E_k \quad (2)$$

where λ denotes brake-force distribution, α is the heat-partition factor to the disc, and β accounts for side/contact distribution.

The average thermal power is [1, 2]:

$$P_{avg} = Q_d / t_b \quad (3)$$

and the contact heat flux was calculated as [3, 11]:

$$q = P_{avg} / A_b \quad (4)$$

where tb is braking duration and Ab is the effective contact area.

For severity ranking, the simulation outputs were normalised using min-max normalisation within each vehicle group [13]:

$$X_n = (X - X_{min})/(X_{max} - X_{min}) \quad (5)$$

The following equal-weight SI formulation was considered [14]:

$$SI=(T_n+q_n+u_n+\sigma_n)/4 \quad (6)$$

The index is dimensionless and is used only for relative ranking of the simulated cases. It does not replace material strength verification or experimental validation.

3. Results and discussion

The complete set of 27 simulation cases is summarized in Table 3. The table presents the normalized values of maximum temperature, heat flux, elastic deformation and von Mises stress, together with the calculated severity index. This compact representation allows the thermo-mechanical response of the three brake-disc models to be compared under the same braking profiles. Instead of evaluating each output separately, the normalized results provide a clearer basis for identifying the most demanding operating conditions and for ranking the simulated cases according to their overall severity.

Table 3. *Raw FEM response values and equal-weight severity index*

Case	Veh.	T, °C	q, W/mm²	U, mm	σvM, MPa	SI
1	A180	128.920	1.050	0.159	106.550	0.596
2	A180	115.480	0.422	0.151	75.530	0.324
3	A180	210.840	1.070	0.280	161.740	1.000
4	A180	69.912	0.467	0.070	66.976	0.149
5	A180	64.057	0.191	0.070	55.327	0.038
6	A180	108.400	0.487	0.136	76.390	0.315
7	A180	67.600	0.171	0.070	51.580	0.030
8	A180	64.120	0.158	0.070	50.595	0.019
9	A180	61.370	0.152	0.060	50.036	0.000
10	E220	104.480	0.917	0.160	107.230	0.565
11	E220	82.751	0.300	0.149	88.178	0.226
12	E220	160.490	0.917	0.230	148.920	1.000
13	E220	58.775	0.400	0.130	96.152	0.191
14	E220	49.190	0.136	0.120	83.480	0.017
15	E220	83.600	0.408	0.158	97.520	0.316
16	E220	53.000	0.127	0.120	80.960	0.013
17	E220	51.490	0.127	0.119	80.950	0.007
18	E220	50.140	0.127	0.118	80.944	0.002
19	E350	82.300	0.674	0.160	104.020	0.653
20	E350	66.500	0.266	0.148	91.488	0.287
21	E350	120.300	0.675	0.200	115.450	1.000
22	E350	48.900	0.300	0.148	100.100	0.314
23	E350	42.040	0.119	0.132	88.824	0.071
24	E350	66.200	0.300	0.151	95.374	0.342
25	E350	44.300	0.093	0.126	84.469	0.012
26	E350	43.240	0.093	0.126	84.364	0.008
27	E350	42.300	0.093	0.125	84.300	0.001

The results confirm that repeated high-speed braking is the dominant severity condition for all three vehicles. The maximum values of temperature, heat flux, elastic deformation and von Mises stress occurred in cases 3, 12 and 21, corresponding to the repeated 120-0-120-0 km/h braking cycle. This is consistent with the heat build-up mechanism: the second braking event starts while the disc still stores heat from the first event.

The normalized severity index also confirms that the repeated high-speed cycle is the most severe case within each vehicle group. However, because the normalization was performed within each vehicle group, the SI values should be interpreted as relative rankings inside each vehicle category. Therefore, cross-vehicle comparison should be based on the raw response values reported in the table.

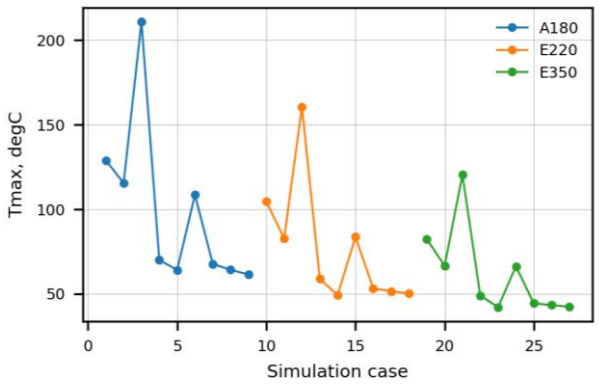


Fig. 2. *Maximum disc temperature over the full set of 27 simulation cases*

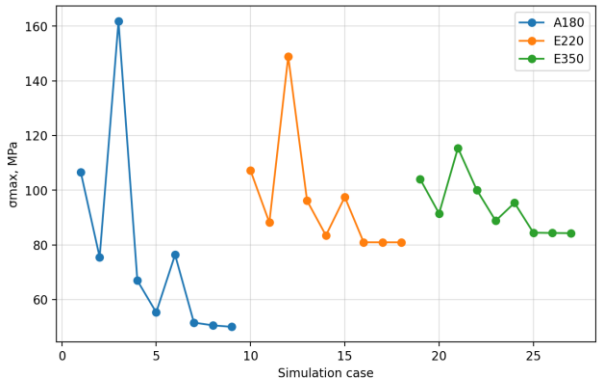


Fig. 3. *Maximum equivalent stress over the full set of 27 simulation cases*

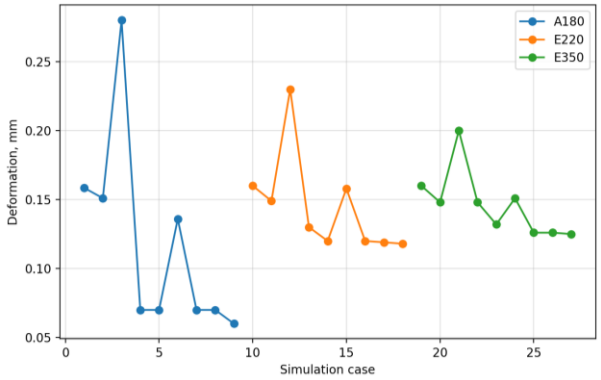


Fig. 4. *Maximum elastic deformation over the full set of 27 simulation cases*

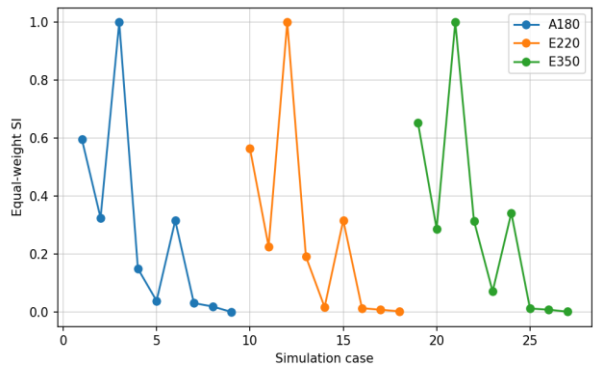


Fig. 5. *Equal-weight four-parameter severity index over the full set of simulation cases*

The high-speed regime shows the strongest contrast between emergency, progressive and repeated braking. For A180, changing from a single 120-0 km/h stop in 4 s to the repeated 120-0-120-0 profile increases the maximum temperature from 128.90 ^{0}C to 210.85 ^{0}C. For E220, the same change increases the maximum temperature from 104.48 ^{0}C to 160.49 ^{0}C, while for E350 it increases from 82.36 ^{0}C to 120.38 ^{0}C. This confirms that repeated braking is more critical than braking time alone.

In the interurban 80 km/h regime, the repeated cases again produce the highest temperature within each vehicle group, but the absolute values are substantially lower than in the 120 km/h regime. The A180 repeated 80 km/h case reaches 108.41 ^{0}C, E220 reaches 83.65 ^{0}C and E350 reaches 66.20 ^{0}C. These results are consistent with the kinetic energy relation, since the energy to be dissipated decreases with the square of speed.

In the urban 50 km/h repeated regime, the influence of recovery interval becomes visible. The cases with longer recovery time have lower maximum temperature, especially for A180. This is a useful design observation because it shows that thermal accumulation during frequent low-speed braking may be controlled by cooling opportunity between stops, even when each individual stop is not severe.

Table 4: *Critical thermo-mechanical response for each vehicle*

Vehicle	Case	Tmax, ^{0}C	q, W/mm^2	u, mm	σvM, MPa
A180	3	210.85	1.070	0.280	161.74
E220	12	160.49	0.917	0.230	148.92
E350	21	120.38	0.675	0.200	115.45

The A180 reached the highest maximum temperature, 210.85 °C, together with the highest von Mises stress, 161.74 MPa, and the largest elastic deformation, 0.280 mm. The corresponding values for E220 were 160.49 °C, 148.92 MPa and 0.230 mm, while the E350 critical repeated high-speed case reached 120.38 °C, 115.45 MPa and 0.200 mm. These values show that the thermal and mechanical severity is not controlled by vehicle class alone. Disc diameter, effective thermal capacity, exposed cooling area and heat-flux distribution strongly influence the final response.

Using 400 °C as an adopted conservative thermal reference for the gray cast iron brake disc, the critical A180 case reaches approximately 52.7% of this reference value, while E220 and E350 reach 40.1% and 30.1%, respectively. This comparison provides an additional absolute thermal-utilization indicator, but it should not be interpreted as a failure-temperature assessment.

The stress results follow the same severity ordering in the repeated high-speed cases: A180 > E220 > E350. The numerical results indicate that the equivalent von Mises stresses remain within the elastic structural range considered in the model. Therefore, the simulated cases do not suggest plastic deformation under the analysed loading conditions. However, thermal cracking and fatigue-related damage were not directly modelled and should be addressed in future experimental or coupled fatigue analyses.

The urban repeated cycles show much lower thermal severity. For A180, the urban temperature maximum varies from 61.37 °C to 67.60 °C; for E220, from 50.14 °C to 53.08 °C; and for E350, from 42.30 °C to 44.30 °C. Increasing the recovery interval from 10 s to 30 s reduces the accumulated temperature, especially in A180, while the changes in stress and deformation are smaller. This indicates that the cooling interval mainly affects the thermal field, whereas the local structural response also depends on geometry and support constraints.

Table 5. *Mean thermo-mechanical response for each vehicle*

Vehicle	Tmax, ^{0}C	q, W/mm^2	u, mm	σvM, MPa
A180	98.97	0.463	0.118	77.19
E220	77.12	0.384	0.145	96.04
E350	61.80	0.290	0.146	94.26

The average temperature response decreases from A180 to E350, whereas the average von Mises stresses for E220 and E350 remain close to each other and are higher than the average A180 stress. This non-proportional relationship between thermal and structural response is important, because it shows that brake-disc performance cannot be assessed from temperature response alone. A meaningful design comparison must consider the coupled thermo-mechanical behavior, including heat input, heat dissipation, elastic deformation and stress distribution.

Because the SI values were calculated using normalized response parameters within each vehicle group, they are used for relative ranking of braking cases inside the same vehicle category. Cross-vehicle comparison should therefore be based on the raw FEM

response values, particularly maximum temperature, heat flux, deformation and von Mises stress.

4. Conclusion

A comparative thermo-mechanical severity assessment of automotive brake discs was developed for Mercedes-Benz A180, E220 and E350 using 27 FEM simulation cases. The analysis leads to the following conclusions.

First, repeated high-speed braking from 120-0-120-0 km/h is the most critical condition for all vehicles. Second, A180 shows the highest absolute peak response among the analysed cases, with T_{max} = 210.84 °C, σ_{vM} = 161.74 MPa and u = 0.280 mm. Third, E220 and E350 show lower peak thermal response in the same repeated braking cycle, which confirms the influence of disc geometry, thermal capacity and cooling surface. Fourth, all simulated peak temperatures remain below the adopted conservative thermal reference temperature, while the stresses remain within the elastic structural range reported by the numerical model. Therefore, no plastic deformation or thermal-structural failure is expected for the scenarios investigated. Finally, the proposed SI scenarios provide a compact way to rank braking duty cycles and show that the ranking is stable under both equal-weight. The added reference framework also shows how the FEM outputs can later be linked to Archard wear modelling and EMEP/EEA emission-factor estimates, without claiming measured wear or PM emissions in the present paper.

5. References

1. Limpert R. Brake Design and Safety. SAE International, Warrendale, 2011.
2. Belhocine A., Bouchetara M. Thermomechanical modelling of dry contacts in automotive disc brake. International Journal of Thermal Sciences. 2012;60:161-170.
3. ANSYS Inc. Ansys Mechanical User's Guide: Transient Thermal and Static Structural Analysis. Canonsburg, PA: ANSYS Inc.; 2024.
4. FE analysis of the brake pad and brake disc wear with thermal-structure interaction. Wear. 2025;582-583:206331. doi:10.1016/j.wear.2025.206331.
5. UNECE. UN Global Technical Regulation No. 24: Laboratory Measurement of Brake Emissions for Light-Duty Vehicles. United Nations Economic Commission for Europe; 2023.
6. EMEP/EEA. Air Pollutant Emission Inventory Guidebook 2023: Road Transport, Tyre and Brake Wear. European Environment Agency; 2023.
7. European Parliament and Council. Regulation (EU) 2024/1257 on Euro 7 emission standards, 2024.
8. Grigoratos T., Mathissen M., Vedula R. T., Giechaskiel B., et al. Interlaboratory study on brake particle emissions - Part I: Particulate matter mass emissions. Atmosphere. 2023;14(3):498.
9. Mathissen M., Grigoratos T., Lahde T., Vogt R., et al. Interlaboratory study on brake particle emissions - Part II: Particle number emissions. Atmosphere. 2023;14(3):424.
10. Storch L., Hamatschek C., Hesse D., Feist F., Bachmann T., Eichler P., Grigoratos T. Comprehensive analysis of current primary measures to mitigate brake wear particle emissions from light-duty vehicles. Atmosphere. 2023; 14(4):712. doi:10.3390/atmos14040712.
11. Meresse D., Harmand S., Siroux M., Watremez M., Dubar L. Experimental disc heat flux identification on a reduced scale braking system using the inverse heat conduction method. Applied Thermal Engineering. 2012;48:202-210.
12. Yevtushenko A., Topczewska K., Zamojski P. The heat partition ratio during braking in a functionally graded friction couple. Materials. 2022;15(13):4623. doi:10.3390/ma15134623.
13. Vafaei N., Ribeiro R. A., Camarinha-Matos L. M. Normalization techniques for multi-criteria decision making: Analytical Hierarchy Process case study. In: Camarinha-Matos L. M., et al., editors. Technological Innovation for Cyber-Physical Systems. IFIP Advances in Information and Communication Technology, vol. 470. Cham: Springer; 2016. p. 261-269. doi:10.1007/978-3-319-31165-4_26.
14. Hwang C. L., Yoon K. Multiple Attribute Decision Making: Methods and Applications - A State-of-the-Art Survey. Lecture Notes in Economics and Mathematical Systems, vol. 186. Berlin: Springer-Verlag; 1981. doi:10.1007/978-3-642-48318-9.

Using AI agents to create work instructions for NDT and VT product inspection in heavy industry.

Marek Grega, Janette Brezinová
Technical University in Kosice, Faculty of Mechanical Engineering, Department of Technology and Materials engineering, Mäsiarska 74, 04001 Košice, Slovakia.
Email: marek.grega@student.tuke.sk, janette.brezinova@tuke.sk

Abstract: *This paper investigates the efficacy of generative artificial intelligence in automating the creation of technical documentation for non-destructive testing (NDT). The research focuses on a comparative performance analysis between a specialized AI agent, built on the Gemini 3.1 Flash platform, and certified human NDT Level 2 experts. A comparative cross-sectional study was conducted using three distinct industrial forging products. Both the AI agent and two human experts were tasked with generating Visual Testing (VT) work instructions based on a 14-point framework derived from the STN EN 13018 and ISO 9712 standards. The outputs were evaluated by a blind-reviewing Level 3 expert using a modified HEAT (Expertise, Accuracy, Trust) rubric, focusing on regulatory compliance, technical precision, and readability. he results demonstrate that the AI agent achieved a 98.4% reduction in generation time, averaging 54.5 seconds per instruction compared to 57.3 minutes for human experts. While the AI agent consistently outperformed humans in text clarity and structural consistency (scoring 5.0 in usability), it exhibited "conservative technical hallucinations," such as prescribing unnecessary magnification tools and incorrect defect-coding standards (ISO 6520-1 instead of CSN 421240). Furthermore, cloud-based API instabilities (HTTP 503 errors) were identified as a critical reliability risk for real-time industrial deployment. The study concludes that while AI agents are highly effective as rapid drafting tools, they cannot currently replace certified personnel due to lack of situational engineering judgment and legal accountability. A "Human-in-the-loop" model remains mandatory, where a certified Level 2 or 3 professional must verify and approve all AI-generated NDT documentation to ensure industrial safety and regulatory compliance...*
KEYWORDS*: NON-DESTRUCTIVE TESTING, VISUAL TESTING, LARGE LANGUAGE MODELS, ARTIFICIAL INTELLIGENCE, WORKING INSTRUCTION, TECHNICAL AUTHORING*

1. Introduction

Non-destructive testing (NDT) represents a cornerstone of quality assurance in the metallurgical and specifical in heavy industries, where structural integrity is paramount for safety-critical components. Among various NDT methods, Visual Testing (VT) is often the primary and most frequent inspection technique. However, the reliability of VT is not solely dependent on the inspector's visual acuity but is fundamentally rooted in the quality and accessibility of the preparatory documentation. According to international standards such as ISO 9712 [1], STN EN 13018 [2] and ISO 11971 [3], a visual inspection cannot be formally executed without a precisely defined work instruction or work procedure.

The technical integrity of a VT inspection is governed by the strictness of its written procedures. Current industry regulations mandate that work instructions must contain a specific minimum set of attributes to ensure reproducibility and accuracy. These include the definition of the object and scope, inspection techniques, surface preparation requirements, and precise acceptance criteria. Furthermore, environmental factors—specifically lighting conditions (type, intensity, and direction) and the technical equipment used—must be documented to mitigate subjective errors.

A critical aspect of the NDT workflow is the verification of these procedures using reference bodies or "gold standard" specimens that mirror the texture, reflectivity, and accessibility of the actual components. Despite these rigorous requirements, the preparation of such documentation remains a labour-intensive task, traditionally performed by Level 2 or Level 3 certified personnel. This creates a bottleneck in high-volume production environments, such as drop forging, where diverse geometries require frequent updates to technical instructions.

The advent of Large Language Models (LLMs) and specialized AI agents has introduced a paradigm shift in technical documentation. Models LLMs such as DeepSeek, Gemini, ChatGPT, Claude have demonstrated a high proficiency in processing complex technical data and adhering to structured regulatory frameworks [4]. Current research in other technical domains suggests that LLMs can generate technical artifacts, such as unit tests or software documentation, that rival or even surpass traditional automated tools in terms of coverage. In manual software testing, LLM-generated verifications have been judged comparable to human-written ones in approximately 40% of cases, although hallucinations remain a significant concern [5]. Despite these advancements, a critical "research gap" exists: there is currently no empirical study directly comparing LLM-generated NDT work instructions with those produced by human experts in a specialized industrial setting.

While LLMs demonstrate high proficiency in general instruction-following benchmarks [6], their reliability in safety-critical and domain-specific contexts—such as NDT—requires rigorous validation. Existing studies emphasize that human oversight is mandatory in these specialized settings to mitigate the risk of technical errors [7]. This study aims to fill this gap by evaluating a specialized AI agent (developed on model Gemini 3.1 Flash) against human experts, focusing on regulatory compliance and technical precision within the heavy industry.

While existing literature has examined AI's role in automated defect recognition (ADR) and software testing, there is a significant lack of empirical evidence regarding the use of LLMs for generating regulatory-compliant NDT work instructions. Specifically, the ability of an AI agent to interpret technical drawings and synthesize them into a procedure that meets the "minimum requirements" of NDT standards has not been formally compared against human expert benchmarks [8].

This study aims to bridge this gap by conducting a comparative analysis between human NDT Level 2 experts and an AI agent (Gemini 3 flash). The research focuses on two primary objectives:

Evaluating the ability of AI to generate VT instructions that satisfy all mandatory regulatory attributes (object scope, technique, surface state, and lighting).

Assessing the technical accuracy and "usability" of these instructions when verified against physical reference bodies in a simulated industrial environment.

By establishing the first performance benchmark for AI-assisted technical authoring in NDT, this paper provides a foundation for modernizing quality management workflows while maintaining the rigorous safety standards required by the industry.

2. Methods and methodologies

The primary objective of this study is to conduct a comparative analysis between human experts and AI agent developed by LLM (Gemini 3 flash) in the generation of technical work instructions for Non-Destructive Testing, specifically visual testing. Given the absence of direct empirical studies in the NDT domain, this

methodology adapts established evaluation frameworks from software engineering to the specific regulatory requirements of industrial inspection.

2.1. Experimental design

This study utilizes a comparative cross-sectional design. Following best practices identified in recent literature for safety settings, we adopted a "Human-in-the-loop" design [9]. This approach integrates AI-generated drafting and writing with expert human validation, which has proven effective in technical environments where absolute accuracy is required [7].

The experiment compared the outputs of two distinct subjects:

- Human experts: Two certified NDT Level 2 professionals who received the assignment as a written set of instructions.
- AI Agent: A specialized model based on the Gemini 3.1 Flash architecture, implemented with a comprehensive "System Instruction" (System Prompt).

2.2. Materials and input data

The baseline for the instruction generation was a technical drawing of a specific steel products (forging and casting). The input data provided to both groups included:

- The technical drawing (Image format).
- General parameters of the production process in internal documents – Working procedure for non-destructive testing – visual testing .
- The mandatory requirements of the ISO 9712 and STN EN 13018 standards.

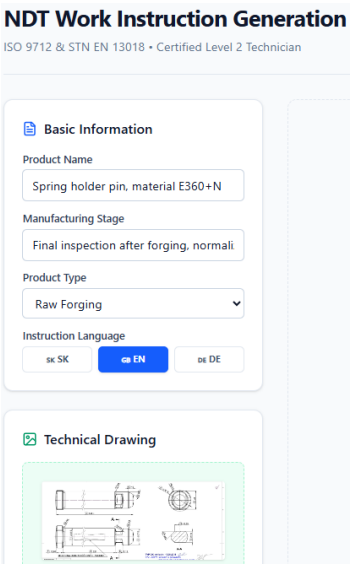


Fig. 1 Picture from AI agent with ***input data***

2.3. Generative protocols and prompt engineering

To ensure objectivity and reproducibility, a unified framework of requirements was defined for both experimental groups. This framework was based on the EN 13018 standard and was adapted to reflect the real-world conditions of industrial production for forgings and castings.

The system instruction defined the AI agent as a certified NDT Level 2 technician and mandated the development of a work instruction containing the following 14 points:

- Controlled object: Description of the object and its geometry based on the provided technical drawing.
- Scope and purpose of inspection: Definition of the exact inspection area (e.g., 100% of the surface, including specific welds if applicable).
- Technique and sequence of steps: A step-by-step chronological procedure for direct visual testing, including a requirement for a sketch to record identified indications in the protocol.
- Surface state and workstation requirements: Description of the required surface condition (e.g., cleanliness, roughness according to drawing data) and environmental requirements for the inspection site.
- Surface preparation: Specification of cleaning methods and the removal of contaminants (scale, sand, or spatter depending on the product type).
- Production stage and inspection timing: Identification of when the inspection occurs within the process (input, in-process after forging/welding, or final).
- Personnel requirements: Definition of qualification levels according to ISO 9712 (Level 1 under supervision, Level 2 for evaluation).
- Acceptance criteria: References to relevant standards, including ISO 5817 (welds), ČSN 42 1240 (castings), and internal regulation PI-H2.4-8 (Surface Defect Catalog for forgings), including definitions for linear (L > 3W) and non-linear indications.
- Lighting conditions: Minimum intensity limits (min. 500 lx for local / min. 160 lx for general inspection) and the use of a lux meter for measurement.
- Used equipment: A list of tools and instruments (measuring devices, lux meter, markers, color spray) with a mandatory reference to their metrological calibration/verification.
- Verification of test sensitivity: Definition of the procedure used to verify the sensitivity of the test before commencement.
- Documentation of results: Method of recording results, defect coding (based on acceptance criteria), and marking of parts (compliant, repairable, scrap).
- Verification and product release: Procedure for sorting parts and separating non-conforming objects.
- Health, Safety, and Environment (HS&E): Mandatory Occupational Health and Safety (BOZP) rules and the specification of Personal Protective Equipment (PPE/OOPP).

This detailed structure allowed for an exact evaluation of the Compliance Index and technical accuracy for both subjects. Providing identical instructions to both the human experts and the AI agent eliminated information asymmetry and established a robust foundation for the subsequent statistical analysis of the results.

This method of using a standardized rubric to guide LLMs has shown moderate-to-strong correlation with expert human ratings in other technical fields [10].

2.4. Evaluation framework (Metrics)

To ensure scientific rigor, we adapted the HEAT (Human experience, Expertise, Accuracy, Trust) and QUEST frameworks [11]. The instructions were evaluated across four quantitative and qualitative dimensions using a 5-point Likert scale:

- Regulatory compliance (RC): Adherence to EN 13018 mandatory elements (e.g., equipment calibration, lighting requirements, surface preparation) [5].
- Technical Accuracy (TA): Measured against a "Gold Standard" provided by a Level 3 expert [12].
- Clarity and usability (CU): The degree to which a Level 1 technician can execute the task without further clarification (Readability).
- Safety and risk mitigation (SR): Inclusion of necessary health and safety protocols specific to the testing environment.

The Compliance Index (CI) was calculated as:

$$CI = \left(\frac{\sum Achieved\ Mandatory\ Elements}{\sum Total\ Mandatory\ Elements} \right) \times 100\%$$

2.5. Validation and "Gold standard"

To mitigate bias, a "blind review" process was implemented. A certified NDT Level 3 expert, acting as the "Gold Standard" evaluator, reviewed all generated instructions without knowing their origin (AI vs. Human). This expert utilized a standardized rubric and an Error Taxonomy to classify potential failures into three categories:

- Omissions (missing steps),
- Hallucinations (technical requirements not found in the drawing/norm),
- Incorrect formatting.

3. Result

The experimental phase focused on a direct performance comparison between human NDT Level 2 experts and the Gemini 3.1 Flash AI agent across three distinct forging products. The results were categorized into quantitative efficiency, regulatory compliance, and qualitative technical evaluation.

3.1. Comparative efficiency and generation time

A significant divergence was observed in the temporal efficiency of instruction generation. The human experts required an average of 57.3 minutes to complete a single VT instruction. In contrast, the AI agent generated instructions in an average of 54.5 seconds (excluding the system latency during the third trial).

The AI agent demonstrated a 98.4% reduction in processing time, highlighting its potential as a tool for rapid documentation drafting in high-volume industrial environments.



Fig. 2*: Generated sketch and part of text from AI agent*

3.2. Regulatory compliance and technical quality

Table 1 summarizes the performance metrics across the three evaluated products (forgings and casting).

Metric	Human expert 1	Human expert 2	AI Agent
Avg. Time (min:sec)	60:00	53:40	00:54
STN EN 13018 Compliance (%)	87.5%	100%	87.5%
Technical Accuracy (1-5)	3.3	4.0	3.7*
Clarity and Usability (1-5)	3.3	3.7	4.0*

*Scores significantly impacted by the failure in Trial 3.

The AI agent maintained a consistent compliance rate of 87.5% in the first two trials, matching one of the human experts but failing to reach the 100% threshold due to specific omissions in lighting parameters (e.g., specifying general vs. local illumination). Notably, the AI-generated text received the highest scores for Clarity and Usability (5.0) in successful trials, suggesting superior formatting and readability compared to human-written drafts.

3.3. Error taxonomy and hallucination Analysis

Despite high readability, the AI agent exhibited a consistent pattern of "technical hallucinations." In all successful trials, the model introduced requirements not present in the source documentation or necessary for standard VT of forgings:

- Methodological hallucinations: Mandatory use of magnifying lenses (zoom 2x to 7x) and mirrors for radii, which were not required for the specific geometries.
- Process errors: Inclusion of chemical cleaning stages and final surface treatments (galvanization, lacquering) not requested in the work order.
- Standardization mismatches: Incorrectly citing ISO 6520-1 [13] for defect coding instead of the industry-specific ČSN 42 1240 [14] (castings), or internal regulation PI-H2.4-8 (forgings).

3.4. System reliability and model failure

A critical finding of this study relates to the reliability of cloud-based LLMs in a production workflow. During the evaluation of the third product, the Gemini 3.1 Flash model reported a Server Error 503.

Following the restoration of the service, the subsequent output exhibited a marked degradation in quality:

1. Contextual Inaccuracy: The model incorrectly identified the component's function without sufficient data.
2. Technological Mismatch: It prescribed inspection protocols for weldments (welding seams) on a seamless forging.
3. Parameter Failure: It assigned an incorrect surface roughness value (Ra 12.5), which contradicted the technical drawing requirements.

This failure underscores a significant risk in the autonomous use of AI for NDT documentation, where environmental or server-side instabilities can lead to "silent failures" and the generation of technically dangerous instructions.

4. Conclusions

This study provides the first empirical comparison between the capabilities of generative artificial intelligence and certified human experts in the creation of technical documentation for non-destructive testing (NDT). While the results demonstrate extraordinary potential for AI in terms of temporal efficiency and

text structuring, they simultaneously reveal critical risks that currently preclude the full automation of this process.

4.1. Analysis of technical limitations and hallucinations

The findings indicate that the Gemini 3.1 Flash model achieves high structural consistency but is prone to "technical hallucinations." This aligns with recent observations in other technical domains where LLMs generate artifacts that rival traditional automated tools in coverage but require expert review for semantic correctness [8]. The inclusion of redundant requirements—such as the mandatory use of magnifying glass (e.g., 2x to 7x zoom) and substitute general standards for industry-specific ones (e.g., ISO 6520-1 instead of CSN 421240) mirrors the "hallucination concerns" noted in software testing documentation research [5]. These errors confirm that AI agent developed by LLM, while instruction-tuned, may struggle with the deep logic required for specialized engineering tasks [5].

4.2. System reliability and risks of cloud-based solutions

The encountered server-side instabilities (HTTP 503 and 429 errors) during Trial 3 highlight a critical bottleneck for real-time industrial deployment. These "silent failures" and the subsequent degradation of output quality—such as prescribing welding protocols for seamless forgings—demonstrate the necessity of structured error counting and safety framing [5,9]. As suggested by current literature, the lack of situational awareness in LLMs remains a primary barrier to their autonomous use in safety-sensitive settings [5,7].

4.3. Regulatory framework and certification requirements

A critical conclusion of this research is the confirmation that, at present, it is neither legally nor normatively permissible to automatically generate and directly apply NDT instructions created solely by AI. According to current ISO 9712 and EN 13018 standards every work instruction for VT must be:

1. Drafted by a certified NDT professional (at least Level 2).
2. Verified and approved with a signature by a responsible person with the appropriate certification.

Our results support the adoption of a "Human-in-the-loop" (HITL) framework, which has been validated in other sectors to combine AI's scalability with human expert judgment [11]. In this model, the AI agent serves as an advanced drafting assistant, while the certified Level 2 or Level 3 technician remains the final authority for verification and product release - in this research, work instruction. This approach ensures that the "Human experience, Expertise, Accuracy, and Trust" (HEAT) principles are maintained throughout the quality assurance workflow [11].

4.4. Practical recommendations

Despite the identified shortcomings, AI agents can be classified as highly effective drafting and writing tools. Their primary benefits include:

1. Enhanced clarity: The AI consistently achieved higher scores (5.0) in text clarity compared to human experts.
2. Format standardization: Elimination of subjective stylistic differences between various inspectors.
3. Time savings: Reducing preparation time from hours to seconds allows certified experts to focus on technical validation rather than administrative text generation.

In conclusion, the implementation of AI into NDT processes within the heavy industry is currently feasible only under a "Human-in-the-loop" model. In this framework, artificial intelligence serves as an assistant, while the certified human expert remains the final guarantor and author of the instruction. Future research should focus on the fine-tuning of models on specific sets of technical standards to eliminate the identified technical hallucinations.

4.5. Technical resilience and infrastructure stability

The deployment of the AI agent highlighted a significant technical barrier regarding cloud-based infrastructure. During the evaluation of Trial 3, the system encountered HTTP 503 (Service Unavailable) and 429 (Quota Exhausted) errors. These failures are critical from a research perspective, as they define the "Reliability Gap" between laboratory testing and real-time industrial application. To mitigate these risks, the study implemented an Exponential backoff strategy—an automated retry mechanism with increasing delays. This approach proved essential for maintaining workflow continuity. Furthermore, the transition from experimental versions to a stable model alias (Gemini 2.0 Flash) significantly reduced latency and improved consistency, suggesting that for NDT applications, model stability must be prioritized over experimental features.

4.6. Strategic outlook for industrial implementation

The technical challenges encountered during this research lead to a vital strategic conclusion: the current state of public API-based LLMs is not yet ready for "zero-latency" mission-critical tasks in NDT without robust fallback systems. For an AI agent to be truly integrated into a workspace, where any delay in generating instructions can halt the manufacturing process, several conditions must be met:

1. **Guaranteed SLA (Service level agreement):** Shifting from free tiers to paid, enterprise-grade cloud services to eliminate 429 quota errors.
2. **Edge computing or local LLMs:** Future research should explore the deployment of quantized models on local servers to remove dependency on external API availability and internet stability.
3. **Real-time error synchronization:** The user interface must provide immediate, transparent feedback regarding model status, allowing the certified Level 2 technician to respond appropriately (e.g., manual drafting during outages).

By addressing these technical hurdles, the transition of AI from an experimental assistant to a reliable industrial tool becomes feasible, provided that human-led oversight remains the final authority in the NDT workflow.

Acknowledgments: This research is the result of a project supported by project Visegrad Fund fellowship No. 62610056 - Scientific Cooperation in Advanced Surface Engineering: Joint Research on PTA and Laser Cladding for Die-Casting Mold Renovation, Slovak Research and Development Agency VEGA Scientific Grant Agency "Possibilities of applying laser additive technologies in the restoration of functional surfaces" (1/0597/23),

Cultural and Educational Grant Agency KEGA "Hybrid education of students for the current needs of the automotive industry" (024TUKE-4/2025), "Innovative approaches to the restoration of functional surfaces by laser surface treatment" (APVV-20-0303) and "Integrity of protective multilayers under high-temperature exposure conditions" (APVV-24-0381).

5. References

1. EN ISO 9712:2022. Non-destructive testing — Qualification and certification of NDT personnel. International Organization for Standardization. (2022).
2. STN EN 13018. *Non-destructive testing. Visual inspection. General principles.* Bratislava: Office for Standardization, Metrology and Testing SR, (2016).
3. *ISO 11971:2020. Steel and iron castings – Visual testing of surface quality.* 3rd ed. Geneva: INTERNATIONAL ORGANIZATION FOR STANDARDIZATION, (2020)
4. Wang, R., Guo, J., Gao, C., Fan, G., Chong, C., & Xia, X. ,Can LLMs Replace Human Evaluators? An Empirical Study of LLM-as-a-Judge in Software Engineering. *Proceedings of the ACM on Software Engineering*, *2*, 1955 - 1977. (2025). https://doi.org/10.1145/3728963.
5. Asgari, E., Brown, N., Dubois, M., Khalil, S., Balloch, J., Yeung, J., & Pimenta, D. *A framework to assess clinical safety and hallucination rates of LLMs for medical text summarisation.* NPJ Digital Medicine, 8. (2025). https://doi.org/10.1038/s41746-025-01670-7.
6. Cengiz, A., Sever, A., Umutlu, E., Erdem, N., Aytan, B., Tufan, B., Topraksoy, A., Darici, E., & Toraman, C. *Evaluating the Quality of Benchmark Datasets for Low-Resource Languages: A Case Study on Turkish*. ArXiv, abs/2504.09714. (2025). https://doi.org/10.48550/arxiv.2504.09714.
7. Hu, X., Chen, Q., Wang, H., Xia, X., Lo, D., & Zimmermann, T. *Correlating Automated and Human Evaluation of Code Documentation Generation Quality*. ACM Transactions on Software Engineering and Methodology (TOSEM), 31, 1 - 28. (2022). https://doi.org/10.1145/3502853.
8. Gregori-Giralt, E., & Menéndez-Varela, J. *The content aspect of validity in a rubric-based assessment system for course syllabuses.* Studies in Educational Evaluation, 68, 100971. (2021). https://doi.org/10.1016/j.stueduc.2020.100971.
9. Kroll, M., & Kraus, K. *Optimizing the role of human evaluation in LLM-based spoken document summarization systems*. ArXiv, abs/2410.18218. (2024).https://doi.org/10.21437/interspeech.2024-2268.
10. Teterevenkov, D. *EXPERT-ORIENTED METHODS FOR EVALUATING THE QUALITY OF TEXTUAL GENERATION OF LARGE LANGUAGE MODELS*. SOFT MEASUREMENTS AND COMPUTING. (2025). https://doi.org/10.36871/2618-9976.2025.05.003.
11. Verhulsdonck, G., Weible, J., Stambler, D., Howard, T., & Tham, J. *Incorporating Human Judgment in AI-Assisted Content Development: The HEAT Heuristic.* Technical Communication.. (2024). https://doi.org/10.55177/tc286621.
12. Tam, T.Y.C., Sivarajkumar, S., Kapoor, S. *et al. A framework for human evaluation of large language models in healthcare derived from literature review*. npj Digit. Med. **7**, 258 (2024). https://doi.org/10.1038/s41746-024-01258-7
13. ISO 6520-1:2007. *Welding and allied processes — Classification of geometric imperfections in metallic materials — Part 1: Fusion welding*. Geneva: International Organization for Standardization (2007)
14. ČSN 42 1240, *Casting defects. Nomenclature and classification of defects.* Prague: Office for Standardization and Measurement. (1965)

Mesh-Converged Modal Profile Assessment of Functionally Graded Spur Gears

Shkelzen Shabani[1,*], Halil Demolli[1]
University of Prishtina, Faculty of Mechanical Engineering, Prishtina, Kosovo[1]
shkelzen.shabani@uni-pr.edu

Abstract: *This study presents a mesh-converged finite element assessment of functionally graded spur gears. Two gear models are studied: a fully graded gear and a half-metal/half-graded gear. The material properties vary gradually from aluminum alloy to zirconia according to power-law distribution. The modal analysis is carried out in ANSYS using SOLID187 elements and the Block Lanczos method. A mesh-convergence study is performed, and a 0.25 mm mesh is adopted for the results. The study compares the natural frequencies and normalized mode-shape profiles of the two models. The results show how the material layout influences the vibration behavior of the gear.*
Keywords*: FUNCTIONALLY GRADED GEAR, FINITE ELEMENT ANALYSIS, MODAL ANALYSIS, NATURAL FREQUENCIES, MODE-SHAPE PROFILE, MESH CONVERGENCE*

1. Introduction

Gears are important parts of many mechanical transmission systems, and their vibration behavior has a direct effect on noise, reliability, and service life [1]. For lightweight applications, the choice of material is especially important, because reducing weight should not cause an unfavorable change in stiffness or natural frequencies.

Functionally graded materials offer a useful way to improve this balance. In these materials, the properties change gradually from one material to another, instead of changing suddenly at a sharp interface. For gears, this means that a lighter metallic region can be combined with a stiffer ceramic-rich region near the tooth surface.

Previous studies have shown that material gradation can affect the mechanical and dynamic response of rotating components and gears. Functionally graded discs have been investigated for stress, vibration, critical speed, and elastic behavior using analytical, numerical, and finite element approaches [2] [3] [4] [5] [6] [7]

More recently, finite element models have also been used to study stress, stiffness, weight reduction, and natural frequencies of intact and cracked functionally graded gears [8] [9] [10]. However, modal results are usually presented mainly through frequency values and general mode-shape contours.

In this article, functionally graded spur gears are studied using a mesh-converged finite element model. Two material layouts are compared: a fully graded gear and a half-metal/half-graded gear. The comparison is based on natural frequencies and normalized mode-shape profiles along a selected gear-tooth path. This gives a simple way to compare both the overall vibration response and the local bending-sensitive regions of the two gear models.

2. Materials and methods

2.1. Gear geometry and material gradation law

Two spur-gear models are considered in this work. The first model is a fully functionally graded gear, where the gear body is divided into 30 layers of equal thickness. The second model is a half-metal/half-graded gear, where the inner part is metallic and the outer part is divided into 15 graded layers (see Figure 1). In both models, the gradation follows the tooth profile and the material changes from aluminum alloy in the inner region to zirconia near the outer surface.

The material property P(r) is assigned according to the power-law relation:

$$P(r) = P_i + (P_0 - P_i)V_0(r) \quad (1)$$

$$V_0(r) = \left(\frac{r-R_i}{R_0-R_i}\right)^k, R_i \le r \le R_0, 0 \le k \le \infty \quad (2)$$

Here, P represents the material property, V_0 is the ceramic volume fraction, r is the radial coordinate, and R_i and R_o are the inner and outer radii of the graded region. The subscripts i and o refer to the metallic and ceramic phases, respectively. The parameter k is the gradation index.

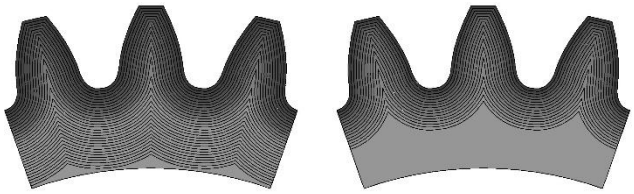


Fig. 1 *Spur gear models: (a) fully graded gear; (b) half-metal/half-graded gear.*

Table 1: *Gear parameters.*

Parameter	Value
Number of teeth	28
Module	3.1750
Pressure angle	20^o
Face width	5 mm

Table 2: *Material properties [11].*

Material	Elastic Modulus (GPa)	Density (kg/m3)	Poisson's ratio
Aluminum alloy	70	2700	0.3
Zirconia	200	5700	0.3

2.2. Finite element model and modal formulation

The gear geometry is prepared in KISSsoft using the selected gear parameters (see Table 1) and material properties (see Table 2). The model is then imported in Autodesk Inventor, creating multi-layer model. After that the model is imported in ANSYS for modal analysis. The three-dimensional finite element model is meshed using SOLID187 ten-node tetrahedral elements. The natural frequencies and mode shapes are extracted using the Block Lanczos eigen solver. The boundary conditions are used in that way to match the cantilever boundary conditions.

For the intact gear, the free-vibration eigenvalue problem is written as [10]:

$$[K - \omega^2 M]\Phi = 0 \quad (3)$$

where $[K]$ and $[M]$ are the global stiffness and mass matrices, ω is the natural angular frequency, and Φ is the corresponding mode-shape vector.

2.3. Mesh Convergence

A mesh-convergence study is carried out before comparing the two gear models. The percentage change between two consecutive mesh sizes is evaluated as :

$$\left|\frac{\Delta\omega}{\omega}\right|(\%) = \left|\frac{\omega_i - \omega_{i-1}}{\omega_i}\right| \times 100 \quad (4)$$

where:

ω_i - is the natural frequency on the finer mesh and ω_{i-1} is the natural frequency on the coarser mesh.

The mesh is refined until the first three natural frequencies show only negligible changes (see table 3). Based on this check, an element size of 0.25 mm is adopted for the final modal analysis.

Table 3: *Mesh-convergence results for the fully graded gear model.*

Elem, edge (mm)	ω_1 (kHz)	$\lvert\Delta\omega_1/\omega_1\rvert$ (%)	ω_2 (kHz)	$\lvert\Delta\omega_2/\omega_2\rvert$ (%)	ω_3 (kHz)	$\lvert\Delta\omega_3/\omega_3\rvert$ (%)
0.50	311.58	-	437.36	-	472.05	-
0.45	311.59	3.0 × 10-5	437.36	0	472.06	2.0 × 10-5
0.40	311.65	1.9 × 10-4	437.42	1.4 × 10-4	472.16	2.1 × 10-4
0.35	311.70	1.6 × 10-4	437.44	5 × 10-5	472.20	9 × 10-5
0.30	311.74	1.3 × 10-4	437.47	7 × 10-5	472.24	9 × 10-5
0.25	311.80	1.9 × 10-4	437.52	1.1 × 10-4	472.32	1.7 × 10-4
0.20	311.93	4.2 × 10-4	437.61	2.1 × 10-4	472.42	2.1 × 10-4
Max ($\lvert\Delta\omega/\omega\rvert$)		4.2 × 10-4				

3. Solution of the problem examined

The examined problem is solved by applying the mesh-converged finite element model to two gear configurations. The first configuration is a fully graded gear, while the second is a half-metal/half-graded gear. To reduce computational time, a three-tooth gear sector is used instead of the complete gear. The same sector geometry, boundary conditions, mesh size, element type, and modal extraction method are applied to both configurations, so that the effect of the material layout can be compared directly.

The natural frequencies and mode shapes are extracted using the Block Lanczos method. The results are then compared through the first three natural frequencies, the corresponding mode-shape contours and normalized mode-shape profiles. This procedure allows the global vibration response and the local bending-sensitive behavior of the two healthy gear models to be evaluated.

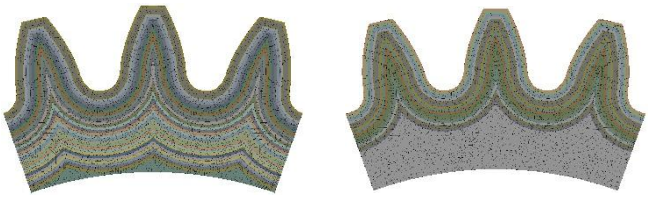


Fig. 2 *Finite element model of healthy gear: (a) fully graded gear; (b) half-metal/half-graded gear.*

4. Results and discussions

The modal results of the two healthy gear configurations are presented and compared in this section. The discussion is organized according to three aspects: natural frequencies and normalized mode-shape profiles. The aim is to show how the material layout affects both the global vibration response and the local bending-type behaviour of the gear tooth.

4.1. Natural frequencies

Figures 3–5 show the change of the first three natural frequencies with the power index *k* for the fully graded and half-metal/half-graded gear models. The value of *k*changes the amount of ceramic and metal in the graded part of the gear. For small values of *k*, the gear has more ceramic contribution near the outer region, so the stiffness is higher. When *k* increases, the gear becomes more metal-rich. Since aluminum alloy is less stiff than zirconia, the stiffness of the gear decreases. At the same time, the mass also decreases because aluminum has lower density than zirconia.

For the fully graded gear, the first natural frequency decreases from $k = 0.1$ to $k = 5$. In this range, the loss of stiffness has the main effect. For larger values of *k*, the first frequency increases slightly, because the reduction in mass starts to compensate for part of the stiffness loss. This effect is more visible in the first mode, which represents a more global vibration of the gear.

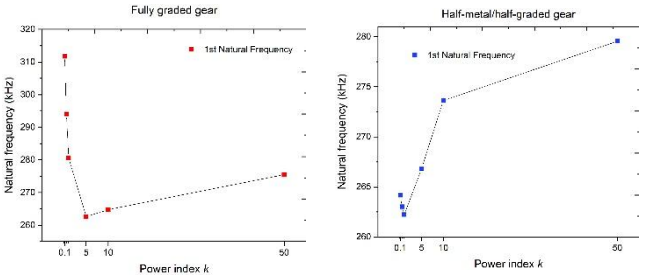


Fig. 3 *The effects of various power index (k) in the first natural frequency: a) Full graded gear; b) Half graded, half metal gear.*

The second and third natural frequencies of the fully graded gear decrease more strongly with increasing *k*. These modes have more complex deformation patterns and are more sensitive to stiffness changes. After $k = 10$, the curves become nearly stable, indicating that further changes in material distribution have a smaller influence.

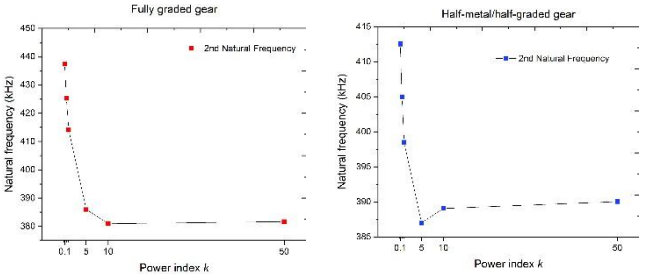


Fig. 4 *The effects of various power index (k) in the second natural frequency: a) Full graded gear; b) Half graded, half metal gear.*

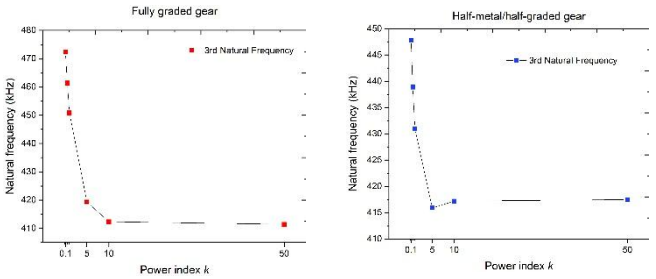


Fig. 5 *The effects of various power index (k) in the third natural frequency: a) Full graded gear; b) Half graded, half metal gear.*

For the half-metal/half-graded gear, the frequencies are generally lower than those of the fully graded model because a larger part of the structure is made of aluminum alloy, which reduces the overall stiffness. In the first mode, the frequency increases with *k*, as the mass reduction becomes more influential. For the second and third modes, the frequencies first decrease and then remain almost constant. Overall, the fully graded gear gives higher natural frequencies, while the half-metal/half-graded model shows a lower but more stable modal response at higher *k*.

4.2. Normalized mode-shape profiles

The directional deformation mode shapes of the fully graded and half-metal/half-graded gears are shown below (see Figure 6).

The deformation values were extracted along the central tooth path, from the root region to the tooth tip, using the same path for both gear models.

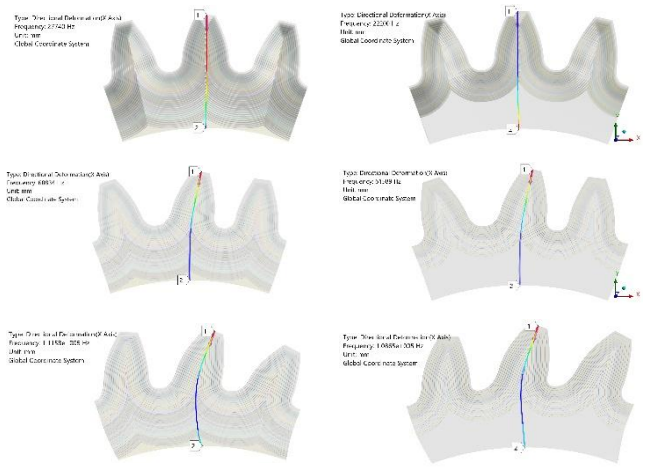


Fig. 6 *Mode shapes contours along the x axis: (a) fully graded gear; (b) half-metal/half-graded gear.*

As shown in Figure 7, the first mode has a smooth profile without a sign change, indicating a mainly global bending response. The second mode also follows a continuous trend, but with stronger curvature, showing greater sensitivity to the stiffness distribution along the tooth. In the third mode, the profile changes sign, meaning that different tooth regions deform in opposite directions. This indicates a more complex local bending behavior.

These results show that the two material layouts differ not only in natural frequencies, but also in deformation distribution. The fully graded gear shows a more pronounced higher-order bending response, especially in the third mode, while the half-metal/half-graded gear gives smoother normalized profiles. Therefore, Figures 6 and 7 confirm that material gradation affects both global modal behavior and the local tooth bending response.

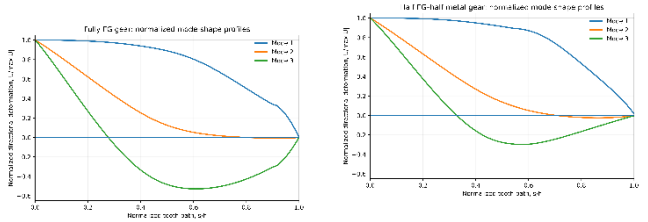


Fig. 7 *Normalized mode shapes along the x axis: (a) fully graded gear; (b) half-metal/half-graded gear.*

5. Conclusions

This study presented a mesh-converged finite element modal analysis of fully graded and half-metal/half-graded spur gears.

• The results show that the material layout plays an important role in the vibration behavior of the gear.

• The fully graded gear generally gives higher natural frequencies because it contains a larger ceramic-rich region, which increases the overall stiffness.

• The half-metal/half-graded gear gives lower natural frequencies, but its normalized mode-shape profiles are smoother and more stable.

• The normalized profiles show that material gradation affects not only the frequency values, but also how the tooth deforms along with its profile.

6. References

1. S. P. Radzevich, *Dudley's Handbook of Practical Gear Design and Manufacture* (2021).

2. M. Bayat, M. Saleem, B. B. Sahari, A. M. S. Hamouda, and E. Mahdi, Mech. Res. Commun. **35**, (2008).

3. E. Bagheri and M. Jahangiri, Int. J. Appl. Mech. **11**, 1950020 (2019).

4. J. N. Sharma, D. Sharma, and S. Kumar, International Journal for Computational Methods in Engineering Science and Mechanics **14**, (2013).

5. Ö. C. Farukoğlu, I. Korkut, and A. Motameni, ZAMM Zeitschrift Fur Angewandte Mathematik Und Mechanik **103**, (2023).

6. R. Madan, P. Khobragade, and S. Bhowmick, Multidiscipline Modeling in Materials and Structures **20**, 1192 (2024).

7. H. Callioglu, S. Muftu, and C. N. Koplay, Multidiscipline Modeling in Materials and Structures **21**, 98 (2024).

8. B. Singh, R. S. Mulik, and S. P. Harsha, Mechanics Based Design of Structures and Machines **51**, (2023).

9. B. Singh, R. S. Mulik, and S. P. Harsha, Proceedings of the Institution of Mechanical Engineers, Part L: Journal of Materials: Design and Applications **237**, (2023).

10. S. Shabani, F. Idrizi, R. Morina, E. F. Erdurcan, and H. Demolli, Proceedings of the Institution of Mechanical Engineers, Part D: Journal of Automobile Engineering **0**, 09544070251410619 (2026).

A new paradigm for analyzing the work of transport operators based on sEMG and MyoMotion studies

Iwona Grabarek[1], Sylwia Bęczkowska[2*], Katarzyna Grzybowska[3], Zuzanna Zysk[4]
Warsaw University of Technology, Faculty of Transport, Poland[1,2,3,4]
sylwia.beczkowska@pw.edu.pl

Abstract: *The article presents a new paradigm for analyzing the work of transport system operators, based on the use of surface electromyography (sEMG) and the MyoMotion motion analysis system. The proposed approach is illustrated through the example of a paramedic performing a selected medical procedure in a medical ambulance. The conducted study enabled the identification of working postures adopted during the execution of the selected medical procedure under real working conditions. The analysis included simultaneous measurement of muscle activity and recording of movement kinematics, allowing for a comprehensive assessment of biomechanical loads. The obtained results indicate the high utility of the proposed approach in identifying risk factors associated with musculoskeletal overload and provide a basis for developing more effective ergonomic interventions in the working environment of transport operators.*
Keywords*: sEMG, MYOMOTION, ERGONOMICS, WORK OF TRANSPORT OPERATORS, MEDICAL AMBULANCE*

1. Introduction

Contemporary transport systems impose increasingly demanding requirements on operators in terms of efficiency, safety, and long-term ability to perform tasks under changing environmental conditions [13], [9]. This results, among other factors, from progressive automation, increasing traffic intensity, and growing pressure to optimize logistics processes [5]. The nature of the work performed by drivers, machine operators, and logistics personnel is associated not only with cognitive workload, involving the continuous need for decision-making and environmental monitoring, but also with significant physical strain, often of a static and repetitive nature [9].

Long-term exposure to this type of biomechanical load significantly increases the risk of developing musculoskeletal disorders. According to the latest results of the 2021 Global Burden of Disease (GBD) study, musculoskeletal disorders affect approximately 1.69 billion people worldwide [12]. They constitute one of the leading causes of functional impairment and occupational absenteeism, generating substantial health-related, social, and economic consequences. Prolonged maintenance of forced body postures, performance of monotonous tasks, and limited opportunities for recovery may lead to increasing fatigue, reduced concentration, and a higher risk of operational errors [1], [14]. Consequently, these factors negatively affect both work efficiency and the level of safety in transport systems. In the transport sector in particular, reduced physical fitness of employees may contribute to an increased risk of occupational accidents, deterioration of passenger and cargo transport safety, and additional costs associated with medical treatment and rehabilitation processes. For this reason, issues related to ergonomics and workload management are becoming increasingly important in the design and improvement of modern transport systems [13].

Consequently, the importance of precise methods for assessing musculoskeletal workload and identifying risk factors leading to overload and injury is increasing. Existing approaches to the analysis of transport operators' work have been based primarily on ergonomic observation methods (e.g., RULA, REBA) and subjective assessments of perceived fatigue [4], [6], [10]. Although these methods are widely applied in practice, they rely largely on expert evaluation and workers' self-reports, which may limit their objectivity and accuracy in the analysis of real working conditions [15]. As a result, the obtained outcomes may not fully reflect the actual level of worker workload, thereby limiting their predictive value.

The development of modern measurement technologies creates new opportunities for objective and multidimensional analysis of human work. The application of advanced measurement technologies enables a more precise determination of biomechanical loads. In this context, particular importance is attributed to techniques such as surface electromyography (sEMG), which enables the recording of muscle bioelectrical activity, and MyoMotion analysis systems, which allow precise tracking of body segment movements. The integration of these two approaches provides the foundation for the development of a new research paradigm that combines physiological and biomechanical data for a comprehensive assessment of transport operators' work. Presenting such an approach constitutes the objective of this article.

The results of the study will be illustrated using the example of a paramedic working in a medical ambulance. The application of the aforementioned techniques enabled the identification of working postures adopted during the performance of medical procedures under real-life conditions and allowed for a detailed assessment of both muscle tension and ranges of motion during the execution of professional tasks. It should be emphasized that the measurement methods applied in this study have not previously been used in the analysis of workload in the paramedic profession.

2. Methodology for Identifying Working Postures During Medical Procedures

The identification of working postures adopted by the paramedic during work was carried out using two methods applied in ergonomics, namely the measurement of muscle tension by means of surface electromyography and the measurement of the paramedic's body movement kinematics using the MyoMotion method. The measurements were conducted in a Mercedes ambulance, which is widely used in the emergency medical services system. Two experienced paramedics participated in the study. Their task was to perform 17 medical procedures both while the ambulance was stationary and while it was in motion. The duration of individual procedures ranged from 2 to 5 minutes.

The medical procedures were performed on a medical simulator acting as a patient, ensuring full compliance with procedures carried out under real-life conditions. In this article, the analysis was limited to a detailed examination of one medical procedure, namely the monitoring of basic vital functions (ECG).

Figure 1 presents the research workstation, including the interior of the medical ambulance with complete equipment and a patient simulator placed on a stretcher.

2.1. Measurements of selected muscle tension using surface electromyography (sEMG) during selected medical procedures

The surface electromyography method was used to record the electrical activity of muscles [2], enabling, among other things, the assessment of musculoskeletal workload and fatigue. Electrical phenomena occurring in muscles, associated for example with changes in muscle tension, can be recorded using a specialized measurement system. The electromyographic signal reflects the

electrical activity of a muscle accompanying its contraction and force generation [11].

The tests were conducted according to the following procedure:

• preparation of the participant for the tests (before placing the sensors, the skin of the tested person was properly cleaned),

• attachment of electrodes to measure electrical muscle activity (EMG),

• measurement of the maximum muscle force for the tested muscles in order to determine the value of maximum muscle tension (MVC – Maximum Voluntary Contraction),

• measurements for individual medical procedures,

• removal of electrodes and completion of the test.



Fig. 1. *Test workstation – the interior of an ambulance equipped with complete medical equipment and a medical simulator placed on a stretcher [authors' own source]*

2.2. Recording of movement kinematics during the performance of a selected medical procedure (MyoMotion)

A forced and improper posture adopted by the paramedic during the performance of medical procedures results not only in high muscle tension but is also characterized by constrained body positioning within the workspace. The degree of postural constraint can be determined by measuring the ranges of motion in selected joints active during the execution of medical procedures. As part of the study, a non-invasive method using the MyoMotion system was employed to investigate movement kinematics.

The study utilized the MyoMotion system developed by Noraxon. This system combines wireless data transmission technology with inertial sensors for the assessment of any movement in 3D space. The set includes inertial sensors (each integrating an accelerometer, gyroscope, and geomagnetic field sensor), accessories for sensor attachment, and software enabling both data acquisition and comprehensive analysis [7].

The experimental study included fifteen anatomical angles of body elements (joints). The analysis considered the angles on both sides of the body, including the left and right sides. The investigated angles are presented in Table 1.

The determination of anatomical angles was performed in accordance with the principles of the medical neutral/zero method. It is assumed that, in a person standing upright, all joints are in the zero position, even if there is a deviation from the geometric zero angle. For example, the geometric angle in the ankle joint is 90°, whereas the anatomical angle is 0°.

Each sensor contains labels for the X, Y, and Z axes. All sensors were positioned on body segments in such a way that, in the standing position, the X-axis vector indicated on the sensor label was oriented vertically along the direction of the gravitational force axis. The inertial sensors were placed symmetrically on the right and left sides of the examined paramedic's body in order to record accelerations in accordance with the MyoMotion protocol described in the user manual [3].

Table 1. *List of Investigated Anatomical Angles of Body Elements*

No.	Name
1	Cervical Flexion
2	Cervical Lateral
3	Cervical Axial
4	Lumbar Flexion
5	Lumbar Lateral
6	Lumbar Axial
7	Thoracic Flexion
8	Thoracic Lateral
9	Thoracic Axial
10	Hip Flexion LT
11	Hip Flexion RT
12	Hip Abduction LT
13	Hip Abduction RT
14	Hip Rotation - out LT
15	Hip Rotation - out RT

By placing individual MyoMotion sensors on two adjacent body segments, it was possible to assess the joint range of motion (ROM) located between these segments. This principle can be easily extended from the measurement of a single joint movement to the simultaneous measurement of whole-body motion across all investigated joints. The sampling frequency of the inertial sensors was set to 200 Hz. Although the individual sensors possess identical functionality, they are distinguished within the system by unique serial numbers. The MyoMotion sensors transmit human body movement data directly to the MyoMotion receiver, whose module provides wireless communication with the IMU (Inertial Measurement Unit) sensors at a frequency of 2.4 GHz and with an operational range of 30 m. The parameter recording module was installed in the cabin next to the driver, thereby not restricting the workspace of the paramedic performing medical procedures.

The next step involved sensor calibration, after which the paramedic performed individual medical procedures on the medical simulator located in the ambulance. The measured angles assumed both negative and positive values, with the calibration position defined as the zero value. Negative values indicate left rotation and lateral flexion, whereas right rotations are always represented by positive values [3].

3. Measurement Results

This section presents the results of sEMG signal measurements and the range of motion of the analyzed body segments, together with the identification of cases in which the adopted threshold values were exceeded. The presented data constitute the basis for further analysis.

3.1. sEMG Measurement Results

The obtained results enabled the identification of increased muscle tension in individual muscles.

Table 2 presents the resting, maximum, and mean RMS values of 11 investigated muscles, while Figure 2 shows the percentage muscle activation during each procedure relative to the maximal

capacity of each muscle. Resting muscle tension was measured prior to the procedure in a free standing position.

It was assumed that muscle activation exceeding 20% of the maximum strength for a given muscle indicates abnormal static muscle tension resulting from a forced or uncomfortable posture during the performance of medical tasks.

Table 2. *Resting, maximal, and mean RMS values of the examined muscles during the ECG procedure.*

No.	Muscle	Mean RMS (root mean square)	RMS max	Resting RMS (root mean square)	Mean value (%) relative to maximal RMS (RMSmax)
1	CERVICAL PS RT	45	292	9,96	15,4
2	CERVICAL PS LT	34,7	226	13,1	15,3
3	UPPER TRAP. RT	65,2	460	14,6	14,1
4	UPPER TRAP. LT	58	569	25,6	10,1
5	BICEPS BR. RT	79,3	3410	2,37	2,3
6	BICEPS BR. LT	79,4	2045	4,72	3,8
7	THORACIC ES RT	97,9	264	17,9	37,0
8	THORACIC ES LT	57,6	245	5,87	23,5
9	LUMBAR ES RT	105	271	10,4	38,7
10	LUMBAR ES LT	118	232	20,4	50,8
11	RECTUS FEM. LT	30,1	747	28,8	4,0

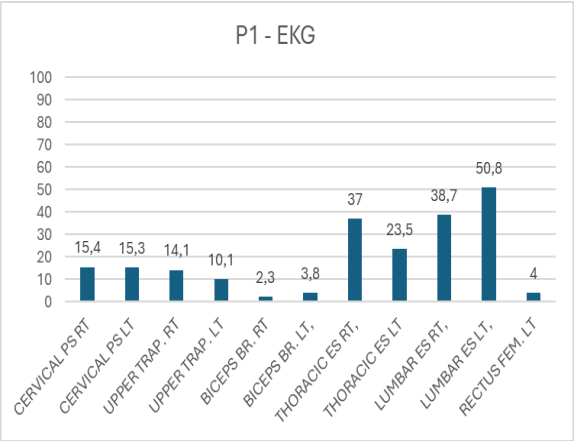


Fig. 2. *Percentage values of muscle tension in the examined muscles during the ECG procedure.*

During the ECG medical procedure, muscle activation exceeding 20% of the maximum voluntary contraction for a given muscle was observed in the following muscles:
• THORACIC ES RT – right thoracic erector spinae muscle,
• THORACIC ES LT – left thoracic erector spinae muscle,
• LUMBAR ES RT – right lumbar erector spinae muscle,
• LUMBAR ES LT – left lumbar erector spinae muscle.

3.2. Results of motion kinematics recording

The article presents the results for the ranges of motion of the cervical, thoracic, and lumbar spine, as well as the hips. The measured values of angular ranges during the performed medical procedures are presented in Table 3.

Table 3. *Values of the measured ranges of the analyzed movements for individual medical procedures and exceedances of the normal ranges of motion during the performed procedures (MV – measured values, E – exceedances).*

Body segment / type of movement	EKG	
	MV	E
Cervical spine flexion	105,3	**32,8(+)**
Cervical lateral flexion	103,8	**54,62(-)**
Cervical spine rotation	144,1	**69,68(-)**
Lumbar spine flexion	44,08	-
Lumbar lateral flexion	27,3	-
Lumbar spine rotation	24,39	**14,71(-)**
Thoracic spine flexion	61,76	**13,34(+)**
Thoracic lateral flexion	48,29	**15,35(-)**
Thoracic spine rotation	80,42	**32,55(-)**
Left hip flexion	74,64	-
Right hip flexion	74,52	-
Left hip abduction	35,18	-
Right hip abduction	45,46	-
Left hip external rotation	63,2	-
Right hip external rotation	101,8	**38,98(-)**

The values highlighted in bold in Table 3 exceed the normal range of motion adopted in the ISOM standard [8].

During the ECG medical procedure, the measured ranges of motion for lumbar rotation, thoracic flexion, and thoracic lateral flexion were outside the normal physiological ranges; however, these values did not exceed 20 degrees. In contrast, the measured ranges of motion for cervical flexion, cervical lateral flexion, cervical rotation, thoracic rotation, and external rotation of the right hip joint exceeded the normal ranges of motion by more than 30 degrees. It can therefore be observed that performing the ECG medical procedure in an ambulance has the most adverse effect on the cervical and thoracic spine.

4. Results and discussion

The conducted studies indicate that emergency medical personnel working in ambulances are exposed to significant musculoskeletal overload, primarily resulting from the adoption of forced, often uncomfortable, and static body postures. Limited workspace, the necessity for rapid response, and the need to adapt to the patient's position and the arrangement of medical equipment frequently require paramedics to work in bent, twisted, or kneeling positions, leading to excessive loading of the spine, particularly in the lumbar and cervical regions. Long-term exposure to such conditions may contribute to the development of overload syndromes and chronic pain disorders. Furthermore, the dynamic nature of emergency interventions, the necessity of transferring patients and equipment, as well as stress associated with life-threatening situations additionally increase the risk of musculoskeletal injuries and disorders. This issue constitutes a significant challenge in the context of workplace ergonomics and occupational health prevention among emergency medical personnel.

The obtained research results enabled the identification of increased muscle tension in specific muscle groups of paramedics during the performance of the medical procedure of electrocardiography (ECG). During ECG performance, a significant

increase in the activation of the back and lumbar muscles was observed. This muscular response results from the necessity of prolonged leaning over the patient and performing precise hand movements, which causes static overload of the upper body.

Motion kinematics recording further demonstrated that performing the ECG procedure in an ambulance has the most adverse effect on the cervical and thoracic spine.

The conducted studies indicate a clear overload of selected muscle groups even during basic medical activities, which in the long term may lead to the development of pain disorders, reduced mobility, and decreased work efficiency. It should be emphasized that numerous procedures are performed in ambulances, many of which are considerably more complex than ECG measurement.

The conducted studies demonstrate that paramedics experience musculoskeletal overload resulting from adopting forced postures while performing medical procedures in ambulances. It should be clearly emphasized that the research methods applied in this study constitute an innovative approach in the context of assessing workload in the profession of paramedics. Previous analyses of this type have not employed the tools discussed herein, making the present study a significant contribution to the advancement of knowledge regarding the working conditions of this professional group.

The study results clearly demonstrate the necessity of introducing modifications to the workspace in ambulances in order to improve the ergonomics of their spatial structure. The presented methodology for identifying burdens resulting from the working postures adopted by paramedics during medical procedures constitutes the basis for an original method of assessing the ergonomic level of a paramedic workstation in an ambulance, ultimately enabling the formulation of guidelines addressed to ambulance manufacturers. It should be noted, however, that the ergonomic assessment is formulated on the basis of the analysis of a larger number of procedures and not solely the single procedure presented in this article.

5. Conclusion

The article presents a new paradigm for the analysis of the work of transport system operators, based on the use of surface electromyography (sEMG) and the MyoMotion motion analysis system. The conducted studies confirmed that the application of these methods enables a comprehensive and objective assessment of biomechanical loads occurring during the performance of occupational tasks under real working conditions. The obtained results allowed for the identification of key working postures that may constitute potential sources of overload and injury.

The proposed approach represents a significant extension of previously applied ergonomic methods, which were mainly based on observation and subjective assessment, through the introduction of objective measurement tools. Its application may contribute to improved workstation design, optimization of operational procedures, and implementation of more effective preventive measures aimed at reducing the risk of musculoskeletal disorders.

The study results also indicate the considerable potential of the proposed methodology for application in other areas of transport as well as in occupations involving high physical workload. Future research directions should include increasing the sample size, analyzing a broader range of occupational activities, and integrating biomechanical data with cognitive workload analysis, which would enable an even more comprehensive assessment of operators' working conditions.

6. References

1. Åkerstedt, T. (2006). Psychosocial stress and impaired sleep. Scandinavian Journal of Work, Environment & Health, 32(6), 493–501.
2. Bartuzi P., Roman-Liu D., Ocena obciążenia i zmęczenia układu mięśniowo-szkieletowego z zastosowaniem elektromiografii, CIOP PIB, Bezpieczeństwo pracy nauka i praktyka, 4/2007.
3. Bęczkowska Sylwia, Celiński Daniel, Grabarek Iwona, Grzybowska Katarzyna, Zysk Zuzanna, (Nie)ergonomiczne warunki pracy w ambulansie medycznym, Medycyna Pracy, 2024, vol. 75(1), s.1-14.
4. Gómez-Galán, M., Pérez-Alonso, J., Callejón-Ferre, A. J., & López-Martínez, J. (2020). Musculoskeletal risks: RULA bibliometric review. International Journal of Environmental Research and Public Health, 17(12), 4354.
5. Hancock, P. A., & Desmond, P. A. (2001). *Stress, workload, and fatigue*. Mahwah, NJ: Lawrence Erlbaum Associates
6. Hita-Gutiérrez, M., Gómez-Galán, M., Díaz-Pérez, M., & Callejón-Ferre, Á. J. (2020). An overview of REBA method applications in the world. International Journal of Environmental Research and Public Health, 17(8), 2635.
7. https://lab.awfis.net/?page_id=364 (dostęp: 02.05.2025)
8. International Organization for Standardization. (2000). ISO 11226:2000 Ergonomics — Evaluation of static working postures. ISO.
9. Karwowski, W. (2006). International Encyclopedia of Ergonomics and Human Factors. Boca Raton: CRC Press.
10. Kittijaruwattana, J., et al. (2023). A systematic review of ergonomic risk assessment tools and their applications. Health Science Journal of Thailand.
11. Krawiecki Z., Hulewicz A., Cichocki-Kaiser M., Przetwarzanie i analiza sygnału elektrycznego z mięśni przy użyciu komputerowego stanowiska pomiarowego, University of Technology Academic Journals 88, Electrical Engineering, Poznań 2016.
12. Liu, M., et al. (2025). Global burden of musculoskeletal disorders: analysis based on the Global Burden of Disease Study 2021. *Frontiers in Public Health*
13. Wickens, C. D., Hollands, J. G., Banbury, S., & Parasuraman, R. (2015). Engineering Psychology and Human Performance. New York: Routledge.
14. Williamson, A., Lombardi, D. A., Folkard, S., Stutts, J., Courtney, T. K., & Connor, J. L. (2011). The link between fatigue and safety. Accident Analysis & Prevention, 43(2), 498–515.
15. Zhao, H., et al. (2024). Research on RULA, REBA and OWAS based exposure risk assessment methods. Zhonghua Lao Dong Wei Sheng Zhi Ye Bing Za Zhi.

Traffic safety in Serbia and automotive industry today

Nataša Tomić-Petrović
Faculty of Transport and Traffic Engineering, University of Belgrade, Serbia
natasa@sf.bg.ac.rs

Abstract: *According to a new study by the most influential European consumer association BEUC, new mid-size electric vehicles will generally be cheaper to run than their petrol equivalents as early as 2026, while in 2025 "Sandero" became the best-selling car in Europe. Small city electric cars are forecast to be cheaper only from 2026. However, the EU is abandoning its plan to make all cars electric by 2035. "Ford" is radically reducing investments in electric vehicles - weak demand in the US is also cited.*
Chinese Technology giant Xiaomi is testing a factory of the future where humanoid robots are helping to assemble electric cars at a factory in Beijing. In November 2025, Peugeot changes the rules – the beginning of a new era for drivers - the square steering wheel!
It is interesting that the Chinese company Changan is entering the market of Serbia and the Western Balkans by launching the Deepal So5 and So7 models. These are electric SUV models, and in our city of Belgrade, test drives of these cars are already being scheduled.
In 2026 production of the "Grande Panda" with a gasoline engine has begun in Kragujevac.
In February 2026, the most urban electric car for 2025 was announced, and it was the Byd Dolphin Surf. It was also promoted in Belgrade, Serbia. Serbia was also the first country in Europe to sign an agreement with the American manufacturer of flying taxis, Archer Aviation. The first demonstration flights are expected in 2027, during the specialized exhibition EXPO.
Unfortunately, on our roads in Serbia we had the black month of March 2026. In the first 12 days of the third month, 19 people died in traffic accidents, most of them young people. Since the beginning of the year, 120 people have lost their lives in traffic accidents. (The Traffic Safety Agency).
How to prevent traffic tragedies in our country? Caution is essential for all road users. Smart radars should contribute to compliance with regulations. Recently, stationary radars were installed at a total of 30 "black spots". It is expected that they will significantly improve traffic safety.
Keywords*: TRAFFIC SAFETY, ELECTRIC CARS, ACCIDENTS*

1. Introductory considerations

In October 2025 French carmaker "Citroen" has ordered owners of the current C3 range to immediately stop using their vehicles due to a fault with the brake pedal assembly, and in the UK it affected around 1,100 vehicles. The so-called "stop-drive" recall is issued when there is a serious safety risk. The recall covered all models in the C3 range: the Citroen C3 (2025–), Citroen e-C3 (2024–), Citroen C3 Aircross (2025–) and Citroen e-C3 Aircross (2025–).

Customers of the affected models were offered replacement vehicles until the brake pedal assembly could be checked and repaired. According to an explanation from Stellantis, the owner of the Citroen brand, during regular quality checks it was discovered that certain right-hand drive models have a brake pedal manufactured outside specifications, which can lead to a complete loss of braking ability. However, they assured that the automatic emergency braking and electronic parking brake remained functional. In November 2025, the public learned that Stellantis had moved part of the Citroen-C3 production to Kragujevac.

In November 2025, "Peugeot" changes the rules – the square steering wheel represents the beginning of a new era for drivers!

In March 2026 BMW was recalling more than 360,000 vehicles (around 337,000 vehicles worldwide and 29,000 in Germany, across 5 different models, potentially affected by a fire risk – linked to the wiring in the dashboard).

2. Automotive industry today

Not long time ago, Court dismissed climate activists' lawsuit against Mercedes and BMW.

A new car has appeared in the offer of the Romanian brand "Dacia", the model is a mix of SUV and station wagon and is as long as 4.62 meters. After the "Sandero" became the best-selling car in Europe in 2025, for the second time in a row, the "Daster" took second place in its class.

The latest 3-wheel electric vehicle is designed to slide through traffic. The Trinova, California startup is 85 cm wide.

The first electric "Rolls-Royce" Black Badge Spectre is a blend of luxury and audacity, where tradition and technology are brought together in harmony. With 659 horsepower, it is a true blend of luxury and audacity. The ride is quiet yet powerful in this machine.

"Bugatti" is celebrating its 20th anniversary. The Bugatti Veyron was organized by the legendary gathering of hypercars. It is named after the racer Pierre Veyron.

The icon among jeeps in 2026 is the fully electric Jeep Recon, designed for off-road driving.

At "Fiat", October production was 73% above last year's average. Rubber and plastic production also recorded a positive trend, contributing to the overall growth of the processing sector.

The car from Kragujevac arrives as Fiat's savior in Europe: the "Grande Panda" was the best-selling Fiat in France in 2025 where 892 units of the B-segment model were registered in October. In Germany, 296 "Grande Pandas" were sold in the same month, and 283 in Spain. Much is expected from Turkey, where production of the popular Fiat Tipo will soon cease and sales of the "Grande Panda" will begin. Even more success is expected in 2026, when the car will also start being assembled in "Stellantis" factories in Morocco and Brazil, because the "Grande Panda" is designed as a global model. The "Grande Panda" is also among the seven finalists for the "European Car of the Year 2026!" award.

Fiat "Grande Panda" will be assembled in factory in Algeria. After months of stagnation and a difficult situation in Europe, Fiat has finally seen the light at the end of the tunnel. The reason? The Fiat "Grande Panda", which is starting to be delivered in significant quantities and giving the Italian brand an unexpected boost on the continent. This car has had the most success in Italy, where 1,912 Grande Pandas were registered in October, and the model from Kragujevac is now in 16th place in sales on the Apennine Peninsula.

Kragujevac's "Grande Panda" is not yet in the top 10 best-selling models in Europe. The problem with the car that is assembled in the heart of Šumadija was the lack of labor. Instead of the planned 500 units per day, 100-150 Grande Pandas rolled off the assembly lines, despite excellent demand across the continent. Sellers had to ask customers to be patient, or to be prepared to wait several months for delivery. This was the reason why many turned to another brand. In the meantime, production has stabilized, although it is still not at the desired level. In one period "Volkswagen" was left without key parts due to a shortage of semiconductors, and the cause was a dispute with a Dutch chip manufacturer. Nexperia is a silent giant of the chip industry.

In 2026 production of the "Grande Panda" with a gasoline engine has begun in Kragujevac. The factory employs more than 3,000 workers in three shifts. The "Stellantis" factory produces

three models of the "Grande Panda": electric, hybrid and with a gasoline engine. The production is underway introducing the hybrid model.

Chinese technology giant Xiaomi is testing a factory of the future where robots have begun assembling cars. Humanoid robots are helping to assemble electric cars at a factory in Beijing. Cars are being built every 76 seconds. The robots are currently serving as interns. [1]

It is also interesting that the Chinese company Changan is entering the market of Serbia and the Western Balkans by launching the Deepal So5 and So7 models. These are electric SUV models, and in our city of Belgrade, test drives of these cars are already being scheduled. For more traditional buyers, in the new era of mobility, the gasoline models Changan Cs55 and soon Cs35 and UNI-T are recommended.

3. Traffic safety and the future of electric vehicles

Few years ago, in 2023, the first E1 (E One) Electric Boat Racing Championship has been approved by the Union Internationale Motonautique (UIM), the world's leading body for motorboat racing. The competition was established primarily to create a new, competitive water racing offer, based on clean technologies, to protect our waters and coastal areas. [3]

According to a new study from 2025 by the most influential European consumer association BEUC, new mid-size electric vehicles will generally be cheaper to run than their petrol equivalents as early as 2026. Small city electric cars are forecast to be cheaper from this year. Although if the model of exclusive reliance on public chargers is maintained, petrol cars could remain more affordable for the next six years.

There are less than 1,000 electric vehicles in Serbia, and subsidies of 5,000 euros are planned. In Serbia, applications for subsidies for electric vehicles are submitted from March 1 to September 30, 2026, with the adoption of the Regulation on the conditions and manner of implementing subsidized purchases of new electric vehicles. [2]

The European Parliament and Council have reached a provisional agreement to revise the EU Driving Licence Directive, which will allow drivers with a standard Category B license to drive alternatively fueled vehicles (electric or hydrogen) weighing up to 4.25 tonnes (4,250 kg), starting approximately around 2028-2029. It indicates that from 2028, drivers with a category B driving licence will be able to drive vehicles weighing up to 4.25 tonnes, including camper vans. (this will only apply to those who passed their driving test after 1999). This marks the start of the implementation of the revised EU Driving Licence Directive, which was adopted in 2023. EU member states have 10 years to adapt.

Unfortunately, on our roads we had the black month of March 2026. In the first 12 days of the third month, 19 people died in traffic accidents, most of them young people. Since the beginning of the year, 120 people have lost their lives in traffic accidents / Serbian Ministry of Internal Affairs/. Caution is essential for all road users. Smart radars should contribute to compliance with regulations. Recently, stationary radars were installed at a total of 30 "black spots".

The Traffic Safety Agency has launched the "Get in the Car Without Alcohol" campaign, which is being implemented under the slogan "On the way to zero with zero per mille", and continues to promote that alcohol and driving never go together.

4. Conclusion

The EU is abandoning its plan to make all cars electric by 2035. Ford is radically reducing investments in electric vehicles - weak demand in the US is also cited.

According to a new study by the most influential European consumer association BEUC, new mid-size electric vehicles will generally be cheaper to run than their petrol equivalents as early as 2026, while in 2025 "Sandero" became the best-selling car in Europe. Small city electric cars are forecast to be cheaper only from 2026. However, the EU is abandoning its plan to make all cars electric by 2035.

How to prevent traffic tragedies in our country? Caution is essential for all road users. Smart radars should contribute to compliance with regulations. Recently, stationary radars were installed at a total of 30 "black spots". It is expected that they will significantly improve traffic safety.

In February 2026, the most urban electric car for 2025 was announced, and it was the “Byd Dolphin Surf”. It was also promoted in Belgrade, Serbia. Serbia was also the first country in Europe to sign an agreement with the American manufacturer of flying taxis, Archer Aviation. The first demonstration flights are expected in 2027, during the specialized exhibition EXPO. Welcome!

5. References

[1] Hong Huo, Qiang Zhang, Michael Q. Wang, David G. Streets, and Kebin He, Environmental Implication of Electric Vehicles in China, *Environ. Sci. Technol.* (2010), 44, 13, 4856–4861.

[2] Ministry of Environmental Protection of Serbia. (2022). Environmental Protection Strategy until 2030 (Ministarstvo zaštite životne sredine Srbije. (2022). Strategija zaštite životne sredine do 2030. godine) in Serbian

[3] Nautical lifestyle magazin, 68, 2023, p. 36 & 37.

Technical validity of motorcycles and mopeds as a factor of road safety in the Republic of Croatia

Luka Zovak[1], Goran Košir[2], Goran Zovak[2], Marija Ferko[1]
Faculty of Transport and Traffic Sciences, Zagreb, Croatia[1]
Centre for vehicles Croatia, Zagreb, Croatia[2]

Abstract: *This paper examines the technical validity of motorcycles and mopeds registered in the Republic of Croatia as a factor of road safety, analysing data from the Centre for Vehicles of Croatia (CVH) for the period 2023–2025. The study focuses on three dimensions: the age structure of the registered L category vehicle fleet, aggregate periodic technical inspection (PTI) defect data for all L category vehicles in 2025, and disaggregated inspection outcomes for L1 (mopeds) and L3 (motorcycles) subcategories. Results indicate that the Croatian PTW fleet is structurally aged, with over 57% of vehicles exceeding ten years of age in 2025. The overall PTI failure rate stands at 8,28%, with mopeds recording a substantially higher rate of 10,79% compared to 6,73% for motorcycles. The most prevalent defect categories are lighting and signalling devices (32,64%) and tires and suspension (25,15%). The findings highlight the need for strengthened PTI enforcement and targeted public awareness campaigns.*

Keywords*: ROAD SAFETY, MOTORCYCLES, MOPEDS, PERIODICAL TECHNICAL INSPECTION, VEHICLE DEFECTS*

1. Introduction

Motorcycles, mopeds, motor tricycles and quadricycles, collectively classified under European Union vehicle categories L1 through L7, occupy a distinctive and growing position within the contemporary transport system of the Republic of Croatia. Although this vehicle group encompasses three-wheeled and four-wheeled variants, many registered vehicles within this category are powered two-wheelers, and the term PTW (powered two-wheeler) will be used throughout this paper to refer to all L category vehicles collectively. Their relatively low acquisition and operating costs, combined with superior maneuverability in congested urban traffic, have rendered them an increasingly popular mode of transport, particularly during the spring and summer months when conditions in the Adriatic and continental regions are favorable for two-wheel travel. The registered PTW fleet in Croatia has grown steadily over recent years, reaching 184,555 L-category vehicles by 2025.

Despite their practical utility, powered two-wheelers are associated with a markedly elevated road safety risk profile relative to enclosed motor vehicles. PTW riders are among the most vulnerable participants in road traffic, lacking the structural crash protection available to car occupants and frequently exposed to the consequences of both their own riding behavior and the actions of other road users. Road fatality statistics across Europe consistently demonstrate that PTW riders are overrepresented in accident outcomes relative to their share of total vehicle kilometers travelled.

The causes of PTW accidents are multifactorial. Human behavioral factors, including excessive speed, impaired riding, and inadequate hazard perception, are widely recognized as primary contributors. However, the technical condition of the vehicle itself represents an equally important, independently addressable dimension of accident risk. Mechanical failures such as deteriorated braking systems, defective tires, malfunctioning lighting equipment, or non-compliant modifications can directly precipitate loss of vehicle control or impair a rider's capacity to respond effectively to road hazards. In Croatia, the periodic technical inspection (PTI) is the primary institutional mechanism through which safety-relevant vehicle deficiencies are identified and mandated for correction. The Centre for Vehicles Croatia (*Centar za vozila Hrvatske, CVH*) oversees PTI operations and maintains the national vehicle registration database. Despite the clear public safety relevance of PTW technical condition, systematic empirical analyses of inspection outcomes specific to this vehicle class remain limited in the Croatian research literature.

This paper addresses that gap by providing a comprehensive, data-driven examination of three interrelated dimensions: the age structure of the Croatian registered PTW fleet for the period 2023–2025; the aggregate defect profiles recorded at PTI for all L-category vehicles in 2025; and the disaggregated inspection outcomes and most prevalent defects for L1 (moped) and L3 (motorcycle) subcategories. The overarching objective is to assess the extent to which the structural and technical characteristics of the Croatian PTW fleet constitute a road safety concern, and to formulate evidence-based policy recommendations. The paper is structured as follows: Section 2 establishes the legislative and institutional framework; Section 3 analyses fleet age structure; Section 4 presents aggregate PTI defect data; Section 5 provides disaggregated L1 and L3 analysis; Section 6 discusses road safety implications; and Section 7 presents conclusions and recommendations.

2. Legislative and institutional framework

The regulation of powered two-wheelers in the Republic of Croatia is embedded within a layered framework of European Union and national legislation. At the EU level, Regulation (EU) No. 168/2013 of the European Parliament and of the Council on the approval and market surveillance of two- or three-wheel vehicles and quadricycles establishes the type-approval requirements for L-category vehicles and defines the subcategories L1 through L7 according to engine displacement, maximum design speed, and number of wheels [1]. This classification directly determines the applicable inspection periodicity and technical safety standards. With respect to roadworthiness testing, Directive 2014/45/EU of the European Parliament and of the Council on periodic roadworthiness tests for motor vehicles and their trailers sets out the minimum harmonised standards for PTI procedures across EU member states [2]. Croatia has transposed this Directive into national law through the Act on Road Traffic Safety (*Zakon o sigurnosti prometa na cestama*) and accompanying secondary legislation, including the Ordinance on Technical Inspection of Vehicles (*Pravilnik o tehničkom pregledu vozila*) [3]. Under the applicable Croatian legal regime, mopeds and motorcycles are subject to mandatory periodic roadworthiness testing.

The institutional responsibility for PTI oversight is vested in the CVH, which also maintains the Central Vehicle Register (*Središnji registar vozila*). The CVH collects and publishes annual statistical data on vehicle registrations and inspection outcomes, which constitute the primary data sources for the present analysis [4]. It is important to note that the PTI data examined in this paper pertain exclusively to vehicles actually presented for inspection; vehicles operated with expired technical validity that were not presented for inspection fall outside the captured dataset — an inherent limitation of administratively sourced inspection data that should be borne in mind when interpreting the figures presented in subsequent sections.

3. Age structure of registered motorcycles and mopeds (2023. – 2025.)

The age profile of a vehicle fleet serves as a leading structural indicator of its likely technical condition and road safety risk. For powered two-wheelers where brake, tire, or lighting failure can be immediately life-threatening, monitoring fleet age assumes particular importance. Research consistently demonstrates that the

risk of safety-relevant technical defects increases substantially with vehicle age, and that vehicles older than ten years exhibit disproportionately elevated defect rates at periodic inspection [5]. Furthermore, older vehicles lack the advanced active safety technologies such as anti-lock braking systems (ABS) that have become progressively standard on newer PTW models and that contribute meaningfully to crash prevention [6]. The following analysis draws on CVH registration data for the period 2023 – 2025 and encompasses all L1–L7 category vehicles registered in the Republic of Croatia [4].

As shown in Figures 1, 2 and 3, and summarised in Table 1, the Croatian PTW fleet is characterised by a persistent and marked structural ageing across all three years examined. In 2023, a total of 165,260 L-category vehicles were registered, of which 115,192 units, representing 69.69% of the fleet, were older than ten years. Vehicles in the six-to-nine-year age bracket numbered 17,735 (10.74%), those aged two to five years accounted for 19,747 registrations (11.95%), and newly registered vehicles up to one year of age constituted 12,586 units (7.62%) [4].

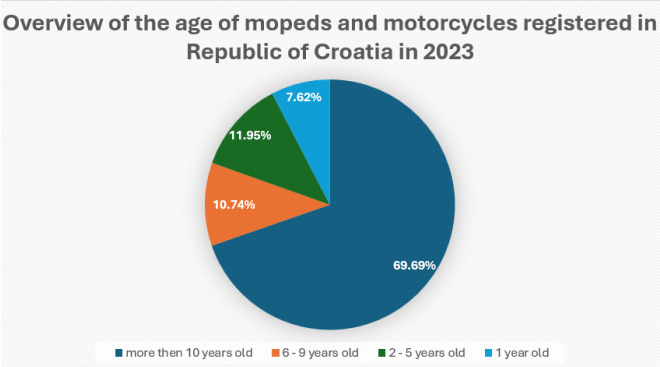


Figure 1. Age structure of registered mopeds and motorcycles in the Republic of Croatia, 2023 [4]

In 2024, the total registered fleet increased to 175,410 vehicles, reflecting year-on-year growth of approximately 6.14%. The over-ten-years cohort remained dominant, accounting for 117,431 vehicles (66.93%), while the six-to-nine-year bracket comprised 20,092 units (11.46%), the two-to-five-year cohort 21,716 vehicles (12.39%), and newly registered vehicles 16,171 units (9.22%). The proportional decline in the oldest cohort, from 69.69% in 2023 to 66.93% in 2024, is marginal and does not indicate a substantive structural shift in fleet composition [4].

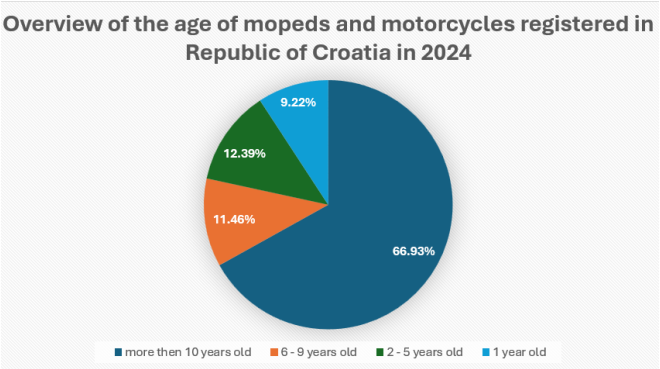


Figure 2. Age structure of registered mopeds and motorcycles in the Republic of Croatia, 2024 [4]

By 2025, the registered fleet had grown further to 184,555 vehicles, cumulative increase of 11.67% compared to 2023. The most notable development in the 2025 data is a more pronounced decline in the proportional share of vehicles older than ten years, which fell to 57.58% (118,896 units). This reduction of approximately 12 percent relative to 2023 is primarily driven by the substantial growth of the six-to-nine-year cohort, which expanded from 10.74% in 2023 to 21.56% in 2025 (22,605 units), suggesting a partial maturation of vehicles registered in the 2016–2019 period now entering this age bracket. The two-to-five-year and up-to-one-year cohorts showed moderate growth in absolute terms, registering 25,963 units (12.58%) and 17,091 units (8.28%) respectively [4].

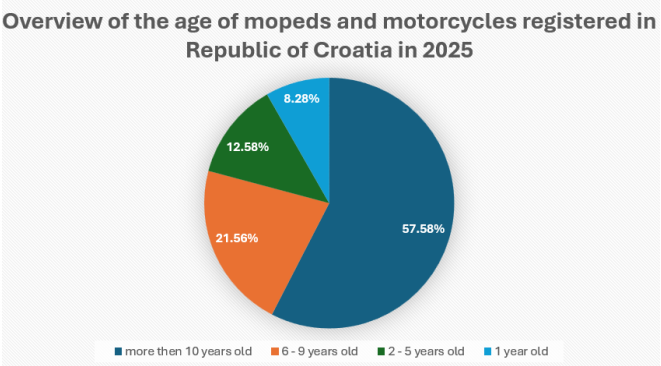


Figure 3. Age structure of registered mopeds and motorcycles in the Republic of Croatia, 2025 [4]

Table 1. Age structure of registered L – category vehicles in Croatia, 2023 – 2025

Age category	2023		2024		2025	
	number	%	number	%	number	%
>10 years old	115,192	69.69%	117,431	66.93%	118,896	57.58%
6 - 9 years old	17,735	10.74%	20,092	11.46%	22,605	21.56%
2 - 5 years old	19,747	11.95%	21,716	12.39%	25,963	12.58%
1 year old	12,586	7.62%	16,171	9.22%	17,091	8.28%
TOTAL	**165,260**	**100%**	**175,410**	**100%**	**184,555**	**100%**

Source: [4]

Notwithstanding the encouraging directional trend in 2025, the data presented in Table 1 confirm that the Croatian PTW fleet remains structurally aged. Even in 2025, vehicles six or more years old collectively accounted for 79.14% of the total registered fleet. The European Road Safety Observatory has documented that PTW riders are consistently overrepresented in road fatality statistics across EU member states, with motorcyclists alone accounting for approximately 16% of all road deaths in 2022 [7]. The persistence of such a large proportion of aged vehicles therefore constitutes a structural road safety risk that cannot be adequately addressed through fleet renewal alone but requires robust technical inspection enforcement as a complementary measure [5].

4. Aggregate defect profile of L – category vehicles at periodic technical inspection (2025)

The periodic technical inspection constitutes the primary formal mechanism through which safety-relevant technical defects in the vehicle fleet are identified, documented, and mandated for correction. A systematic review of the international evidence base has demonstrated that the proportion of road crashes attributed to vehicle defects ranges from 3% to 19% in high-income countries, and that PTI programs are an effective mechanism for identifying and compelling correction of such deficiencies [5]. An analysis of the aggregate PTI defect data for all L-category vehicles inspected in Croatia in 2025 provides a systemic overview of the most prevalent technical failure modes within the national PTW fleet. CVH recorded a total of 34,426 individual defects across all inspected L-category vehicles during 2025, distributed across fifteen standardized component system categories as presented in Table 2 [4].

Of the 165,908 L category vehicles submitted for PTI in 2025, a total of 13,734 were found to have at least one defect, yielding an overall malfunction rate of 8.28%. The average number of defects per defective vehicle was 2,507, indicating that vehicles presenting with at least one fault typically exhibited multiple concurrent deficiencies. a pattern consistent with the established relationship between vehicle age and compounding mechanical wear [5].

Table 2. Number of recorded errors and malfunctions by system category, all L – category vehicles, 2025

TERM	NUMBER OF ERRORS	% IN THE TOTAL DETERMINED NUMBER OF L CATEGORY DEFECTS	AVERAGE NUMBER OF ERRORS PER DEFECTIVE L CATEGORY VEHICLE
VEHICLE IDENTIFICATION	977	2.84	0.07
CONTROL DEVICES	238	0.69	0.02
BRAKING DEVICE	2,389	6.94	0.17
LIGHTING AND LIGHT SIGNALLING DEVICES	11,236	32.64	0.82
DEVICES THAT ENABLE NORMAL VISIBILITY	1,805	5.24	0.13
SELF-SUPPORTING BODY, CHASSIS AND OTHER PARTS	1,979	5.75	0.14
AXLES, WHEELS, TIRES AND SUSPENSION	8,657	25.15	0.63
ENGINE	1,611	4.68	0.12
ENVIRONMENTAL IMPACT	275	0.80	0.02
ELECTRICAL DEVICES AND INSTALLATIONS	165	0.48	0.01
TRANSMISSION MECHANISM	365	1.06	0.03
CONTROL AND SIGNALING DEVICES	2,794	8.12	0.20
COUPLING OF TOWING AND ATTACHED VEHICLE	25	0.07	0.00
OTHER DEVICES AND VEHICLE PARTS	210	0.61	0.02
VEHICLE EQUIPMENT	1,700	4.94	0.12
TOTAL ERRORS	**34,426**	**100.00**	**2.51**
TOTAL NON-DEFECTIVE L VEHICLES	**13,734**		
TOTAL L VEHICLES REVIEWED	**165,908**		
% OF L VEHICLE MALFUNCTIONS	**8.28**		

Source: [4]

As shown in Table 2, the most prevalent defect category by a considerable margin was Lighting and Light Signaling Devices (Label 03), which accounted for 11,236 defects, equivalent to 32.64% of all recorded deficiencies. This finding is particularly significant from a road safety perspective, as lighting defects directly impair the visibility of PTW riders to other road users and simultaneously reduce the rider's own ability to perceive the road environment under low-light conditions. Research into PTW accident causation has consistently identified conspicuity deficits, including defective lighting and missing reflectors as contributing factors in collision scenarios, particularly in interactions with other motor vehicles [8]. The average number of lighting defects per defective vehicle (0.82) suggests that lighting failures are among the most frequently occurring individual fault types across the entire fleet.

The second largest defect category was Axles, Wheels, Tires and Suspension (Label 06), responsible for 8,657 defects or 25.15% of the total. Tire and suspension deficiencies are directly implicated in vehicle stability and performance, particularly in emergency breaking and evasive maneuver scenarios. The high prevalence of this category is consistent with the fleet age structure documented in Section 3, as rubber degradation and suspension wear are strongly age and mileage dependent failure modes.

Control and Signaling Devices (Label 11) constituted the third most frequent defect group, with 2,794 occurrences (8.12%), followed by the Braking Device category (Label 02) with 2,389 defects (6.94%). Brake deficiencies represent one of the most direct safety-critical failure modes for any vehicle and are particularly consequential for PTWs, where braking performance is the primary means of emergency speed reduction in the absence of structural crash protection. The Rechnitzer et al. report on vehicle roadworthiness confirmed a statistically significant relationship between brake deficiencies and elevated crash risk, particularly for single-vehicle accident scenarios [9]. The combined share of braking, lighting, tire, and suspension defects accounts for approximately 70% of all recorded PTI deficiencies, a concentration that highlights the primary technical risk domains within the Croatian L category fleet.

Vehicle Equipment (Label 15) recorded 1,700 defects (4.94%), while Self-Supporting Body, Chassis and Other Parts (Label 05) accounted for 1,979 deficiencies (5.75%). Devices Enabling Normal Visibility (Label 04) registered 1,805 defects (5.24%). Defect categories with comparatively low frequencies included Environmental Impact (Label 08, 0.80%), Coupling of Towing and Attached Vehicles (Label 13, 0.07%), and Electrical Devices and Installations (Label 09, 0.48%). These lower-frequency categories nonetheless carry road safety relevance, and their presence reinforces the case for comprehensive PTI coverage across all vehicle system groups [2].

5. Disaggregated technical inspection analysis of L1 and L3 vehicle category

5.1. Overall inspection outcomes

While the aggregate L category defect data presented in Section 4 provides a system-level overview, a disaggregated analysis of the L1 (moped) and L3 (motorcycle) subcategories reveals important structural differences in inspection outcomes with significant implications for targeted road safety intervention. Table 3 presents the PTI results for L1 and L3 vehicles individually and in combination, based on CVH inspection records for 2025 [4].

Table 3. PTI outcomes for L1 and L3 category vehicles, 2025

Vehicle category	Failed PTI	Passed PTI	Total	Failure rate (%)
L1	6,592	54,907	61,547	**10.79**
L3	6,732	94,058	100,848	**6.73**
L1 & L3	13,324	148,965	162.395*	**8.20**

Source: [4]

Of the 61,547 L1 category vehicles (mopeds) subjected to PTI in 2025, a total of 6,592 failed the inspection, yielding a failure rate of 10.79%. By contrast, of the 100,848 L3 category vehicles (motorcycles) inspected, 6,732 failed, corresponding to a markedly lower failure rate of 6.73%. The combined failure rate for L1 and L3 vehicles was 8.20%, closely aligned with the overall L category rate of 8.28% [4].

The substantially higher failure rate for mopeds relative to motorcycles, a differential of approximately 4%, warrants careful interpretation. Research on PTW accident risk has established that mopeds and motorcycles exhibit meaningfully different crash profiles, user demographics, and maintenance behavior patterns [10]. Mopeds are typically lower-cost vehicles whose users may prioritize cost minimization over systematic vehicle upkeep. Furthermore, the specific technical requirements applicable to L1 vehicles, notably the mandatory speed limiter, introduce a category-specific failure mode with no direct analogue in L3 vehicles, as discussed in Section 5.3. The Croatian context is particularly relevant: a study of motorcyclist behavior among 842 Croatian riders confirmed that younger riders exhibit significantly higher rates of risky behaviors and non-compliance patterns [11], a profile consistent with the moped user demographic.

5.2. Defect severity distribution

Beyond the binary pass/fail outcome, the CVH inspection data permit disaggregation of recorded defects by severity classification, specifically between minor defects, which do not preclude passage of PTI, and major defects, which result in PTI failure. Table 4 presents this distribution for L1 and L3 vehicles separately and in combination [4].

Table 4. Distribution of minor and major defects at PTI – L1 and L3 categories, 2025

Number of recorded errors at PTI of L1 & L3 categories	L1 - mopeds	L3 - motocycles	Combined L1 & L3
Minor defect / passed PTI	3,974	6,190	10,164
Failed PTI	11,387	11,987	23,374
Total defects	**15,361**	**18,177**	**33,538**

Source: [4]

A total of 33,538 individual defects were recorded across L1 and L3 vehicles combined, of which 23,374, representing 69.70% were classified as major defects resulting in PTI failure, and 10,164 (30.30%) constituted minor defects compatible with PTI passage. For L1 mopeds, 15,361 defects were recorded in total, with 11,387 (74.12%) classified as major and 3,974 (25.88%) as minor. For L3 motorcycles, 18,177 total defects were recorded, with 11,987 major (65.95%) and 6,190 minor (34.05%). The higher proportion of major defects among L1 vehicles is consistent with the higher overall failure rate observed for this subcategory.

It is noteworthy that even minor defects, not individually sufficient to cause PTI failure, may contribute to incremental increases in accident risk when present in combination with other vehicles, riders or environmental factors. A PTW with several concurrent minor defects may exhibit meaningfully degraded handling or conspicuity characteristics that, while falling below individual failure thresholds, collectively represent an elevated risk profile. The overview by Vlahogianni confirms that risk factors in PTW accidents operate in combination rather than in isolation, reinforcing the case for monitoring minor defect prevalence as a complementary safety indicator alongside the failure rate [8].

5.3. Most prevalent defects – L1 category (mopeds)

Table 5 presents the ten most frequently recorded individual defects for L1 category vehicles at PTI in 2025, classified by number of occurrences and defect severity (P = minor/passed; F = major/failed). This ranking provides granular insight into the specific technical failure modes most commonly affecting the moped sub-fleet [4].

Table 5. Ten most frequently recorded defects – L1 category (mopeds), 2025

Defect description	No. of occurrences	Classification
Tires, need replacement of tires soon	2052	Minor (P)
Speed limiter on mopeds, does not work	1882	Major (F)
Service brake executive elements, insufficient braking efficiency (braking coefficient)	631	Major (F)
Rear position lights, one or more lights not working	512	Major (F)
Tires, tread depth, small	493	Major (F)
Reflectors, missing	474	Major (F)
Brake lights, one or more lights not working	443	Major (F)
Indicators, one or more lights not working	425	Major (F)
Short light not working	407	Major (F)
Short light, minor glass or lens cloud	310	Minor (P)

Source: [4]

The most frequently recorded defect among L1 vehicles was tire condition requiring imminent replacement (2,052 occurrences), classified as a minor defect. The second most prevalent defect, and the most common major defect resulting in PTI failure, was the non-functioning speed limiter (1,882 occurrences), a deficiency specific to the L1 category. Under Croatian and EU law, mopeds are required to be limited to a maximum design speed of 45 km/h; a non-functional speed limiter represents both a registration non-compliance and a direct road safety hazard, as it permits the vehicle to operate at speeds exceeding the design parameters of its braking and stability systems [1]. This deficiency has no equivalent in the L3 category and accounts for a substantial portion of the differential in failure rates between the two subcategories.

Braking deficiencies ranked third, with 631 recorded instances of insufficient braking efficiency in service brake executive elements, a major defect with direct accident causation potential. The Rechnitzer analysis of vehicle roadworthiness and crash incidence confirmed that brake-related defects are among the most causally significant technical failure modes in PTW accident sequences [9]. Rear position light failures (512), tread depth deficiencies (493), missing reflectors (474), brake light failures (443), indicator failures (425), and headlight malfunctions (407) collectively represent a cluster of lighting, visibility, and signaling deficiencies. Research on PTW safety risk factors has consistently identified conspicuity and lighting as critical variables in collision scenarios involving other motor vehicles [8, 12].

5.4. Most prevalent defects – L3 category (motorcycles)

Table 6 presents the equivalent defect ranking for L3 category vehicles (motorcycles) at PTI in 2025. The defect profile of the L3 sub-fleet exhibits both points of similarity and meaningful divergence relative to that of L1 vehicles, reflecting the different vehicle characteristics, use patterns, and rider demographics documented in the comparative PTW literature [4, 10].

Table 6. Ten most frequently recorded defects – L3 category (motorcycles), 2025

Detected defects	No. of occurrences	Classification
Tires, need replacement of tires soon	3075	Minor (P)
First aid box (container), missing	1129	Minor (P)
Reflectors, missing	952	Major (F)
Tires, tread depth, small	941	Major (F)
Exhaust system, modification that is not permitted or approved	589	Major (F)
Direction indicators, modification that is not permitted or approved	522	Major (F)
Reflective vest, missing	482	Minor (P)
Brake lights, one or more lights not working	428	Major (F)
Rear postion lights, one or more lights not working	408	Major (F)
Direction indicators, one or more lights not working	366	Major (F)

Source: [4]

As with L1 vehicles, the most common defect among L3 motorcycles was tire wear requiring imminent replacement (3,075 occurrences, minor). The second most frequent defect was the absence of a first aid box (1,129, minor) — reflects a Croatian legal requirement for motorcycles to carry a mandatory first aid kit [3]. Missing reflectors ranked third (952, major), followed by insufficient tire tread depth (941, major).

A particularly notable feature of the L3 defect profile is the relatively high frequency of non-approved modifications: exhaust system modifications were recorded 589 times (major), while non-approved direction indicator modifications accounted for 522 defects (major). Such modifications may compromise structural integrity, emissions compliance, or the effectiveness of mandatory signaling equipment, and they represent a category of non-compliance that is specific to the motorcycle sub-culture and has no direct equivalent in the utility-focused moped segment [11]. Missing reflective vests (482, minor) ranked seventh, reflecting an equipment requirement under Croatian law [3]. Brake light failures (428, major), rear position light failures (408, major), and direction indicator failures (366, major) complete the top ten, reinforcing the systemic importance of lighting and signaling deficiencies identified in Section 4 [8, 12].

6. Discussion – road safety implications

The findings presented in Sections 3–5 collectively paint a coherent and concerning picture of the technical condition of the Croatian PTW fleet. Three principal road safety implications merit sustained analytical attention.

First, the structural ageing of the fleet represents a persistent background risk factor that amplifies the likelihood of safety-critical technical failures. With over 57% of registered PTWs exceeding ten years of age in 2025, and more than 79% surpassing six years of age, the Croatian fleet is operating at a structural age profile that generates elevated defect risk across multiple safety-critical systems simultaneously. According to the European Road Safety Observatory, motorcyclists are 49 times more likely to die in a crash per vehicle kilometer than car drivers, a disparity that existing research attributes in part to the absence of passive crash protection and to the technical vulnerabilities of older vehicles [12]. The progressive mainstreaming of active safety systems, including ABS, traction control, and electronic stability control, on newer PTW models underscores the importance of fleet renewal as a long-term road safety lever [6], even as PTI enforcement addresses the immediate deficiency landscape.

Second, the concentration of defects in lighting, tire, and braking systems is not coincidental. These three system categories are precisely those most directly implicated in PTW accident causation in the European in-depth research literature. The overview by Vlahogianni similarly confirmed that lighting, tire, and braking conditions are among the critical vehicle-related risk factors for PTW accident involvement and severity [8]. The alignment

between the Croatian PTI defect profile and this established body of European accident causation evidence strongly suggests that targeted enforcement focusing on these defect categories would yield commensurate improvements in road safety outcomes.

Third, the significantly higher failure rate of L1 mopeds (10.79%) relative to L3 motorcycles (6.73%) suggests that subcategory-differentiated intervention strategies may be more effective than uniform fleet-wide approaches. Comparative research by Blackman and Haworth established that mopeds and motorcycles exhibit distinct crash profiles driven by differences in vehicle design, speed capability, and user demographics [10]. The concentration of speed limiter failures and braking deficiencies in the L1 sub-fleet, combined with the risk behavior patterns documented among younger Croatian riders [11], points toward a user group and vehicle type that may benefit particularly from enhanced enforcement activity and targeted public information campaigns emphasizing the safety rationale for speed limitation compliance.

7. Conclusion and policy recommendations

This paper has presented a comprehensive, data-driven analysis of the technical validity of motorcycles and mopeds in the Republic of Croatia, drawing on CVH registration and PTI data for the period 2023–2025. The findings across the three analytical dimensions examined lead to several clear and consistent conclusions.

The Croatian L category vehicle fleet is structurally aged, with the majority of registered PTWs exceeding ten years of age in all three years examined. While a gradual directional improvement is observable between 2023 and 2025, driven primarily by growth in the six-to-nine-year age cohort, over 79% of the fleet remained six or more years old in 2025. The overall PTI failure rate of 8.28% for L category vehicles, with a particularly elevated rate of 10.79% for mopeds, indicates that a substantial share of the fleet presents for inspection in a condition that fails to meet minimum roadworthiness standards. The dominant defect categories, lighting and signaling, tires and suspension, and braking systems are precisely those most directly associated with accident causation in European PTW crash research. Non-approved modifications represent an additional and growing category of concern specific to the motorcycle sub-fleet.

Based on these findings, three principal policy recommendations are advanced. First, enforcement of PTI compliance obligations for L category vehicles should be strengthened, with particular emphasis on the higher-risk moped subcategory and older vehicles. Targeted roadside inspection campaigns focusing on lighting, tire condition, and braking performance would complement the existing PTI framework and help capture vehicles operated with expired technical validity that fall outside the administrative dataset.

Second, public awareness campaigns addressing the road safety rationale for speed limiter compliance in mopeds, and the risks associated with non-approved vehicle modifications in motorcycles should be developed in collaboration with rider associations, insurers, and road safety authorities. Such campaigns should be targeted at the specific user groups most associated with these failure modes.

Third, longitudinal research linking PTI defect records to accident data should be commissioned to enable causal estimation of the road safety impact of specific technical deficiency types. The current analysis is limited to inspection outcomes and does not permit direct quantification of the accident contribution of individual defect categories. Closing this evidence gap would substantially strengthen the basis for future policy development. Future research should also examine the spatial distribution of PTI outcomes across Croatian counties, the economic determinants of maintenance behavior, and the potential safety dividend of accelerated fleet renewal incentive schemes.

Literature

[1] European Parliament and Council. (2013). Regulation (EU) No 168/2013 on the approval and market surveillance of two- or three-wheel vehicles and quadricycles. Official Journal of the European Union, L 60, 52–128. Available at: https://eur-lex.europa.eu/eli/reg/2013/168/oj/eng [Accessed: 3.4.2026.]

[2] European Parliament and Council. (2014). Directive 2014/45/EU on periodic roadworthiness tests for motor vehicles and their trailers. Official Journal of the European Union, L 127, 51–128. Available at: https://eur-lex.europa.eu/eli/dir/2014/45/oj/eng [Accessed: 3.4.2026.]

[3] Republic of Croatia. (2023). Zakon o sigurnosti prometa na cestama (Act on Road Traffic Safety). Narodne novine, Zagreb. Available at: https://www.zakon.hr/z/78/zakon-o-sigurnosti-prometa-na-cestama [Accessed: 3.4.2026.]

[4] Centar za vozila Hrvatske (CVH). (2025). Statistical Data on Vehicle Registration and Periodic Technical Inspection Outcomes for L-Category Vehicles in the Republic of Croatia, 2023–2025. CVH, Zagreb. Available at: https://www.cvh.hr/gradani/tehnicki-pregled/statistika/ [Accessed: 3.4.2026.]

[5] Gómez-Lantada, C., Simó-Solsona, M., & Sallent-Ribes, J. (2021). Effect of Periodic Vehicle Inspection on Road Crashes and Injuries: A Systematic Review. International Journal of Environmental Research and Public Health, 18(12), 6476. https://doi.org/10.3390/ijerph18126476 [Accessed: 6.4.2026.]

[6] Savino, G., Giovannini, F., & Pierini, M. (2020). Active safety systems for powered two-wheelers: A systematic review. Traffic Injury Prevention, 21(1), 78–86. https://doi.org/10.1080/15389588.2019.1700408 [Accessed: 6.4.2026.]

[7] European Commission – European Road Safety Observatory. (2020). Facts and Figures: Motorcyclists and Moped Riders. Publications Office of the European Union, Brussels. Available at: https://road-safety.transport.ec.europa.eu/system/files/2021-07/facts_figures_p2w_final_20210323.pdf [Accessed: 6.4.2026.]

[8] Vlahogianni, E.I., Yannis, G., & Golias, J.C. (2012). Overview of critical risk factors in Power-Two-Wheeler safety. Accident Analysis & Prevention, 49, 12–22. https://doi.org/10.1016/j.aap.2012.04.009 [Accessed: 6.4.2026.]

[9] Rechnitzer, G., Haworth, N., & Kowadlo, N. (2001). The Effect of Vehicle Roadworthiness on Crash Incidence and Severity. Monash University Accident Research Centre, Report No. 164. Melbourne. Available at: https://www.monash.edu/__data/assets/pdf_file/0017/216710/The-effect-of-vehicle-roadworthiness-on-crash-incidence-and-severity.pdf [Accessed: 6.4.2026.]

[10] Blackman, R.A., & Haworth, N.L. (2013). Comparison of moped, scooter and motorcycle crash risk and crash severity. Accident Analysis and Prevention, 57, 1–9. Available at: https://www.researchgate.net/publication/236598676_Comparison_of_moped_scooter_and_motorcycle_crash_risk_and_crash_severity [Accessed: 6.4.2026.]

[11] Ferko, M., Babić, D., Brijs T., Babić D., Pirdavani A. (2025). Understanding risky riding: Factors influencing crashes, near-crashes, and traffic fines among motorcyclists in Croatia. Transportation Research Part F: Traffic Psychology and Behaviour. Available at: https://www.sciencedirect.com/science/article/abs/pii/S1369847825002529 [Accessed: 6.4.2026.]

[12] European Road Safety Observatory (ERSO). (2024). Road Safety Thematic Report — Powered Two-Wheelers. European Commission, Brussels. Available at: https://www.efa-eu.com/wp-content/uploads/2024/11/8-ERSO-TR-Powered-two-wheelers-20240912.pdf [Accessed: 6.4.2026.]

Methodological foundations for the organization of local transport systems in georgia

Izolda Dangadze, Teimuraz Kochadze, Gvantsa Ardjevanidze, Jumber Chogovadze, Romanoz Topuria
Akaki Tsereteli State University, 59 Tamar Mepe St., Kutaisi 6400, Georgia
Izolda.dangadze@atsu.edu.ge , temko1954@gmail.com , Gvantsa.arjevanidze@atsu.edu.ge , Jumberi.chogovadze@atsu.edu.ge , romtop54@gmail.com

Abstract:*The development of market economic relations in Georgia requires the application of management principles that take into account the interests of management objects. Consequently, there is an objective need to apply logistics management methods at both micro and macro levels. In this study, a transport-logistics polygon has been investigated. The initial study of the transport-logistics polygon demonstrated that, at the initial stage of analysis, it is necessary to determine the possible combinations of logistics channels constituting the transport-logistics polygon. Since market relations provide a wide variety of transport service forms, the selection of potential local transport systems represents a search process. An algorithmic block diagram for studying the transport services market has been developed, along with recommendations for planning and organizing technological processes of local transport systems in Georgia.*
KEYWORDS: *LOGISTICS POLYGON; LOCAL TRANSPORT SYSTEM; BLOCK DIAGRAM; ALGORITHM; TRANSPORT SERVICES MARKET.*

1. Introduction

Under conditions of severe energy resource shortages, it became evident that logistics management methods are capable not only of effectively solving raw material supply and inventory management problems, but also of successfully ensuring the rational organization of production processes. During periods of economic crisis, those companies survived that were able to implement a logistics-oriented organizational approach despite operating under identical technical and technological conditions. The obtained results identified logistics not only as an instrument for influencing the external environment, but also as an effective means for ensuring the efficient functioning of internal organizational processes.The development of market economic relations in Georgia requires the implementation of management principles that consider the interests of management objects. Consequently, there is an objective necessity to apply logistics management methods at both micro and macro levels.

Our studies have shown that, at present, there are two concepts for establishing the optimal operating variant of a transport system using mathematical-economic methods.

The first concept describes the transport system, i.e. the planning object, as a unified "global" economic-mathematical model. It should be noted that, during this period, transport companies underwent decentralization and were divided into small transport enterprises that acquired economic independence. Therefore, there is no unified coordinating body for the real management of the transport network. As a result, the first approach to transport systems is associated with numerous theoretical and practical difficulties [1].

The second concept considers the transport system as an integrated whole consisting of individual links of different transport modes. The development of an optimal plan for transport system functioning is regarded as a process of planning the economic-mathematical models of the functioning of separate transport mode components [2].

Under current conditions, the advantages of the second concept are evident, since the main structural elements of the logistics organization of material flows are the individual links of the material flow chain within a unified transport system, which are capable of adequately responding to changes in external conditions.

The most important stage in the formation of a logistics transport system is the analysis, selection, and rational coordination of transport system variants operating under different ownership structures within the transport services market. Naturally, the organization process of a logistics transport system involves a sequence of actions that ensure:

- Formation of a logistics transport system based on market analysis of transport services;
- Identification of compatible groups from the available market offers that can be integrated into alternative subsystems;
- Determination of unified transport-logistics system elements for all compatible groups;
- Selection of the most appropriate alternative local transport system according to qualitative performance indicators and transportation conditions;
- Determination of quantitative indicators of the production process of the local transport system and substantiation of a rational work schedule on this basis.

At the same time, an important problem remains the coordination of technical-economic interests among the participants of the logistics process, which determines the organizational transition of the system from immanence to synergy.

1. Preconditions and Means for Resolving the Problem

A transport-logistics polygon was investigated in the present study. The polygon was represented as a combination of logistics channels formed for the transportation of consumer goods (Fig. 1).

The following operations are performed within the indicated zones:

- **Zone A** – Formation of cargo units (CU) and consolidated cargo units (CCU) in the sphere of material production, including packaging operations;
- **Zone B** – Additional consolidation of CCUs, involving the assembly of larger cargo units;
- **Zone C** – Delivery of CCUs to the circulation sphere, including loading, transportation, and unloading operations performed by various transport companies;
- **Zone D** – Partial disassembly of CCUs, since their further transportation in the same form may be impossible or economically inefficient;
- **Zone I** – Delivery of cargo units to the final consumption point and complete disassembly of cargo units.

The initial study of the transport-logistics polygon showed that, at the initial stage of the search process, it is necessary to determine the possible combinations of logistics channels constituting the transport-logistics polygon. Since market relations provide a broad selection of service forms, the selection of potential local transport systems represents a search process.

The search process involves deciding whether to accept the proposed variant or continue the search in the hope of identifying better alternatives with improved technical-economic characteristics. Consequently, it becomes necessary to determine the moment for terminating further information search, because the time and material costs associated with the search process reduce the overall technical-economic efficiency [3].

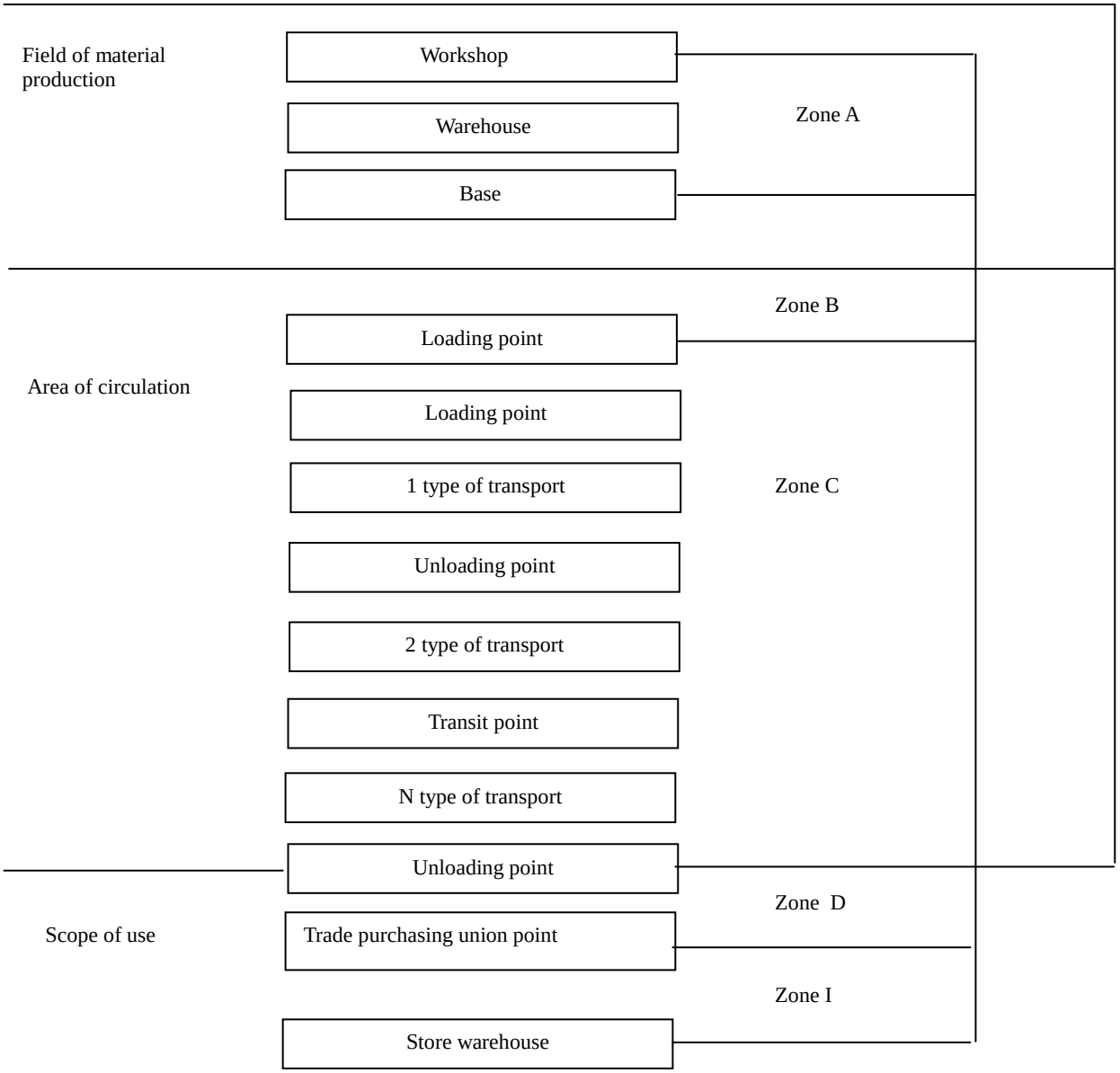


Fig. 1. Generalized structure of a logistics channel

In any case, the selected local transport system represents, on the one hand, a variant identified through random observations, while there remains a probability of discovering a more effective alternative. On the other hand, information search requires both time and financial expenditures. Therefore, at a certain stage, the search for local transport system variants should be terminated, since the expected effect of further search may exceed the anticipated costs.

The efficiency of local transport system selection can be determined from the following relationship:

(1)

$$\bar{\ell} = \frac{\sum_{j=1}^{n} \ell_j}{n}$$

where: ℓ – efficiency of the local transport system;

J – number of variants in the investigated transport services market;
n – number of initial random observations.

The variance *Dn_* is calculated by the following relationship:

(2)

$$D_n = \frac{\sum_{j=1}^{n} (\ell_j - \bar{\ell})^2}{n-1}$$

The standard deviation σ is determined as:

:

$$\sigma = \sqrt{D_n} = \sqrt{\frac{\sum_{j=1}^{n} (\ell_j - \bar{\ell})^2}{n-1}} \qquad (3)$$

The reliability of the maximum value of l *may be determined by:*

$$\ell'_{min} = \bar{\ell} - \sigma$$

(4)

The reliability of the minimum value of l is expressed as:

$$\ell min1 = \ell - \sigma$$

(5)

At the subsequent stage, the search process for the optimal variant of the local transport system should be terminated when:

$$\geq$$

(6)

Otherwise, the search process should continue.

A block diagram algorithm for the methodology of transport services market research was developed and is presented in Fig. 2.

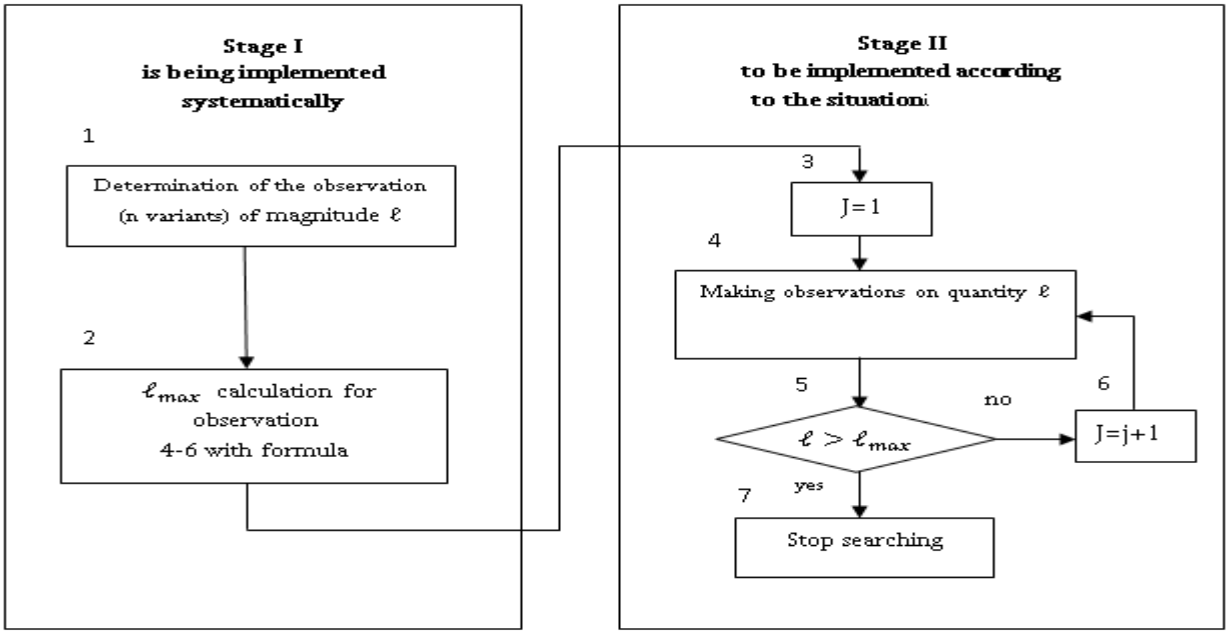


Fig. 2. Algorithm of the block diagram for transport services market research methodology

The above-mentioned technologies may be applied comprehensively by transport companies, thereby ensuring a high level of customer service and stimulating transportation demand under conditions of increased competition.

The analysis of research results demonstrated that, although logistics approaches are currently developing both worldwide and in Georgia, there remains a deficiency in methods for organizing technological processes aimed at improving the efficiency of transport systems at the micro level ("production–sector" link). In this regard, it is advisable that the planning and organization of technological processes of local transport systems in Georgia should be implemented as follows:

- The organizer of freight transportation should be the cargo owner (legal entity) rather than the carrier. The cargo owner is responsible for achieving transportation objectives before higher management bodies and, within the limits of authority, concludes contracts with transport vehicle owners, performs payments for completed transportation services, and carries out the commercial functions of consignor and consignee;
- The cargo owner should attract transport vehicle owners for the creation of a local transport system. The elements of the local transport system are interconnected through unified technological processes, while the owners are interested in the overall results of system functioning;
- The coordination of the immanent interests of participants within the local transport system should be performed by the cargo owner;
- The cargo owner or intermediary should assign coordinated transportation tasks to the participants of the local transport system.

3. Conclusion

- A transport-logistics polygon was investigated and represented as a combination of logistics channels formed for the transportation of consumer goods;
- An algorithmic block diagram for the methodology of transport services market research was developed;
- Recommendations for planning and organizing technological processes of local transport systems in Georgia were developed for the Georgian transport services market.

2. References

1. World Bank (2019) *Belt and Road Economics: Opportunities and Risks of Transport Corridors*. Available at: https://openknowledge.worldbank.org/bitstream/handle/10986/31878/9781464813924.pdf (Accessed: 19 March 2024).
2. UNESCAP (2013) *Intergovernmental Agreement on Dry Ports*. Available at: https://www.unescap.org/sites/default/files/2022-02/EN_IntergovernmentalAgreement_Dry_Ports_Consolidated2022.pdf (Accessed: 11 March 2024).
3. Starr, F. (2018) 'Missing Links: Eurasia's Southern Corridor', *Horizons*, Spring 2018. Available at: https://www.cirsd.org/files/000/000/005/66/1d1259bbb0dc30c9fe46cbedb-47be277a57b0d93.pdf (Accessed: 19 March 2024).

Analysis of the Effectiveness of Remediation of Identified Hazardous Locations in the Republic of Croatia

Željko Šarić, Ivana Vuk, Tomislav Kučinić, Andrej Kunštek

Faculty of Traffic and Transport Sciences – University of Zagreb, Croatia

zeljko.saric@fpz.unizg.hr

Abstract: *The safety of road network users is a fundamental goal of a modern transportation system. Safety is most commonly assessed by the number of traffic accidents and the severity of their consequences. In the Republic of Croatia, hazardous locations on the road network are continuously identified, and their remediation plays an important role in reducing the number of traffic accidents and mitigating their consequences. This paper analyzes the extent to which the processes of identifying and remediating hazardous locations have contributed to reducing the number of traffic accidents. The research includes a comparative analysis of a three-year period before and a three-year period after the implementation of remediation measures, with the objective of providing relevant insight into the effectiveness of the applied measures and their contribution to increasing road safety.*

KEYWORDS: ROAD TRAFFIC SAFETY, IDENTIFICATION OF BLACK SPOTS, METHODOLOGY, TRAFFIC ACCIDENTS, STATE ROADS, FATALITIES, INJURIES, REMEDIATION MEASURES

1. Introduction

Road traffic safety is a key indicator of the quality of a country's transportation system. Identifying and remediating hazardous locations, commonly known as "black spots," is an important method for reducing traffic accidents and their consequences. In the Republic of Croatia, this process follows a defined methodology for identifying hazardous locations on the road network.

This paper analyzes how the procedures for identifying and remediating hazardous locations have contributed to reducing traffic accidents. A comparison of the three-year periods before and after remediation forms the basis for evaluating the implemented measures, providing clear insight into how the proposed solutions have improved the overall level of road safety.

2. Methodology for identifying hazardous locations on the road network

A certified road safety auditor implements the methodology for identifying hazardous locations on the road network. The process begins by identifying locations with an above-average number of traffic accidents and consists of four key steps: (1) parameter definition, (2) location screening, (3) statistical evaluation of the safety risk associated with the identified locations, and (4) location ranking [1].

In the first step, the search parameters are defined, including criteria related to accident consequences (e.g., at least one fatality within a three-year period) and the geometric characteristics of road sections (such as curves, intersections, and similar elements). After accident locations are selected according to these parameters, the data are processed based on the identification method and the road element under consideration. When the fixed-length road section segmentation method is used, the segment boundaries are analyzed, and accidents occurring immediately before or after a segment are assigned to the primary segment, up to a maximum distance of 1,000 meters. For intersection identification, the analysis also includes the associated area of influence, which is determined by traffic signs and road markings or, if such control measures are absent, extends up to 20 meters from the intersection of the road edges. A similar approach is applied to other road elements, such as tunnels and curves.

The next step is the statistical assessment of hazard levels, which begins with calculating the traffic accident rate. This rate is the ratio of the number of traffic accidents to a measure of risk exposure. Traffic volume serves as the measure of exposure; at intersections, it is the total number of vehicles entering the intersection, while on road sections, it is the total number of vehicles traveling in both directions during a specified period, considering the length of the road section. The traffic accident rate for a state road section expresses the number of accidents in relation to the traffic volume on the road segment and is calculated according to Equation (1):

$$C_R = \frac{PN}{M} \qquad (1)$$

Where: CR – traffic accident rate, PN – total number of traffic accidents, M – average traffic volume at the location during the observed period.

The average traffic volume over a one-year period at the observed location, referred to in some international literature as location exposure, is calculated using Equation (2):

$$M = \frac{Q \times 365 \times d}{1.000000} \qquad (2)$$

Where: Q – AADT (Average Annual Daily Traffic), d – length of the analyzed road section [km].

If the traffic accident rate is calculated for intersections, the average annual traffic volume at the observed location is determined using Equation (3), and the resulting accident rate is expressed in million vehicle-kilometers.

$$M = \frac{Q \times 365}{1.000000} \qquad (3)$$

The final stage of the statistical assessment involves calculating the critical accident rate for each location. This value is based on the average accident rate of all analyzed locations and is calculated using Equation (4):

$$C_{CR} = CR_A + k \times \sqrt{\frac{CR_A}{M} + \frac{1}{2 \times M}} \qquad (4)$$

Where: C_{CR} – critical accident rate, CR_A – average traffic accident rate across all analyzed locations, k – statistical significance level coefficient (Table 1).

Table 1. Values of the coefficient k for different significance levels

Significance level	k
90 %	1,282
95 %	1,645
99 %	2,323

If the traffic accident rate exceeds the defined critical accident rate, the location is statistically considered potentially hazardous and requires further inspection. Otherwise, the location is not considered hazardous, and no inspection is required [2].

After identifying potentially hazardous locations that require more detailed analysis, an expert team, including a certified road safety auditor, conducts a field inspection using a pre-prepared form for data collection and processing. Before the site visit, the expert team members review the geographical and traffic characteristics of the location, analyze available traffic accident data, and enter basic site information into the inspection form. The inspection form is divided into three sections. The first section provides basic information on recorded traffic accidents, including their key characteristics and circumstances. The second section contains maps, orthophoto imagery, and photographic documentation of the location, offering a clearer understanding of the spatial context and traffic conditions in the study area. The third section is used to record technical data collected during the field inspection, including measured values and the condition and quality of road design elements, traffic signs and markings, road equipment, and other components of the transport infrastructure.

During the inspection, all identified deficiencies, irregularities, or damages that may affect road traffic safety are recorded and photographically documented. After completing the field inspection, the expert team conducts a detailed analysis of the collected data and compares the identified deficiencies with the characteristics and causes of recorded traffic accidents. Special attention is given to determining any potential causal relationship between the condition of the road infrastructure and the occurrence of traffic accidents.

If deficiencies in the existing road infrastructure identified during the field inspection are found to be potentially related to the occurrence or severity of traffic accidents, the location is classified as hazardous. For these locations, a detailed problem analysis is conducted, and appropriate remedial measures aimed at improving road traffic safety are defined. The proposed measures may include short-, medium-, and long-term solutions and are presented to the road authority for planning and implementation, with the goal of reducing the risk of future traffic accidents.

3. *Analysis of Identified Hazardous Locations on State Roads in the Republic of Croatia*

Between 2018 and 2020, fourteen (14) hazardous locations were identified on the state road network in the Republic of Croatia.

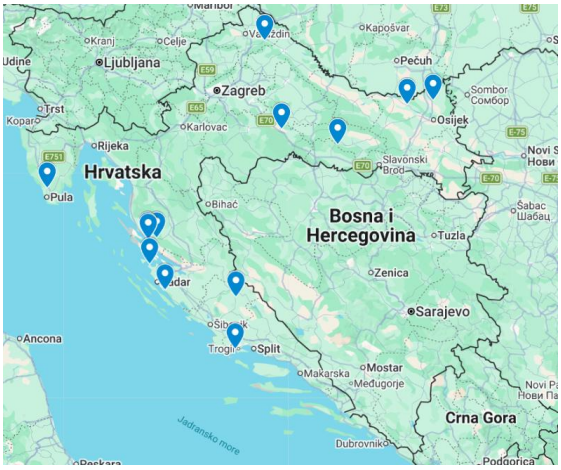


Figure 1. Identified hazardous locations on the state road network in the Republic of Croatia

Based on inspections conducted by the expert team, remedial measures were defined to further improve road traffic safety in accordance with the aforementioned methodology. The listed locations are shown in Figure 1.

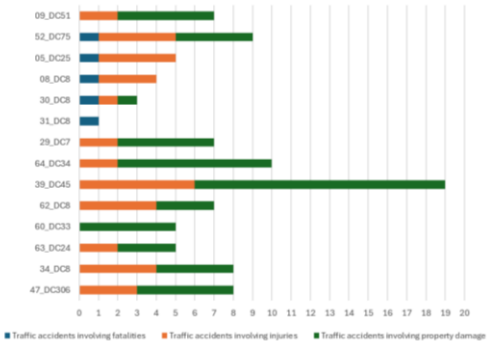


Chart 1. Total number of traffic accidents by severity of consequence

According to records from the Ministry of the Interior, traffic accidents at identified hazardous locations on the state road network in the Republic of Croatia during the observed three-year period vary in frequency and severity depending on the location [3, 4, 5]. Chart 1 shows the total number of traffic accidents by their consequences at these locations. To determine priorities for implementing road traffic safety improvement measures at these sites, the locations were ranked according to the assessed level of hazard. The hazard level was defined based on the number and severity of traffic accidents, traffic volume, and the length of the observed location. The list of hazardous locations ranked by this hazard level is presented in Table 2.

Table 2. List of hazardous locations ranked by hazard level

No.	Location name	Hazard level
1.	05_DC25	1,88
2.	08_DC8	1,78
3.	09_DC51	1,73
4.	29_DC7	1,34
5.	30_DC8	1,34
6.	31_DC8	1,34
7.	34_DC8	1,3
8.	39_DC45	1,19
9.	47_DC306	1,14
10.	52_DC75	1,11
11.	60_DC33	1,07
12.	62_DC8	1,06
13.	63_DC24	1,06
14.	64_DC34	1,06

4. *Remedial Measures for Identified Hazardous Locations on State Roads in the Republic of Croatia*

For the fourteen identified hazardous locations on the state road network, remedial solutions focused on improving road traffic safety and reducing the frequency of traffic accidents. To show which measures were most frequently proposed, they were classified according to specific road condition indicators. These indicators include horizontal and vertical sight distance, geometric road elements, pavement damage, horizontal and vertical traffic control devices, traffic and clearance profile, sidewalks, shoulder, cycle paths, safety barriers, and public lighting [6].

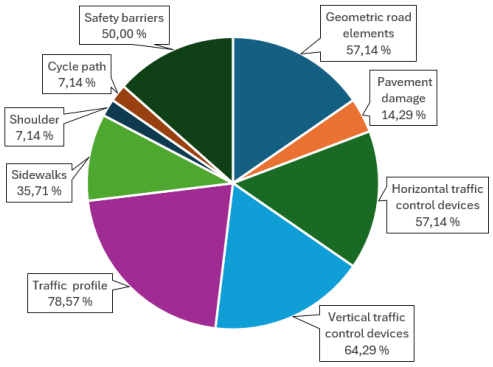


Chart 2. Share of Identified Deficiencies (%)

The analysis of the proposed solutions, presented in Chart 3, shows that the most frequently recommended measures are related to the traffic profile (78.57%), vertical signage (64.29%), horizontal signage (57.14%), and geometric road elements (57.14%). Less frequently proposed measures include safety barriers (50.00%) and sidewalk construction (35.71%), while the smallest share of measures refers to pavement repairs (14.29%), shoulder improvements (7.14%), and bicycle paths (7.14%).

5. *Review of Remediated Identified Hazardous Locations on State Roads in the Republic of Croatia*

Road traffic safety in the Republic of Croatia has been significantly improved through the systematic inspection and remediation of identified hazardous locations on state roads. By analyzing sites with a higher number of traffic accidents, a certified road safety auditor defines remedial measures to reduce risks for all road users. This review covers the interventions implemented, their effectiveness, and their contribution to the overall improvement of safety conditions on state roads, providing insight into a systematic approach to addressing traffic risks.

For traffic accident analysis, a comparative method using three-year periods was applied. The period from 2018 to 2020 represents the baseline condition, while the period from 2023 to 2025 [7,8,9] serves as the evaluation period. To determine the relevant post-implementation safety conditions, location 47_DC306 was analyzed, where all proposed measures were implemented after the hazardous location was identified. Section 47_DC306, previously ranked ninth in terms of hazard level, was successfully remediated through the implementation of the proposed measures.



Figure 2. Comparative view of location 47_DC306 before and after remediation

At the observed location, a sidewalk was constructed, significantly improving pedestrian safety and reducing the risk of conflicts with motor vehicles. In addition, a traffic surveillance camera was installed, enabling continuous monitoring of the traffic situation, contributing to the prevention of traffic violations, and enhancing overall road traffic safety. A comparative view of the site conditions before and after remediation is shown in Figure 2.

6. *Analysis of Traffic Accidents Following the Remediation of Identified Hazardous Locations on State Roads*

The main objective of this study was to determine the impact of the implemented remedial measures on road traffic safety in the observed road section. To achieve this, traffic accident data from before and after the implementation of the remedial measures were compared, with particular emphasis on changes in accident frequency and severity. Chart 2 presents a comparison of the number of traffic accidents by severity of consequences in the periods before and after remediation at location 47_DC306.

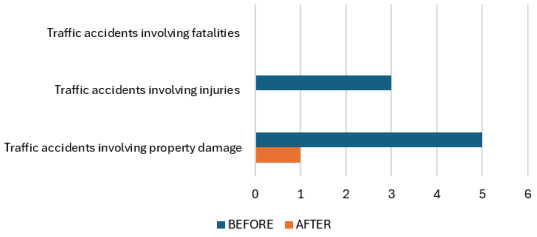


Chart 3. Results of the Before-and-After Analysis at Location 47_DC306

The results show a highly positive trend and improved safety on the observed road section, as the total number of accidents decreased by 87.50%. In the category of traffic accidents involving fatalities, no cases were recorded in either period. The most significant improvement is seen in accidents involving injuries, where the number decreased from three to zero, representing a 100.00% reduction. Additionally, the number of property-damage-only accidents was reduced from five to one, marking an 80.00% decrease, which confirms the high effectiveness of the implemented measures.

7. *Conclusion*

The methodology for identifying hazardous locations on the road network is a systematic process that includes parameter definition, location screening, statistical analysis, and ranking of road sections and intersections with increased numbers of traffic accidents. The analysis involves calculating the traffic accident rate and determining a critical risk level, which enables the identification of locations that require priority safety measures. During the three-year period from 2018 to 2020, fourteen hazardous locations were identified on state roads. A detailed analysis of the identified deficiencies at these locations led to the proposal of remedial measures, primarily related to the traffic profile (78.57%), improvements to vertical (64.29%) and horizontal signage (57.14%), and enhancements of geometric road elements (57.14%). A comparative analysis of the baseline period (2018–2020) and the evaluation period (2023–2025) showed that the proposed remedial measures were successfully implemented at location 47_DC306, including the construction of a sidewalk and the installation of traffic surveillance cameras, resulting in improved safety conditions. The evaluation recorded a 100.00% reduction in traffic accidents involving injured persons and an 80.00% reduction in property-damage-only

accidents, confirming the justification and effectiveness of the implemented remediation.

The identification and remediation of hazardous locations require a systematic and continuous approach, including regular monitoring and evaluation of the effectiveness of implemented measures. Although significant safety improvements have been achieved at certain locations, some road sections still present an elevated safety risk. The results indicate the need for continued research on the remaining identified hazardous locations to ensure the safety of all road users.

8. References

[1] Šarić, Ž. *Model for Identifying Hazardous Locations in the Road Traffic Network*. Doctoral dissertation, University of Zagreb, Faculty of Transport and Traffic Sciences.Hrvatske ceste. *Methodology for the Identification of Hazardous Locations on the Road Traffic Network of the Republic of Croatia*. Zagreb: Hrvatske ceste d.o.o., 2021.

[2] Republic of Croatia, Ministry of the Interior. *Road Traffic Safety Bulletin 2018*, Issue XLV. Zagreb, 2019.

[3] Republic of Croatia, Ministry of the Interior. *Road Traffic Safety Bulletin 2019*, Issue XLVI. Zagreb, 2020.

[4] Republic of Croatia, Ministry of the Interior. *Road Traffic Safety Bulletin 2020*, Issue XLVII. Zagreb, 2021.

[5] Šarić, Ž., Kunštek, A., Kučinić, T., Vuk, I. *Review and Analysis of Traffic Accident Locations Involving Pedestrian Fatalities on County, Local, and Other Non-Classified Roads in the Republic of Croatia*. In: Roads 2025: 49th International Road Conference & Expo, Proceedings of Papers, Plenoria (ed.). Rovinj: Plenoria, 2025, pp. 279–290.

[6] Republic of Croatia, Ministry of the Interior. *Road Traffic Safety Bulletin 2023*, Issue XLX. Zagreb, 2024.

[7] Republic of Croatia, Ministry of the Interior. *Road Traffic Safety Bulletin 2024*, Issue XLX. Zagreb, 2025.

[8] Ministry of the Interior of the Republic of Croatia. *Traffic Accident Data for 2025*. Zagreb: Ministry of the Interior of the Republic of Croatia, 2026.

Determining the use indicators of the wagon vehicle and improving the efficiency of the transportation process

Israil Shukur Oglu Elyazov, Etibar Bakhtiyar Oglu Guliyev
Azerbaijan University of Architecture and Construction, Baku

ABSTRACT. *The primary function of the Azerbaijan Railways wagon fleet is to ensure the transportation process is continuously supplied with serviceable and operational wagons. Given the continuous growth in transit freight volumes along international transport routes passing through our country, Azerbaijan Railways CJSC successfully continues to modernize and expand its wagon fleet to ensure the efficient and safe transportation of goods. To this end, studying the wagon fleet structure, analyzing optimal wagon fleet utilization indicators, and determining the required number of wagon fleets are currently considered pressing issues. Accordingly, determining the structure of wagons within and outside the railway wagon fleet is of particular importance. Accounting for freight wagon fleets is crucial for regulating, standardizing, and utilizing the wagon fleet for its intended purpose in managing rail transport to meet the needs of the national economy for freight and passenger transportation. The operating freight car fleet includes both local cars operated by Azerbaijan Railways CJSC and transit freight cars from abroad located on the tracks of industrial enterprises. Efficient use of the freight car fleet is an important factor influencing the operational performance, cost structure, and service reliability of rail transport systems. This study develops a comprehensive methodological framework for determining the efficiency of the freight car fleet and proposes an integrated performance assessment model. Key performance indicators, including car turnaround time, technical availability, load factor, downtime rate, and daily productivity, are analytically formalized. An integrated performance function is proposed for assessing overall operational efficiency. The results demonstrate that reducing turnaround time, minimizing downtime, increasing technical availability, and implementing digital fleet management systems significantly improve the efficiency of rail freight transportation. The proposed model can be applied to comparative analysis, strategic planning, and optimization of rail crew work at railway enterprises.*

KEY WORDS*: WAGON, WORKING FLEET, BALANCE METHOD, WAGON TURNOVER, MILEAGE, TRIP, TRANSPORTATION, WAGON SHOULDER, TECHNICAL STATION, PRODUCTIVITY, RAILWAY.*

INTRODUCTİON. The existing fleet also includes wagons belonging to other ministries and companies, each with an eight-digit inventory number beginning with 5, belonging to CIS member states, whose access to the common railway network has been authorized by the Directorate of the CIS Railway Transport Council and the railway director for the transportation of freight specified in the declaration within the railway (in suburban service). Accordingly, the structure of changes in the number of wagons belonging to the railway's wagon fleet, the methodical sequential calculation of fleet utilization indicators, and the methodology for calculating the required quantity are distinguished by their relevance [1, 2, 4]:

Research work conducted in the field of wagon management varies in its specifics. It is known that the existing freight wagon fleet on Azerbaijan Railways is modified by the following transport reports:

- new wagons arriving from industrial enterprises, factories, and imported ones;
- wagons arriving from Caspian Sea ferry crossings (Turkmenbashi, Aktau, Kuryk) from the Alyat International Sea Trade Port ferry;
- wagons from the inventory of wagons of CIS member states and the Baltic Republics, as well as wagons of enterprises and organizations of other ministries and departments that have permission to enter the general CIS railway network, and wagons received from Iranian Railways at Julfa station;
- wagons of enterprises and organizations of other ministries and departments that have permission to enter the general CIS railway network in the established manner and that have been accepted from bypass tracks;

At the same time, it can be said that the existing fleet of freight cars on the railway may also be modified by:

- cars decommissioned due to technical condition,
- cars received from Alat, delivered from the International Sea Trade Port of Turkmenbashi, Aktau, and the Kuryk ferry crossing,
- cars from the inventory of the Union member states and the Baltic Republics, owned by enterprises and organizations of other ministries and departments that have, in accordance with the established procedure, permission to enter the common railway network of the CIS, and delivered to the Iranian Railway at the Julfa station,
- freight cars from the inventory of Azerbaijan Railways CJSC on the balance sheet of companies, enterprises, and organizations of other ministries and departments of the Republic of Azerbaijan,
- freight cars delivered to bypass routes, owned by enterprises and organizations of other ministries and departments that have, in accordance with the established procedure, permission to enter the common railway network of the Commonwealth country Independent States.

MAİN PART. The increase in the volume of freight transportation by rail leads to changes in the structure of the wagon fleet and the purchase of new wagons. In connection with this, both the inventory and available fleet of freight wagons on the railway are constantly changing. The inventory and available fleet of freight wagons on the railway always differ. The current fleet of freight wagons is determined for each station, section of the road, railway and the entire railway network of the CIS country. It is known that the initial data for calculating the inventory of freight wagons on the railway by versatility, purpose, type and technical condition are determined on the basis of the main results of the physical inventory in accordance with the numerical records of wagons, conducted in the periods established by the Directorate of the Council of Railway Transport of the Commonwealth of Independent States [10,11]. Regardless of the turnover of wagons, the availability of freight wagons at all stations and railway lines during the reporting period is calculated using the balance method [3], based on the integral efficiency function.

$B = f(N_{in}, N_{to}, N_{ss}, N_{is}) = \mathrm{N_{in}} - \mathrm{N_{to}} - -\mathrm{N_{ss}} + \mathrm{N_{is}}$
(1)

here, N_{to} -is the required fleet size during the planning period; N_{in} - is the number of freight cars in the fleet at the beginning of the planning period; N_{ss} is the number of cars whose service life has expired; and N_{is} -is the number of newly manufactured (accepted into the fleet) cars. At all stations with a daily turnover of 50 or more freight cars, freight car turnover is based on records of the number of received and dispatched freight cars reflected in the company's balance sheet. At all stations with a daily turnover of 50 or fewer cars, turnover is based on data from the locomotive and train movement desk log. In cases where the balance of freight cars at stations does not correspond to the actual availability of freight cars, the section manager, upon submission by the heads of the transportation, statistics, and economic analysis departments, establishes a procedure for recording the actual number of cars and, based on the results, makes a decision to change the balance of freight cars at the station.

Adjustments to the balance of freight cars on section tracks may only be made with the permission of the head of the department of statistics and economic analysis, and on the entire railway, with the permission of the head of the "Directorate of the Council for Railway Transport of the CIS Country."

The movement of all freight cars between railway sections and roads is recorded both by total quantity and by type, categorizing them as empty, loaded, and not included in the working inventory. The functional and structural composition of the existing freight car fleet of Azerbaijan Railways CJSC (ARC CJSC) [6] is primarily divided into two main groups.

1. Freight car fleet operated by CJSC Azerbaijan Railways,
2. Freight car fleet not operated by CJSC Azerbaijan Railways.

According to statistical data for 2025 [7], Table 1 presents the structural composition of the wagon fleet of CJSC Azerbaijan Railways.

The freight car fleet operated by CJSC Azerbaijan Railways includes freight cars from the existing inventory, excluding freight cars leased to companies, organizations, and enterprises of other committees, ministries, and departments located on their sidings and stations, as well as those provided to new sections of the country's railways under construction. Changes in the composition and structure of the freight car fleet at the disposal of the country's railways occur due to changes in the existing car fleet, as well as for the following reasons:

- the provision and return of cars from the inventory car fleet of CIS railways to railways under construction;
- the leasing and transfer of cars to and from the sidings of enterprises, as well as the return of cars from leases.

Freight cars owned by enterprises and organizations of other ministries and departments, with an eight-digit number beginning with 5, and duly authorized to enter the unified interstate network of the CIS, when transferred to a railway under construction, are counted as owned cars assigned to the enterprises' bypasses. When transferring such cars from railways under construction to the general CIS railway network, they are counted as cars arriving from the enterprises' bypasses. The entire fleet of freight cars at the railway's disposal is divided into two main groups:

1. Operating freight car fleet,
2. Non-operating freight car fleet (cars removed from the operating fleet).

Working fleet includes cars on trains assigned to implement the operational freight transportation plan and cars located on the tracks of the railway's marshalling yard. Depending on their technical and operational condition, working fleet cars are divided into two groups: loaded and empty.

Loaded rail cars are further divided into cars for unloading on the track, local freight cars intended for marshalling, and cars leaving the track (transit loaded cars).

Freight cars on the local railway include cars destined for railways under construction, railways in foreign countries, as well as cars destined for railways under construction and railways adjacent to foreign countries.

Table 1 - Freight car fleet of Azerbaijan Railways CJSC [7]

№	Car type	Total number of cars	Including cars from the Nakhchivan ARc	Cars with expired service life	Cars with unexpired service life
A	**General Purpose Cars**	**4944**	**538**	**1700**	**3164**
1.1	Box Cars	807	155	364	443
1.2	Flat Cars	1129	57	396	733
1.3	Gondola Cars	1261	233	261	1000
1.4	Tank Cars	1199	42	211	988
1.5	Isothermal Cars	548	51	468	-
B	**Special-Purpose Cars**	**941**	**32**	**180**	**761**
2.1	Hopper Cars	110	-	10	100
2.2	Dump Cars	64	-	4	60
2.3	Flat Cars with Fittings	228	17	27	201
2.4	Cement Cars	103	3	3	100
2.5	Grain Cars	407	6	107	300
2.6	Transporters	27	4	27	-
2.7	Other Special Cars	2	2	2	-
	General Car FleetThe	5885	570	1880	3925

Transit loaded cars include loaded cars transiting via the Baku-Turkmenbashi, Baku-Aktau, and Baku-Kuryk ferries. Freight cars, snowplow cars, and transport cars, as well as cars equipped for special freight, commercial, and passenger transportation, located at wagon preparation points for transportation, are always accepted as empty cars in the railway's inventory. Cars decommissioned are referred to as non-operational cars. The non-operational cars include the following freight cars:

- technically faulty freight cars,
- freight cars in the railway administration's reserve,

- freight cars used for other railway section operations,
- freight cars intended for sanitary, technical, and special railway section needs.

All railway freight cars held in reserve by Azerbaijan Railways CJSC, as well as cars intended for occasional seasonal agricultural transportation (grain, wheat, and other food products), must be accounted for in accordance with local authorities' decisions. The rules for the placement, storage, issuance and accounting of wagons in reserve of Azerbaijan Railways CJSC are established in a special charter.

Technically defective wagons are freight cars that do not meet the standards and requirements of the Technical Operating Rules, are considered unfit for transport operations due to their technical condition, are unsuitable for storing and protecting the transported cargo, and have been opened and repaired by railway crews or wagon inspectors. All defective wagons in the CIS railway fleet, as well as defective wagons of enterprises and organizations of other ministries, companies, and departments, whose eight-digit number begins with the number 5 and which have received permission to enter the CIS interstate network in accordance with the established procedure, are subject to mandatory numbering.

Freight wagons held in reserve by Azerbaijan Railways Closed Joint-Stock Company, wagons operated for technical and special purposes, and wagons used for other technical purposes, when accepted for repair from the time of issuance of a warning letter on Form VU-23 until the time of issuance of a warning letter on Form VU-36. The group of wagons identified during inventory after repairs (major and depot), but not in service, includes all freight wagons intended for sanitary, special, and utility purposes, as well as wagons used for other technical purposes in the industry.

It is known that the rules for registering the existence, condition, and use of freight wagons are determined by special instructions [12]. According to paragraph 3.7 of these instructions [12], the group of wagons allocated for technical and special needs of railways includes wagons used from the inventory fleet of Azerbaijan Railways CJSC.

Therefore, it is proposed to include the following special cars in the group of all freight cars intended for economic, technical, and special needs on the railway:

- mobile road section workshops and laboratory cars,
- cars used for medical and sanitary needs,
- flat cars and cars for rail welding trains,
- cantilever and overhead railway cranes,
- cars for fire and repair trains,
- cars at road machine stations and diagnostic cars,
- cars for the transportation of raw materials, spare parts, and materials,
- cars for the storage and transportation of refrigerants, compressed gases, oil and petroleum products,
- hopper-dispensers for the transportation of crushed stone and sand from storage warehouses,
- cars used to prevent and eliminate washouts and damage to railway tracks and artificial railway structures (bridges, tunnels, viaducts, overpasses, etc.) as a result of floods and floodwaters,
- cars used for electrification and power generation, locomotive operations, civil engineering, construction and water supply, and other technical and special railway needs. In accordance with the instruction [12], all freight cars intended for economic, sanitary-technical, diagnostic-control and special needs on the Azerbaijan Railways are divided into the following groups of special cars:

1. Cars for medical and sanitary purposes,
2. Flatcars for railway welding trains,
3. Cantilever and bridge railway cranes,
4. Cars for fire and repair trains,
5. Cars at road equipment stations and diagnostic cars,
6. Laboratory cars and mobile workshops of road sections,
7. Cars for the transportation of raw materials, spare parts and materials,
8. Cars for the storage and transportation of refrigerants, compressed gases, oil and petroleum products,
9. Hopper cars (dosing cars) for the transportation of gravel and sand from warehouses,
10. Cars used for the prevention and Elimination of washouts and damage to tracks and artificial structures (bridges, siphons, crossings, tunnels, viaducts, etc.) of railways resulting from floodwaters and inundations.
11. Carriages used for electrification and power generation, locomotive operation, civil engineering, construction and water supply, as well as for other technical and special needs of railways [12, Articles 4-7].

Carriages for technical, economic, and special needs are allocated within limits established by the Chairman of Azerbaijan Railways CJSC. The rules for the use and accounting of such cars are regulated by special provisions and rules. The transfer of cars from the inventory working fleet to the non-working fleet and vice versa is formalized by notification form DU-6. In many cases, cars from the exchange fleet, provided to the railway company in excess of the norm, are regularly included in the working fleet.

The transfer of cars from the operating inventory fleet to the non-operating fleet and vice versa is documented in accordance with relevant regulations and documents. The transfer time is considered to be the time the document is drawn up; for the railway administration's reserve fleet, it is the time the cars are issued; and for the reserve fleet, it is the time the station receives an order from Azerbaijan Railways JSC to release cars from the reserve fleet. Freight car fleet not under the control of Azerbaijan Railways JSC includes:

- cars provided for temporary use to enterprises and organizations of other ministries and departments on leased tracks with the permission of the chairman of Azerbaijan Railways JSC or his first deputy, under contracts, and on leased tracks. Both sides of these cars must be marked with stencils indicating the name of the leasing company (for "Rental," "Urgent Return"), the station, and the route of registration. Inventory of freight car fleet on the Horadiz-Agbend, Barda-Khankendi, and other railways under construction. The primary information for accounting for the availability of freight cars on the railways under construction is the results of a freight car inventory in physical terms. Current freight car availability on the railways under construction is accounted for using the balance sheet method.

The correct selection and application of freight car utilization indicators is considered a key factor in optimizing the transportation process in rail transport. Freight car utilization indicators are determined based on the fleet of cars operating at stations, depots, track sections, and the railway as a whole. In the rolling stock industry, the key quantitative and qualitative indicators of freight car utilization are the number of cars in the fleet and the volume of freight transported by rail, which are managed by the railway station, the railway, and the national rail network as a whole [1, 11]. In basic studies [8, 9] on wagon management based on freight wagon utilization indicators, the following parameters are considered: The average turnaround time of freight wagons on the railway is calculated in days or hours. The average turnaround time of freight wagons (wagon turnover) is taken to be equal to one

period of the average operating time of the freight wagon fleet during transportation, that is, the time required for loading (unloading) and subsequent re-loading (unloading) of a wagon. Thus, the average turnaround time (in days) of freight wagons is calculated by dividing the number of wagons in the existing operational fleet by the number of completed transport operations according to formula (2);

$$T_o = \frac{\sum N_{rp}^v}{\sum U_{dr}} = \frac{\sum N_{rp}^v}{\sum U_{qr} + \sum U_{pr}} \qquad (2)$$

here $\sum N_{rp}^v$ –-is the total inventory of freight cars on a railway. The primary workload of a railway or track section is defined as the sum of loaded cars $\sum U_{pr}$, $\sum U_{qr}$, and loaded cars received from adjacent tracks or railways.

Many researchers [1,5,9] have calculated the average turnaround time of various types of cars according to known rules using a universal method. However, calculating turnaround time, taking into account car travel time, stops at intermediate stations, technical and commercial operations at technical stations, and freight operations, varies in importance. This article uses special formulas to calculate the average car turnaround time, taking these time parameters into account. Thus, the optimal car turnaround time is calculated to ensure train traffic intensity and railway safety.

1. Wagon turnaround time due to movement is the number of hours wagons spend en route, divided by the time spent in operation, minus the time spent at intermediate railway stations:

$$T_{dov} = \frac{\sum NT_{dv}}{\sum U_{ps}} = \frac{\sum NT_{dv}}{\sum U_{gr} + \sum U_{pr}}, \qquad (3)$$

here, $\sum NT_{dv}$ -is the travel time along the track sections,

2. The turnaround time of wagons depending on the intermediate stations is determined by dividing the wagon-hours during which freight wagons are parked at intermediate railway stations by the wagon operating time,

$$T_{fot} = \frac{\sum N_r}{\sum U_{rv}} = \frac{\sum NT_{ft}}{\sum U_{gr} + \sum U_{pr}}, \qquad (4)$$

here, $\sum NT_{ft}$ - is the time freight wagons spend at intermediate railway stations.

3. Car turnaround time depending on technical stations – by dividing the car-hours during which transit freight cars are idle for work:

$$T_{tor} = \frac{\sum N_r}{\sum U_{tv}} = \frac{\sum NT_{tr}}{\sum U_{gr} + \sum U_{pr}}, \qquad (5)$$

here, $\sum NT_{tr}$ -is the time during which transit cars are idle for work,

4. Car turnaround time for freight operations – by dividing the car-hours during which freight cars are idle for work:

$$T_{gor} = \frac{\sum NT_{gr}}{\sum U_{pv}} = \frac{\sum NT_{gr}}{\sum U_{gr} + \sum U_{pr}}, \qquad (6)$$

here, $\sum NT_{gr}$ - is the time during which the cars are idle under freight handling

Thus, in general, the average car turnaround time can be calculated as follows, taking into account the main characteristics of the cars during freight transportation

$$\theta_{dov} = T_{dov} + T_{fot} + T_{tor} + T_{gor} \qquad (7)$$

The main operational and performance indicator of a railway is labour productivity. Therefore, one of the key performance indicators of a railway is the productivity of wagons, which is determined by the daily freight turnover per wagon of the entire rolling stock in operation. The average daily productivity of freight wagons on a railway shows the average volume of work performed by one wagon in the operational fleet and is defined in net km [9]. This indicator is determined by dividing the net km of wagon fleet operation by the average daily working time of freight wagons in the fleet and multiplying by the number of working days in the reporting period. Therefore, one of the main performance indicators of a rolling stock fleet is the productivity of wagons, which is determined by the daily freight turnover (in ton km net) per wagon of the entire rolling stock in operation [9]. The average daily productivity of freight cars shows the average volume of work performed by one car in the operating fleet and is measured in net tonne-kilometers. This indicator is determined by dividing the net tonne-kilometer of car fleet operation by the average daily operating time of freight cars in the fleet and multiplying by the number of working days in the reporting period:

$$W_v = \frac{\sum(PL)_n}{\sum N_{rb}^g \cdot T}, \qquad (8)$$

hhere, $\sum(PL)_n$–is the freight turnover for the reporting period, called the net tonne-kilometer volume of rail transportation or road operation, and T is the number of working days in the reporting period.

When calculating technical and economic indicators, static and dynamic car loading are distinguished. As is well known, the average dynamic load of a freight car is the mass of cargo transported by the rolling stock on the road during its entire service life, expressed in tons. Thus, the average dynamic load of a freight car in an inventory fleet can be calculated by dividing the net ton-kilometer of road service by the total number of car-kilometers of the freight car fleet in operation [12, pp. 3-5]:

$$Q_{rb} = \frac{\sum(PL)_n}{\sum N^g \cdot S} \qquad (9)$$

here, $\sum N^g \cdot S$ is the total mileage of freight cars in the operating fleet, called a car-kilometer.

The average dynamic load per loaded car, which is considered one of the key operational indicators of a railway, is determined by dividing the operational ton-kilometer of loaded cars in the rolling stock by car-kilometers

$$Q_{qr} = \frac{\sum(PL)_n}{\sum N_{qr} \cdot S}, \qquad (10)$$

here $\sum N_{qr} \cdot S$ -is the mileage of loaded cars in the operating rolling stock of the railway in car-kilometers.

One of the key quantitative indicators of the transportation process is the average daily mileage of a freight car. The average daily mileage of a freight car is the distance traveled by a freight car in the operating fleet over a reporting period (year, quarter, month, week, and day). Thus, the average daily mileage of a freight car is determined by dividing the total mileage of freight cars in the operating fleet by the number of freight cars in the operating fleet and multiplying by the number of days in the reporting period [12, pp. 4-6]:

$$S_v = \frac{\sum N^g \cdot S}{\sum N_{rb}^g \cdot T}, \qquad (11)$$

Technical operations are primarily performed at divisional and marshalling yards. Therefore, such stations are called technical stations, and the movement of cars in this area is determined by a car section or car leg. The average distance between service stations (car sections) is called the average mileage of a freight car in the operating depot between adjacent service operations. The average mileage between service stations is calculated by dividing the car-km traveled by all freight cars in the operating depot by the number of empty transit cars from other lines:

$$L_v = \frac{\sum N^g \cdot S}{\sum N_{tr}}, \qquad (12)$$

here, $\sum N_{tr}$ - is the total number of transit freight cars from other railways.

The loaded and empty trips of freight cars in a fleet are different. As is well known, a freight car's empty trip is equal to the average distance traveled by a freight car during one complete transportation cycle in the operating fleet, that is, during the car changeover period (in both loaded and empty operations). Thus, a freight car's empty trip is determined by dividing the total mileage of freight cars in the operating fleet in car-km by the railroad's car work:

$$R_{pr} = \frac{\sum N^{g} \cdot S}{\sum U_{op}} = \frac{\sum N^{g} \cdot s}{\sum U_{gr} + \sum U_{pr}}, \quad (13)$$

It is known that the loaded trip of a wagon is the average mileage of a loaded wagon over the entire period of its movement, which is included in the total mileage of the loaded wagon. This indicator is calculated by dividing the mileage of loaded wagons in the operating wagon fleet in transport kilometers by the volume of work performed by the wagon fleet:

$$R_{gr} = \frac{\sum N^{g} \cdot S}{\sum U_{gp}} = \frac{\sum N_{gr} \cdot S}{\sum U_{gr} + \sum U_{pr}}, \quad (14)$$

Table 2 *- Key indicators of freight wagon utilization on the railway network of Azerbaijan Railways CJSC*

№	Indicator Name	Unit	2024 year	2025 year
1	Freight Car Turnover	day	6,5	7,2
2	Average Daily Mileage	km	286	294
3	Average Daily Useful Mileage	km	186	196
4	Static Load	ton	52,4	53,5
5	Dynamic Load of a Working Car	ton	34,5	34,9
6	Dynamic Load of a Loaded Car	ton	54,4	55,7
7	Average Daily Productivity*	ton·km netto	8345	8452

Technical work (inspection, technical commercial inspection, etc.) on wagons is performed at technical stations. Operations such as commercial inspection, inspection, and diagnostic testing of wagons, carried out at the technical station, increase the travel time of wagons, both loaded and fully loaded, which leads to a change in wagon turnover [5, 8].

Following these reports, the required number of freight wagons can be calculated by multiplying the number of loaded wagons per day by the type of rolling stock and the wagon turnover θv:

$$N_{po} = \sum_{i=1}^{n} \left(U_{qr}^{i} \cdot \theta_{в} \right), \quad (15)$$

Currently, the technical and operational indicators for the utilization of the freight wagon fleet of Azerbaijan Railways are calculated using the formulas (1-15) given above. The values obtained by calculating the indicators of rolling stock utilization on the Azerbaijan Railways using formulas (1-15) given in the article are presented in Table 2. Thus, a comparative analysis of the obtained values of rolling stock utilization indicators over the past years requires updating the rolling stock structure and acquiring new freight cars, which allows for an increase in the volume and efficiency of transportation processes in the railway transport of the Republic of Azerbaijan.

CONCLUSİONS. This article examines the freight car fleet structure and the technical performance characteristics of both those operated by Azerbaijan Railways CJSC and those not operated by it, and determines the optimal composition of operational and non-operational cars based on the freight transportation process.

This article systematizes the structure and composition of the entire freight car fleet operated by Azerbaijan Railways CJSC and presents the key functional characteristics of freight cars operating on the country's railways and transit cars from abroad traveling on the railways.

To improve the efficiency of transportation processes in the freight car fleet of Azerbaijan Railways CJSC, a methodology for calculating car fleet utilization indicators has been developed. A formula has been adopted for determining the required number of cars in the fleet based on car fleet utilization indicators. This methodology for selecting freight car fleet utilization indicators will enhance the role of the car fleet in the transportation process, while ensuring the safety and efficiency of freight transportation.

REFERENCES

1. Wagon economy: Textbook / Ustich, I.I. Khaba, V.A. Ivashov, et al.; edited by P.A. Ustich. - M .: Marshurut, 2003.-560 p.
2. Lapshin V.F., Orlov M.V. Fundamentals of technical maintenance of wagons: a trai-ning manual. Ekaterinburg: Ural State Uni-versity of Railway Transport, 2006, 375 p.
3. Gursky, E. P. Multifactor model for calculating the required fleet of freight cars / Bulletin of BelGUT. - 2007. - No. 1-2. - P. 90-94
4. Treshina, N.P. Economics of railway transport / N.P. Crack, B.M. Lapidis, M.F. Trikhinkov. -M.: UMK, Ministry of Railways of Russia, 2011,-597 p
5. Anikeeva-Naumenko L. O. Methods for Improving the Efficiency of Freight Car Use in Rail Transport. Author's dis. for Cand. Sci. (Econ.), Moscow, MGUPS (MIIT) – 2014, 24 p. Defended on 14.05.2014
6. "State Program for the Development of the Railway Transport System of the Republic of Azerbaijan in 2010-2014" Order No. 1002, Baku, July 6
7. Azerbaijan Railways CJSC: Baku 2025, www.railway.gov.az
8. Carriages. Fundamentals of design and exami-nation of technical solution / edited by V. N. Ko-turanova. – Moscow : Marshrut. – 2004. – 490 p. – ISBN 5-89035-256-3
9. Improving the structure of the wagon fleet. Railway transport and technology: Collection of works of the Scientific and Practical Conference, Issue 1 (256): Ural State University of Railway Transport, October 29-30, 2023. Yekaterinburg, Russia, 2024. Articles 17-19.
https://council.usurt.ru/b/rtt-7ex-mme-wsy
10. Elyazov I.Sh., Hasanli E.H., Hasratova L.M. Railways, Textbook. "Cooperation" editi. Baku 2014. 504 p.
11. Elyazov I.Sh, Bagirov B.I., Huseynov I.D., Nazarov A.A., Abdullayev R.R. Railway transport vehicles //Textbook for technical higher schools. Baku: 2023,–324p.
https://www.research-gate.net/publi-cation/376981431_DMIR-YOL_NQLIYYATI-NIN_HRKT_VASITLRI

12. Instructions for recording the availability, condition and use of freight cars (Approved by the Ministry of Railways of the Russian Federation dated 03.08. 2000. No. CD-TsChU/771).

INFORMATİON ABOUT THE AUTHORS

1. **Elyazov Israil Shukur ogly**
Azerbaijan University of Architecture and Construction, Baku,
Department of Transport and Logistics
Candidate of Technical Sciences,
Associate Professor,
e-mail: elyazov1962@mail.ru
https://orcid.org/0000-0002-7690-9996

2. Guliyev Etibar Baktiyar oglu
Azerbaijan University of Architecture and Construction, Baku,
Department “Transport and Logistics”
Candidate of Technical Sciences,
Associate Professor,
e-mail: etibar.guliyev@azmiu.edu.az
https://orcid.org/0000-0001-9512-4599

Simulation Modeling of Vehicle Passage Over a Road Irregularity for Forensic Accident Reconstruction

Svilen Stefanov, Tihomir Yotkov, Yoana Kotseva
National Military University "Vasil Levski" Veliko Tarnovo, Bulgaria
tyotkov@gmail.com, joneyjoney@abv.bg

***Abstract**: A planar dynamic model of a vehicle is proposed, incorporating a radial-spring tire model that accounts for the longitudinal component of the elastic force arising from tire deformation. The model enables the analysis of vehicle response when either the left or right wheels encounter a road irregularity, thereby allowing the assessment of its impact on handling and stability. Although relatively simple, the proposed model provides sufficient accuracy for applications in car accident reconstruction. The model has been validated and has been applied to an actual road situation.*

***Keywords**: CAR ACCIDENT RECONSTRUCTION, VEHICLE DYNAMICS SIMULATION, RADIAL-SPRING TIRE MODEL, ROAD IRREGULARITY*

1. Introduction

In the field of forensic accident reconstruction, technical evaluations frequently require investigating how a vehicle's negotiation of a specific road irregularity impacts its handling and directional stability. While analytical studies of obstacle negotiation can employ simulation models of varying fidelity, deploying high-precision finite element methods (FEM) or multi-body systems with numerous degrees of freedom within standard automotive expert assessments is generally impractical, as the required computational time, costs, and specialized expertise disproportionately exceed the scope of the investigation. To address this, this paper proposes and implements a planar, pitch-plane dynamic vehicle model integrated with a radial tire stiffness model. This formulation enables the analysis of either the left or right track of the vehicle as it encounters road irregularities.

2. Dynamic Model

In classical ride comfort models, the wheel-to-road contact is simplified to a single point, and the elastic force generated by the tire is assumed to have only a vertical component. This approach precludes the possibility of accounting for the tire's influence on the vehicle's longitudinal dynamics. In this paper, a radial spring model is proposed to simulate the tire-road interaction (Fig. 1b). The overall dynamic model of the vehicle is illustrated in Fig. 1a.

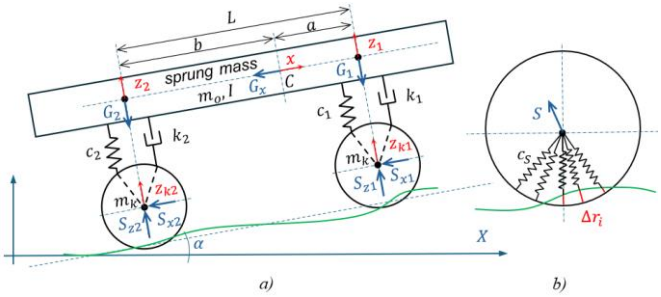


Fig. 1.

The model is governed by the following differential equations:

$$m\ddot{x} = \sum F_{xi} + S_{x1} + S_{x2}$$

$$\frac{m_o b^2 + I}{L^2}\ddot{z}_1 = \frac{m_o ab - I}{L^2}\ddot{z}_2 - c_1(z_1 - z_{k1}) - k_1(\dot{z}_1 - \dot{z}_{k1}) - G_1$$

$$\frac{m_o a^2 + I}{L^2}\ddot{z}_2 = \frac{m_o ab - I}{L^2}\ddot{z}_1 - c_2(z_2 - z_{k2}) - k_1(\dot{z}_2 - \dot{z}_{k2}) - G_2$$

$$m_k\ddot{z}_{k1} = S_{z1} - c_1(z_{k1} - z_1) - k_1(\dot{z}_{k1} - \dot{z}_1) - G_k \qquad (1)$$

$$m_k\ddot{z}_{k2} = S_{z2} - c_2(z_{k2} - z_2) - k_2(\dot{z}_{k2} - \dot{z}_2) - G_k$$

The ride dynamics equations are derived using the Lagrange method. The generalized coordinates chosen for the system are the vehicle's longitudinal displacement x, the vertical displacements of the sprung mass at the front and rear locations z_1, z_2, and the vertical displacements of the wheels (unsprung masses) z_{k1}, z_{k2}. The following notations are used:

L – wheelbase of the vehicle;
a – distance from the front axle to the center of gravity (CG);
b – distance from the rear axle to the CG;
m – total mass (vehicle curb mass and passengers);
m_k – unsprung mass of a wheel assembly;
m_o – half of the sprung mass (chassis and passengers);
I – mass moment of inertia of the vehicle about the lateral y-axis;
c_1, c_2 – stiffness coefficients of the front and rear suspension;
k_1, k_2 – damping coefficients of the front and rear suspension.

G_1, G_2, and G_k denote the projections of the gravitational forces along the local z-axis acting on the front sprung mass, rear sprung mass, and wheel assembly, respectively. They are used to determine the positions of the model elements under static equilibrium conditions. $S_{x1}, S_{z1}, S_{x2}, S_{z2}$ represent the components of the tire elastic forces S_1 and S_2 projected onto the axes of the local coordinate system for the front and rear tires. To determine these elastic forces, a radial tire model formulation inspired by [1] was adopted; however, an alternative implementation methodology is proposed here. The core concept is formulated as follows: the circumference of the wheel is discretized into sectors defined by a predefined central angle. The peripheral arc of each sector is assumed to act as a rigid tread segment connected radially to the wheel hub via an independent spring element. Under the action of the gravitational load acting at the wheel hub, the tire is pressed against the road surface, causing the spring elements within the contact patch zone to compress. This compression generates radial elastic forces. The total elastic force exerted by the tire is the vector sum of the forces produced by all compressed radial springs:

$$\vec{S} = \sum_{i=1}^{n} C_i\overrightarrow{\Delta r_i}, \qquad (2)$$

where:

C_i – stiffness coefficient of the i-th radial spring element;
n – total number of compressed spring elements within the contact patch;
$\overrightarrow{\Delta r_i}$ – radial deflection (compression) of the of the i-th spring.

Assuming a perfectly flat, horizontal road profile and a symmetrical distribution of the radial springs relative to the center of the tire-road contact patch, the resultant elastic force will act strictly along the vertical axis, yielding a zero longitudinal force component. In this context, a "flat" profile denotes the absence of local geometric irregularities, while "horizontal" implies a zero longitudinal road gradient. Conversely, the presence of a road irregularity within the contact patch induces non-uniform deflection among the individual radial springs. This non-uniformity alters both the magnitude and the line of action (direction) of the resultant tire force. In the event of wheel lift (loss of tire-road contact), the force $\vec{S}$ drops to zero.

To effectively implement this wheel model, two distinct computational tasks must be resolved:

- determination of the compression magnitude of the individual springs ($\overrightarrow{\Delta r_i}$) during tire-road interaction;

- determination of the stiffness coefficient C_i of the individual springs in the spokes.

An approach based on similar triangles was proposed in [1] to resolve the first task. While this allows for a highly simplified mathematical framework and performs adequately for roads with smoothly varying profile elevations, it introduces significant errors in the presence of sharper (e.g., step-like) irregularities. To eliminate these inaccuracies, the authors propose an alternative methodology. The road profile is approximated by a set of line segments defined by the coordinates of their endpoints. Concurrently, the position of the wheel hub is obtained in coordinate form as a direct solution of the system of differential equations (1). The peripheral coordinates of each radial spring element can be determined via the wheel radius r_k and its respective angular position. The coordinates of the intersection point between a given spring element and a road segment are then obtained by solving the parametric equations of a line:

$$\begin{aligned} x_{p1j} + t_{pj}\left(x_{p2j} - x_{p1j}\right) &= x_{ok} + t_{si}(x_{s2i} - x_{ok}) \\ z_{p1j} + t_{pj}\left(z_{p2j} - z_{p1j}\right) &= z_{ok} + t_{si}(z_{s2i} - z_{ok}) \end{aligned} \quad (3)$$

where:

x_{p1j}, z_{p1j} – coordinates of the starting point of the j-th road segment;

x_{p2j}, z_{p2j} – coordinates of the endpoint of the j-th road segment;

x_{ok}, z_{ok} – coordinates of the wheel axle center;

x_{s2i}, z_{s2i} – coordinates of the peripheral point of the i-th radial spring in its uncompressed state

The system of algebraic equations is solved with respect to the parameters t_{pj} and t_{si}. For an intersection point to exist between the j-th road segment and the i-th radial spring, the conditions ($0 \leq t_{pj} < 1$) and ($0 \leq t_{si} < 1$) must be satisfied simultaneously. In this case, the coordinates of the intersection point are determined by the parametric equation of the line collinear with the spring element, which subsequently yields both the magnitude and the direction of its compression.

To resolve the second task, it is assumed that all radial springs of the wheel share an identical stiffness coefficient C_s. Consequently, Equation (2) takes the following form:

$$\vec{S} = C_s \sum_{i=1}^{n} \overrightarrow{\Delta r_i} \quad (4)$$

Under static equilibrium, the elastic force S must balance the gravitational force acting on the wheel assembly G_k, from which it is obtained

$$C_s = {G_k}\Big/{\sum_{i=1}^{n} \Delta r_i} \quad (5)$$

This expression indicates that the stiffness coefficient of a single radial spring, C_s, is determined by the compression of the springs under static wheel conditions.

The overall tire stiffness coefficient depends on a multitude of factors (such as tire inflation pressure, temperature, tire construction, and material properties, etc.) and is conventionally determined through experimental testing. Knowing this coefficient, the static deflection of the wheel axle can be readily determined:

$$\Delta r_{ok} = {G_k}\Big/{C_t}, \quad (6)$$

where C_t is the overall tire stiffness coefficient.

The total deflection of the springs under static conditions is determined by means of a numerical experiment. The wheel is positioned above a flat, horizontal road surface at a distance $r_k - \Delta r_{ok}$, after which the deflections of the individual radial springs are calculated using the methodology described above. The accumulated result is then substituted into Eq. (5) to explicitly compute the stiffness coefficient of a single radial spring.

It is well known that tire stiffness varies significantly under larger deformations. Various methodologies exist to model this non-linear behavior. In this study, the approach described in [4] was adopted, wherein the stiffness coefficient increases tenfold once the deformation exceeds 80% of the tire section height (sidewall height). If the deformation exceeds the total section height-corresponding to a rim-strike- a logical condition is triggered to terminate the simulation.

This wheel model lacks the damping element in classical ride comfort models. Omission stems from the fact that the described radial wheel model effectively operates under quasi-static conditions, serving solely to determine the magnitude and direction of the resultant elastic force for a given wheel position. Subsequently, the projections of this force along the axes of the moving coordinate system, attached to the vehicle's center of gravity (CG), are utilized as input data to solve the system of differential equations (1). This formulation precludes the assumption inherent in classical ride comfort models—namely, that the vehicle is initially in a state of static equilibrium with gravitational and elastic forces perfectly balanced. Consequently, at the initiation of the simulation ($t = 0$), the vehicle must be positioned on a flat, horizontal road segment, allowing it to dynamically settle into its equilibrium state during the integration of the differential equations.

It must be noted that the coordinates of both the road profile and the wheel must be defined within an inertial coordinate system to properly determine the deflection of the individual radial springs. Consequently, the calculated force projections are also initially obtained in this inertial frame. Therefore, the resultant tire force must be transformed into the moving (body-fixed) coordinate system before being incorporated into the differential equations.

When accounting for road irregularities, the road grade must be defined in a specific manner. The pitch angle of the chassis cannot be used for this purpose, as it inherently encompasses the road grade, the transient effects of local road irregularities, and the vehicle body dynamics. However, once the coordinates of the contact points between the radial springs of each wheel and the road segments are determined via the aforementioned methodology, it becomes possible to establish an equivalent road grade using these data points. For instance, by selecting the nominal vertical spring positioned directly beneath the axis of each wheel, the slope of the straight line connecting their respective road contact points can be computed. This value corresponds to the equivalent grade of a virtual flat road profile over which the vehicle is traversing at that specific time step.

3. Validation and Application of the Model

The described model is solved numerically within the MATLAB computational environment. To verify the fidelity of the proposed framework, model validation was performed using data presented in [4]. A simulation was conducted to replicate an Acura (Honda) 3.2TL passenger car traversing a road irregularity with a length of 60 cm and a depth of 24 cm at a constant speed of 32 km/h, capturing the responses of both the front and rear wheels. Fig. 2a illustrates the vertical wheel forces (tire loads) obtained from the cited literature, while Fig. 2b presents the plots for the same quantities derived from the proposed model.

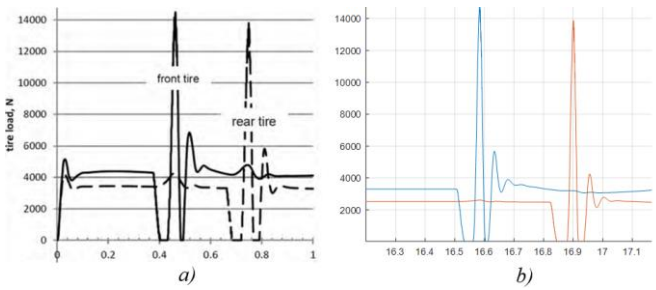


Fig. 2.

The model was applied to address the requirements of an actual accident reconstruction, which aimed to determine whether a Volkswagen Caddy traversing a road irregularity with a length of 60 cm and a depth of 6 cm could induce a deviation in the vehicle's

directional path and a subsequent loss of control. In this specific case, the parameters of the model are defined as follows:

- $L = 2{,}68\ m$;
- $a = 1{,}18\ m$;
- $b = 1{,}50\ m$;
- $m = 1770\ kg$;
- $m_k = 20\ kg$;
- $m_o = 845\ kg$
- $I = 2800\ kgm^2$;
- $c_1 = 29.10^3\ N/m, c_2 = 18.10^3\ N/m$;
- $k_1 = 25.10^2\ Ns/m, k_2 = 18.10^2\ Ns/m$.

The tires fitted to the vehicle are of size 195/65 R15, with a sidewall height of 0.127 m. It is assumed that prior to encountering the road irregularity, the vehicle is in a state of uniform motion and $\sum F_{xi} = 0$ (the driver maintains equilibrium between the driving force and the total aerodynamic and rolling resistance forces).

The road profile is approximated by a sequence of line segments defined by the coordinates of their respective endpoints. A local irregularity with a depth of 6 cm and a length of 60 cm is superimposed onto an otherwise flat road profile.

The model was solved for various vehicle speeds. Fig. 3 illustrates the simulation results obtained when traversing the road irregularity at a constant speed of 100 km/h.

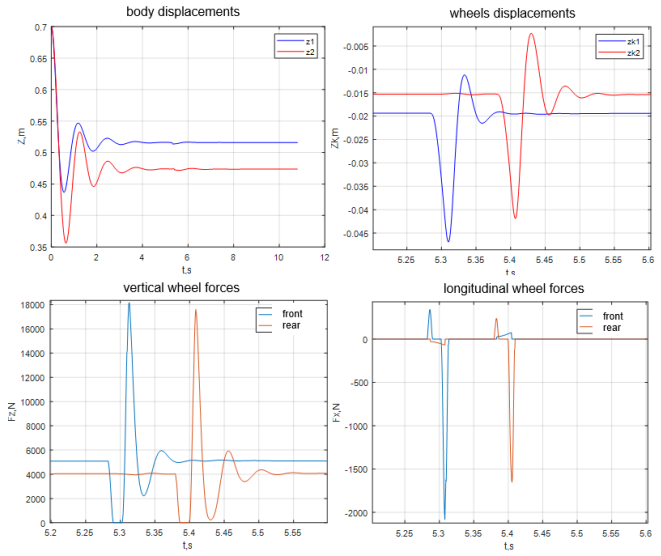


Fig. 3. *Simulation results at a vehicle speed of 100 km/h*

The "body displacements" plot illustrates the vertical displacements of the front and rear sections of the sprung mass across the entire simulation time interval. At the initiation of the interval, a distinct transient response is observed, representing the dynamic convergence of the system toward its static equilibrium state. The displacements resulting from traversing the road irregularity are marginal—approximately 2 millimeters. The displacement of the front section initiates at 5.3 seconds, followed shortly thereafter by that of the rear section.

The "wheels displacements" plot reveals that axle center of the front wheel assembly shifts downward upon encountering the road irregularity, reaching a maximum displacement of 2.8 centimeters. Upon exiting the irregularity, the axle exhibits a rebound phase, ascending up to 8 millimeters above its nominal static equilibrium baseline. A similar, albeit time-delayed, displacement response is observed for the axle center of the rear wheel assembly.

The "vertical wheel forces" plot is of critical importance. It demonstrates that the vertical force of the front wheel drops to zero within the time interval of 5.29–5.3 s, corresponding to a duration of 0.01 s. The initiation of this interval coincides with the wheel traversing the leading edge of the road irregularity, while its termination is marked by the tire establishing contact with the trailing edge. Following this initial impact with the trailing edge, the dynamic reaction escalates to a peak value of 18 kN. Subsequently, during the rebound phase where the wheel shifts upward driven by the stored potential energy, the force decreases to just over 2 kN, though contact with the road surface is continuously maintained. The transient process completely stabilizes 0.22 seconds after the onset of the force reduction, with the vertical reaction returning to its static equilibrium value.

The "longitudinal wheel forces" plot reveals that the horizontal component of the elastic force acting on the wheel hub transiently reaches a value of 2.1 kN. This force escalates from zero to its peak and subsequently attenuates back to zero within a brief duration of 0.03 seconds.

Fig. 4 illustrates the road profile alongside three distinct positions of the front wheel with its radial spring elements. The darkened zones highlight the compressed springs. The line extending upward from the wheel hub center represents both the magnitude and direction of the resultant elastic force vector. It is evident that the tire does not reach the bottom of the road irregularity during the traversal.

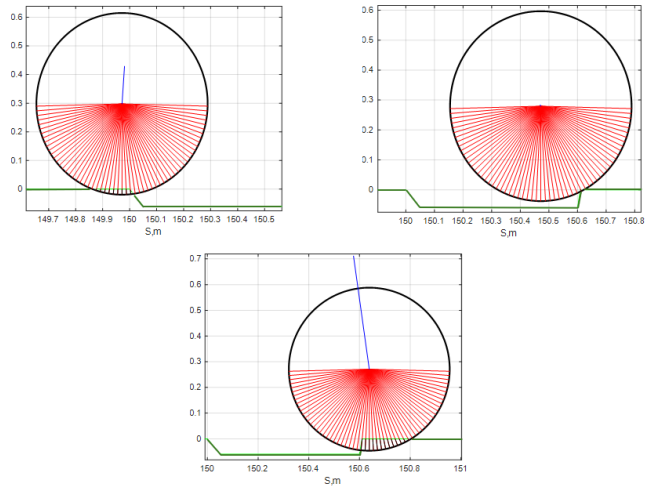


Fig. 4.

Fig. 5 illustrates the simulation results obtained when traversing the road irregularity at a speed of 70 km/h, while Fig. 6 presents the corresponding results at a speed of 40 km/h.

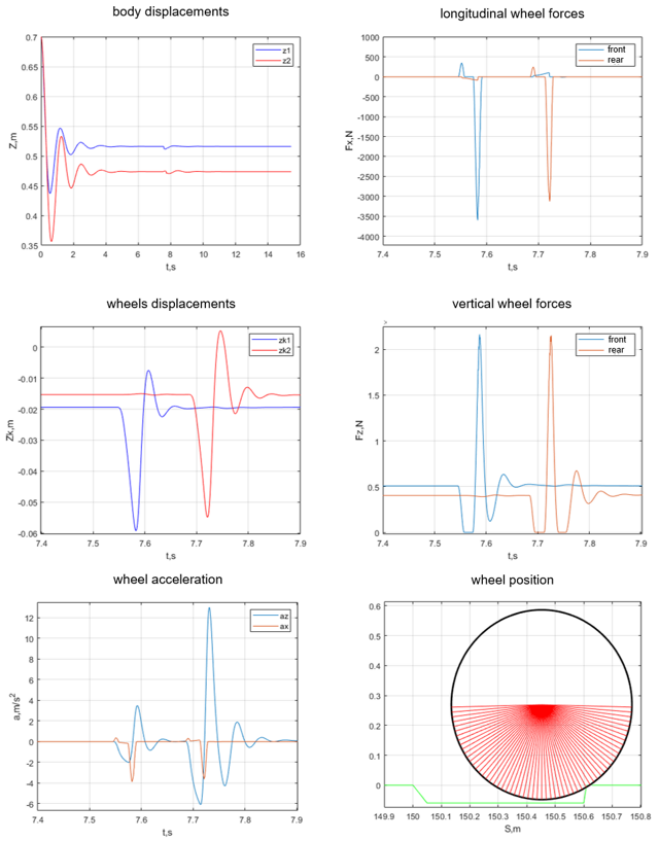


Fig. 5. *Simulation results at a vehicle speed of 70 km/h*

In the former case, the tire does not reach the bottom of the road irregularity, whereas in the latter case, it does. At both speeds, upon exiting the irregularity, the rear tire experiences a brief rebound phase, causing the vertical dynamic reaction to diminish to zero for a transient duration of less than 0.02 seconds; however, the front tire maintains uninterrupted contact with the road surface.

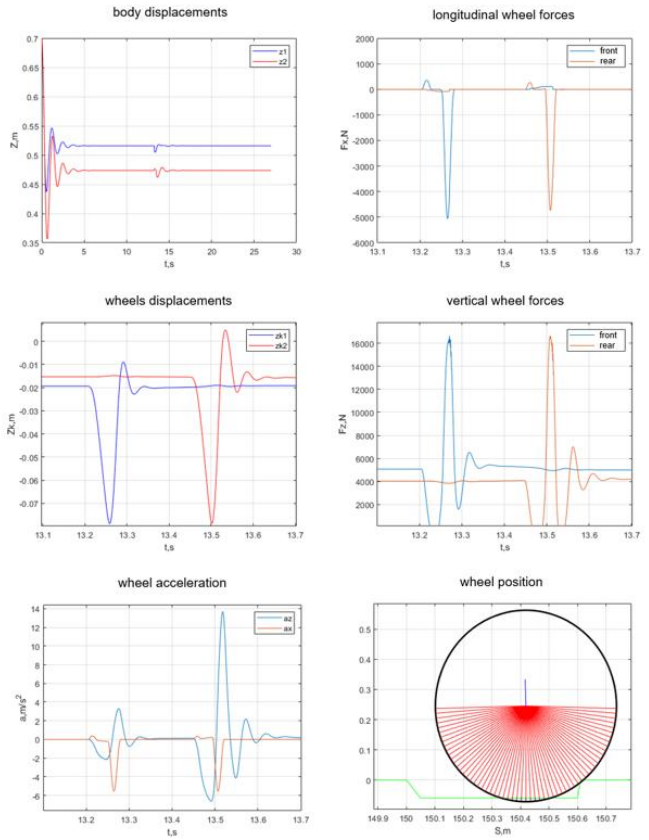


Fig. 6. *Simulation results at a vehicle speed of 40 km/h*

It is evident that the horizontal component of the elastic force increases as the vehicle speed decreases, reaching approximately 5 kN at a speed of 40 km/h.

Based on the results of the analytical investigation, it is concluded that traversing the road irregularity at speeds between 70 and 100 km/h induces neither a deviation in the vehicle's directional path nor a loss of control by the driver. This finding has been further validated through experimental testing.

4. Conclusion

The proposed vehicle model enables the investigation of the front and rear wheels on either the left or right side traversing a road irregularity, establishing how such events affect vehicle handling and directional stability. Although relatively simple, the model provides sufficient accuracy required for forensic accident reconstruction. It has been validated against experimental data published in peer-reviewed literature and successfully applied to a real-world traffic scenario to address specific technical objectives within a forensic investigation.

References:

1. Davis, D. C. (1975). A Radial-Spring Terrain-Enveloping Tire Model. *Vehicle System Dynamics: International Journal of Vehicle Mechanics and Mobility*, 55-69
2. Day, T. D. (2005). Simulation of Tire Interaction with Curbs and Irregular Terrain. *Engineering, Environmental Science*
3. Jazar, R. N. (2008). *Vehicle Dynamics: Theory and Application.* New York: Springer
4. Metz, L. D., & Sneddon, J. (2015). Vehicle Dynamics Simulation Associated with Pothole Encounters Using the HVE SIMON Program and Radial Spring Tire Model. *SAE Technical Paper 2015-01-1572*
5. Rudny, D. F., & Sallmann, D. W. (1996). Analysis of Accidents Involving Alleged Road Surface Defects (i.e., Shoulder Drop-offs,Loose Gravel, Bumps and Potholes). *SAE Technical Paper 960654*.

Development of a methodology for improving the performance of diesel engines using the acoustic emission method

Viktor Prokopenko[1], Maris Hauka[2], Juris Gutans[3], Guntis Strautmanis [4], Leonid Vinogradov[5],
Institute of Machine Building, Aerospace Technology and Transport of Riga Technical University, Riga, Latvia[1, 2, 3, 4, 5]
E-mail: viktors.prokopenko@rtu.lv, Maris.Hauka@rtu.lv, Juris.Gutans@rtu.lv, Julija.Soldatova@rtu.lv, leonids.vinogradovs@rtu.lv

Abstract: *The main concept concerns the application of the acoustic emission (AE) method to develop a methodology for real-time monitoring and diagnosis of the technical condition of diesel engines, which will reduce the time required for repair and maintenance. The investigation of new signal-processing tools is one of the most topical research areas in the contemporary signal-processing community. The approach adopted is consistent with acoustic emission methods, in which the principal diagnostic parameter is the temporal evolution of event intensity, including analysis of the slope of the cumulative-event curve. The practical application of the results of this study will help optimize diesel-engine monitoring and maintenance while simultaneously reducing the associated costs. AE-based monitoring can serve as an effective diagnostic and prognostic tool, improving safety, energy efficiency, and environmental performance. In the study, AE sensors were installed at specified locations on the engine, and AE signals were recorded using two different AE systems. The results were analyzed to determine the sources of the AE signals.*
KEYWORDS*: ACOUSTIC EMISSION METHOD, INTERNAL COMBUSTION ENGINE, MONITORING, DIAGNOSTICS OF TECHNICAL CONDITION, DEFECT.*

1. Introduction

This article is devoted to the development of structural operation management based on the results obtained from continuous and periodic monitoring systems using the acoustic emission (AE) method. The primary purpose of stationary and periodic structural monitoring systems is not only parameter control but also the diagnosis of defective states. The most important function of such systems is to organize condition-based structural operation management. Formulating this objective for the application of monitoring systems enables service and repair costs to be minimized without reducing the reliability of structural operation.[1]
Although the purpose of a condition-based structural operation management system appears straightforward, its practical implementation requires the solution of a number of tasks, among which the following may be distinguished:
Ensuring effective and reliable monitoring of the current technical condition; for this purpose, the monitored equipment must be equipped with monitoring and rapid diagnostic tools.
The main concept concerns the application of the acoustic emission method to develop a methodology for real-time monitoring and diagnosis of the technical condition of diesel engines, which will reduce the time required for repair and maintenance.[2] The investigation of new signal-processing tools is one of the most topical research areas in the contemporary signal-processing community. The approach adopted is consistent with acoustic emission methods, in which the principal diagnostic parameter is the temporal evolution of event intensity, including analysis of the slope of the cumulative-event curve. The practical application of the results of this study will help optimize diesel-engine monitoring and maintenance while simultaneously reducing the associated costs.[3]

2. Object of the Study

The aim of the study is to provide scientific justification for, and to develop methods and tools to improve, the fuel-economy and environmental performance of diesel engines by enhancing fuel-supply and mixture-formation processes, ensuring the stability of fuel-system parameters, and enabling operational diagnostics during service.[6.7.8]
A 4Ch 8.5/11 diesel-generator rated at 16 kW was selected as the research object.

The engine fuel system consists of a lift pump, a filter, a high-pressure fuel pump, injectors, a valve mechanism, and pipelines. The piston-type lift pump, which supplies fuel at a pressure of 1-1.5 kg/cm², is mounted directly on the high-pressure in-line fuel pump.



Fig. 1. *4Ch 8.5/11 diesel-generator, 16 kW*

3. Instruments and equipment for acoustic emission research and control

Methods and Instrumentation
Processing and analysis of acoustic emission testing (AET) data using specialized system software.
The A-Line 32D AE system is designed for the acquisition and processing of AE information through a serial high-speed digital data-transmission channel.



Fig. 2*. A-Line 32D AE system*

The A-Line 32D (DDM) is a four-channel portable AE system for field operation with recording and processing of AE signals. It can be used both for mobile periodic inspection and for stationary continuous inspection (monitoring), with the capability to control the monitored object (Fig. 2), for example, by automatically stopping the test bench when a diagnostic criterion exceeds its limiting value.

The DAQ-4-AE experimental measuring sensor system (Fig. 3), in its current implementation, is a laboratory prototype intended to

demonstrate the principle of event-based recording. It is applicable to laboratory measurement systems comprising piezoelectric sensors, analog signal-processing modules, and digital data-acquisition systems.



Fig. 3. *DAQ-4.1-AE tracking system for AE data acquisition and processing*

A distinctive feature of the approach is that a single act of mechanical excitation can generate a series of events whose parameters depend on the input-signal waveform and the specified threshold level.

Tests are performed under normal conditions without shielding.

- Cables are routed in a comparable manner.
- The gain is fixed.
- Threshold levels are fixed or recorded.

Measurements are performed sequentially using a single-channel oscilloscope.

Sensor configurations are investigated in sequence under comparable conditions.

The evaluation is conducted on the basis of visual indicators:

- signal waveform
- baseline stability
- noise level
- occurrence of spurious pulses

An event-based model is implemented on the basis of the output signal:

- each event is defined by the triggering of the threshold condition;
- the cumulative event function N(t) is formed;
- the event rate dN/dt is calculated over fixed time windows;

In addition, changes in the event rate are considered as an indicator of process dynamics.

4. *Acoustic Emission Testing (AET) Procedure*

AE testing of the fuel-system operation was carried out on an engine running at idle speed, with a holding period of 1 minute, in order to record possible AE phenomena detected by the AE equipment.

After installation of the piezoelectric AE sensors (PAE), the AE systems were switched on and the AE channels were calibrated using the Hsu-Nielsen method and a test specimen. The diesel-generator research methodology included the installation of AE piezoelectric transducers on the engine injectors, the pipeline, and the high-pressure fuel pump. The engine was operated at idle under fixed conditions, during which two different AE systems recorded AE signals associated with the fuel-supply process. The obtained results were then analyzed in order to identify the sources of the acoustic signals.

The AE sensor was mounted on the engine injector body symmetrically with respect to the cylinders, as well as on the pipeline and the high-pressure pump housing. Signals initiated by fuel delivery were transmitted from the PAE through a preamplifier to the AE instruments for further amplification. When the pressure increased in one of the pipelines, the sensor generated a pulse signal that was transmitted to the AE instrument. The AE signals characterize noise effects in the ultrasonic vibration range during the increase in fuel pressure in individual pipelines (maximum pressure: 18 MPa) over one operating cycle of the engine.

5. *Results*

AE parameter plots from the A-Line 32D system during AE testing

The AE signal measurement results obtained using the A-Line 32D system are presented in Fig. 4. During engine operation at idle speed, most acoustic signals correspond to friction processes. Owing to their low intensity, the amplitude of the generated AE pulses does not exceed 50 dB. As the process develops, a decrease in the intensity of friction is observed, and the development of impulsive signals becomes the main source of AE.

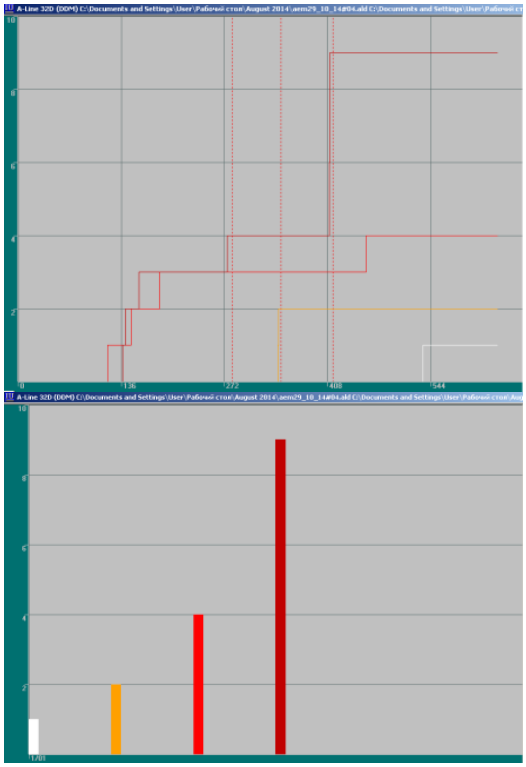


Fig. 4. *A-Line 32D parameter plots*

On the basis of waveform morphology, AE signals are classified as discrete, which corresponds to stepwise increases in loading and the presence of a large number of low-amplitude AE sources. The pulse waveform and spectrum of the AE signals obtained during the experiment indicate that, during engine operation at idle speed, the main source of AE is the variability of impulsive signals. This indicates non-uniform fuel delivery.

AE parameter plots obtained using the DAQ-4.1-AE experimental equipment

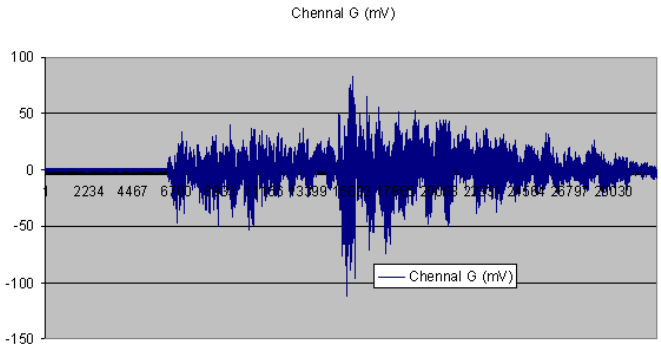


Fig. 5. *Signal from a single section of the fuel pump*

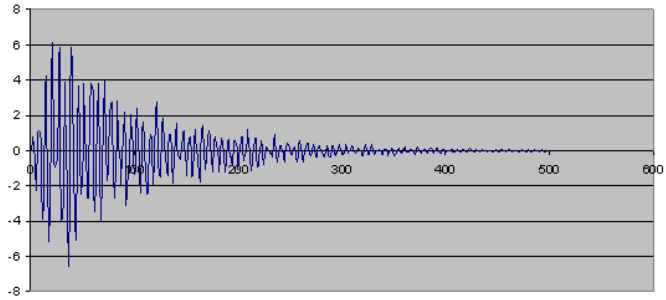


Fig. 6. *Signal in the pipeline of the second cylinder*

The obtained oscillograms indicate that the time interval between individual pulses reflects the form of the positive half-period of the signal.

The number of individual pulses increases as the amplitude or frequency of the input signal increases.

The study shows that the obtained AE signals are initiated by the fuel-supply system. It is evident that the amplitude of the AE signal from cylinder No. 2 changed and differs substantially from the normal fuel-supply condition observed for the other cylinders. In addition, the structure of the recorded signals indicates that fuel delivery to the cylinders is non-uniform and that differences are present, characterizing uneven operation of the high-pressure fuel-pump sections.

It is of interest to examine AE signals generated by the operation of a single fuel-supply section.

1- AE signal from a single fuel-supply section;
2- pulse signal from the piezoelectric fuel-delivery sensor (PAE) installed on the pipeline of the second cylinder.

The presented AE signal plots (recorded in the channels of different AE systems) show a surge in fuel delivery to the injectors (injector No. 2).

It can be observed that, in the interval from the onset of pressure increase to the moment of fuel injection into the second cylinder, the AE signal is characterized as “explosive.”

Conclusions

The character of AE variation under loading conditions has a specific form. In this case, the amplitude and energy have relatively low values and vary within certain limits, reflecting fuel movement through the pipeline and operation of the fuel pump. However, during the normal fuel-pumping process, a substantial increase in the AE level was recorded by all instruments. This indicates an abnormal operating mode of the fuel pump during fuel delivery to cylinder No. 2 and demonstrates non-uniform fuel delivery to the injectors. The analysis conducted makes it possible to identify the main limitations of existing methods for diagnosing diesel-engine units and to minimize soot emissions, i.e., particulate matter in the exhaust, produced during operation of an internal-combustion engine using diesel fuel.

1. The possibility of effectively applying the acoustic emission method to functional diagnostic tasks for piston diesel engines has been demonstrated.
2. The principles of functional AE diagnostics for piston diesel engines have been developed.
3. Several circuit-based solutions for the practical use of AE as a functional diagnostic tool for piston engines have been proposed.

Funding

The contribution of co-author V.Prokopenko to this work was supported by the EU Recovery and Resilience Facility within Project No 5.2.1.1.i.0/2/24/I/CFLA/003 “Implementation of consolidation and management changes at Riga Technical University, Liepaja University, Rezekne Academy of Technology, Latvian Maritime Academy and Liepaja Maritime College for the progress towards excellence in higher education, science and innovation” academic career doctoral grant (ID 1141).

References

[1] K. Carjova, M. Banov, L. Vinogradov, S. Kravchenko, and G. Strautmanis, “Acoustic Emission Method as a Means of Quality Control in Multilayer Welding of Thick-Walled Welded Joints,” *Latvian Journal of Physics and Technical Sciences*, vol. 60, no. 4, pp. 40–51, Aug. 2023, doi: 10.2478/lpts-2023-0023.

[2] V. Barat *et al.*, “Assessment of the Structural State of Dissimilar Welded Joints by the Acoustic Emission Method,” *Applied Sciences*, vol. 12, no. 14, p. 7213, Jul. 2022, doi: 10.3390/app12147213.

[3] N. P. Aleshin, Ed., *Metody akusticheskogo kontroli a metallov*. Moskva: Mashinostroenie, 1989.

[4] R. M. Douglas, J. A. Steel, and R. L. Reuben, “A study of the tribological behaviour of piston ring/cylinder liner interaction in diesel engines using acoustic emission,” *Tribology International*, vol. 39, no.

[5] “Banov M., Konjaev E., Troenkin D. Method for determining the fatigue strength of gas turbine blades by the acoustic emission method. Flaw detection, 1981, Vol. 2, p. 26-28. (in Russian).”

[6] K. Carjova, M. Banov, A. Unbedahts, G. Strautmanis, L. Vinogradov, and I. Kurjanovics, “Characteristics of Mathematical Modeling of Acoustic Emission Method for Diagnosis of Fatigue Cracks in the Elements of Marine Power Plants,” *Latvian Journal of Physics and Technical Sciences*, vol. 60, no. 5, pp. 3–14, Oct. 2023, doi: 10.2478/lpts-2023-0026.

[7] Vinogradovs, L., Nasibullins, A., Banov, M., Soldatova, J., Gutāns, J. Experience of Applying the Acoustic Emission Method for Monitoring Systems. Trans Motauto World, 2024, Vol. 9, No. 2, 43.-45.lpp. ISSN 2367-8399. e-ISSN 2534-8493.

[8] Vinogradovs, L., Strautmanis, G., Gutāns, J., Soldatova, J., Prokopenko, V., Ivlijev, A. Application of Acoustic Emission Method for the Diagnosis of Underground Gas Pipeline without Taking It out of Operation. Security & Future, 2024, Vol. 8, No. 3, pp.91-93. ISSN 2535-0668. e-ISSN 2535-082X.

Impact of Ammonia Fuel on Waste Heat Availability in Marine Engines

Ozren Bukovac*, Zvonimir Klasan
University of Rijeka, Faculty of Engineering, Croatia
ozren.bukovac@riteh.uniri.hr

Abstract: *The transition to low-carbon fuels introduces new challenges for the design of energy systems based on internal combustion engines. This paper addresses the effects of ammonia as one of the prime fuels for highly efficient two-stroke engines, e.g., based on MAN high-pressure injection technology. Even if these prime movers can maintain a high effective efficiency over a wide load range, the thermodynamic features of the ammonia combustion have a strong impact on the waste heat pattern. The analysis indicates that the lower adiabatic flame temperature and the chemical composition of the exhaust gases reduce the exhaust temperature, while variations in the specific heat capacity of the exhaust mixture reduce the exergy. This phenomenon is directly related to a reduced potential of working fluid generation in waste heat recovery (WHR) systems. The paper concludes that to maintain high overall plant energy efficiency, advanced technologies, such as organic Rankine cycles (ORC), have to be applied to compensate for the loss of the thermal potential, especially at off-design load conditions.*

Keywords*: AMMONIA FUEL, WASTE HEAT RECOVERY, ORGANIC RANKINE CYCLE, TWO-STROKE ENGINES*

1. Introduction

International shipping contributes about 3% of global anthropogenic greenhouse gas emissions. The International Maritime Organization (IMO) updated its greenhouse gas strategy to address climate change, establishing an explicit pathway to net-zero GHG emissions by or around 2050. To meet this timeline, it is necessary to move away from interim carbon-reduction approaches (such as vessel speed optimisation or liquefied natural gas) and adopt fundamentally zero-carbon marine propulsion architectures [1].

To achieve this ambitious target, the maritime sector is shifting from fossil-based heavy fuel oil to zero-carbon fuels. Hydrogen and ammonia do not contain carbon atoms. Methane, methanol and ethanol do contain (Fig. 1) but are acceptable in transition to net zero as intermediate solution.

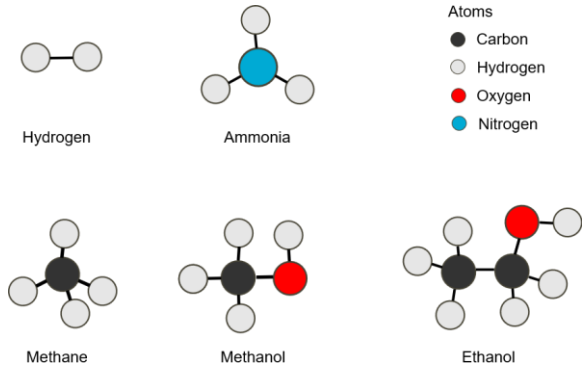


Fig. 1 *Alternative fuels to diesel.*

Ammonia (NH_3) has emerged as a prominent candidate because as it is carbon-free and the existing global transportation infrastructure that supports its use. In contrast to LNG carriers, which have long been permitted to utilize their cargo or boil-off gas (BOG) as fuel, using ammonia cargo as fuel was historically prohibited by the IMO's IGC Code because ammonia is strictly classified as a toxic product [2]. Ammonia fuel can be stored as a liquid at −33°C under atmospheric pressure or under mild pressure (~ 8–10 bar) at ambient temperature, thus making it a highly practical alternative to liquid hydrogen despite serious challenges in deployment due to its low volumetric energy density, high toxicity, narrow flammability limits, and slow laminar burning velocity[3].

This work is targeted at the application of ammonia in large deep-sea propulsion systems, primarily slow-speed two-stroke dual-fuel (DF) marine engines, with some comparisons against auxiliary medium-speed four-stroke dual-fuel engines. These advanced prime movers feature high effective engine thermal efficiency over a wide load range, achieved through high-pressure direct injection [4] or lean-burn pre-chamber combustion [5]. CO_2 and CO emissions are not generated because the chemical formula of ammonia does not include carbon atoms. However, the unique thermodynamic and chemical properties of ammonia combustion alter the waste heat pattern downstream.

Large slow-speed two-stroke diesel engines have historically been among the most thermodynamically efficient prime movers, with brake thermal efficiencies (BTE) in the range of 50–55%. However, a waste heat recovery system (WHRS) is necessary to achieve that high efficiency [6]. The engine releases waste heat that was not converted into mechanical work. This waste heat is released through a variety of systems, such as scavenge air coolers, jacket cooling water, lubricating oil systems, and exhaust gases. A traditional WHRS captures this energy by directing high-temperature exhaust gases into an exhaust gas boiler (EGB) to produce superheated steam. Steam then powers a steam turbine or a hybrid steam-gas turbine generator. The integration of a robust WHRS can improve the overall efficiency of the vessel's plant by 8–12%. The application of alternative fuels modifies the basic thermal and exergy balance of the prime mover, thus requiring a complete revision of the waste heat recovery system architecture [7].

The reduction of exhaust gas temperature and decrease of total exergy are the result of the lower adiabatic flame temperature, the choice of pilot fuel, and the variation of chemical compositions. The bottoming cycles are analysed in relation to recent academic studies and industrial configurations to identify the required performance adaptations. Additionally, advanced recovery concepts such as organic Rankine cycles (ORCs) and thermochemical recuperation (TCR) are discussed, while existing research gaps are clearly outlined.

The utilization of ammonia fuel, possessing a lower lower heating value (LHV) than diesel (Table 1), noticeably influences the exergy of exhaust gases due to two interrelated thermodynamic factors: elevated mass flow demands and substantial latent heat of vaporization.

Table 1: *Alternative fuel comparison by Lower Calorific Value, Energy density and Fuel tank size relative to MGO [8]*

	Energy content, LHV, MJ/kg	Energy density, MJ/L	Fuel tank size relative to MGO
Ammonia (NH_3) (liquid, -33°C)	18.6	12.7 (-33°C) 10.6 (45°C)	2.8 (-33°C) 3.4 (45°C)
Methanol (CH3OH) (65°C)	19.9	14.9	2.4
LPG (liquid, -42°C)	46.0	26.7	1.3
LNG (liquid, -162°C)	50.0	21.2	1.7
LEG (liquid, -89°C)	47.5	25.8	1.4

Hydrogen (H2) (liquid, -253°C)	120	8.5	4.2
MGO	42.7	35.7	1.0

2. Dual-Fuel Engines on Ammonia

The commercialisation of marine ammonia engines is strongly dependent on dual-fuel (DF) technologies. Ammonia has a very high auto-ignition temperature and a narrow flammability range; therefore, reliable ignition using compression alone cannot be achieved at the compression ratios that are typical of marine engines. A secondary pilot fuel with high ignitability is consequently required to initiate the combustion process [9].

Primary deep-sea propulsion is provided by low-speed two-stroke crosshead engines operating on a high-pressure dual-fuel direct-injection principle (analogous to the diesel cycle). Key platforms, such as MAN Energy Solutions' ME-LGIA (new name for MAN Energy Solutions is Everllence) and WinGD's X-DF-A, employ a dedicated pilot fuel injection system that injects a small quantity of conventional or renewable pilot fuel near the top dead centre (TDC), generating a high-temperature flame kernel. That pilot fuel can be Marine Gas Oil (MGO), Very Low Sulphur Fuel Oil (VLSFO), or bio-derived alternatives, such as hydrotreated vegetable oil (HVO).

For standard LNG dual-fuel engines, the pilot fuel is minimal, about 1.5%. However, because ammonia is extremely slow-burning and difficult to ignite, MAN's official testing has established that the initial ME-LGIA engines require a pilot energy fraction of 5% at 100% load (L1 rating) [10]. This means 95% of the combustion energy comes from ammonia, and 5% from the diesel pilot fuel.

Ammonia is kept in liquid form onboard, and it must stay liquid all the way through the injectors. High-pressure liquid ammonia is then injected directly into that flame front. The total mass flow rate of fuel, $\dot{m}_f$, is dictated by the balance of energy share:

$$\dot{m}_f \cdot \mathrm{LHV}_{\mathrm{mix}} = \dot{m}_{\mathrm{NH_3}} \cdot \mathrm{LHV}_{\mathrm{NH_3}} + \dot{m}_{\mathrm{pilot}} \cdot \mathrm{LHV}_{\mathrm{pilot}}$$

In this context, LHV refers to the lower heating value. The ammonia energy share for these systems is typically 80-95%, which limits the pilot fuel share to 5-20% of the total thermal input. This optimisation provides maximum carbon reduction while maintaining high, effective engine efficiency.

Specific fuel consumption is determined by utilizing the brake power, which refers to the actual kilowatts supplied to the propeller shaft. For a dual fuel system, it can be expressed as

$$\eta_{\mathrm{e,LGIA}} = \frac{3600 \cdot 10^3}{(SFAC \cdot LCV_{\mathrm{NH\,3}}) + (SPOC \cdot LCV_{\mathrm{pilot}})}$$

where $\eta_{\mathrm{e,LGIA}}$ is engine brake thermal (effective) efficiency in ammonia mode; $SFAC$ is specific fuel ammonia consumption (g/kWh); $LCV_{\mathrm{NH\,3}}$ is lower calorific value of ammonia (18600 kJ/kg); $SPOC$ is specific pilot oil consumption (g/kWh) and LCV_{pilot} is lower calorific value of the liquid pilot fuel (MDO/MGO, standard at 42700 kJ/kg).

Auxiliary power generation and propulsion of smaller vessels, however, use medium-speed four-stroke engines. These engines often use a low-pressure premixed combustion concept (similar to the Otto cycle), where ammonia is port-injected or added to the scavenge air intake at low pressure, resulting in a lean air-fuel mixture during the induction stroke.

Ignition is achieved by a micro-pilot fuel injection (<5% of energy share in most cases) with an advanced pre-chamber spark or compression setup. Four-stroke engines are more prone to unburned ammonia slip and knocking at high loads, but they have a higher baseline exhaust temperature than two-stroke configurations due to their lower expansion ratios, which results in a different waste heat profile.

Effect of Alternative Fuels on Waste Heat Availability

The shift from heavy fuel oil to ammonia will greatly change the thermodynamic, fluid dynamic, and chemical makeup of the engine exhaust. For modern prime movers that operate efficiently across a wide load range, the combustion of alternative fuels deteriorates the quality of the exhaust gas due to their thermodynamic properties.

Fuels with higher hydrogen content, when combusted, create more water vapor than do diesel fuels. Moreover, the ammonia combusts as:

$$4\mathrm{NH_3} + 3\mathrm{O_2} \rightarrow 2\mathrm{N_2} + 6\mathrm{H_2O} + \text{Heat Energy}$$

This higher water vapor content raises the specific heat capacity of the exhaust gas mixture ($C_{p,\mathrm{exh}}$). Furthermore, the adiabatic flame temperature for ammonia combustion (~ 1800°C) is below that of marine diesel oil (~ 2100°C). This directly reduces the bulk temperature of the exhaust gases leaving the cylinder (T_{exh}).

The total waste heat enthalpy flow is then:

$$\dot{Q}_{\mathrm{exh}} = \dot{m}_{\mathrm{exh}} \cdot C_{p,\mathrm{exh}} \cdot (T_{\mathrm{exh}} - T_{\mathrm{amb}})$$

The mass flow rate at exhaust $\dot{m}_{exh}$ varies due to different stoichiometric air-to-fuel ratios, and the changes in specific heat capacity and the lower thermal grade basically reduce the:

$$\dot{E}x_{\mathrm{exh}} = \dot{m}_{\mathrm{exh}} [(h_{\mathrm{exh}} - h_{\mathrm{amb}}) - T_{amb} (s_{\mathrm{exh}} - s_{\mathrm{amb}})]$$

This loss of exergy directly reduces the potential for working fluid generation (such as superheated steam) in standard waste heat recovery systems, making it difficult to drive conventional steam turbogenerators efficiently.

Pilot Fuel Influence and Chemical Interferences

The exhaust gas properties are strongly determined by pilot fuel type and quantity. When conventional petroleum-derived pilot fuels (MGO or VLSFO) are used, sulphur dioxide (SO_2) is released to the exhaust stream. In the presence of unburned ammonia slip (NH_3) from incomplete combustion following reaction occurs at the 180°C to 230°C temperature range:

$$\mathrm{NH_3} + \mathrm{SO_2} + H_2O + 1/2\mathrm{O_2} \rightarrow (\mathrm{NH_4})\mathrm{HSO_4}$$

The product is ammonium bisulphate (ABS), a sticky, highly corrosive material that sticks to heat exchanger tubes, causing severe fouling, reduced heat transfer efficiency and accelerated low-temperature corrosion. To avoid ABS formation, designers must either adopt ultra-low-sulphur or bio-derived pilot fuels (e.g., hydrotreated vegetable oil – HVO) or keep the WHRS exhaust gas temperature artificially above the ABS precipitation threshold, further penalising thermal energy recovery.

Aftertreatment Interactions: SCR

Ammonia combustion is inherently associated with risks of high emission rates of fuel-borne nitrogen oxides (NO_x) and unburned ammonia slip. Managing these requires a selective catalytic reduction (SCR) unit. The position of an SCR relative to the WHRS is critical, because an SCR has to work between 300°C and 400°C to operate efficiently [11]:

- Upstream SCR (High-Pressure Layout): Placed before the turbocharger or WHRS boiler. It preserves aftertreatment efficiency but extracts high-grade thermal energy, leaving a cooler, lower-exergy gas stream for the downstream WHRS.
- Downstream SCR (Low-Pressure Layout): Placed after the WHRS. It optimizes heat recovery but poses a risk of functioning below the active catalytic temperature, particularly under low-load or off-design conditions.

Advanced WHRS Concepts for Ammonia Vessels

The engine waste heat profile shifts to a lower thermal grade where conventional steam Rankine cycles are less effective. This is particularly relevant for off-design load conditions where advanced technologies should be applied to compensate for the loss of thermal potential and keep the overall plant's energy efficiency high. Table 2 provides an overview of a comparative analysis of WHRS characteristics for HFO- and ammonia-fuelled marine engines.

Organic Rankine Cycles (ORC)

ORCs are a highly viable solution when dealing with the lower grade of the exhaust temperatures and the reduced exergy typical of alternative fuel combustion [12].

Instead of water/steam, ORCs use organic working fluids with lower boiling points and lower latent heats of vaporisation. This enables efficient evaporation of the fluid at considerably lower temperatures, similar to the low-to-medium temperature streams of two-stroke ammonia engines. This results in improved net efficiency for the recovery of low-temperature energy from exhaust, jacket water, and scavenging air subsystems under both design and partial-load (off-design) conditions.

Thermochemical Recuperation (TCR)

Instead of using secondary fluids to convert waste heat into electricity, TCR uses the sensible heat of the exhaust gas to perform an endothermic fuel-reforming reaction on board [13]. Ammonia can be catalytically dissociated to hydrogen (H_2) and nitrogen (N_2) at exhaust temperatures of 300°C to 600°C.

$$2NH_3 \rightarrow N_2 + 3H_2 (\Delta H_r > 0)$$

By passing the liquid ammonia fuel through an exhaust-heated reformer before cylinder injection, the waste heat can be effectively stored as chemical energy in the cracked hydrogen fuel. This increases the net heating value of the injected fuel, enhances flame propagation in the cylinder, reduces the pilot fuel fraction required, and improves overall brake thermal efficiency.

In Table 2. Is given an overview of WHRS characteristics

Table 2: *Comparative analysis of WHRS characteristics for HFO and ammonia-fueled marine engines*

	HFO Two-Stroke WHRS	Ammonia-Fueled Two-Stroke WHRS	Ammonia-Fueled Four-Stroke WHRS
Primary WHRS Tech	Steam Turbogenerator	Organic Rankine Cycle/TCR	Multi-stage ORC/Heat Pumps
Thermal Quality	High exergy, high T_{exh}	Reduced exergy, low T_{exh}	Moderate exergy, higher T_{exh}
Fouling Risk	Sulfuric Acid (~120°C)	ABS fouling (~180-230°C)	ABS fouling (~180-230°C)
Exhaust Gas C_p	Baseline	Elevated (H_2O vapour fraction)	Elevated (H_2O vapour fraction)
Off-Design Vulnerability	Severe efficiency drop	Mitigated via fluid optimisation	Mitigated via variable turbine geometry

WHR Integration Gaps in Marine Engine Systems

Preliminary studies have mapped independent alternative fuel combustion, but critical data gaps remain on the complete integration of waste heat at the system level on active vessels:

1. *Dynamic Transient Matching*: Marine engines, particularly low-speed ones, operate in a very dynamic environment (e.g., rough seas, manoeuvring, and varying ambient temperatures). Current models are mainly limited to steady-state operation. Research is needed on how the slow thermal response of advanced ORC architectures and fuel-cracking TCR reactors responds to rapid engine load variations.

2. *Fouling and Degradation Kinetics of ABS*: Quantitative experimental data on the specific deposition rates of ammonium bisulphate on different heat exchanger tube geometries and materials at marine flow velocities are scarce.

3. *Optimal Combined Cycle Layout*: There is no consensus on the optimal multi-stage layout. It is not yet conclusively demonstrated by scholars that a combined SCR → TCR → ORC array has better net lifetime exergy efficiency than a combined high-pressure SCR → dual-pressure steam Rankine cycle layout.

4. *Safety and latent heat recovery*: Cold energy recovery from liquid ammonia storage (by using it as a low-temperature heat sink for a bottoming cycle) has been proposed in a conceptual manner, but safety risks associated with running toxic ammonia lines near electrical power generation spaces have not been addressed fully.

3. Conclusion

The switch to ammonia fuel in marine engines is crucial for the IMO's aim of net-zero GHG emissions by or around 2050 and profoundly modifies the concepts of waste heat recovery in the maritime industry. The low adiabatic flame temperature and high specific heat capacity of ammonia lower the temperature of the exhaust gases and the exergy potential in slow-speed two-stroke engines, making conventional steam cycles less attractive. Medium-speed four-stroke engines have a slightly higher thermal rating, but they have different optimisation problems.

Advanced bottoming technologies such as organic Rankine cycles and thermochemical recuperation are needed to recover the lost thermal potential, which is critical for the overall plant efficiency, especially during off-design dynamic operations. Filling out the highlighted deficiencies in transient modelling is crucial for the design of next-generation zero-carbon and non-ABS fouling kinetics, as well as integrated system safety.

4. References

1. https://www.zerocarbonshipping.com/files/implications-of-the-2023-imo-ghg-strategy-for-the-shipping-industry.pdf 2026
2. International Maritime Organization (IMO), IGC Code, Paragraph 16.2
3. A. Yadav, B. Jeong, J. Int. Marit. Saf. Environ. Aff. Shipp., **6 (2-3)**, 99-116 (2022)
4. Z. Wang, J. Zhu, X. Liu, J. Huang, H. Wang, Z. Fu, J. Zhong, J. Mar. Sci. Eng., **14(4),** 354 (2026)
5. P. Sharma, A. Dhar, *Ammonia and Hydrogen for Green Energy Transition*, 167-185 (Springer Nature Singapore, 2024)
6. E. O. Olaniyi, G. Prause, J. Mar. Sci. Eng., **8(10)**, 811 (2020)
7. A. Qasemian, S. J. Haghparast, P. Azarikhah, M. Babaie, Sustainability, **13(11)**, 5921 (2021)
8. https://www.man-es.com/docs/default-source/document-sync/man-b-w-two-stroke-engine-operating-on-ammonia-eng.pdf 2026
9. P. A. Duong, H. Kang, Fuel Process. Technol., **272,** 108205 2025
10. https://www.ama-andros.gr/wp-content/uploads/2023/09/MAN-Ammonia-Engine-Development.pdf 2026
11. J. Jang, S. Ahn, S. Na, J. Koo, H. Roh, G. Choi, Energies, **15(12),** 4306 2022
12. L. A. Díaz-Secades, R. González, N. Rivera, Cleaner Energy Systems, **6,** 100083 2022
13. S. P. Kane, W. F. Northrop, Energies, **14(22)**, 7540 2021

Experimental Analysis of Diesel Engine Performance Using the Intelligent Common Rail CR/EDC15 Injection System

Naser Lajqi, Shpetim Lajqi*, Ilir Doçi, Kushtrim Lajqi
University of Prishtina / Faculty of Mechanical Engineering, Republic of Kosovo
*E-mail: shpetim.lajqi@uni-pr.edu

Abstract: *Modern diesel engines are increasingly equipped with intelligent electronic control systems aimed at improving engine performance, optimizing fuel consumption, and reducing exhaust gas emissions. This paper analyses the "Common Rail Diesel Injection System – CR/EDC15" controlled by the Bosch EDC15 electronic control unit. The research was conducted using the AutoEDU laboratory platform installed in the Automotive Mechatronics Laboratory at the Faculty of Mechanical Engineering. The platform enables real-time monitoring of engine operating parameters, OBDII diagnostics, and analysis of intelligent sensors and actuators used in modern diesel engines. The study investigates the influence of the electronic control system on fuel injection optimization, acceleration response improvement, combustion efficiency, and emission reduction. The obtained results show that the CR/EDC15 system provides higher engine performance, improved operational stability, lower fuel consumption, and reduced environmental pollution compared to conventional mechanical injection systems.*

Keywords*: DIESEL ENGINE, COMMON RAIL, INTELLIGENT SENSOR SYSTEM, ECU, ELECTRONIC DIAGNOSTICS, GAS EMISSIONS*

1. Introduction

The rapid development of automotive electronics and intelligent control systems has significantly contributed to the increase in the performance, safety, efficiency and reliability of modern vehicles [1], [2]. Conventional mechanical fuel injection systems have been gradually replaced by electronically controlled systems, which enable more precise fuel injection and optimal management of the combustion process.

One of the most advanced systems used in modern diesel engines is the *"Common Rail Diesel Injection System – CR/EDC15"*, which is controlled by the Bosch EDC15 electronic control unit (ECU) [1], [5], [16]. This system performs precise control of the injection pressure, injection time and fuel quantity depending on the engine operating conditions.

The purpose of this paper is to analyze the operation of the CR/EDC15 intelligent system through a laboratory simulation platform and evaluate its impact on improving the performance of diesel engines [7], [9], Figure 1.



Fig. 1. *Common Rail Diesel Injection System - CR/EDC15 simulation platform*

2. Research methodology and experimental equipment

The research was carried out at the Automotive Mechatronics Laboratory using the simulation platform produced by the company AutoEDU Lithuania. The platform is controlled by the Bosch EDC15C3-4 electronic unit and enables the analysis of engine operating parameters in real time [8], [15].

The platform consists of, Figure 1:

- Electronic system for controlling engine operation;
- High-pressure pump and injectors;
- Electrical system diagrams;
- OBDII diagnostics;
- Simulation of more than 20 errors;
- Devices for measuring voltages and electrical signals.

As part of the analysis, the main engine parameters were monitored through intelligent sensors such as:

- MAP sensor;
- MAF sensor;
- Engine temperature sensor;
- Fuel pressure sensor;
- Accelerator pedal sensor;
- Air temperature sensor;
- EGR sensor.

Diagnostics were performed through OBDII connection and Bosch diagnostic equipment (Figure 1 and Figure 2).

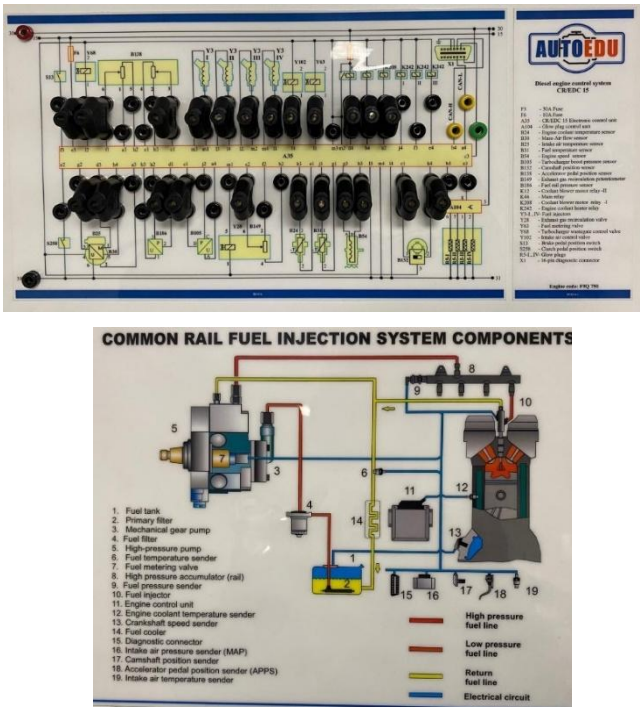


Fig. 2. *Connection diagram of the CR/EDC15 system parts*

3. CR/EDC15 system sensors

The engine control system measures the position of the accelerator pedal and the parameters of live engine and vehicle operating mode with the help of the sensors. The CR/EDC15, which is controlled by the Bosch EDC15 electronic unit has the sensors:

- Accelerator pedal sensor;
- MAP sensor;
- MAF sensor;
- Engine temperature sensor;
- Fuel pressure sensor;
- Air temperature sensor;

The CR/EDC15 intelligent system operates on the basis of signals obtained from sensors and commands that are implemented through actuators [1], [3], [15]. The electronic control unit (ECU) processes all signals in real time and optimizes the engine's operating parameters.

3.1. The accelerator pedal position sensor

The accelerator pedal sensor (B138) determines the position of the pedal and sends the corresponding signal to the ECU. Based on this signal, the amount of fuel to be injected is determined. The accelerator pedal module contains a sensor used by the engine control unit (ECU) to determine the position of the accelerator pedal. When the accelerator pedal is pressed, it rotates around its axis, causing a change in voltage proportional to the position of the pedal.

The accelerator pedal position sensor assembly (Figure 3) consists of the pedal platform, a shaft and a return spring. The spring ensures that the pedal returns to its original position after being released. The sensitive part usually consists of a potentiometer containing a carbon strip and a sliding contact (wiper). The engine control unit supplies direct current (DC) voltage to the carbon strip through the corresponding terminals. The wiper is connected to the output terminal, through which the ECU measures the output voltage and determines the position of the pedal.



Fig. 3. Accelerator pedal position sensor

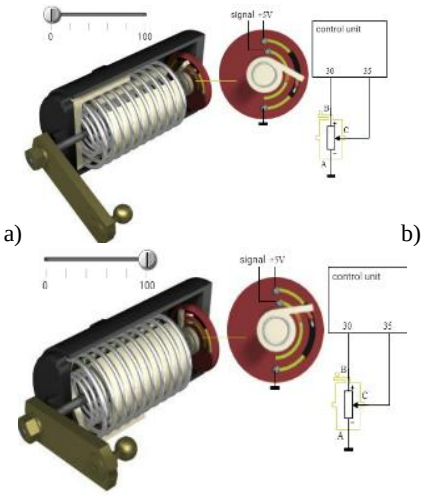


Fig. 4: *Accelerator pedal position sensor operation diagram: a) Pedal not pressed; b) Pedal pressed to the maximum*

Accelerator pedal position sensor can be checked using computer diagnostics. Sensor measurement field is defined by 0 – 100 %. When the engine is switched off and the pedal is not pressed, the shown value is 0 – 5 % (Figure 4.a). Having pressed the pedal to the floor the value is 95 – 100 % (Figure 4.b). When measuring the voltage (maximum value is 0 – 5 V), the voltage value coming out of the sensor is 0.5 – 0.9 V, when the pedal is not pressed. Having pressed the pedal to the floor the voltage value is 3.5 – 4.0 V. When pressing the pedal, the voltage and the pressing size percentage value must increase without jumps or breakups.

Sensor characteristics recorded into the engine control unit recalculates the measured voltage on pedal pressing (Figure 5).

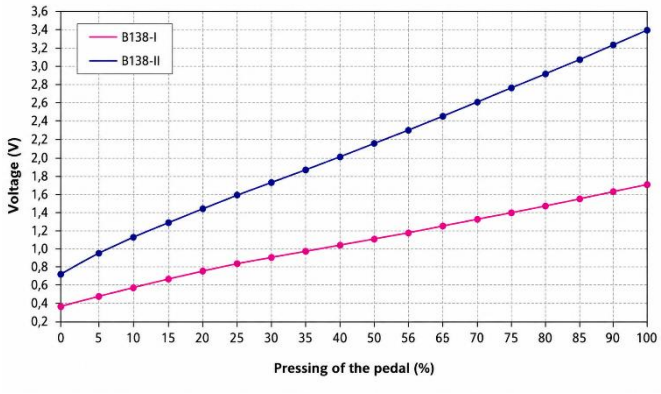


Fig. 5. *Voltage dependence on pedal pressing*

3.2. Crankshaft speed sensor

The crankshaft speed sensor (B54) is an inductive sensor used to determine the engine speed and crankshaft position.

The crankshaft speed sensor is usually placed near the flywheel which contains a gear (Figure 6). The gap between the tip of the sensor and the gear is usually only a few millimeters and is specified by the manufacturer.

The sensor consists of: a plastic body, a coil of wire, a permanent magnet, and a soft iron core.

As the gear teeth pass the sensor, the magnetic field changes continuously, inducing an alternating voltage in the coil according to Faraday's law of electromagnetic induction:

$$V = c' \times N \times (\Delta\Phi/\Delta t) \quad (1)$$

where:

V - induced voltage
c' - constant coefficient
N - number of windings of the coil
$\Delta\Phi/\Delta t$ - represents the rate of change of the magnetic flux

The ECU determines the engine speed by measuring the frequency of the generated AC signal. As the flywheel speed increases, the frequency of the induced voltage also increases.



Fig. 6. *Crankshaft Position Sensor*

To identify the Top Dead Center (TDC) reference position, a tooth on the gear wheel is intentionally removed. The ECU detects this missing tooth through frequency interruption and uses it as a positional reference for synchronizing the engine shaft.

3.3. MAP Sensor

The MAP sensor measures the absolute pressure in the intake manifold (boost pressure sensor-B 105) and allows the ECU to determine the engine load.

The Manifold Absolute Pressure (MAP) sensor measures the pressure in its manifold (between outlet the compressor and the intake manifold of engine) in the reference vacuum chamber, allowing the Electronic Control Unit (ECU) to estimate the mass of air entering the engine.

The sensor is mounted either directly on its manifold, or connected via a vacuum tube. The MAP sensor (Figure 7) consists of: a sensing element, a membrane (diaphragm), a Wheatstone bridge circuit, and an amplifier circuit (amplifier).



Fig. 7. *MAP Sensor*

The pressure difference between the manifold and the diaphragm deformation chamber, evaluating their values in the Wheatstone bridge. The differential voltage generated is amplified and converted into an output signal in the range of 0 to 5 V. The measurement range of the MAP sensor usually varies from (0 – 250 kPa or 0 – 2,5 bar or 0-2500 mbar).

Sensor characteristics recorded into the engine control unit recalculates the measured voltage into the air pressure mbar. Figure 8 presents the relationship between air pressure and sensor output voltage. The results indicate an approximately linear increase in voltage with increasing air pressure. The output voltage rises from about 1.65 V at 900 mbar to approximately 3.35 V at 1800 mbar, demonstrating stable sensor sensitivity throughout the operating range. This behavior confirms the suitability of the sensor for pressure measurement and monitoring applications.

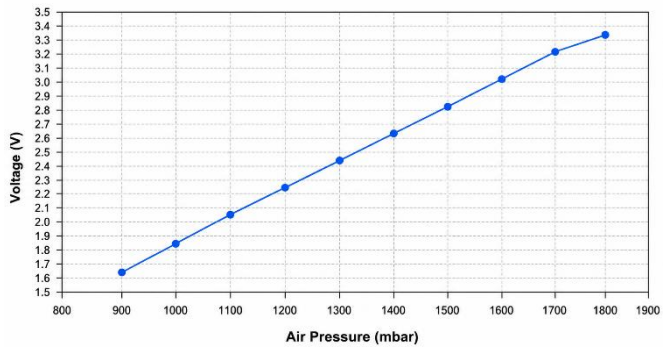


Fig. 8. *Voltage dependence on pressure*

3.4. Mass Air Flow Sensor (MAF)

The Mass Air Flow sensor (MAF) measures the amount of air entering the engine's intake system and is used to accurately calculate the amount of fuel [2], [11], [15].

The ECU uses this information primarily to determine the required amount of fuel injection and to regulate systems such as Exhaust Gas Recirculation (EGR).

The Mass Air Flow sensor is located in the intake pipe (Fig. 9), after the air filter. The MAF sensor -B 30 typically consists of: tube which directs the air flow, the hot wire fitted in the tube, and the temperature sensor. When the air flows through the tube, the temperature of the hot wire decreases. Integrated electronic flow controller changes the hot wire current strength so that the temperature of the hot wire all the time is about 120 °C, Figure 9. In order to maintain a constant temperature of the wire, it is necessary to increase the current strength. These changes of the flow strength are recorded and transmitted to the engine control module. Control unit processes the information received from the air mass meter and other sensors and accordingly regulates the fuel amount.



Fig. 9. *Mass Air Flow Sensor (MAF)*

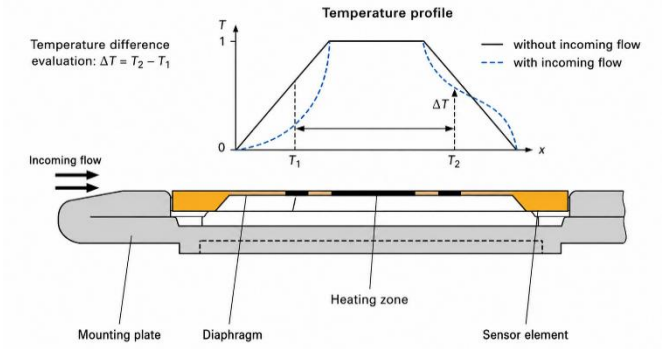


Fig. 10. *Measuring principle of the Mass-Air flow sensor*

Evaluation electronics installed in the sensor converts resistance difference into an analog voltage signal of 0 – 5 V adjusted to the engine control unit. Using recorded sensor characteristics, the measured voltage is converted into air mass flow rate (kg/h or g/s). Characteristic is made so that the engine control unit could recognize the errors of the air flow sensor.

The measuring range of the air mass meter is 0 – 300 g/s. As the engine runs and reaches its operating temperature, the air flow is 10 – 13 g/s. Having increased the engine crankshaft speed up to 2500 min^{-1}, the air flow becomes equal 23 – 26 g/s. The air flow through the air-mass sensor is simulated with the help of the fan mounted in front of the measurer (Figure 9). The air flow of this fan can be changed by rotating a switch of the potentiometer „B30 Simulator “

Sensor characteristics recorded into the engine control unit recalculates the measured voltage into the mass air flow rate, g/s, Figure 11.

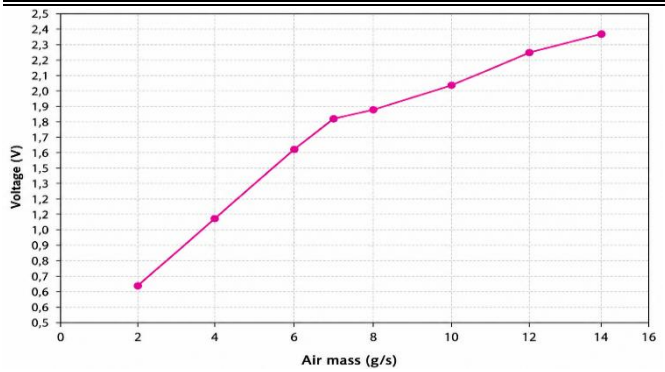


Fig. 11. *Voltage dependence on the air mass*

Figure 11 shows the relationship between air mass flow rate and sensor output voltage. As the airflow increases from 2 to 14 g/s, the output voltage rises from approximately 0.81 V to 2.40 V, confirming the sensor's ability to detect variations in air mass flow. The response exhibits a nonlinear trend, with higher sensitivity at lower flow rates.

3.5. Intake air temperature sensor

Intake air temperature sensor - B25 (measuring range -40 +200 ºC) registers the temperature of the intake air. Air temperature and pressure are required to calculate the intake air mass. Furthermore, the loops of the exhaust recirculation and boost pressure control can be adjusted to the air temperature. Temperature sensor is a semiconductor measurement resistor whose resistance changes depending on the temperature. Temperature sensors are usually with a negative (Negative Temperature Coefficient – NTC) and positive (Positive Temperature Coefficient – PTC) temperature coefficient. With increasing ambient temperature NTC sensor resistance decreases and PTC sensor resistance increases. NTC sensors are used more often. Temperature sensors are powered with the voltage of 5V. Voltage measured beside the sensor depends on resistance, which varies depending on the ambient temperature. This voltage measured beside the sensor is scanned through the analog digital converter and is a temperature measurement beside the sensor. Characteristics is recorded into the engine control module, which assigns the appropriate temperature to each resistor or to the outlet voltage value, Figure 12.

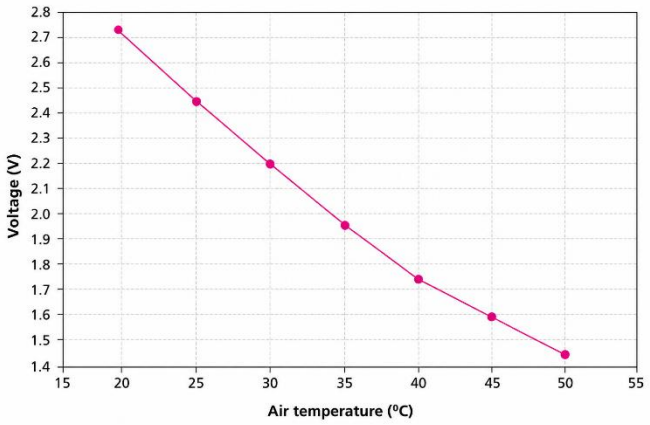


Fig. 12. *Voltage dependence on air temperature*

4. Performance of diesel engine with CR/EDC15

Engine performance is analyzed for diesel engine with capacity 1.9 L with CR/EDC15 (engine code is F9Q 750), and engine idle speed is 750 – 850 min^{-1}.

4.1. Mass air flow and air fuel ratio

Correct Mass air flow is crucial for modern engine with Common Rail Diesel Injection System – CR/EDC15, to improved engine performance, fuel efficiency, optimized air/ fuel ratio, maintaining efficient engine operations.

The fundamental formula to calculate the **Mass Air Flow** (g/s) in an internal combustion engine for a 4-stroke is:

$$\dot{m}_{air} = \rho \cdot V_d \cdot \frac{N}{60} \cdot \frac{n_{cyl}}{2} \cdot \eta_v \qquad (2)$$

Where:

$\dot{m}_{air}$ [kg/s or g/s] - mass Air Flow rate
V_d [m^3] - engine displacement
N [rpm] - engine speed
η_v - volumetric efficiency (a dimensionless decimal)
ρ [kg/m^3] - density of the intake air

For a highly accurate theoretical model, rho (ρ) is replaced using the **Speed-Density ideal gas law**:

$$\rho = \frac{MAP}{R \cdot IAT} \qquad (3)$$

where:

MAP [kPa] - Manifold Absolute Pressure
IAT [K] - Intake Air Temperature
R - Specific gas constant for air (~287 J/kg · K)

Mass air flow, expressed in grams per second (g/s), is the most common unit in Live Data diagnostics via devices such as Delphi, Launch.

The performance data presented in Figures 13–18 were obtained from ECU calibration data, experimental measurements and theoretical analysis of the F9Q 750 engine operating under stock, Stage 1 remap and naturally aspirated conditions.

The graph Figure 13 shows the mass air flow in g/s for stock settings and Stage 1 remap as a function of RPM, for the 1.9 dCi (F9Q 750 engine code) engine.

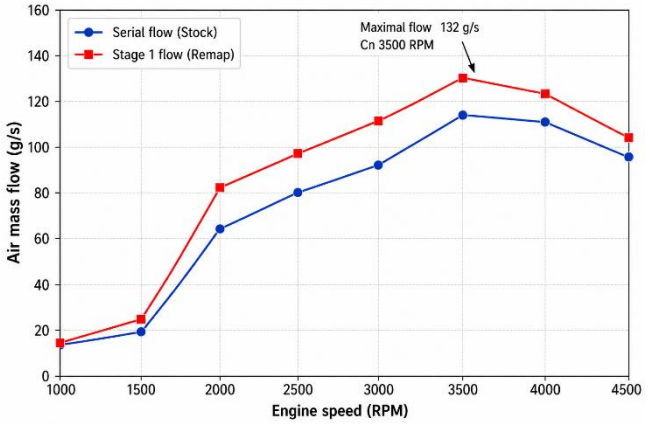


Fig. 13. *Mass air flow in g/s for stock settings and Stage 1 Remap as a function of engine RPM.*

Figure 13 shown:

- Idle sped (~850 RPM): 14.5 g/s. (at the case when EGR is open, the value drops to about 8–10 g/s, because the engine is sucking in exhaust gases instead of clean air).
- Full turbine pressure is near engine speed at 2000 RPM: The stock engine pulls 82 g/s, while Stage 1 pushes 98 g/s into the engine due to the higher turbine pressure (1.8 bar).
- Maximum flow is near engine speed at 3500 RPM: This is the peak of performance. The stock engine reaches 115 g/s. With the Stage 1 remap, this value rises to 132 g/s.

In this engine is used turbocharger **Garrett GT1749V.** The graph presented at Figure 14 that shows the operating range and mass air flow (in g/s) as a function of the absolute pressure charged at the compressor section of the Garrett GT1749V turbine.

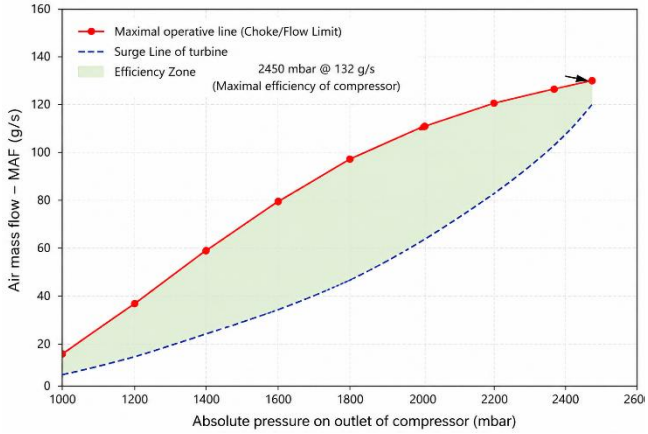


Fig. 14. *Operation range and mass air flow (in g/s) as a function of the absolute pressure charged at the compressor section of the Garrett GT1749V turbine*

Figure 14 illustrates the Compressor Operating diagram:

- Limits Surge (Pumping/Swing Zone) is the left-hand limit of compressor diagram (is presented with blue color) . At the case when the engine is operated at low engine speed and throttle is opened full, the engine not consuming enough air at a given pressure, the air will start to oscillate back through the compressor, causing harmful vibrations. For the GT1749V, this limit at a pressure of 2.0 bar occurs at air mass flows lower than approximately 35 (g/s).
- Optimal range efficiency: The highest efficiency (between (72% and 75%)) is found at pressure ratios between 1.5 and 2.1 (around 1.5 to 2.1 bar as the absolute pressure) and at mass flows between (50 to 95 g/s).
- Choke limit: The right-hand limit of the diagram (is presented with red color) where the air velocity in the compressor reaches the speed of sound. The efficiency drops sharply below (58%) and the turbine starts to over-rotate. The maximum absolute mass flow rate that a standard GT1749V can deliver at the far right limit at high pressure (2.2 - 2.5 bar) is around (135 – 145 g/s).

The amount of fuel is determined based at Clean-burning (black smoke-free).

Clean-burning (black smoke-free) diesel engines require an air-fuel ratio (AFR) of at least 17:1 (17 grams of air to 1 gram of fuel) under full load. At 115 g/s of air (stock) the computer allows a maximum of 6.76 g/s of fuel to be injected. At 132 g/s of air (Stage 1) the computer can safely allow a maximum of 7.76 g/s of fuel to be injected. This directly creates that extra Power.

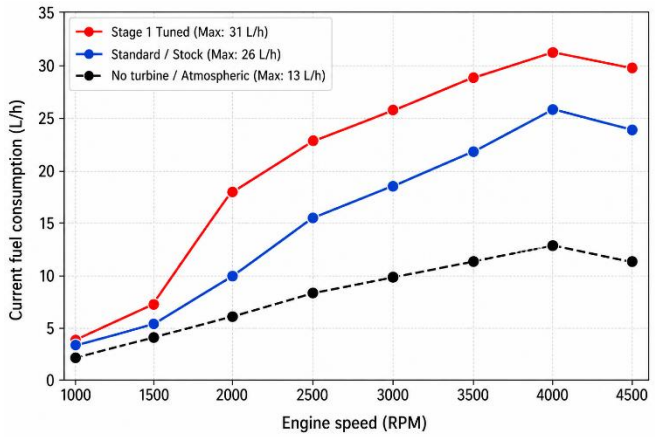


Fig. 15. *Current fuel consumption (L/h) as a function Engine RPM*

In Fig. 15 is presented:

- At idling speeds around 800 min^{-1}, all three configurations converge to an identical baseline consumption of 2.5 to 3 L/h because fueling is not air-limited under zero-load conditions.
- At peak torque around 2000 min^{-1}, engine has a consumption: without Turbine 6.1 L/h, Standard (Stock): 10.1 L/h and Stage 1: 18.2 L/h.
- At engine speed 3000 min^{-1}, engine has a consumption: Without Turbine: 10.1 L/h, Standard (Stock) 18.2 L/h and Stage 1:21.1 L/h.
- At Peak Power around 4000 min^{-1}, engine has a consumption: Without Turbine: 13 L/h, Standard (Stock): 22 L/h and Stage 1:31 L/h.

When the car is stationary and we press the accelerator, the engine only needs a minimal amount of energy (fuel) to rotate its own mass (shaft, pistons, flywheel). The amount of injection per stroke is minimal. However, when accelerating up a hill at full throttle, the engine has to overcome the weight of the vehicle and air resistance, so the computer opens the injectors to their technical limit. When operating at a standstill or maintaining a constant speed, the stage 1 program does not increase consumption, since the required torque is low.

4.2. Engine Torque

Engine torque for diesel engine with capacity 1.9 L with CR/EDC15 (engine code is F9Q 750), and without turbine is presented in Figure 16.

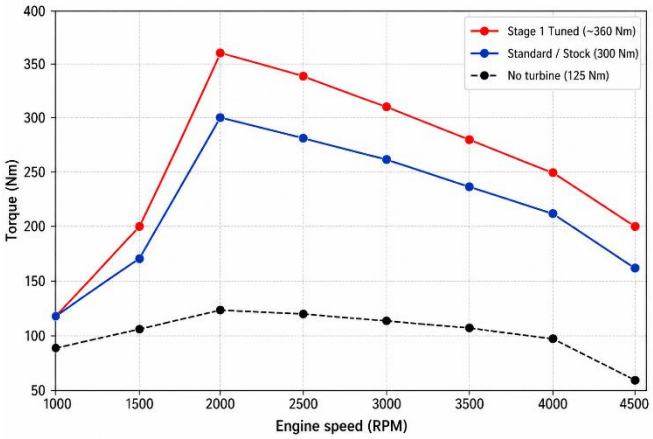


Fig. 16. *Torque (Nm) as a function Engine RPM*

Figure 16 presents, the main stages of torque in operation:

- Stage 1 (Optimization): A software change to the computer (ECU) increases the turbine pressure and the amount of fuel injected. The result is more torque 60 Nm (360 Nm). The curve becomes steeper, the car pulls noticeably stronger in the middle revs, and the response to the accelerator pedal is faster.
- Standard (stock): A balanced curve designed for a long life of the clutch, flywheel and turbine itself. Torque is limited to 300 Nm so as not to overload the gearbox.
- No turbocharger (Atmospheric): If the turbine were to be removed from this engine (or if the pressure regulation fails), it would switch to atmospheric operation. Since the diesel engine does not have a throttle valve and operates with excess air, without a turbine it loses more than half of its torque. The curve becomes completely flat (linear), and the engine is extremely slow and unresponsive.
-

4.3. Engine Power

Engine torque for diesel engine with capacity 1,9 litre with CR/EDC15 (engine code is F9Q 750), and without turbine is presented in Figure 17.

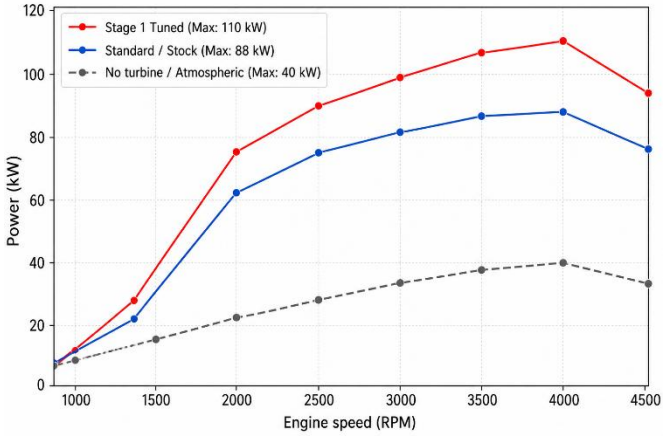


Fig. 17. *Engine Power (kW) as a function Engine RPM*

In Fig. 17 are shown the technical highlights of the powertrain:

- Efficiency at engine speed 2000 RPM: Although maximum power is not reached until 4000 rpm, the Stage 1 engine develops 75 kW at 2000 rpm (when torque is at its maximum), which is almost equal to the full power of the naturally aspirated version.
- Curve drop: It is noticeable that after 4000 RPM the power curve drops sharply for all three versions. This happens because the engine can no longer "breathe" effectively (gas exchange through the valves becomes too fast, and the turbine pressure starts to drop intentionally to protect the components).

4.4. Specific fuel Consumption of engine

Specific fuel Consumption of engine for diesel engine with capacity 1.9 L with CR/EDC15 (engine code is F9Q 750), and without turbine is presented in Figure 18.

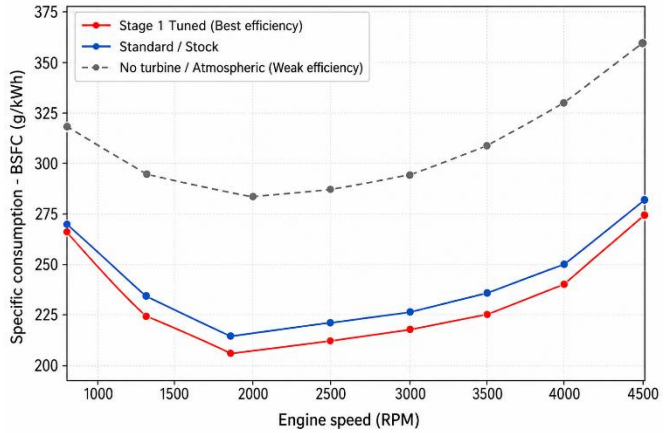


Fig. 18. Specific consumption (g/kWh) as a function Engine RPM

Based on Figure 18 the efficiency analysis is presented below:

Why does Stage 1 achieve lower values (better efficiency)?

- At stage 1, by optimizing the pre-injection (timing) and higher common-rail pressure, the fuel is atomized into smaller droplets. The higher turbine pressure adds more oxygen, so the fuel burns faster and more completely in a shorter time. This increases the thermodynamic efficiency of the engine.
- At the engine speeds 2000 RPM, the volumetric efficiency (intake air) and the combustion rate are in perfect balance with the mechanical losses (friction of the pistons and bearings). This is reason that this area is the most economical for constant driving.

The Bosch EDC15 electronic unit receives signals from intelligent sensors and based on them:

- Calculates the exact amount of air mass entering the intake manifold, through signals from: Absolute pressure at the outlet of the compressor (manifold absolute pressure – MAP), atmospheric pressure at the inlet of the compressor, RPM, Intake air temperature. Previously, the mass air flow sensor located behind the air filter provides information about the air flow entering the manifold.
- Manages Operation range at turbocharger.
- Operation range at EGR Valve
- Injection time;
- Injection duration;
- Injection pressure

5. Conclusions

This paper presented an experimental analysis of the intelligent Common Rail diesel injection system CR/EDC15 controlled by the Bosch EDC15 electronic control unit. The research conducted through the AutoEDU laboratory platform demonstrated the importance of intelligent electronic management systems in modern diesel engine operation and optimization.

The experimental results confirmed that the CR/EDC15 system enables highly precise control of fuel injection parameters, including injection timing, injection pressure, and fuel quantity according to real-time engine operating conditions. Through the integration of intelligent sensors such as MAP, MAF, intake air temperature, fuel pressure, and accelerator pedal sensors, the ECU continuously processes operating data and optimizes the combustion process.

The analysis of mass air flow, turbocharger operation, and air–fuel ratio demonstrated that the optimized Stage 1 configuration significantly improves engine performance compared to the standard factory settings. Increased air mass flow and optimized injection control contributed to higher torque and power output while maintaining efficient combustion and reducing black smoke emissions. The study also showed that optimized common rail pressure and injection timing improve fuel atomization, combustion efficiency, and thermodynamic performance of the engine.

Furthermore, the research highlighted the importance of the intelligent CR/EDC15 system in reducing fuel consumption, improving engine response, increasing operational stability, and lowering harmful exhaust emissions. The integration of OBDII diagnostics and real-time monitoring additionally enables faster fault detection and more efficient maintenance procedures.

In conclusion, the CR/EDC15 intelligent electronic injection system represents an advanced and efficient technology for modern diesel engines, contributing significantly to improved engine performance, energy efficiency, environmental protection, and compliance with contemporary ecological and emission standards.

6. References

[1]. Heinzmann GmbH &Co., *Engine Management, Porwerful technology for diesel engines*, 2022
[2]. Bosch R., *Automotive Handbook*, 11th Edition, John Willey & Sons Ltd., 2022.
[3]. Reif Konrad., *Diesel Engine Management*, Springer, 2014.
[4]. Heywood J.B., *Internal Combustion Engine Fundamentals*, 2nd Edition, McGraw-Hill, 2018.
[5]. Bosch EDC15 Technical Documentation, https://manual.ecu-service.info/MULTI_CAN/MANUALS/EDC-15.html

[6]. Stone R., *Introduction to Internal Combustion Engines*, 4th Edition, Sae Intl, 2017.
[7]. Ornella Chiavola, P. Giulianelli, *Modelling and Simulation of Common Rail Systems.* SAE Technical Papers, 2001.
[8]. *AutoEDU Training Platform Documentation*, https://autoedu.com/
[9]. Kushtrim Lajqi, *Përmirësimi i përformancave të motorëve të automjeteve motorike duke aplikuar sistemet inteligjente të kontrollit "Bosch Motronic Med 7.5.10" dhe "CR EDC 15",* Master Thesis, Prishtina, 2023.
[10]. Ferguson C., Kirkpatrick A., *Internal Combustion Engines Applied Thermosciences*, 3rd Edition, Wiley, 2015
[11]. Vijay Vailaya Shashidhara, et al., *Optimizing diesel engine performance and emissions with heated high-pressure fuel lines: an experimental study*, World Journal of Engineering (2026) 23 (2).
[12]. Lino Guzzella, Christopher Onder, *Introduction to Modeling and Control of Internal Combustion Engine Systems*, 2nd ed., Springer, 2010.
[13]. Eastwood P., *Exhaust gas aftertreatment for light-duty diesel engines*, Woodhead Publishing, 2010.
[14]. Vanja Jurić, Dino Županović, *Ecological Impacts of Diesel Engine Emissions***,** Promet-Traffic & Transportation 24(2), 2012.
[15]. *Laboratory documentation of the Faculty of Mechanical Engineering*.
[16]. *Bosch technical materials for the CR/EDC system 15*.

Prospects for the use of liquefied gas in marine diesel engines

Romanoz Topuria[1], Teimuraz Kochadze[1], Mikheil Lejava[2], Zaza Shubladze[2], Malxaz Tavdgiridze[2]

Akaki Tsereteli State University, 59 Tamar Mepe St., Kutaisi 6400, Georgia[1]
Batumi State Maritime Academy, 53 Rustaveli Ave., Batumi 6010, Georgia[2]
romtop54@gmail.com , temko1954@gmail.com , m.lejava@bsma.edu.ge , z.zhubladze@bsma.edu.ge , malxazi2938@mail.ru

Abstract: *the paper discusses the preparation of a fuel mixture consisting of liquefied gas and diesel fuel in marine diesel engines through the implementation of the gas–diesel process, where diesel fuel is used as pilot fuel. This approach reduces the ignition delay period compared to conventional liquid fuels, shortens combustion duration, and extends the flammability limits of the working mixture. Improved mixture formation leads to an increase in combustion rate and more complete combustion during the active combustion phase, causing the engine cycle to approach the Otto cycle. As a result, the environmental and performance characteristics of the diesel engine are significantly improved compared to conventional diesel and standard gas–diesel engines. The paper also analyzes the dependence of ignition delay on combustion parameters and fuel injection timing.*

KEYWORDS: *GASEOUS FUEL, LIQUEFIED GAS, MARINE DIESEL ENGINE, PILOT FUEL, DUAL-FUEL COMBUSTION, IGNITION DELAY.*

1. Introduction

During recent decades, the number of transport piston engines operating on liquid petroleum fuels has significantly increased, while gasoline, diesel fuel, and heavy fuels still remain the primary energy sources. Consequently, global petroleum consumption has risen considerably, whereas oil reserves continue to decline. According to current extraction and consumption rates, proven oil reserves are estimated to last approximately 40 years, while natural gas reserves may last about 60 years [2].

Despite optimistic forecasts regarding the discovery of new deposits and the development of advanced extraction technologies, it is evident that petroleum resources are finite. Over time, oil extraction will become increasingly difficult and expensive. There may eventually come a point when oil reserves remain available, but their extraction becomes economically impractical due to excessive production costs. Therefore, the actual cost of petroleum fuels will inevitably continue to rise.

Under these circumstances, several important questions arise:

1. Is there an alternative to piston internal combustion engines, or will they retain their dominant role in global energy systems?
2. Which fuels should be considered перспективіve in the near and long-term future?
3. What structural modifications will be required for piston engines to adapt to new fuel types?

As noted in [1], answers to these questions should be based on accumulated scientific knowledge, engineering experience, and the forecasts of leading specialists in the field of piston engines.

Historically, transport fuel transitioned from coal-based fuels to petroleum fuels approximately one hundred years ago. Today, another major transition is underway, this time toward natural gas. According to increasingly strict international environmental regulations, LNG (Liquefied Natural Gas) is regarded as one of the fuels of the future. Experts predict that LNG will become widely used in large-scale transportation systems. According to DNV (Det Norske Veritas), LNG conversion represents one of the most promising solutions for marine propulsion engines.

The high price of diesel fuel and growing environmental concerns have accelerated the development of technologies based on economical and environmentally friendly fuels such as natural liquefied gas. Compared to petroleum fuels, LNG offers significant advantages in terms of environmental protection, safety, reliability, and fuel economy. Research has shown that the use of LNG considerably reduces sulfur oxide (SOx) emissions and substantially decreases carbon dioxide (CO_2) and nitrogen oxide (NOx) emissions. LNG-fueled engines can achieve nearly zero sulfur oxide emissions, which is particularly important following the implementation of ECA regulations in 2015 and subsequent international standards. Due to the lower carbon content of LNG, harmful CO_2 emissions are reduced by approximately 25%.

Internal combustion piston engines remain among the most efficient thermal engines currently available, which explains their widespread application in all transport sectors. However, one of their major disadvantages is the dependence on petroleum-based liquid fuels. Therefore, further development prospects for these engines are directly associated with the transition toward gaseous and alternative fuels.

Diesel engine conversion can be implemented either through the gas–diesel cycle or through spark-ignition operation using gaseous fuels. The gas–diesel process is technically advantageous because the engine retains the ability to operate in conventional diesel mode when necessary. Gas–diesel engines typically employ qualitative load regulation. At the same time, combined regulation is recommended in order to avoid excessively rich mixtures, which increase hydrocarbon (CnHm) emissions and deteriorate fuel economy.

2. Preconditions and Methods for Solving the Problem

An important issue is the determination of the influence of pilot fuel dosage and injection advance angle on gas–diesel engine operation. To evaluate the influence of pilot fuel dosage, the dynamic factor is introduced as:

$$K=G_{di}/G_{gi} \quad (1)$$

where: G_{di} – quantity of pilot diesel fuel; G_{gi} – quantity of gaseous fuel.

It is also important to determine the equivalent excess air coefficient:

$$\alpha_{\text{eqv}} = \frac{L}{m_g l_g + m_d l_d} \quad (2)$$

where: *mg* – quantity of gaseous fuel; *lg* – air required for complete combustion of gaseous fuel; *md* – quantity of liquid fuel; *ld* – air required for complete combustion of liquid fuel; *L* – quantity of air entering the cylinder.

The ignition delay period plays a decisive role in ensuring an efficient engine working cycle. Therefore, when converting diesel engines to gaseous fuels and designing advanced dual-fuel engines, it is necessary to establish reliable relationships for determining the

ignition delay period τi\tau_iτi, allowing sufficiently accurate prediction of combustion onset.

Currently known ignition delay equations may generally be divided into two groups [2]. The first group includes equations based on the fundamental theory of chain reactions, particularly the equation proposed by Academician N.N. Semenov:

$$\tau_i = const p^{-n} e^{\frac{E}{RT}} \quad (3)$$

where: n – constant; R – universal gas constant; p – pressure; T – temperature; E – activation energy.

Some researchers introduced additional coefficients accounting for the specific features of the piston engine cycle, as proposed by Hiroyasu and co-authors [4]. Nevertheless, these equations remain variations of Equation (3) and generally contain exponential functions.

Consequently, obtaining reliable relationships for calculating ignition delay when diesel engines operate on various gaseous fuels

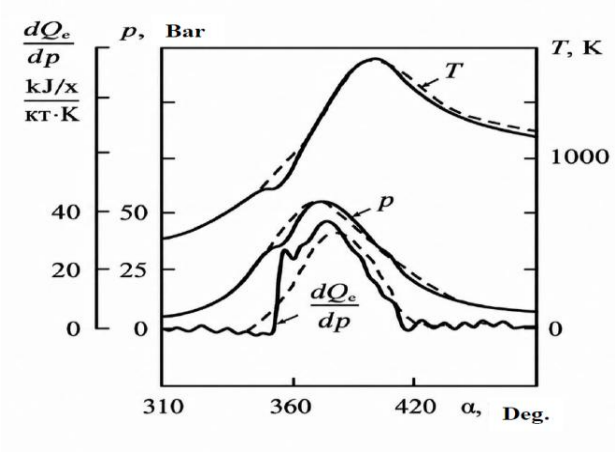


Fig. 1. *Pressure variation in the cylinder of a diesel engine converted to dual-fuel operation (LNG + pilot diesel fuel): experimental (solid line) and calculated (dashed line) results.*

The heat release rate variation $dQx/d\varphi=f(\varphi)$ during the working cycle is determined by processing the indicator diagram.

During fuel evaporation, heat absorption occurs when $dQx/d\varphi<0$, which subsequently changes into heat release after ignition when $dQx/d\varphi>0$ (Fig. 1). The instant when: $dQxd\varphi=0$ is accepted as the beginning of ignition.

Temperature and heat release rates were obtained from indicator diagram processing using Wiebe's law with combustion parameter m=2.03m = 2.03m=2.03.

The heat release characteristics in a dual-fuel engine confirm the statement of A.L. Boehman and O. Le Corre that the combustion process in dual-fuel engines consists of four stages:

1. ignition delay period - $dQx/d\varphi<0$
2. kinetic combustion of the pilot diesel fuel;
3. kinetic combustion of natural gas;
4. diffusion combustion of natural gas together with the remaining pilot fuel.

Among the factors determining good engine performance characteristics (power, torque, efficiency, etc.), combustion completeness and combustion rate are of decisive importance.

— compressed natural gas, liquefied gas, and hydrogen-containing synthesis gas — remains an important scientific and practical task. When operating on liquefied gaseous fuel, external mixture formation occurs because mixing begins in the intake system. Subsequently, the gas–air mixture is compressed inside the cylinder, while ignition is initiated near the end of compression through injection of a pilot dose of diesel fuel.

The volume between the gas injector and the combustion chamber must be carefully selected. Although a larger volume improves mixture homogenization, incorrect volume selection may produce undesirable effects. After the intake valve closes, a certain amount of gaseous fuel may remain trapped in this volume, potentially igniting in either the intake or exhaust systems.

In dual-fuel operation mode, the ignition delay period τi\tau_iτi is defined as the time interval between pilot diesel fuel injection and self-ignition of the liquefied gas–air mixture. The accuracy of determining τi\tau_iτi primarily depends on the method used to identify ignition onset. Several methods have been proposed [2]; in the present work, a method based on heat release rate analysis was employed.

Therefore, the adjustment of fuel supply system parameters and fuel injection advance angle must consider these factors.

The completeness of combustion for two-phase fuel combustion is calculated according to Wiebe's equation:

$$x = \beta \cdot x_1 + (1-\beta) \cdot x_2,$$

or:

$$x = \beta \cdot \left\{1 - e^{\left[a_1\left(\frac{\varphi-\varphi_{10}}{\Delta\varphi_1}\right)^{m_1+1}\right]}\right\} + (1-\beta) \cdot \left\{1 - e^{\left[a_2\left(\frac{\varphi-\varphi_{20}}{\Delta\varphi_2}\right)^{m_2+1}\right]}\right\},$$

where β is the phase separation coefficient. When the pilot diesel fuel quantity is approximately 10%, the coefficient for the first phase are: $\beta \approx 0.10-0.15$, and for the second phase – 1- β $\approx 0.85-0.90$.

The combustion rate with respect to crankshaft rotation angle is expressed as:

$$W_\varphi = \frac{dx}{d\varphi} = -\beta \cdot \frac{a_1(m_1+1)}{\Delta\varphi_1} \cdot \left(\frac{\varphi-\varphi_{10}}{\Delta\varphi_1}\right)^{m_1} \cdot e^{\left[a_1\left(\frac{\varphi-\varphi_{10}}{\Delta\varphi_1}\right)^{m_1+1}\right]} -$$

$$-(1-\beta) \cdot \frac{a_2(m_2+1)}{\Delta\varphi_2} \cdot \left(\frac{\varphi-\varphi_{20}}{\Delta\varphi_2}\right)^{m_2} \cdot e^{\left[a_2\left(\frac{\varphi-\varphi_{20}}{\Delta\varphi_2}\right)^{m_2+1}\right]}$$

Using the above relationships, calculations of combustion completeness and combustion rate for the diesel fuel + liquefied gas mixture were performed as functions of crankshaft rotation angle. Calculations and graphical analyses were carried out using Microsoft Excel Worksheet.

The following initial parameters were used:

- Phase separation coefficients: $\beta=0.1$, $1-\beta=0.9$;
- Shape coefficients: $m1=1$, ; $m2=2.5$;
- Combustion start angles: $\varphi 10=335^0$, $\varphi 20=340^0$;
- Combustion durations: $\Delta\varphi 1=12^0$, $\Delta\varphi 2=50^0$;
- Maximum combustion completeness: $x10max=0.999$, $x20max=0.999$;
- Constants: $a1=-6.908$, $a2=-6.908$.

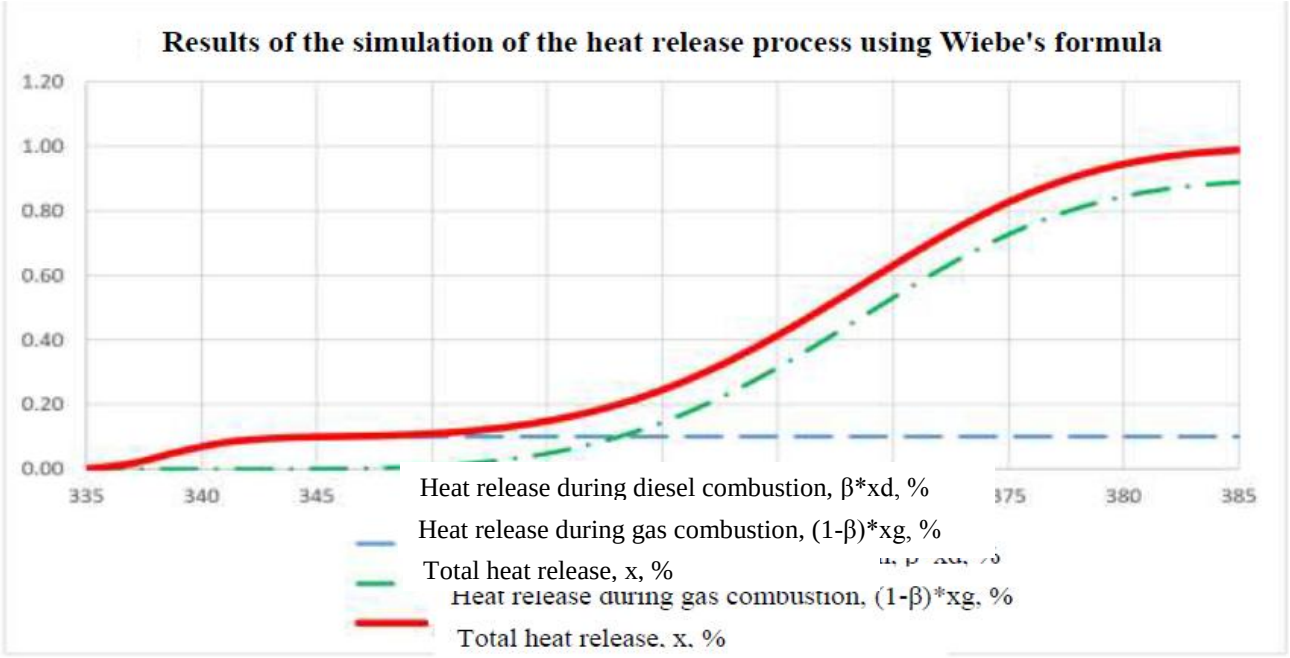


Fig. 2. *Dependence of combustion completeness on crankshaft rotation angle at $\varphi_{10}=335^0$; $\varphi_{20}=340^0$.(Other settings are the same)*

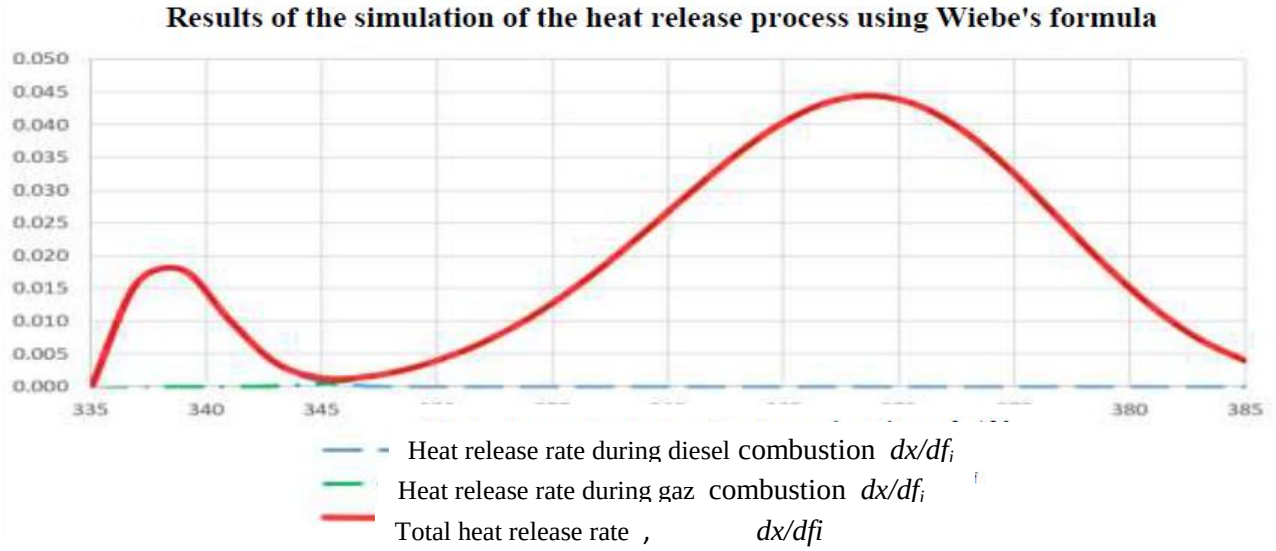


Fig. 3. *Dependence of heat release rate on crankshaft rotation angle at $\varphi_{10}=335^0$; $\varphi_{20}=340^0$.(Other settings are the same)*

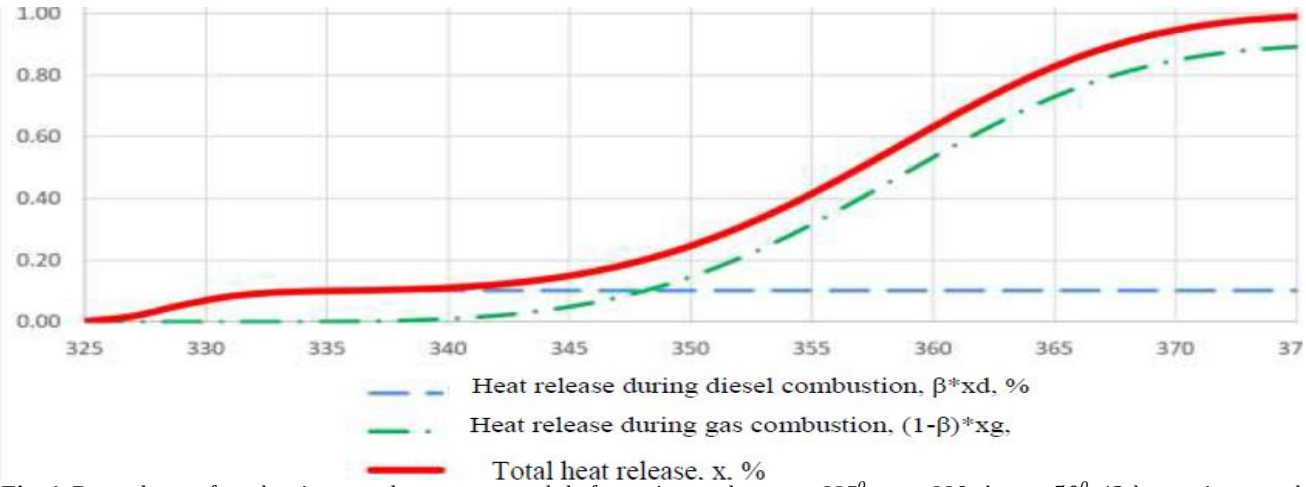


Fig. 4. *Dependence of combustion completeness on crankshaft rotation angle at $\varphi_{10}=335^0$, $\varphi_{20}=330$; $\Delta\varphi_2 = 50^{0\prime}$ (Other settings are the same)*

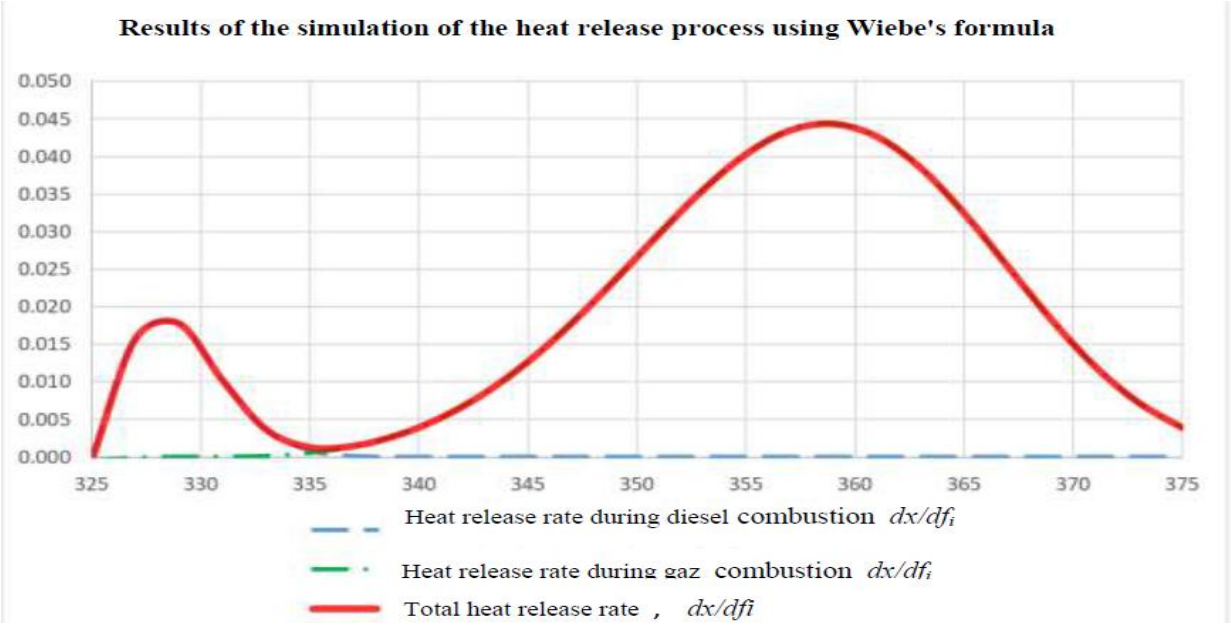


Fig. 5. *Dependence of heat release rate on crankshaft rotation angle at $\varphi_{10}=325^0$, $\varphi 20=330^0$. $\Delta\varphi_2 = 50^0$, (Other settings are the same)*

3. Conclusion

Figure 2 shows the dependence of combustion completeness on crankshaft rotation angle when pilot fuel injection occurs at 335∘335^\circ335∘. Under these conditions, combustion of both fuels is completed within the range of $335–385^0$ indicating a reduction in ignition delay and consequently improved effective engine parameters.

Figure 3 demonstrates that the maximum heat release rate for liquid fuel reaches 0.018 at 338^0, whereas for liquefied gas fuel the maximum value of 0.045 is achieved at 368^0 .

Figures 4 and 5 illustrate the same parameters when liquid fuel injection occurs earlier, at 325^0. In this case, complete combustion occurs within the range of $325^0–375^0$. The maximum heat release rate for liquid fuel reaches 0.018 at 327^0 , while for gaseous fuel it reaches 0.045 at 357^0 . Such an early injection advance is not acceptable because the piston has not yet reached top dead center, while the heat release rate already reaches its maximum value. This leads to piston deceleration and consequently reduces effective engine performance parameters.

Therefore, analysis of the theoretical research results demonstrates that combustion duration and heat release rate depend on pilot fuel properties (particularly self-ignition temperature), pilot fuel quantity, and injection advance angle. The theoretical investigation established that for liquefied natural gas and pilot diesel fuel operation, fuel injection at nominal engine speed should occur at a crankshaft rotation angle of approximately 335^0∘.

4. References

1. Galyshev Yu.V., Magidovich L.E. *Prospects for the Use of Gaseous Fuels in Internal Combustion Engines.* Dvigatelestroyeniye, 2001, No. 3, pp. 31–35.
2. Kavtaradze R.Z. *Theory of Piston Engines. Special Chapters.* Moscow: Bauman Moscow State Technical University Publishing House, 2008, 720 p.
3. Boehman A.L., Le Corre O. *Combustion of Syngas in Internal Combustion Engines.* Combustion Science and Technology, 2008, Vol. 180, No. 6, pp. 1193–1206.
4. Hiroyasu H., Kadota T., Arai M. *Fuel Spray Characterisation in Diesel Engines.* In: Mattavi J.N. and Amann C.A. (eds.), *Combustion Modeling in Reciprocating Engines.* Plenum Press, 1980, pp. 369–408.

Piston secondary dynamics and their effect on blow-by, friction and power loss.

Erjon Selmani[1], Shpresa Caslli[1], Fadil Likaj[2]
Polytechnic University of Tirana, Albania[1]
European University of Tirana, Albania[2]
eselmani@fim.edu.al

Abstract: *In this paper the effect of the piston secondary dynamics was investigated. The piston secondary dynamics comprises the rotation around the pin axis and the translation of the piston body between the two sides of the liner. The most prominent situation of this motion arises on diesel engines. For this purpose ©Ricardo RINGPACK simulation suite was used to simulate the behavior of the piston and rings of a turbodiesel engine. In particular, three aspects of the work of the engine were analysed: Gas blow-by, friction and power losses of the pack. In order to detect the magnitude of the secondary dynamics of the piston, the engine was simulated in two conditions, with and without the secondary motions of the piston. According to results, the rings of a piston without the secondary motion, maintain a more stable position in relation with the piston groove and are more able to prevent gas flows. Furthermore, the secondary motions elimination seems to decrease the friction between components and thus to slightly improve the power loss of the assembly, although at a smaller magnitude with respect to the blow-by gasses.*

Keywords*: PISTON SECONDARY DYNAMICS, PISTON RINGS, BLOW-BY, POWER LOSS.*

1. Introduction

The piston is responsible to transmit the power and torque to the crankshaft while the rings are responsible to seal the combustion chamber. They work together and affect each other at the same time. The rings have three degrees of freedom, axial, radial and twist, and their motion is a combination of inertia, gas pressures and friction forces [1-2]. The piston primary motion is the translation between the dead centers, however it undergoes also to a secondary motion which is a combination of a rotation and a displacement perpendicular to the axis. The secondary dynamics negative effects associated with this movement are engine noise (especially when the engine is cold), wear of the surfaces and cavitation of the lubricating oil [3-4]. The secondary motion is related to the eccentricity of the wrist-pin axis and to the gap between the piston skirt and the liner. Previous studies have highlighted several factors affecting the gas dynamics [5, 6]. In literature, previous analyses [7] have thoroughly considered the tribological performance, in [yang] the structural parameters on the secondary motion are analysed, [8-9] detailed a model of the piston secondary motion for understanding the vibration due to the piston slap.

This study is designed to understand how secondary piston dynamics affect ring sealing capacity and package power losses, as a combined effect rather than separate approaches.

The present work features a specific analysis which will be done comparing the same engine with and without the secondary motion. The mathematical model of the problem was formulated in terms of ring, gas and piston dynamics and solved in ©Ricardo RINGPAK and elaborated in Matlab®. The analysis was applied to a turbo diesel engine and the performance of the ring-pack was evaluated in terms of inter-ring pressures, ring axial and radial dynamics, ring-liner clearances and blow-by gases. The results are then discussed and compared between the cases and the work ends with the conclusions stemming from the discussions.

2 Piston Secondary Motion Model

The secondary dynamics of the piston are shown in Figure 1, it reflects the displacement of the piston normal to the axis (slap) and the rotation around the wrist pin (tilt).

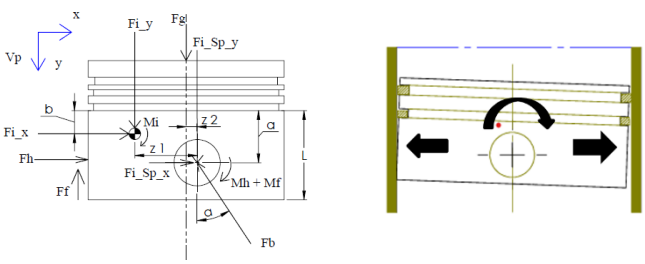


Fig. 1 *Free body diagram of the piston and piston secondary motions*

The equations (1)-(3) below are necessary to model the piston secondary dynamics are written below. Those equations include gas and inertial forces, but also the hydrodynamic forces related to the oil film pressure and its viscous friction effect.

(1) $$F_g - F_f + F_{i\_y} + F_{i\_Sp\_y} - F_b * cos\alpha = 0$$

Where: F_g is the gas force, F_f is the friction force, F_{iy} is the inertia force on y, F_{ispy} is the inertia force on the wrist pin, F_b is the connecting rod force.

(2) $$F_h + F_{i\_x} + F_{i\_Sp\_x} - F_b * sin\alpha = 0$$

Where: F_h is the hydrodynamic force, F_{ix} is the inertia force on x, F_{ispx} is the inertia force on the wrist pin.

(3) $$M_h + M_f + M_i - F_b * z2 - F_{iy} * z1 + F_{i_y} * (a - b) = 0$$

Where :M_i inertia moment on the piston, M_h, M_f, hydrodynamic and friction moments on the wrist pin, a, b, z1 z2 dimensions,
L skirt length.
The hydrodynamic pressure exerted by the oil on the surfaces can be calculated using the 2-dimensional Reynolds equation with partial derivatives (4).

(4) $$\frac{\vartheta}{\vartheta_y}\left(h^3\frac{\vartheta_p}{\vartheta_y}\right) + \frac{1}{R^2}\frac{\vartheta}{\vartheta_\varphi}\left(h^3\frac{\vartheta_p}{\vartheta_\varphi}\right) = -6\mu V_p\frac{\vartheta_h}{\vartheta_y} + 12\mu\frac{\vartheta_h}{\vartheta_t}$$

Where : h is the oil film thickness, μ is the dynamic viscosity, Vp is the piston velocity. R is a conversion factor.

3.1 Modelling Of Gas And Ring Dynamics

In order to compute the inter-ring gas pressures and flows, the ideal gas equation (4) is coupled with the continuity equation (5).

(4) $$\left(\frac{dp}{dt}v + \frac{dv}{dt}p\right) = \left(\frac{dm}{dt}\right)RT + mR\left(\frac{dT}{dt}\right)$$

Where : p is the pressure, v is the volume, m is the gas mass, R is gas constant and T is the inter-ring temperature.

(5) $$\frac{dm}{dt} = Q_{in} - Q_{out}$$

Where Qin, Qout are the mass flow entering and exiting a crevice

The flow through the gap can be modeled using the orifice-flow model for a laminar and compressible flow, meanwhile the temperature of the gas can be assumed to have an isothermal distribution and thus be equal to the temperature of the surrounding walls.

Consequently, the equilibrium equations (Newton's second law) for axial, radial and torsional motion of each ring can be written according to equations (6) to (8).

(6) $$m_r\frac{d^2x}{dt^2} = F_P - F_i - F_s - F_f$$

Where mr is the mass of the ring, indexes mean pressure, inertia, squeeze from oil, friction.

(7) $$m_r \frac{d^2y}{dt^2} = F_{gas_{back}} + F_{tension} - F_{gas} - F_{Poil}$$

Where the forces are exerted in radial faces of the ring

(8) $$I \frac{d^2\alpha}{dt^2} = M_{gas} + M_{gr\_oil} + M_{l\_oil} - M_{pre}$$

Where I is the ring moment inertia,α is the ring rotation.

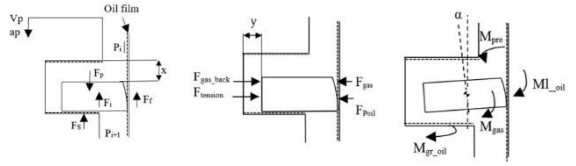


Fig. 2 *Free body diagram of the rings*

4.3 Modelling Of Boundary And Lubricated Contact

In this work, the clearance between the two interacting surfaces when there is contact is modeled using the Greenwood-Tripp model, equation (9). It is a statistical contact mechanics model based on the clearance distribution h and the composite asperity parameters (surface roughness), when the lubricating film becomes thin enough that surface asperities begin to touch. The outcome of the model is the so called asperity pressure profile Pa .

(9) $$P_a = \frac{16\sqrt{2}}{15}\pi(\eta\beta\sigma)^2 E \sqrt{\frac{\sigma}{\beta}} F\left(\frac{h}{\sigma}\right)$$

Where: η is the composite asperity density, β is the composite radius of curvature of asperities, σ is the composite R.M.S. surface asperity height, E is the elastic modulus of the contact surfaces.

After the asperity pressure, we calculated the asperity shear stress, according to equation (10) below.

(10) $$\tau_a = C * P_a$$

Where C is the friction coefficient of the coupled surface.

Then the calculation of the power loss due to asperities (11).

(11) $$P_{a\_loss} = F_{asperities}\, v = \int_{x1}^{x2} L\, \tau_a\, v\, d_x$$

Where $F_{asperities}$ is the asperities friction force, L is the ring length, v is the velocity.

The total friction which the rings are subjected is composed of two parts, as given in equation (12)

(12) $$Ftotal = Fhydrodynamic + Fasperities$$

The hydrodynamic or viscous friction force can be computed according to equation (13) below.

$$F_{hydrodynamic} = \int \tau_\omega\, dA$$

Where τ_ω is the oil shear stress and is a function of the oil velocity and dynamic viscosity μ, which can be easily computed from the Reynolds theory of thin-film lubrication.

3 Simulation

Theoretically speaking, the piston dynamics affects the ring dynamics and both are able to interfere in the gas flow due to the equilibrium of forces and moments.

Each ring is allowed to have three degree of freedom, so does the piston, while the gas flows through a complex series of channels and crevices between two large volumes (combustion chamber and crankcase). Previous authors have investigated other parameters and factors that affect the ring dynamics and gas flow, but in none of these cases has the effect of the secondary piston movement been specified as the only parameter investigated.

At this purpose RINGPAK Solver of ©Ricardo was used to perform simulations. In this case a turbodiesel 4-cylinder engine was used as a reference, running at full load condition and three speed regimes: 2000, 3000 and 4000 rpm.

The geometry and dimensions of the rings are given in figure 3.

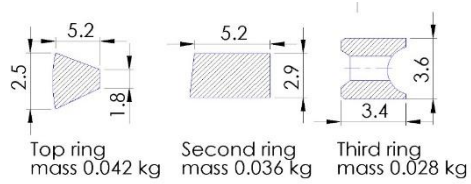


Fig. 3 *Ring geometry, dimensions and masses*

The model requires also the oil type and properties, as well as the lubrication model and respective boundary conditions. For this purpose a SAE Grade 5W30 oil was used, on the other hand Navier-Stokes lubrication model with half-Sommerfeld ring-liner boundary conditions is adopted. The ring-liner contact is depicted in figure 4.

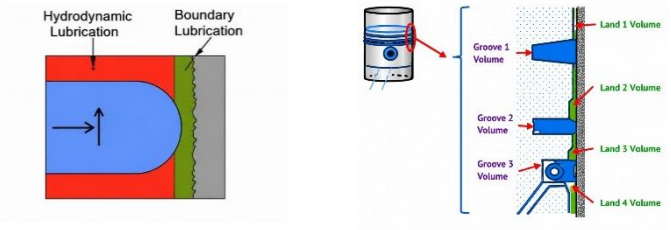


Fig. 4 *Ring – Liner contact under boundary and hydrodynamic lubrication (left). Inter ring crevices (right)*

In order to proceed with the solution of the mathematical model, some assumptions are needed with respect to the gas-flow model. We will assume a uniform gas pressure in each land and groove volume. The gas used is assumed to behave as an ideal gas, hence it obeys to the ideal gas equation, with its temperatures in the several orifices to be assumed iso-thermal. To calculate the gas mass flow rate, the isentropic gas flow model has been used.

Given the large clearance at the piston edge, the crown top land pressure can be set equal to the cylinder pressure, while the piston bottom land pressure equal to the crankcase.

The surface asperity profile and data are taken from the engine manufacturer, while the piston and cylinder liner distortions have been accounted from previous works, figure 5.

The cylinder bore distortion affects the ring conformation the correct through the radial contact of the ring face to the liner.

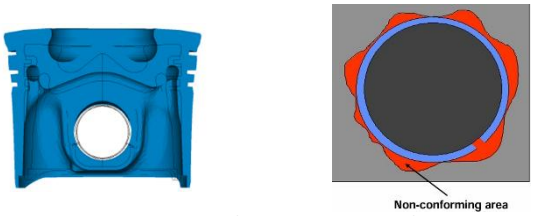


Fig. 5 *Piston distortion (left) and ring non conformability to a distorted bore (right)*

The simulations were repeated twice for each speed value, with and without the piston secondary motion. A series of outcomes were

then analysed, in particular the ring motions, the inter ring pressures, the piston dynamics, the gas flow,the blow-by the friction forces and the power loss form the ringpack. The results were analysed and compared between the two cases taken in exam.

4 Simulation, results and discussion.

4.1 Base Case: 2000 rpm, piston secondary motion enabled.

In figure 6, are depicted the ring axial locations during a complete cycle of 720 degree of the crank angle, for the 2000 rpm case. The first ring lifts substantially only during the exhaust and intake stroke of the working cycle, when the gas pressure above this ring is lower than the pressure below it. The second ring shows a nearly unstable position, while the third ring is always seated.

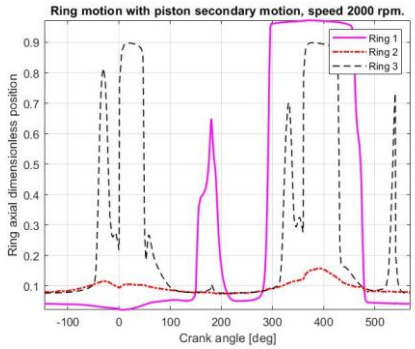


Fig. 6 *Ring axial positions during a cycle*

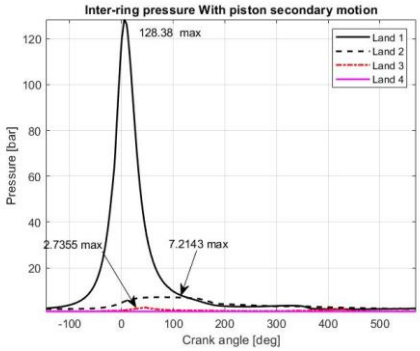


Fig. 7 *Inter-Ring pressures*

Figure 7 shows the inter-ring pressures during a cycle with the respective maximal values, while figure 8 shows the blow-by curves. The positive area is the downward direction of the gas, the negative area is the upward direction, the difference in area represents the lost gasses to the crankcase or blow-by.

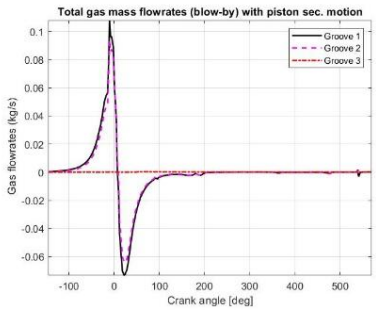


Fig. 8 *Blow-by for a complete cycle*

In figure 9 are represented the ring friction force curves. As depicted, the maximal value of this force is reached from the top ring during the beginning of the expansion stroke, with a maximal value of 650 Newton. In the following figure 10, are depicted together the asperity and hydrodynamic forces. As it clearly showed, the asperity friction if the far most important of the two.

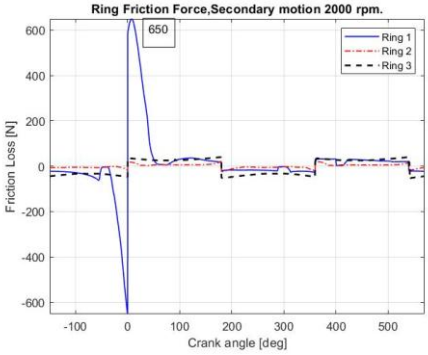


Fig. 9 *Ring friction force*

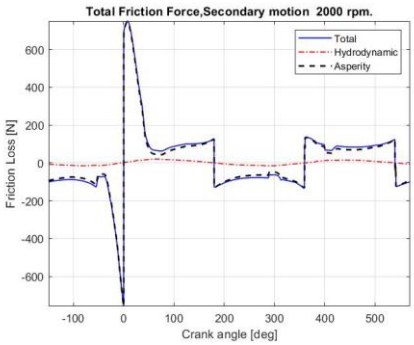


Fig. 10 *Total ring friction force*

In the following figure 11 and 12 are depicted the power losses for this case for a cycle. As figures witness, the total power loss from the ring pack, for a cycle is nearly 3.8 kw. Just for clarity, the effective power of the engine is 115 kw.

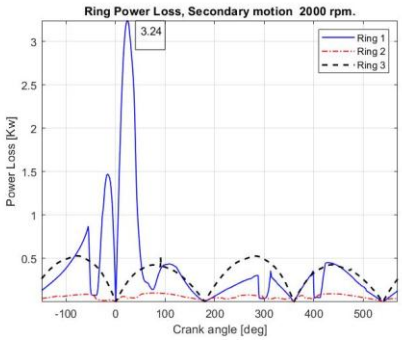


Fig. 11 R*ing power loss*

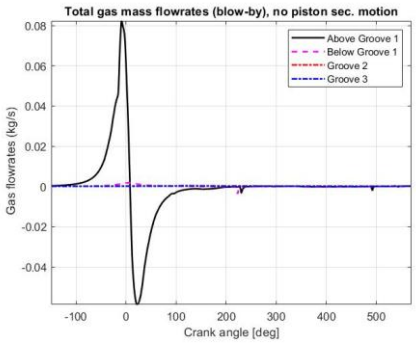


Fig. 12 *Total Ring power loss*

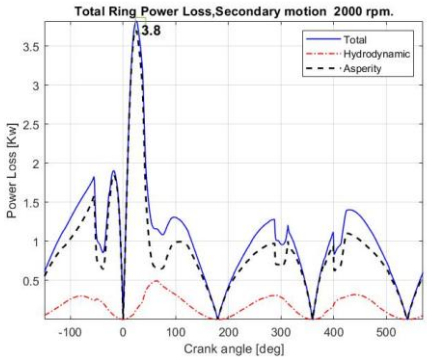


Fig. 13 *Ring axial positions, no secondary motion during a cycle*

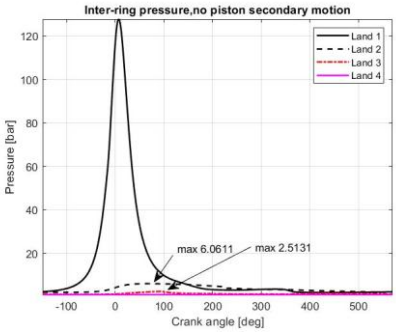


Fig. 14 *Inter-ring pressures, no secondary motion*

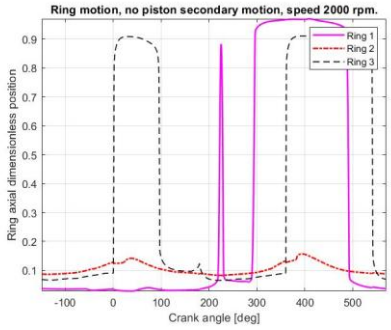


Fig. 15 *Blow-by, no secondary motion.*

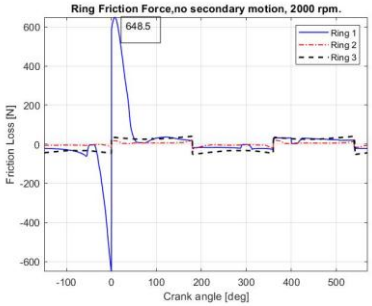


Fig. 16 *Ring friction force, no secondary motion*

4.2 Alternative Case: 2000 rpm, piston secondary motion Disabled.

In figures 13 are depicted the ring axial locations. As we can see, the top ring has a similar behavior, while the second ring seems to be more stable. According to figure 14, the peak pressure of the second land is lower in comparison to the previous case, which is a clear sign of a better sealing of the first ring. At last, in figure 15 the blow-by values are clearly lower. In figures 16 to 18 are depicted the friction forces and power losses for the ring pack. In this case, the curves are similar to the previous case but the friction and the power loss are higher.

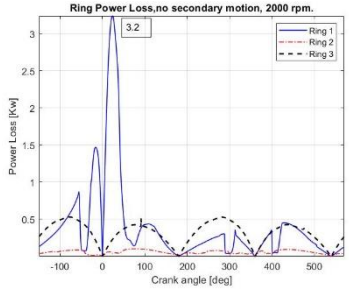


Fig. 17. R*ing power loss, no secondary motion*

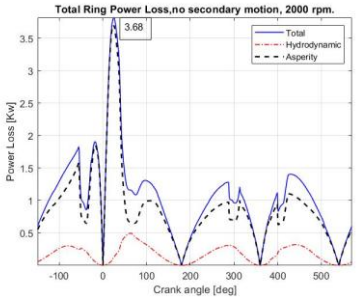


Fig. 18. *Total power loss, no secondary motion*

4.3 Comparison for 3000 and 4000 rpm case.

In table 1 below, are reported the values of gas blow-by for the other two cases, namely 3000 and 4000 rpm and compared to the 2000 already described.

In table 2 instead, are reported the values of ring friction forces and power losses for the other cases and compared between them.

Table 1*. Total blow-by gas in mass for every simulated case*

	Blow-by		
Case	2000 rpm	3000 rpm	4000 rpm
Base (secondary motion enabled)	0.1194 [kg]	0.102 [kg]	-0.00785 [kg]
Secondary motion disabled	0.00612 [kg]	0.0053 [kg]	0.00403 [kg]

Table 2: *Ring one Friction force and total Power loss for every case analysed.*

	Total Ring 1 friction force [N]/total power loss [kW]		
Case	2000 rpm	3000 rpm	4000 rpm
Base Case (secondary motion enabled)	650/3.8	728.4/5.56	729.4/7.46
Secondary motion disabled	648.5/3.68	726/5.45	727/7.40

According to the results of table 1, increasing the engine speed the blow-by level reduces, the reduction is more remarked in the case of the original setup with the secondary motion included. When the secondary motion of the piston is disabled, the blow-by undergoes to a steady reduction, which can be synonymous of a normal functioning of the piston and the ring-pack. On the other hand, the negative value for the base case and 4000 rpm speed can be related to a irregular working condition of the rings, namely axial flutter and radial collapse, as described in certain references. Figure 19 explains how the ringpack performs with and without the secondary motion.

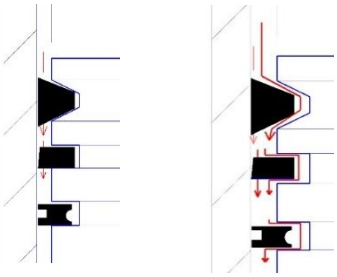


Fig. 19. *Piston-liner clearances with and without secondary motion.*

From the values reported in table 2, it is possible to note how the engine performance drops in terms of friction force and power loss. Increasing the engine speed increases the friction force due to asperities, which is always the dominant factor. On the other hand, with the secondary motion disabled, the friction forces and consequently the power loss is slightly lower than the base case. This result may be related to the contact pattern of the rings to the liner, which without the secondary motion, it may result in a smaller contact surface,

5 Conclusion.

An internal combustion engine was simulated virtually through ©Ricardo RINGPAK suite to understand the impact of the piston secondary motion on the sealing capability of the ringpack and the effect on the friction force and power losses from the ring pack.

The secondary motion of the piston is a combination of a tilt and a displacement which may occur to the piston during certain strokes, and force the piston to move perpendicularly to the cylinder axis or to rotate around the pin axis. In this analysis a turbo-diesel 4-cylinder engine was used as a test at full load, and three different speeds; 2000, 3000 and 4000 rpm.

According to the analysis and discussion and comparison of the results in table 1, the engine with the disabled secondary motion is able to perform much better in terms of containment of blow-by gasses.

The main reason for this is a better positioning of the piston and the rings both in axial and radial direction in relation to the contact with the groove and the liner wall.

When the piston tilts and twists, it is pushed against one side of the liner, opening more crevices on the opposite side. In this situation, the rings are unable to seal properly because the gas can flow easily through the grooves and past the rings in addition to the ring gaps.

In addition, when the secondary motion is included, the ring twist angles are altered between positive and negative, which is a sign of a non-optimal positioning and possible instability.

On the other hand, without the secondary motion, even the ring friction forces (mainly asperity) and the power losses are lower than with the secondary motion, although of a lower magnitude than the differences in blow-by.

The secondary motion of the piston is used in some diesel engines, for reducing the force component against the cylinder wall, but it may be also a consequence of the wear of the piston skirt and cylinder liner due to the mileage. Its elimination could bring positive effects, but sometimes it is necessary to be accounted.

6. References

1. Keribar, Rifat, Zafer Dursunkaya, and Michael F. Flemming. "An integrated model of ring pack performance." ASME, Transactions, Journal of Engineering for Gas Turbines and Power 113 (1991): 382-389.

2. Wannatong, Krisada, Somchai Chanchaona, and Surachai Sanitjai. "Simulation algorithm for piston ring dynamics." Simulation Modelling Practice and Theory 16.1 (2008): 127-146.

3.Tan, Yeow-Chong, and Zaidi Mohd Ripin. "Analysis of piston secondary motion." Journal of Sound and Vibration 332.20 (2013): 5162-5176.

4. Delprete, Cristiana, Abbas Razavykia, and Paolo Baldissera. "Detailed analysis of piston secondary motion and tribological performance." International Journal of Engine Research 21.9 (2020): 1647-1661.

5. Delprete, Cristiana, Erjon Selmani, and Arian Bisha. "Gas escape to crankcase: impact of system parameters on sealing behavior of a piston cylinder ring pack." International Journal of Energy and Environmental Engineering 10.2 (2019): 207-220.

6. Selmani, Erjon, Cristiana Delprete, and Arian Bisha. "Engine Speed and Load Effect on the Sealing Capacity of a Piston Ring-Pack." International Conference “New Technologies, Development and Applications”. Cham: Springer International Publishing, 2020.

7. Delprete, Cristiana, Abbas Razavykia, and Paolo Baldissera. "Detailed analysis of piston secondary motion and tribological performance." *International Journal of Engine Research* 21.9 (2020): 1647-1661.

8. Tan, Yeow-Chong, and Zaidi Mohd Ripin. "Analysis of piston secondary motion." *Journal of Sound and Vibration* 332.20 (2013): 5162-5176.

9. Yang, Haixiang, et al. "Research on the influence of key structural parameters on piston secondary motion." *Scientific Reports* 11.1 (2021): 19080.